Energy Conversion by Permanent Magnet Machines and Novel Development of the Single Phase Synchronous Permanent Magnet Motor

Richard Johnston Strahan
B.E.(Hons)

A thesis presented for the degree of
Doctor of Philosophy
in
Electrical and Electronic Engineering
at the
University of Canterbury,
Christchurch, New Zealand.

September 1998

ABSTRACT

Energy methods are widely used and well understood for determining the torque or force in machines which do not contain permanent magnets. Energy methods are employed to calculate torques or forces of magnetic origin after determination of the energy stored in the electromechanical coupling field. In this thesis, the energy stored in a permanent magnet system is defined, and the energy-coenergy relationship is determined. It is shown how residual magnetism can be incorporated into classical electromechanical coupling theory. It is therefore shown how equations for torques or forces can be derived for permanent magnet systems using energy methods.

An analytical method of calculating permanent magnet reluctance torque is developed. The method uses an elementary expression for the magnetic field to obtain the stored energy. This enables an analytical expression for the reluctance torque waveform to be obtained. The method is demonstrated to provide a powerful and fast design tool. The method can be generally applied to reluctance torque problems where the airgap is reasonably smooth.

The single phase synchronous permanent magnet motor is used in domestic appliances. It is a motor of very simple construction and high reliability, which is directly connected to an AC mains supply, and runs at synchronous speed. It is becoming increasingly used in preference to the shaded pole induction motor. However, its application is limited by the following characteristics. There is no control over the final direction of rotation, unless a mechanical blocking device is used. There are rotor positions at which only a very small starting torque is available. The characteristic twice electrical frequency torque pulsation yields a speed modulation of the same frequency, which can cause acoustic noise problems. A method of improving torque quality by improving the motor design is proposed to alleviate these limiting characteristics. This is achieved by designing a permanent magnet reluctance torque which cancels out the effect of the backward rotating component of the stator field. In this novel design, the permanent magnet reluctance torque effectively acts as a second balancing phase.

An unconventional technique for starting a single phase synchronous permanent magnet motor is demonstrated. This technique uses an inductive reluctance torque, provided by placing a suitably shaped iron lamination on the rotor, to rotate the rotor to a position from which starting can occur.

ACKNOWLEDGEMENTS

I am very grateful to a number of people who have enabled me to complete the work presented herein. I thank Associate Professor David Watson for his advice and patience, through both my undergraduate and postgraduate years. My interest in electrical machines gathered momentum as a result of his undergraduate machines course. I would like to thank Associate Professor Pat Bodger for his advice and encouragement, and also Associate Professor Harsha Sirisena. I thank Ken Smart for his help in the machines laboratory. I thank Dr John Smaill for his enthusiasm and assistance in the mechanical design of my machines.

I am greatly indebted to Dr J.D. Edwards of the University of Sussex, and to Dr Gerald Altenbernd of the University of Hannover, without whose help this work could not have been possible. I thank Dr Edwards for the finite element analysis work he has done for me, and for his valued correspondence. I thank Dr Altenbernd for kindly answering many questions, and for arranging to send me the single phase motors, courtesy of Siemens.

I thank my postgraduate friends for their help, particularly Dr Rob Van Nobelen for his assistance with mathematical matters. Finally, I thank Rosemary for her care and support during my studies.

CONTENTS

GLOSSARY

Principal Symbols

Vector quantities are denoted by bold face type

A, a	area
a	normalised amplitude of rotor speed modulation
$\mathbf{B}$, B	magnetic flux density
B_r	residual flux density
B_o	residual flux density for a minor demagnetisation loop
D	diameter
D_r	rotor diameter
d	direct
E	RMS electromotive force
e	instantaneous electromotive force
$\mathbf{F}$, F	force
$\mathcal{F}$	magnetomotive force (MMF)
f	electrical frequency (cycles per second)
$\mathbf{H}$, H	magnetic field intensity
H_{cB}	inductive coercive force
I	DC current; RMS current
I_{lkr}	RMS value of the locked rotor current
i	instantaneous current
$\mathbf{J}$, J	current density
J	total moment of inertia
J_r	rotor moment of inertia
$\jmath$	$\pi/2$ operator, $\sqrt{-1}$
K_L	winding inductance constant
K_m	permanent magnet flux linkage constant
K_R	winding resistance constant
L	inductance
L_a	additional inductance component (for inductive start motor)
L_c	conventional inductance component (for inductive start motor)

$L_\circ$	DC value of inductance
$\hat{L}$	amplitude of inductance modulation
L_m, l_m	permanent magnet thickness
L_t	airgap modulation depth
L_{stk}	axial length of the stator lamination stack
l	length
$\mathbf{M}$	induced polarisation
M	mutual inductance
$\mathbf{M}_\circ$	residual magnetisation
N	north pole
N	total number of series connected turns
$\mathbf{n}$	unit normal vector
n	turns per pole
P	power
$\mathcal{P}$	magnetic permeance
P_R	resistive power loss
p	pole pair number
q	quadrature
R	resistance
R, r	radius
$\mathcal{R}$	magnetic reluctance
S	surface
S	south pole
T	instantaneous torque
T_{ind}	inductive reluctance torque, $\frac{1}{2}i^2\frac{dL}{d\theta}$
$T_{ind\,a}$	additional component of inductive reluctance torque
$T_{ind\,c}$	conventional component of inductive reluctance torque
T_l	load torque
T_{ph-m}	mutual phase-magnet torque, $i\frac{d\lambda_m}{d\theta}$
T_r	permanent magnet reluctance torque
$\hat{T}_r$	amplitude of permanent magnet reluctance torque
$\overline{T}$	average torque
$\overline{T}_p$	pullout torque
t	time
V	RMS voltage; DC voltage
V, v	volume
v	instantaneous voltage
W	stored magnetic field energy
W'	magnetic coenergy
W_a	stored magnetic energy of an airgap or magnetically linear region

W_r	total stored magnetic energy for zero currents, $W_r = W(i=0)$
$\hat{W}_r$	amplitude of stored energy modulation for zero currents
W_m	stored magnetic energy of the permanent magnet region
w	stored magnetic energy density
w'	magnetic coenergy density
X	reactance
x	linear displacement
Z	impedance
α	impedance angle defined by arctan $\left(\frac{\omega_e L}{R}\right)$
β_1	phase angle of the fundamental component of the EMF/torque function
Γ	pullout ratio
γ_l	inductance displacement angle
γ_{la}	additional inductance component displacement angle
γ_{lc}	conventional inductance component displacement angle
γ_r	permanent magnet reluctance torque displacement angle
γ_{st}	start angle for the inductive start motor
Δ	incremental difference
ϵ	phase angle of the AC supply voltage
η	efficiency
θ	rotor angle
θ_s	spatial angle
θ_o	load angle
$\dot{\theta}$	instantaneous rotor speed
$\hat{\dot{\theta}}$	amplitude of rotor speed modulation
λ	flux linkage
λ_m	permanent magnet flux linkage
μ	absolute permeability
μ_r	relative permeability
μ_o	permeability of free space ($4\pi \times 10^{-7}$ H/m)
ξ_m	permanent magnet flux linkage factor
ρ_c	resistivity of copper
ϱ_c	mass density
τ	time period
ϕ	magnetic flux
ϕ_m	permanent magnet flux linking a single turn
φ	electrical angle between phasors V and I_1
χ_m	magnetic susceptibility
ω_e	electrical angular frequency

Subscripts

a	airgap or magnetically linear region
g	airgap
l	load
m	permanent magnet
n	normal
s	iron or soft magnetic material
t	tangential
1	first; fundamental component
2	second; second harmonic component
$\parallel$	parallel
$\perp$	perpendicular
$\emptyset$	initial value

Superscripts

$\hat{}$	amplitude
$^\circ$	degrees

Abbreviations

AC, ac	alternating current
DC, dc	direct current
CAD	computer aided design
EDM	electro-discharge machining
EMF	electromotive force
FEA	finite element analysis
MMF	magnetomotive force
PM	permanent magnet
RMS	root-mean-square
RPM	revolutions per minute
TRV	torque per unit rotor volume

PREFACE

The single phase synchronous permanent magnet motor, in terms of construction, is perhaps the simplest of all electric motors. It consists of a U-shaped laminated iron yoke, a copper winding, and a rotor magnet. Given its simplicity, I believed that the single phase motor would be a good starting point from which I could build an understanding of permanent magnet machines, in general. However, I soon discovered that its constructional simplicity was a deceptive lure that masked a motor of great analytical complexity. The dynamic behaviour of the motor is described by nonlinear differential equations, and the often erratic motion of the rotor can only be predicted by numerical computation. Due to this motional behaviour, it has been referred to as a 'chaos' motor. While it is used in domestic appliances, several of its characteristics limit its application. Much of this thesis looks at improving these characteristics. A synopsis of the thesis is described as follows:

Chapter 1 introduces the single phase synchronous permanent magnet motor, and describes the characteristics which limit its application. It is proposed that if a constant instantaneous motor torque can be provided, then some of the limiting characteristics are eliminated. A constant instantaneous torque is achieved through the design of the motor, using a specially *designed* permanent magnet reluctance torque. This concept is implemented in two different motor designs in later chapters.

Chapter 2 presents a subject of fundamental nature in regard to electrical machines. Electromechanical energy conversion theory is introduced. This theory is well understood for electrical machines which do not contain permanent magnets. In this chapter, the energy relationships in a permanent magnet system are defined, and it is shown how the classical theory can accommodate machines which contain permanent magnets. Results of this theoretical analysis are applied elsewhere in the thesis.

The next three chapters are devoted to three novel single phase permanent magnet motors.

Chapter 3 examines a motor design which implements the constant instantaneous torque concept introduced in chapter 1. A permanent magnet reluctance torque of triangular shape is required. This single phase motor has a trapezoidal back EMF and requires a DC to AC inverter. Experimental measurements are presented. To aid in the design of this motor, an analytical method of calculating permanent magnet reluctance

torque is developed.

Chapter 4 examines another motor design which implements the constant instantaneous torque concept. This motor requires sinusoidal voltage and current waveforms. Like the conventional motor, this motor is suitable for direct connection to an AC supply.

Chapter 5 investigates a single phase synchronous permanent magnet motor which uses an unconventional technique for starting. Apart from some small design modifications, this motor is identical to the conventional motor. The technique is demonstrated experimentally.

Chapter 6 summarises conclusions, and presents suggestions for further research. During the course of the work presented in this thesis, the following papers have been prepared:

STRAHAN, R.J., 'Energy conversion by nonlinear permanent magnet machines', *IEE Proc.-Electr. Power Appl.*, Vol. 145, No. 3, May 1998, pp. 193–198.

STRAHAN, R.J. AND WATSON, D.B., 'Effects of airgap and magnet shapes on permanent magnet reluctance torque', *IEEE Trans. Magn.*, Vol. 35, No. 1, January 1999, pp. 536–542.

Chapter 1

INTRODUCTION

Rotating electrical machines perform an important role in almost every aspect of modern society. Electrical machines convert mechanical energy into electrical energy, or vice-versa. These machines range from generators having power capabilities of a thousand megawatts or more, to micromotors of a few milliwatts [Say and Nasar 1987]. Generators produce electrical energy for power supply networks, and electric motors are electrical to mechanical energy converters of a large proportion of this energy. Infact, about 65% of electrical energy is consumed by electric motor drives [Gieras and Wing 1997]. Electric motors, in particular, impact directly on our lives. For example, many domestic appliances contain electric motors, as do personal computers and their peripherals. The number of electric motors in the home can easily exceed fifty [Nasar and Unnewehr 1983]. There are numerous electric motors in modern vehicles. Electric motors are involved in every industrial and manufacturing process.

Electric motors may be broadly categorised as being either small or large. In comparison to large electric motors, [Veinott 1987] states that small electric motors involve "more types, more units, and more money." Most small electric motors have to operate on single phase alternating current because this is the type of energy most readily and most economically available. Most homes are supplied with single phase power. Consequently, most domestic appliances employ single phase motors [McPherson 1981]. Much of this thesis focuses on a small electric motor called the *single phase synchronous permanent magnet motor*, which is used in a variety of domestic appliances. The power output of this motor typically ranges from a few watts to a few tens of watts.

1.1 SMALL ELECTRIC MOTORS

This section identifies where the single phase synchronous permanent magnet motor lies within the family of small motors. A large variety of motor types exist within this category, and each type will be briefly covered. Particular attention is paid to the starting mechanism of each type of motor. Small motors can be generally categorised as being either *synchronous*, *asynchronous* (*induction*), or *commutator* [Veinott 1987].

The small asynchronous and synchronous motors traditionally operate directly from a single phase AC supply and are referred to as single phase motors.

Single phase motors can run on a single winding, usually called the *main winding*. However, they are not self-starting, so a second winding, referred to as the *auxiliary winding*, is usually needed. When only operating from the main winding, the fundamental current-density distribution of the armature can be described by [Kamerbeek 1973]:

$$s = -i_1 Z_1 \sin(\theta_s) \tag{1.1}$$

where

Z_1 = the amplitude of the fundamental of the copper distribution function $Z(\theta_s)$

i_1 = fundamental current

θ_s = spatial angle around the stator circumference

Eqn. 1.1 applies to a single winding which may be distributed or concentrated. It shows that with only a single winding, the fundamental of the current density distribution is zero for $\theta_s = 0$ and $\theta_s = \pi$. This *standing wave* can be resolved into two travelling waves which rotate in opposite directions, where $i_1 = I_1 \cos(\omega t)$:

$$-I_1 Z_1 \sin(\theta_s)\cos(\omega t) = 1/2\, I_1 Z_1 \sin(\omega t - \theta_s) + 1/2\, I_1 Z_1 \sin(-\omega t - \theta_s) \tag{1.2}$$

These travelling stator waves allow a single phase motor to run in either a clockwise or counter-clockwise direction. This applies to either an asynchronously or synchronously running motor. The current-density wave in the opposite direction to the direction of rotation causes a pulsating torque at twice the electrical frequency. For example, the forward running rotor of a synchronous motor rotates at the same speed as the forward travelling wave. However, the rotor rotates at twice the electrical speed in relation to the stator wave travelling in the backward direction. The resulting interaction of the rotor field, and the backward travelling stator wave, is a pulsating torque at twice the electrical frequency. This pulsating torque can be greater than the load torque. For an asynchronous motor, the power factor is lowered and rotor I^2R losses are higher due to the backward wave.

Although both asynchronous and synchronous motors can run on only a single winding, they cannot start using only a single winding. For a synchronous motor, at rotor positions where rotor and stator poles are aligned, there is no starting torque. For an asynchronous motor, motion is required to produce any torque [Veinott and Martin 1986, pp. 39-46].

The auxiliary winding can significantly improve performance. An equation similar to 1.2 can also be written for the auxiliary winding. If the auxiliary winding has a fundamental current density distribution of the same magnitude as the main winding, but is displaced by 90° electrical in both space and time with respect to the main

winding, the sum of the current density waves for both windings is

$$s_{\text{2-phase}} = I_1 Z_1 \sin(\omega t - \theta_s) \tag{1.3}$$

This travelling wave allows motors having two or more phases to produce a starting torque. The auxiliary winding in a single phase machine is usually smaller than the main winding, and has a smaller current. The current distribution may be displaced by less than 90° electrical in both space and time with respect to the main winding. Thus the performance is that of an unbalanced two phase motor.

Asynchronous single phase motors which use an auxiliary winding, for starting at least, are *split-phase*, *capacitor*, and *shaded pole* motors. Each of these types of motors have subcategories. A split phase motor is a single phase induction motor that has a main and an auxiliary (starting) winding. The two windings are spatially displaced by 90° with respect to each other. The auxiliary winding has a higher ratio of resistance to reactance than the main winding in order to achieve a phase-splitting effect. A starting switch cuts it out of the circuit as the motor approaches operating speed. The starting switch is usually centrifugal.

Capacitor motors use a capacitor connected in series to the auxiliary winding to achieve a similar effect. Subcategories of capacitor motors include capacitor start, two-value capacitor, and permanent split capacitor. Similarly to the split-phase motor, a starting switch cuts a starting capacitor out of the circuit as the capacitor start motor approaches operating speed. For the two value capacitor motor, a starting capacitor is switched out by the centrifugal switch and a running capacitor remains connected to the auxiliary winding. For the permanent split capacitor motor, a capacitor is permanently connected to the auxiliary winding.

In a shaded pole motor a short-circuited coil or *shading-coil* creates the second effective phase and a rotating field enabling the motor to start and run. The attractiveness of the shaded pole motor is its simple construction, ruggedness, and reliability. No contacts or switches are required. However, the efficiency and power factor are poorer. This may not be a significant problem at the low power rating of these motors, but the associated losses can be a problem because of the resulting temperature rise.

The synchronous motors are the *reluctance*, *hysteresis*, and the *permanent magnet*. An attractive feature of these motors is preciseness of average speed, which is proportional to the frequency of the AC power system. These motors have the same stators as the asynchronous motors. They can use either a shading coil, or an auxiliary winding with a phase-splitting mechanism.

The reluctance motor can be described as being a single phase version of a three-phase synchronous reluctance machine. A squirrel cage is used to start the motor like an induction motor to enable the rotor to pull into synchronism.

The hysteresis motor is a synchronous motor without salient poles and without DC

excitation that starts as a result of the hysteresis losses induced in its hardened steel rotor member by the revolving field of the stator, and operates normally at synchronous speed because of the retentivity of a secondary rotor core. The torque versus speed characteristic of this motor is ideally constant up to synchronous speed. This occurs because the angle between the rotor magnetisation and the rotating field remains at a fixed value determined by the hysteresis properties of the rotor materials.

All the motors described so far require a rotating stator field to enable starting. Either a shading coil or an auxiliary winding is required. The remaining synchronous motor is the permanent magnet motor, and can be designed to start and run without needing an auxiliary winding, shading coil, centrifugal switch, or capacitor. It is described in detail in the next section.

Mechanically and electronically commutated motors are also found within the small motor category. Two particularly important mechanically commutated motors are the *brushed DC*, and the *universal* motors. The universal motor is a series DC motor [McPherson 1981] and has the ability to run from AC or DC. An advantage of the universal motor is that the speed is not limited by the frequency of the AC supply. For example, a 50 Hz supply limits the speed of a 2-pole synchronous motor to 3000 RPM, whereas a small universal motor can run up to 30,000 RPM, and maybe even up to 50,000 RPM.

Electronically commutated motors combine many of the classical machine types described above with power electronic controllers to form complete drive systems. This enables a wide range of performance characteristics to be achieved, particularly with the use of digital electronics such as microprocessors. New motors have also become feasible because of the development of electronic technologies. Such examples are *linear*, *stepper*, and *switched reluctance* motors. An electronic controller is essential to drive these types of motors.

1.2 THE SINGLE PHASE SYNCHRONOUS PERMANENT MAGNET MOTOR

This motor consists of a single phase stator winding, without an auxiliary winding, and a permanent magnet rotor. Without an auxiliary winding there is a twice electrical frequency speed ripple which typically amounts in amplitude to 20-40% of the mean synchronous speed [Schemmann 1971, Bertram and Schemmann 1976]. Fig. 1.1 shows a drawing of a single phase synchronous motor with a two pole PM (permanent magnet) rotor. The stator is laminated and contains two coils which are connected directly to the mains. The coils can be pre-wound and can be slotted onto the stator laminations. The rotor consists of a cylindrical two-pole magnet which is diametrically magnetised. To allow starting, the stator has an asymmetric airgap. This creates a PM reluctance torque which causes the rotor to come to rest at a position where the magnetic axis of

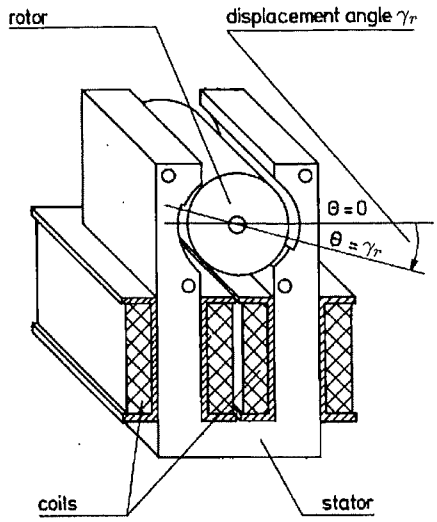

Figure 1.1 Single phase synchronous permanent magnet motor. Single slot or U shape stator design (reproduced from Fig. 1 of [Bertram and Schemmann 1976]).

the rotor is dis-aligned from the direct axis or d-axis of the stator, at a startable rotor position shown by displacement angle γ_r.

The high coercivities of modern ceramic PM materials have made the practical application of this type of motor possible [Bertram and Schemmann 1976, Veinott 1987]. According to [Altenbernd and Wahner 1996], the use of this motor has become increasingly more common since the paper on these motors by [Thees 1965]. The experimental motors demonstrated by Thees had a maximum power output of $P_{out} = 4.5$ W, and an input power of $P_{in} = 9$ W. This power rating limited the commercial usage to applications such as electric can openers, juicers, and aquarium pumps. Since then the power rating has increased for use in higher power applications. [Altenbernd and Wahner 1996] note that since the mid 1980's, this type of motor has been taking the place of shaded pole motors, particularly as a washing machine pump motor with a rating of 15-30 W. This trend is continuing to strengthen.

This synchronous motor has the attraction of being as simple and robust as the shaded pole motor. Efficiency higher than 50% is obtained due to the PM excitation eliminating rotor I^2R loss [Altenbernd and Mayer 1990]. Power output per unit volume is also high [Bertram and Schemmann 1976]. However, due to its starting and stability characteristics, it is suitable only for certain applications. These characteristics are described in the following sections.

1.2.1 Equations of Motion

[Schemmann 1971, Schemmann 1973] presents a theoretical model for the single phase synchronous PM motor. In his model, Schemmann assumes that the PM flux and the PM reluctance torque vary sinusoidally with respect to the rotor position. The PM

flux linking the stator coils is given by

$$\lambda_m = -\hat{\lambda}_m \cos\theta \tag{1.4}$$

where

$\hat{\lambda}_m$ = amplitude of the PM flux linkage (flux-turns)
θ = rotor angle

A theoretical analysis in section 4.7 shows that the assumption of a sinusoidal PM flux linkage for a 2-pole motor is a very good approximation. This is confirmed by the experimental results of section 5.5.3. Schemmann's electrical equation of motion, which enables the electrical behaviour of the motor to be modelled, is given by

$$v = iR + L\, di/dt + \dot{\theta}\hat{\lambda}_m \sin(\theta) \tag{1.5}$$

where

R = stator winding resistance
L = stator winding inductance
$\dot{\theta}$ = $d\theta/dt$

The motor terminal voltage is equal to the AC supply voltage:

$$v = \hat{v}\sin(\omega_e t + \epsilon) \tag{1.6}$$

where

$\hat{v}$ = the amplitude of the AC supply voltage
ω_e = electrical angular speed
ϵ = phase angle of the supply voltage

According to d'Alemberts law, the sum of the torques acting on the rotor is zero. The mechanical equation of motion describing the mechanical behaviour of the motor is given by

$$J\frac{d\dot{\theta}}{dt} + T_l = i\hat{\lambda}_m \sin\theta - \frac{dW(i=0)}{d\theta} \tag{1.7}$$

where

J = moment of inertia of the rotor and load
T_l = load and friction torque
W = stored magnetic energy

The second RHS term is the derivative of the stored magnetic energy set up by the PM as a function of rotor position, and yields the PM reluctance torque. The stored energy of a PM system is defined in section 2.2. The PM reluctance torque is given by

$$T_r = -\frac{dW(i=0)}{d\theta} = -\hat{T}_r \sin[2(\theta - \gamma_r)] \tag{1.8}$$

where

$\hat{T}_r$ = amplitude of the PM reluctance torque

γ_r = PM reluctance torque displacement angle

The inductance is not assumed to vary with either rotor angle or current. Schemmann shows that simulation results using these equations match sufficiently well the measured performance of the motor.

1.2.2 Displacement Angle γ_r and Alternative Designs

From eqn.s 1.7 and 1.8, the acceleration torque is given by

$$J\frac{d\dot{\theta}}{dt} = i\hat{\lambda}_m \sin\theta - \hat{T}_r \sin[2(\theta - \gamma_r)] - T_l \tag{1.9}$$

When the rotor and stator poles are aligned together at angles of $\theta = 0°$ or $\theta = 180°$, the mutual *phase-magnet* torque described by the first RHS term is zero. Near the vicinity of these angles this phase-magnet torque is also small. The PM reluctance torque performs the function of moving the rotor to the startable and stable detent position at $\theta = \gamma_r$ after switch-off. After switch-off, as the rotor slows down to come to rest, the PM reluctance torque must be greater than the friction torque to enable the rotor to move away from the aligned position at $\theta = 0$ to $\theta = \gamma_r$. Therefore a limit is placed on the magnitude of the friction torque such that at $\theta = 0$:

$$\hat{T}_r \sin(2\gamma_r) > T_{friction} \tag{1.10}$$

This limit can be increased by increasing γ_r up to a value of 45°, and by increasing $\hat{T}_r$.

Prior to starting, the rotor position is $\theta = \gamma_r$. At start the stator winding is energised, and the starting torque is given by $i\hat{\lambda}_m \sin\gamma_r$. This torque must be greater than the static friction torque for the rotor to move. Therefore, a limit is placed on the static friction torque such that

$$i\hat{\lambda}_m \sin\gamma_r > T_{static\ friction} \tag{1.11}$$

These equations demonstrate that the initial starting torque available is dependent on the size of the displacement angle γ_r.

The size of the displacement angle depends on the stator shape, and the size of the rotor diameter in relation to the diameter of the stator airgap. For the single slot design of Fig. 1.1, the displacement angle is typically limited to $5 - 12°$ [Altenbernd 1991]. Therefore, the initial starting torque available is not large. Other stator designs are possible which may extend the displacement angle. The stator of a shaded pole induction motor can be used without the shading coil, as shown by Fig. 1.2(a). The slit in the stator affects the PM reluctance, but the displacement angle is still small.

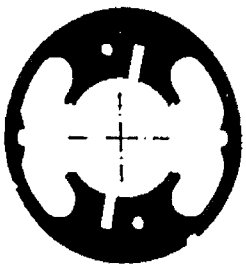

(a) Shaded pole stator.

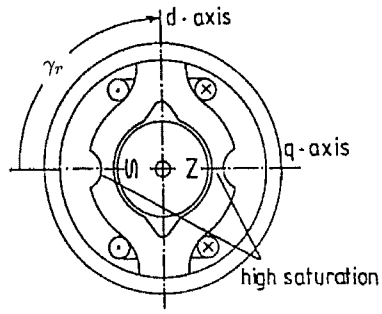

(b) Motor with $\gamma_r = 90°$.

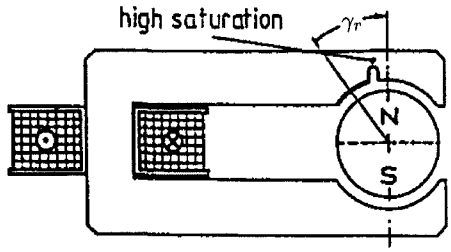

(c) Isolated pole.

Figure 1.2 Single phase synchronous PM motor designs (reproduced from [Altenbernd 1991]). (b) and (c) are described by European patents EP 0 358 805 A1 and EP 0 358 806 A1, respectively.

The design shown in Fig. 1.2(b) allows a displacement angle of 90°, enabling the largest possible starting torque. With the stator de-energised, the widened stator airgaps along the drawn d-axis cause the PM rotor to align with the q-axis where the PM reluctance is minimised. The rotor is shown aligned at this minimum reluctance position of $\theta = \gamma_r = 90°$ in Fig. 1.2(b). During running, when the PM rotor N-S poles are instantaneously aligned with the d-axis at $\theta = 0$, the reduced pole widths along the q-axis saturate. This is due to both the PM flux and the stator current. This saturation prevents a short circuit of PM flux. A disadvantage of this closed slot design is that leakage reduces the PM flux linking the stator coils by typically 25%. The PM reluctance torque is zero at the unstable detent positions of 0° and 180°. The amplitude of the PM reluctance torque $\hat{T}_r$ is limited to $5 - 10\%$ of the rated load in order for the motor to run smoothly [Altenbernd 1991]. Given the angles of the unstable zero reluctance torque positions (aligned with the d-axis), and the limited value of $\hat{T}_r$, this design may be expected to be particularly sensitive to frictional torque adversely effecting the ability of the rotor to come to rest at a startable position.

Fig. 1.2(c) shows another stator design which creates a displacement angle by increasing saturation in the stator laminations. The displacement angle in this design cannot be extended to 90°.

Multiple pole pair versions of the single phase synchronous PM motor are also manufactured, and have very low power outputs, but high torque. These motors employ a single circular stator winding and claw poles to obtain a stator with a high number of poles. For example, a motor manufactured by Crouzet, France, uses a circular winding. The steel casing of this motor is used as the stator yoke. Claw poles extend from each end of the casing to the cavity within the inner diameter of the coil, creating alternating N and S poles at the inner circumference when the coil is energised. A radially magnetised ferrite rotor having the same number of poles is placed in the space inside the coil and stator poles. A displacement angle is obtained by making the lengths of portions of selected stator pole claws shorter. The motor has 10 poles, and is rated at 220 V, 50 Hz, and has a shaft speed of 600 RPM. [Gieras and Wing 1997, p. 235] describe two other multiple pole pair designs which also use a circular winding and claw poles. Multiple pole pair motors are used as timing motors in automatic control systems, electric clocks, movie projectors, and impulse counters, etc. Unlike the 2-pole designs, the primary role of these motors is not the delivery of mechanical power.

1.2.3 Moment of Inertia

When the stator is energised, the stator field changes polarity every half electrical cycle. During starting, the rotor accelerates. For unidirectional motion to be continued through the next half cycle, the rotor is required to have rotated a half cycle. This requires the rotor to reach synchronous speed within a half cycle. Synchronous speed must therefore be reached within 10 ms using a 50 Hz supply. Figure 1.3 shows a

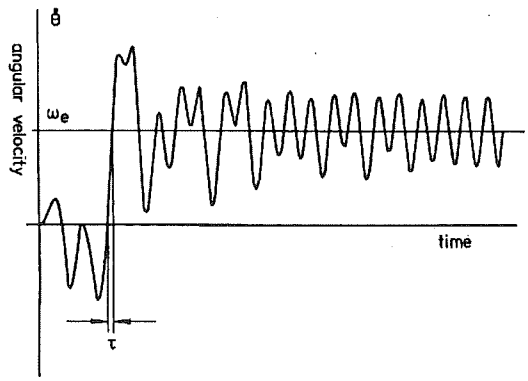

Figure 1.3 Typical starting characteristic. τ = starting time. (reproduced from Fig. 2 of [Bertram and Schemmann 1976]).

typical starting characteristic for this type of motor. In this example, the rotor behaves erratically and reverses direction several times before accelerating to synchronous speed over a very short interval. [Bertram and Schemmann 1976] note that this synchronising step takes less than 6 ms and that the acceleration over this interval is constant. The

required acceleration is then

$$\ddot{\theta}_{min} = \frac{\omega_e}{\tau} \tag{1.12}$$

where $\ddot{\theta} = d\dot{\theta}/dt$, and τ is the starting time required to accelerate from standstill to synchronous speed as shown in Fig. 1.3. The possible acceleration is obtained from equation 1.9. It is found that the synchronising acceleration takes place at an angle where $i\hat{\lambda}_m \sin\theta$ is large. This occurs at about $\theta = 90°$ or $\theta = 270°$. The PM reluctance torque and the load torque can be considered to be less significant in comparison to the phase-magnet torque $i\hat{\lambda}_m \sin\theta$. By neglecting these smaller terms, and by expressing the current in terms of the peak locked rotor current $\hat{v}/Z$, the maximum possible acceleration is approximated as

$$\ddot{\theta}_{max} = \frac{\hat{v}\hat{\lambda}_m}{ZJ} \tag{1.13}$$

where

$$Z = \sqrt{R^2 + (\omega_e L)^2} \tag{1.14}$$

Setting $\ddot{\theta}_{max} > \ddot{\theta}_{min}$ enables an upper limit for the moment of inertia J to be found. This upper limit is very low and places a severe restriction on the applications suitable for this type of motor. For a pump application, a highly elastic rubber impeller blade has been used which bends during starting to reduce the effect of the moment of inertia of the liquid surrounding the impeller blade [Bertram and Schemmann 1976]. The limit to the moment of inertia establishes an upper limit on the size and power rating of these motors, because the rotor inertia is proportional to the fourth power of the rotor diameter.

1.2.4 Direction of Rotation

The final direction of rotation is not predetermined. The final direction depends on the initial values of the system of equations 1.5 and 1.7. This limitation further restricts suitable applications, or requires a mechanical direction correcting device to ensure unidirectional motion.

1.2.5 Stability

[Schemmann 1971, Schemmann 1973] has shown that this type of motor has useful motion only within a limited range of motor parameters. Table 1.1 presents plots of the motions of a motor for various supply voltages, compiled by Schemmann. Useful motion occurs when the motion is *unperturbed*, as shown by examples 6 and 8. The unperturbed motion has a twice electrical frequency speed modulation. Other periodic motions are

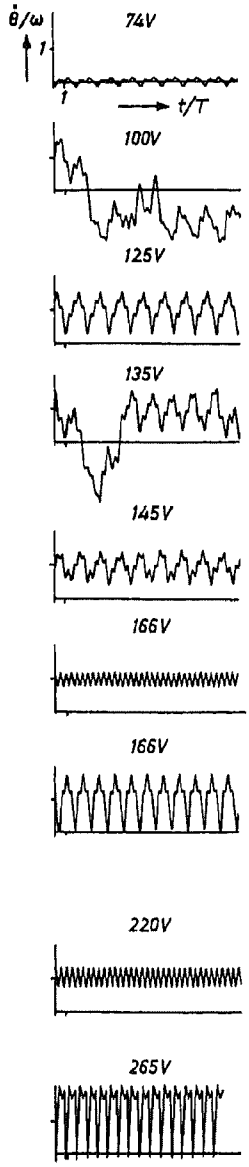

1. At low voltages the motor does not start. The rotor vibrates about the equilibrium position defined by the reluctance torque. (The same situation arises at the nominal voltage if the moment of inertia is too large.)
2. The rotor rotates but the motion is very irregular. The motion is not unidirectional even though the synchronous angular velocity is sometimes momentarily exceeded. The rotor changes its direction of rotation in a quite irregular manner.
3. The rotation has now become unidirectional. However, there are quite large periodic variations superimposed on the synchronous speed. Stroboscopic observations show that a steady-state motion is achieved with a repetition period of two revolutions of the rotor (25 Hz perturbation).
4. As the voltage is increased further the irregularities of the motion do not decrease. On the contrary, large new irregular and aperiodic motions occur in which the rotor again keeps reversing its direction of rotation. Apart from the voltage at which it occurs, this situation is no different from that described under *2*.
5. When the voltage is increased still further, the motion becomes unidirectional again. Strong periodic variations are still present (hunting) but the motor runs with a mean speed equal to the synchronous value.
6. The amplitude of the hunting now becomes smaller; above a particular voltage the oscillations disappear entirely. For the first time the motor assumes its state of unperturbed rotation as at the nominal voltage (see *8*).
7. At the same voltage at which this unperturbed motion occurs, however, the rotor can also run with very large speed variations. The rotor periodically comes almost to rest; the mean rotor speed is, however, the synchronous value. These variations are repeated every $1\frac{1}{2}$ periods ($33\frac{1}{3}$ Hz perturbation). Which of the two states of motion, *6* or *7*, takes place is determined by the phase of the supply voltage at the instant the motor is switched on.
8. At the nominal voltage the rotation is again unperturbed. The angular velocity is now modulated only at twice the mains frequency. The modulation in speed is 20-40% of the mean synchronous value. If a large moment of inertia is coupled to the motor, the modulation depth becomes smaller. The unperturbed motion is stable for voltage variations that are not too large, and the motor can drive a load.
9. Increasing the voltage above the nominal value again gives rise to large variations in the angular velocity. The rotor comes to rest once per revolution and the direction of motion may even be momentarily reversed. Within milliseconds the rotor then assumes velocities far above the synchronous value and is then immediately slowed down (50 Hz perturbation).

   If still higher voltages are applied, the accelerating torques are so large that any regular motion is quite impossible.

Table 1.1 Typical motion characteristics, arranged according to increasing values of the supply voltage (reproduced from Table 2 of [Schemmann 1973]).

identified in the Table, and are called periodic *perturbed* motions. The unperturbed and perturbed periodic motions are described in more detail in sections 4.2.1 and 4.2.2, respectively. Schemmann describes the unperturbed motions as "transition states between the upper limit of the one perturbed region and the lower limit of the next." The unperturbed region of motion must be at least wide enough to cover the variations in supply voltage, load torque, and moment of inertia that might be expected. The motor must also retain this unperturbed motion in regard to the spread in properties of materials used and the production process. Velocity dependent loads which dampen speed ripple are particularly suitable for improving stability.

Because of the development work required, the motor is only really suitable for mass production techniques [Schemmann 1973]. [Diefenbach and Schemmann 1989] describe the motor design process for a shaver application. This description highlights the difficulty that can be involved in the designing of a stable motor.

1.2.6 Acoustic Noise

The modulation in the speed is the result of the pulsating torque caused by the backward rotating field of the single phase winding. For an electrical supply frequency of 50 Hz, the unperturbed speed modulation acts as a source of 100 Hz oscillation. This can lead to problems of acoustic noise, particularly for water-pumping applications [Altenbernd and Wahner 1996]. For the U-shape stator design of Fig. 1.1, the stator laminations act as tuning forks, leading to 1200-1800 Hz resonant harmonic oscillations. [Altenbernd and Wahner 1996] comment that the noise resulting from these oscillations hampers their use in high quality household appliances. It is possible to tune the resonant frequency of the stator yoke to less subjectively annoying frequencies, but the fundamental harmonic remains.

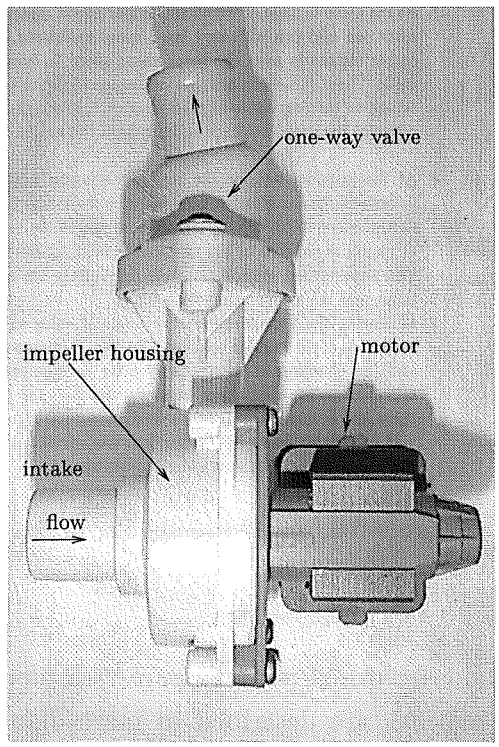

Figure 1.4 Siemens water-pump motor.

Fig. 1.4 shows a photograph of a water-pump motor manufactured by Siemens, which is used in washing machines. Fig. 1.5 shows an exploded view of the motor. Water is drawn through the intake in the impeller chamber and accelerated around the chamber walls, and up through the one-way valve. This action is not affected by the

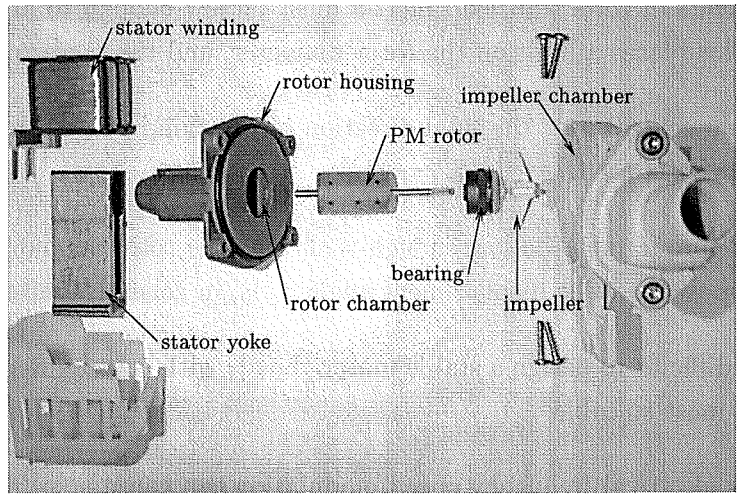

Figure 1.5 Exploded view of the Siemens motor.

direction of rotation. The PM rotor is contained within a plastic rotor housing. Water floods the PM rotor chamber because the bearing does not provide a water-tight seal. The stator laminations fit over the rotor housing. The stator laminations and stator winding are external to the pump housings, and are isolated from the water. This motor is examined in more detail in Chapters 4 and 5.

[Altenbernd and Wahner 1996] note that the rotor speed fluctuation causes additional problems to occur in the water-pump design described above. The pressure fluctuations induced in the axially incoming fluid propagate into the rotor chamber. This burdens the bearing and may lead to premature destruction, and can cause additional resonant noise through the housing. At the pump out-take, pressure fluctuations can be transmitted along the water column, inducing more resonant noise.

1.2.7 Summary of Characteristcs

In relation to other single phase machines, single phase synchronous PM motors have the advantages of

1. high power output per unit volume
2. simple construction
3. high reliability
4. synchronous speed
5. high efficiency

However, the application of these motors is limited by the following characteristics:

1. The moments of rotor and load inertia must be low enough to allow synchronisation. This places a limit on the rotor diameter, and the power rating.

2. There is no control over the final direction of rotation, unless a mechanical correcting device is used.

3. Frictional torque must be low enough such that the rotor can come to rest at a startable position. The displacement angle γ_r is, in general, limited.

4. It can be difficult to design a stable motor. Loads with velocity dependent dampening are most suitable.

5. The twice electrical frequency speed modulation can cause noise problems.

1.3 IMPROVING THE MOTOR CHARACTERISTICS

In this section, possible methods of improving the characteristics of the single phase PM motor are examined.

1.3.1 Electronic Commutation

If a single phase synchronous PM motor is not connected directly to an AC supply, and instead electronically commutated, a motor of the form described by [Mayer and Wasynezuk 1989] or [Hendershot and Miller 1994, p. 3.4] can be obtained. These motors use a bifilar winding, a DC to AC inverter requiring two transistors, and a Hall effect sensor to determine rotor position. Logic circuitry is also required to convert the Hall sensor information into appropriate switching signals for the transistors. These motors are known as *single phase bifilar wound* DC motors. They may have multiple pole pairs, and have an exterior PM rotor. Because they only require a few electronic components, these motors are cost-effective in light duty fan applications [Hendershot and Miller 1994].

[Altenbernd and Wahner 1996] propose the use of simple AC circuitry to extend the power range of the directly connected 2-pole motor. The power output limit for the directly connected 2-pole motor is 50-60 W. This is achieved by extending the length of the rotor, rather than its diameter. The rotor length to diameter ratio is about 3-4, and is difficult to extend further due to the problem of transverse oscillations [Altenbernd and Wahner 1996]. To extend the power range, a triac is placed in series with the motor and the AC supply. A Hall sensor is required, and circuitry monitors the phase of the supply voltage. The current may also be monitored. This scheme removes the inertial constraint for start-up, and improves stability. The power output can be extended to 200 W.

Electronic control alleviates most of the limiting characteristics, that apply to the direct connected motor, listed in section 1.2.7. With electronic control, there is no inertia limitation, the direction of rotation is determined, stability is improved by the use of the Hall sensor to ensure synchronism, and the inertia is generally higher so speed ripple can be better damped. The requirement that the motor must come to rest at a startable position still remains a limitation. On the negative side, the complexity increases due to the electronics, increasing cost and decreasing reliability.

1.3.2 Improving Torque Quality

The other way of improving characteristics is to improve motor design. Both the directly connected and electronically commutated motors described so far have large pulsating torques. The torque pulsates at twice the electrical frequency, dipping to zero or to a negative value every half cycle. An examination of ways to improve the torque quality of a single phase PM motor is a possible starting point for improving characteristics. If the motor torque can be made constant with respect to rotor position, speed ripple and noise problems are eliminated. This also implies that a starting torque is available at all rotor positions. Limiting characteristics 3 and 5, of section 1.2.7, are thereby eliminated. The challenge is to create a constant instantaneous torque using only a single winding. This may be achieved if the two motor torque components, the phase-magnet torque, and the PM reluctance torque, add to equal a constant instantaneous value. The load torque is set equal to the sum of these motor torques, and the acceleration is zero. For a motor which can be modelled adequately by approximating sinusoidal phase-magnet coupling and sinusoidal PM reluctance torque, the current waveform required can be calculated by re-arranging eqn. 1.9 to get

$$i = \frac{T_l + \hat{T}_r \sin[2(\theta - \gamma_r)]}{\hat{\lambda}_m \sin\theta} \tag{1.15}$$

where $J\, d\dot{\theta}/dt = 0$. At rotor positions of $\theta = 0°$ or $\theta = 180°$, the denominator in eqn. 1.15 is zero. Unless the PM reluctance torque $\hat{T}_r \sin[2(\theta - \gamma_r)]$ and the load torque T_l add to zero at these positions, finite current and constant speed cannot be obtained. Appropriate values for $\hat{T}_r$ and γ_r are required to ensure that the required current at these positions is zero.

To maximise the motor torque, $\hat{T}_r$ must have the same magnitude as T_l. Peak values of $\hat{T}_r \sin[2(\theta - \gamma_r)]$ must then coincide with rotor positions $\theta = 0°$ and $\theta = 180°$. Under this requirement, $\gamma_r = 45°$ and $\gamma_r = 135°$ are the optimum displacement angles. For positive (or forward) rotation, $\gamma_r = 45°$ must be chosen whereby $\hat{T}_r \sin(-2\gamma_r) = -\hat{T}_r$.

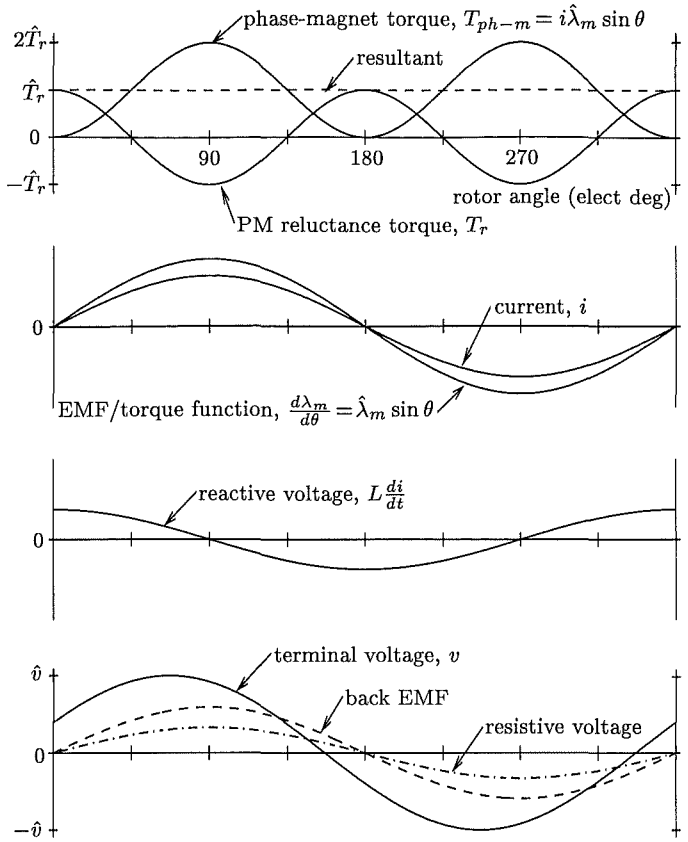

Figure 1.6 Unidirectional single phase synchronous PM motor waveforms.

For forward rotation with $\gamma_r = 45°$ and $T_l = \hat{T}_r$, eqn. 1.15 becomes

$$i = \frac{2\hat{T}_r}{\hat{\lambda}_m} \sin\theta \tag{1.16}$$

and demonstrates that a constant instantaneous torque can be achieved with a sinusoidal current. Fig. 1.6 shows the torque and current waveforms over an electrical cycle. Under these conditions, the PM reluctance torque cancels out the pulsations in the phase-magnet torque $i\hat{\lambda}_m \sin\theta$, and effectively acts as a second balancing phase. The load and rated torques are set equal to the amplitude of the PM reluctance torque, $\hat{T}_r$.

The ability to rotate to a startable rest position is greatly enhanced in relation to the conventional designs. With $\gamma_r = 45°$, eqn. 1.10 shows that the reluctance torque available to move the motor away from the unstartable rotor position of $\theta = 0$ is maximised. In addition, because the amplitude of the reluctance torque is set equal to the rated load, it is relatively large. Once the rotor has come to rest at the stable detent position of $\theta = \gamma_r = 45°$, the starting torque available later when the stator is energised is also high. Eqn. 1.11 shows that 70% of the maximum starting torque is available with $\gamma_r = 45°$.

With reference to eqn. 1.5, the terminal voltage, with the current determined by eqn. 1.16, is

$$\begin{aligned} v &= L\,di/dt + iR + \dot{\theta}\hat{\lambda}_m \sin\theta \\ &= \frac{2L\hat{T}_r\dot{\theta}}{\hat{\lambda}_m}\cos\theta + \left[\frac{2R\hat{T}_r}{\hat{\lambda}_m} + \dot{\theta}\hat{\lambda}_m\right]\sin\theta \end{aligned} \tag{1.17}$$

The acceleration is zero and $\dot{\theta}$ is equal to the synchronous speed ω_e. Therefore this is a sinusoidal voltage equal to $v = \hat{v}\sin(\omega_e t + \epsilon)$. $\hat{v}$ and ϵ are respectively given by

$$\hat{v} = \sqrt{\left(\frac{2\omega_e L\hat{T}_r}{\hat{\lambda}_m}\right)^2 + \left(\frac{2\hat{T}_r R}{\hat{\lambda}_m} + \omega_e\hat{\lambda}_m\right)^2} \tag{1.18}$$

$$\epsilon = \arctan\left(\frac{2\omega_e L\hat{T}_r/\hat{\lambda}_m}{2\hat{T}_r R/\hat{\lambda}_m + \omega_e\hat{\lambda}_m}\right) \tag{1.19}$$

In eqn. 1.18, the amplitude of the current $\hat{i}$ is $2\hat{T}_r/\hat{\lambda}_m$, and the amplitude of the EMF, $\hat{e}$, is given by $\omega_e\hat{\lambda}_m$. $\hat{e}$ and $\hat{i}$ are in phase. $\hat{e}$ and $\hat{i}$ lag the peak inductive voltage $2\omega_e L\hat{T}_r/\hat{\lambda}_m$ by 90°. Both $\hat{e}$ and $\hat{i}$ lag $\hat{v}$ by phase angle ϵ. The electrical waveforms are also shown in Fig. 1.6, and a phaser diagram is shown by Fig. 4.1(b). The *constant instantaneous torque concept* described here provides the basis for two proposed single phase PM motors, which are described in the following sections.

1.4 THE UNIDIRECTIONAL SINGLE PHASE SYNCHRONOUS PM MOTOR

The first of these motors employs the sinusoidal waveforms described in section 1.3.2. This motor is directly connected to a single phase AC supply, and is a special case of the conventional PM motor described in section 1.2. Chapter 4 examines this proposed motor in detail and describes a physical implementation. It is shown that this motor has the capability to start, and to produce a smooth torque under rated load. It is also shown to be *unidirectional*, if designed appropriately. The term *unidirectional* is used here to describe motional behaviour in which, after a brief starting transient, the motor only runs in the forward direction. No mechanical correcting device is necessary. This motor will be referred to as the *unidirectional single phase synchronous PM motor*, or the *unidirectional motor* for short. These aspects of operation are demonstrated by computer simulation using the simulation equations developed by [Schemmann 1971]. The unidirectional motor has the simplicity of its conventional counterpart, and is also intended for domestic application. The constant instantaneous torque concept is thus shown to eliminate limiting characteristic number 2, as well as numbers 3 and 5,

described in section 1.2.7, for a directly connected motor. However, it is shown that the unidirectional motor requires an even tighter inertial constraint than the conventional motor.

1.5 A PM MOTOR WITH TRIANGULAR RELUCTANCE TORQUE

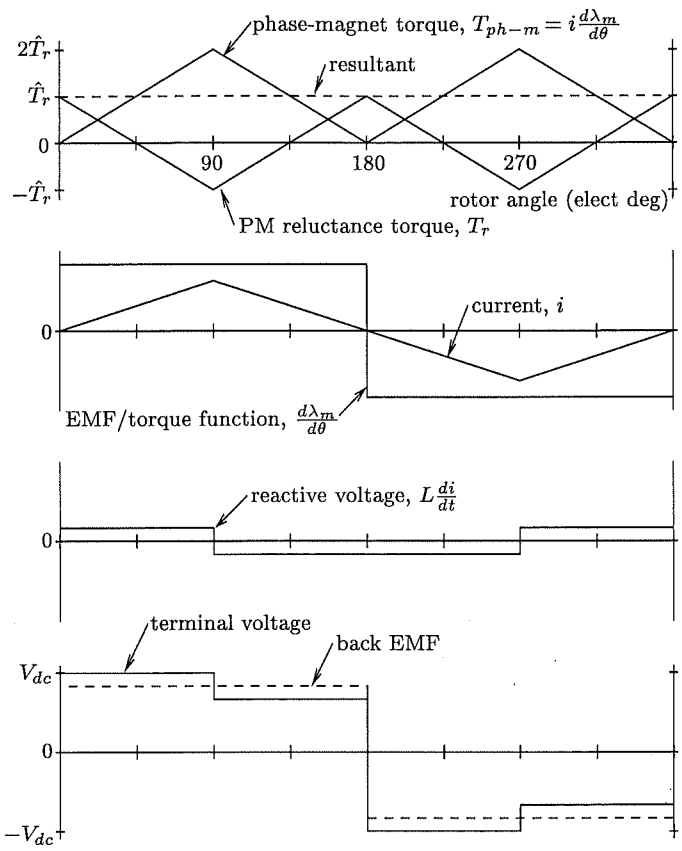

Figure 1.7 Triangular motor waveforms.

It is also possible to implement the constant instantaneous torque concept using non-sinusoidal waveforms. The idealised waveforms of an alternative such implementation are shown in Fig. 1.7. The PM reluctance torque and the phase-magnet torque again add together to provide a constant motor torque. The PM reluctance torque waveform is triangular and completes two cycles per electrical cycle. The current waveform is also triangular, and the motor will be referred to as the *triangular motor* in virtue of these waveform shapes. The back EMF is a square-wave, however a trapezoidal waveform can only be achieved in practice. The inductance ideally remains constant and the armature voltage given by $L\,di/dt$ is a square-wave. The terminal voltage is ideally a square-wave, but has two steps per half cycle. The heights of the steps depend on the magnitude of the inductance. The voltage drop across the winding resistance has been neglected in Fig. 1.7.

The required terminal voltage is non-sinusoidal, therefore the triangular motor is unsuitable for direct connection to an AC supply. A DC to AC inverter and Hall sensors are required to drive the motor. Including electronic control allows all the limiting characteristics described in section 1.2.7 to be eliminated. It is also possible to electronically control the unidirectional motor, but the triangular motor may be more suitable for connection to a DC to AC inverter because its required terminal voltage is closer in shape to a squarewave. A triangular motor has been built to demonstrate that the required non-sinusoidal characteristics can be implemented. This is described in Chapter 3.

1.6 THE EMF/TORQUE FUNCTION

The purpose of this section is to define a quantity which is used throughout the thesis. This quantity is introduced by first describing the constants used to model brushed DC motors. The back EMF of a brushed DC motor is given by

$$E = k_E \dot{\theta} \tag{1.20}$$

where

k_E = back EMF constant

The airgap torque is given by

$$T = k_T I \tag{1.21}$$

where

k_T = torque constant
I = DC current

For the brushed DC motor, k_E and k_T are equivalent if they are in consistent units [Hendershot and Miller 1994, p. 7.3]. In this case a single symbol k could be used to determine both the torque and the EMF, and could be called the *EMF/torque constant.*

For a single phase motor, the instantaneous EMF induced in the winding due to a PM is given according to Faraday's law by

$$e = \frac{d\lambda_m}{dt} = \frac{d\lambda_m}{d\theta}\dot{\theta} \tag{1.22}$$

where

$d\lambda_m/d\theta$ = rate of change of the PM flux linkage with respect to the rotor position

In section 2.5, the torque due to the mutual coupling between the phase and the magnet

is obtained from eqn. 2.64 as

$$T_{ph-m} = i\frac{d\lambda_m}{d\theta} \tag{1.23}$$

A comparison of eqn.s 1.22 and 1.23 shows that $d\lambda_m/d\theta$, or the rate of change of the PM flux linkage with respect to the rotor position, is related to both the instantaneous back EMF and the instantaneous phase-magnet torque for a single phase motor. Like k for a brushed DC motor, $d\lambda_m/d\theta$ may be defined in consistent units such as Nm/A (Newton-metres per Ampere) or V.s/rad (Volt-seconds per radian). Unlike a brushed DC motor where k is essentially constant, $d\lambda_m/d\theta$ may vary as a function of the rotor position. Given these characteristics, $d\lambda_m/d\theta$ will be called the *EMF/torque function.* The EMF/torque function is referred to throughout this thesis, and allows easy calculation of the EMF or torque, derived from a single unifying quantity.

Chapter 2

ENERGY CONVERSION BY PERMANENT MAGNET MACHINES

2.1 INTRODUCTION

Energy methods are widely used and well understood for determining the torque or force in magnetically nonlinear or linear machines that do not contain permanent magnets. Energy methods are employed to calculate torques or forces of magnetic origin after determination of the energy stored in the electromechanical coupling field. The origins of this theory date back at least as far as [Maxwell 1891] where the equation for the force resulting from the "mechanical action between two circuits" in the absence of magnetic material is expressed in terms of currents and inductance coefficients:

$$F_x = \frac{1}{2} i_1^2 \frac{dL_1}{dx} + i_1 i_2 \frac{dM}{dx} + \frac{1}{2} i_2^2 \frac{dL_2}{dx} \tag{2.1}$$

where i_1 and i_2, L_1 and L_2 are the respective currents and inductance coefficients of the two circuits, M, the mutual inductance; F_x, the component of force in the direction of x. With regard to eqn. 2.1, Maxwell stated that "If the motion of the system corresponding to the variation of x is such that each circuit moves as a rigid body, L_1 and L_2 will be independent of x and the equation will be reduced to the form,"

$$F_x = i_1 i_2 \frac{dM}{dx} \tag{2.2}$$

In the case of a single circuit, eqn. 2.1 reduces to

$$F_x = \frac{1}{2} i^2 \frac{dL_1}{dx} \tag{2.3}$$

Eqn. 2.1 was later shown to also hold for circuits which do enclose, or are near iron, provided there is no saturation. Thus Maxwell's equation included the solutions of the cases of one or two circuits involving inductances which are not functions of the current.

Iron saturation in a single circuit electromagnet was considered by [Steinmetz 1911].

The scope of this work was to express the energy relations which occur during a change in position. This constituted the initial step toward the derivation of a general equation for the force of a single circuit, where iron saturation may be present.

The contributions of Maxwell and Steinmetz, amongst others, provide a background of earlier work, as described by [Doherty and Park 1926], for their paper. The scope of the theory was extended by [Doherty and Park 1926] by applying the principle of conservation of energy to provide general equations for an arbitrary number of circuits which may contain iron, either saturated or not, but are assumed to have no hysteresis or residual magnetism. This has been followed by comprehensive treatments of electromechanical coupling theory by [White and Woodson 1959], [Fitzgerald *et al.* 1983], and [Woodson and Melcher 1968].

The increasing use and improving technology of permanent magnet materials has generated a need to incorporate materials exhibiting residual magnetism into this theory. However, the application of energy methods to permanent magnet systems has appeared to be based on plausible assumptions rather than logical derivation. The purpose of this chapter is to show how the classical theory can accommodate residual magnetism. By addressing the magnetisation process it shows how stored energy may be defined in a permanent magnet system. By then examining energy methods, a solid theoretical base for a selection of torque equations[1] used by both machine and CAD system designers, as well as some less obvious equations, is provided. In CAD (computer aided design) systems, energy methods, followed by the *Maxwell stress tensor* method, are the most common approaches used to calculate torques [Lowther and Silvester 1986]. Here energy minimising finite element numerical methods are most popularly applied. It is therefore essential that the energy methods are also correctly understood when permanent magnets are present.

2.2 ENERGY STORED IN A PERMANENT MAGNET SYSTEM

In classical electromechanical coupling theory stored energy is a physical quantity which can be measured experimentally. The stored energy is the energy which can be transferred to or from a conservative electromechanical coupling field via mechanical or electrical terminals. In this section the definition of stored energy extended to a system exhibiting significant residual magnetism or permanent magnetism remains essentially the same. The specification of a conservative electromechanical coupling field thus excludes hysteresis from the calculation of torque.

Fig. 2.1 shows a representation of a permanent magnet system consisting of a winding and a hard magnetic material. The winding has a flux linkage λ and current i and its terminals are depicted in Fig. 2.1. An airgap or linear region and a soft

[1] In this chapter, equations for force may be obtained from torque equations by replacing the rotational displacements with linear displacements.

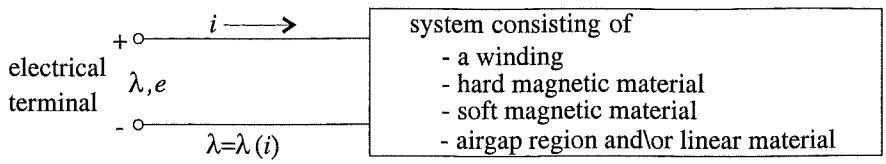

Figure 2.1 Electrical terminal pair representation of a permanent magnet system.

magnetic material may also be included in the system. The soft magnetic material is modelled as being anhysteretic with the **B-H** characteristic passing through the origin. Energy may be transferred to the system electrically or mechanically. To simplify the calculation of energy transferred to the system, the energy transferred to the system is accounted for electrically. This is achieved by treating the hard magnetic material as being initially un-magnetised such that initially $\lambda = 0$ when $i = 0$ and any forces or torques of magnetic origin are zero. All frictional and resistive losses excluding hysteresis loss are modelled externally to the system. The system may therefore be non-conservative during the magnetisation process. The system is first mechanically assembled with λ held at zero and the mechanical energy transferred to the system is zero. The flux linkage is then raised from zero and a voltage $e = d\lambda/dt$ is induced across the electrical terminals by the magnetic field. The energy transferred is obtained, in this case, by the classical equation for stored energy in a singly excited system:

$$\vartheta = \int_0^{\lambda} i d\lambda \tag{2.4}$$

The energy transferred is absorbed as energy which is recoverable (either mechanically or electrically) and also as energy which is not recoverable. However, eqn. 2.4 and the $\lambda - i$ characteristic do not, in general, provide sufficient information to allow the components of recoverable and non-recoverable energy to be determined. Eqn. 2.4 is equivalently expressed in terms of the energy density of the magnetic field corresponding to vectors **B** and **H** integrated over the volume of the system by

$$\vartheta = \int_V \int_0^{\mathbf{B}} \mathbf{H} \cdot d\mathbf{B}\, dv \tag{2.5}$$

The mathematical transformation from eqn. 2.4 to obtain eqn. 2.5 is described in [Stratton 1941, pp. 122-124]. This is a transformation from circuit quantities to field quantities. The field, after commencement of the magnetisation process, may be due to both currents and residually magnetised material. Eqn. 2.5 allows the energy transferred to the system to be separated using **B-H** characteristics into components within elements of the system volume as follows. Fig. 2.2(a) shows a **B-H** characteristic for a hard magnetic material. From $\mathbf{B} = 0$ the characteristic follows the initial magnetisation curve until the saturation flux density $\mathbf{B}_{sat}$ is reached. The energy density corresponding to energy absorbed by this magnet region is depicted by both shaded

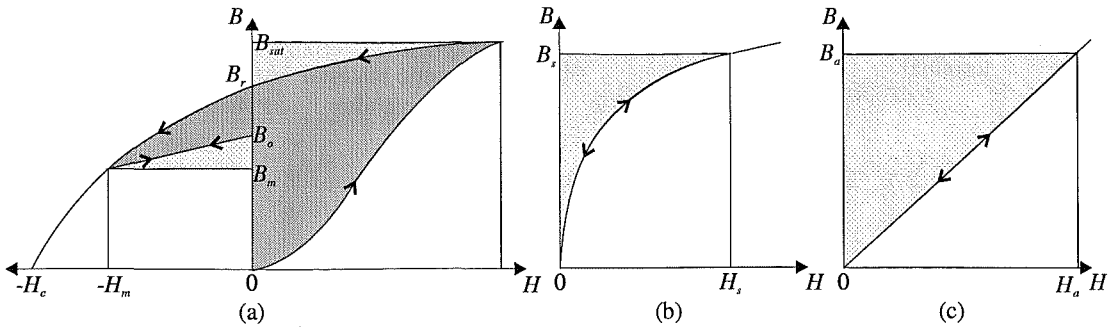

Figure 2.2 **B-H** characteristics and energy densities. (a) Hard magnetic material. (b) Soft magnetic material. (c) Air or linear material.

areas in the first quadrant. The field intensity $\mathbf{H}$ is then reduced to zero and the flux density follows the major hysteresis curve from $\mathbf{B}_{sat}$ to $\mathbf{B}_r$ in which $\mathbf{H} \cdot d\mathbf{B}$ is negative and recoverable energy is returned to the electrical terminals or absorbed by some other region or both. The recoverable energy corresponds to the lighter shaded area in the first quadrant. The darker shaded area corresponds to non-recoverable energy. This energy is non-recoverable because the magnetisation characteristic cannot be retraced back to $\mathbf{B} = \mathbf{0}$ at $\mathbf{H} = 0$ from within the first quadrant[2]. The recoverable energy will be defined as the *stored energy*. At $\mathbf{H} = 0$ with $\mathbf{B} = \mathbf{B}_r$ no more energy is recoverable and the stored energy is zero.

The flux density is now reduced to $\mathbf{B}_m$ by a demagnetising field $\mathbf{H}_m$ during which $\mathbf{H} \cdot d\mathbf{B}$ is positive and energy corresponding to the areas of both shaded regions in the second quadrant is absorbed. The demagnetising field is now reduced to zero and it is assumed that a minor hysteresis loop is followed to $\mathbf{B}_o$. The hysteresis loss in cycling between $\mathbf{H} = 0$ and $\mathbf{H}_m$ is assumed to be small such that the minor loop can be approximated by a recoil line. Therefore upon initially reaching $\mathbf{B}_o$, the darker shaded area in the second quadrant corresponds to non-recoverable energy, and the lighter shaded area to stored energy returned to the electrical terminals or absorbed by some other region or both. For subsequent movement of the operating point along the recoil line, or as long as the characteristic remains single-valued within the limits of integration $\mathbf{B}_o$ to $\mathbf{B}_m$, hysteresis is excluded and the permanent magnet stored energy is given by

$$W_m = \int_{V_m} \int_{\mathbf{B}_o}^{\mathbf{B}_m} \mathbf{H}_m \cdot d\mathbf{B}_m \, dv_m \tag{2.6}$$

Fig.s 2.2(b) and (c) show **B-H** characteristics for a single-valued soft magnetic material,

[2]After completion of a full cycle of a hysteresis loop, the magnetisation is returned to its original condition, and non-recoverable energy has been dissipated as heat called the hysteresis loss [Chikazumi 1964]. Similarly, if the **B-H** characteristic in Fig. 2.2(a) is extended into the 2nd and 3rd quadrants such that a hysteresis loop is compeleted returning to $\mathbf{B} = \mathbf{H} = 0$, the non-recoverable energy of the first quadrant has been dissipated as hysteresis loss.

and air or linear material, respectively. The areas of the shaded regions correspond to stored energies. Given that the hard magnetic material has reached a single-valued state within the limits described above, the electromechanical coupling field is conservative, and the stored energy of the permanent magnet system is given by

$$W = \int_{V_m} \int_{\mathbf{B}_o}^{\mathbf{B}_m} \mathbf{H}_m \cdot d\mathbf{B}_m \, dv_m + \int_{V_s} \int_0^{\mathbf{B}_s} \mathbf{H}_s \cdot d\mathbf{B}_s \, dv_s + \frac{1}{2} \int_{V_a} \mathbf{B}_a \cdot \mathbf{H}_a \, dv_a \qquad (2.7)$$

The inner integrals of the three RHS terms of eqn. 2.7 are the energy density functions of the permanent magnet, soft material, and linear material respectively. Some examples of these energy density functions are given in [Howe and Zhu 1992, Marinescu and Marinescu 1988], and in section 2.3.1.

An equation is given in [Zijlstra 1982] where the stored energy of the permanent magnet system is calculated by integrating over only the volume of the magnet. Integrating over only the volume of the magnet may be of advantage in some circumstances. This equation is

$$W = \frac{1}{2} \int_{V_m} \int \Big[\mathbf{H}_m \cdot d\mathbf{B}_m - \mathbf{B}_m \cdot d\mathbf{H}_m \Big] dv_m \qquad (2.8)$$

By specifying limits of integration, corresponding to second quadrant operating point $(\mathbf{H}_m, \mathbf{B}_m)$, eqn. 2.8 becomes:

$$W = \frac{1}{2} \int_{V_m} \left[\int_{\mathbf{B}_o}^{\mathbf{B}_m} \mathbf{H}_m \cdot d\mathbf{B}_m - \int_0^{\mathbf{H}_m} \mathbf{B}_m \cdot d\mathbf{H}_m \right] dv_m \qquad (2.9)$$

In eqn. 2.9, the permanent magnet stored energy density is given by $\int_{\mathbf{B}_o}^{\mathbf{B}_m} \mathbf{H}_m \cdot d\mathbf{B}_m$. For the example of the single-valued recoil characteristic of Fig. 2.2(a), this stored energy density is represented graphically by the lighter shaded area in the second quadrant.

The rule of differentiation can be applied to any single-valued magnetisation characteristic of any quadrant, whereby $d(\mathbf{H} \cdot \mathbf{B}) = \mathbf{H} \cdot d\mathbf{B} + \mathbf{B} \cdot d\mathbf{H}$. By applying the rule of differentiation over the second quadrant, and then integrating obtains:

$$-\int_0^{\mathbf{H}_m} \mathbf{B}_m \cdot d\mathbf{H}_m = \int_{\mathbf{B}_o}^{\mathbf{B}_m} \mathbf{H}_m \cdot d\mathbf{B}_m - \mathbf{B}_m \cdot \mathbf{H}_m \qquad (2.10)$$

In Fig. 2.2(a), the term $-\int_0^{\mathbf{H}_m} \mathbf{B}_m \cdot d\mathbf{H}_m$ is represented by the second quadrant area which includes the lighter shaded area corresponding to stored energy density, plus the rectangular area $-\mathbf{B}_m \cdot \mathbf{H}_m$ lying directly beneath. The term $-\int_0^{\mathbf{H}_m} \mathbf{B}_m \cdot d\mathbf{H}_m$ has a positive value because $\mathbf{B}_m \cdot d\mathbf{H}_m$ is negative over the specified integration limits.

Substitution of eqn. 2.10 into eqn. 2.9 yields

$$W = \int_{V_m} \int_{\mathbf{B}_o}^{\mathbf{B}_m} \mathbf{H}_m \cdot d\mathbf{B}_m \, dv_m - \frac{1}{2} \int_{V_m} \mathbf{B}_m \cdot \mathbf{H}_m \, dv_m \tag{2.11}$$

Eqn. 2.11 readily identifies an area in the second quadrant of Fig. 2.2(a) which is bounded by lines connecting the origin, operating point $(\mathbf{H}_m, \mathbf{B}_m)$, and $\mathbf{B}_o$. This area has been depicted in the literature, and there has been some confusion as to what it signifies. The first RHS term in eqn. 2.11 is the stored energy in the permanent magnet material. To obtain the energy of the whole permanent magnet system, the second RHS term must then represent the stored energy in the regions external to the permanent magnet. From eqn. 2.73 in section 2.7.2 it can be shown that

$$-\frac{1}{2} \int_{V_m} \mathbf{B}_m \cdot \mathbf{H}_m \, dv_m = \frac{1}{2} \int_{V_a} \mathbf{B}_a \cdot \mathbf{H}_a \, dv_a \tag{2.12}$$

if all currents are zero. This shows that the term $-\frac{1}{2} \int_{V_m} \mathbf{B}_m \cdot \mathbf{H}_m \, dv_m$ represents the stored energy of a linear material or airgap external to the permanent magnet if all currents are zero. As an example, the external region to the magnet may be composed of linear iron and an airgap. Eqn.s 2.8 and 2.11 are therefore not general and are only valid if the region outside the permanent magnet is linear and all currents are zero.

Expressions for $\mathbf{B}$ and $\mathbf{H}$ may be derived as functions of electrical and mechanical terminal variables. These terminal variables are described in section 2.4.1. Mechanical displacement is one of these terminal variables. For rotational displacement θ, $\mathbf{B}$ and $\mathbf{H}$ may therefore be expressed as $\mathbf{B} = \mathbf{B}(\theta)$ and $\mathbf{H} = \mathbf{H}(\theta)$. The stored energy given by Eqn.s 2.7, 2.8, and 2.11 may therefore be expressed as a function of rotational displacement for the calculation of PM reluctance torque. For a rotational displacement θ with the winding de-energised, or removed, the resulting reluctance torque is defined as the negative rate of conversion of stored energy into mechanical energy:

$$T_r = -\frac{dW(i=0)}{d\theta} \tag{2.13}$$

The definition of stored energy given here yields expressions for stored energy which, when used in eqn. 2.13, are shown to give accurate values of permanent magnet reluctance torque [Howe and Zhu 1992, Marinescu and Marinescu 1988].

The definition of stored energy provided here permits determination of the relationship of the mathematical quantity *coenergy* to stored energy where all currents are zero, in section 2.3. Energy methods are examined more generally in sections 2.4.2 and 2.4.3 to include torque calculation for non-zero currents.

2.3 COENERGY OF A PERMANENT MAGNET SYSTEM

Coenergy is a mathematical quantity which can be used to calculate force or torque. For the system described in section 2.2, the transferred coenergy may be determined in an analogous manner to the transferred energy, by the classical equation for coenergy in a singly excited system:

$$\vartheta' = \int_0^i \lambda di \tag{2.14}$$

Eqn. 2.14 is equivalently expressed by

$$\vartheta' = \int_V \int_0^{\mathbf{H}} \mathbf{B} \cdot d\mathbf{H}\, dv \tag{2.15}$$

After completing the magnetising sequence described in section 2.2, the coenergy density corresponding to $\mathbf{H} = -\mathbf{H}_m$ is shown by the shaded area in Fig. 2.3(a). As

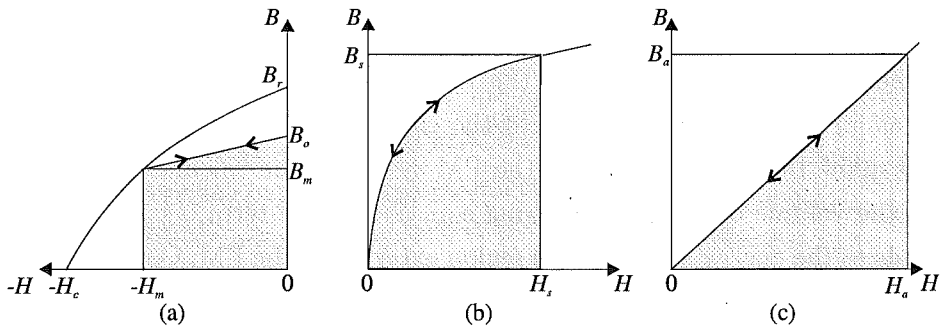

Figure 2.3 Coenergy densities shown by shaded areas. (a) Hard magnetic material. (b) Soft magnetic material. (c) Air or linear material.

long as the demagnetising field remains within limits in which the characteristic remains single-valued, the permanent magnet coenergy is given by

$$W'_m = \int_{V_m} \int_0^{\mathbf{H}_m} \mathbf{B}_m \cdot d\mathbf{H}_m\, dv_m \tag{2.16}$$

Fig.s 2.3(b) and (c) show the areas corresponding to coenergy for a single-valued soft magnetic material and air or linear material respectively. The coenergy of the permanent magnet system is given by

$$W' = \int_{V_m} \int_0^{\mathbf{H}_m} \mathbf{B}_m \cdot d\mathbf{H}_m\, dv_m + \int_{V_s} \int_0^{\mathbf{H}_s} \mathbf{B}_s \cdot d\mathbf{H}_s\, dv_s + \frac{1}{2} \int_{V_a} \mathbf{B}_a \cdot \mathbf{H}_a\, dv_a \tag{2.17}$$

In comparing Fig.s 2.2 and 2.3, the stored energy and coenergy densities in each of the

respective materials or regions are related by

$$\int \mathbf{H} \cdot d\mathbf{B} + \int \mathbf{B} \cdot d\mathbf{H} = \mathbf{B} \cdot \mathbf{H} \tag{2.18}$$

if the magnetisation characteristics are single-valued. Note that eqn. 2.18 holds for the single-valued recoil characteristic of Fig.s 2.2(a) and 2.3(a), and that the coenergy density of Fig. 2.3(a) is negative.

For a permanent magnet system, with the winding de-energised, eqn. 2.75 in section 2.7.2 shows that the total stored energy and coenergy are related by

$$W'(i=0) = -W(i=0) \tag{2.19}$$

Substitution of eqn. 2.19 into eqn. 2.13 shows that the reluctance torque is obtained in terms of coenergy by

$$T_r = \frac{dW'(i=0)}{d\theta} \tag{2.20}$$

2.3.1 Stored Energy and Coenergy in a Linear PM System

This section demonstrates an example of the energy-coenergy relationship in a PM system where the regions external to the PM have linear magnetisation characteristics such as air. The analysis applies to the case where all currents are zero. These conditions allow the energy stored in the PM system to be calculated by integrating over only the volume of the magnet using eqn. 2.11. The term $-\frac{1}{2}\int_{V_m} \mathbf{B}_m \cdot \mathbf{H}_m \, dv_m$ corresponds to the energy stored in the region external to the PM. Comparison of Fig.s 2.2(c) and 2.3(c) shows that the coenergy of the linear region is equal in sign and magnitude to the stored energy in that region. The coenergy of the PM system may then be calculated by integrating over only the volume of the magnet by

$$W' = \int_{V_m} \int_0^{\mathbf{H}_m} \mathbf{B}_m \cdot d\mathbf{H}_m \, dv_m - \frac{1}{2} \int_{V_m} \mathbf{B}_m \cdot \mathbf{H}_m \, dv_m \tag{2.21}$$

A PM material is now modelled which will allow eqn.s 2.11 and 2.21 to be evaluated for a specific example. The demagnetisation characteristic of a PM material may be modelled by[3]

$$\mathbf{B}_m = \mu_o \mu_r \mathbf{H}_m + \mathbf{B}_o \tag{2.22}$$

where μ_r is the relative permeability.

Fig. 2.2(a) shows a demagnetisation characteristic (which corresponds to a direction parallel to the direction of magnetisation) where the recoil line is established at

[3]Eqn. 2.22 is obtained from eqn. 2.65 in section 2.6 by setting $\mu_r = 1 + \chi_m$, and $\mathbf{B}_o = \mu_o \mathbf{M}_o$.

a remanence point given by $B_\circ$. This typically describes an Alnico material. In this section, a major linear demagnetisation characteristic is used. This may correspond to a hard ferrite or rare-earth PM material. In this case, $B_\circ$ is set equal to B_r. The corresponding B-H characteristics, which are respectively parallel and perpendicular to the direction of magnetisation, are given by

$$B_{m||} = \mu_\circ \mu_{r||} H_{m||} + B_r \tag{2.23}$$

$$B_{m\perp} = \mu_\circ \mu_{r\perp} H_{m\perp} \tag{2.24}$$

The stored energy in the parallel direction in the PM material is calculated from eqn. 2.6. The characteristic in the perpendicular direction is the same as that of a linear material, and the stored energy is calculated the same way as a linear material. The stored energy density function for the PM material is therefore given by [Howe and Zhu 1992, Marinescu and Marinescu 1988]:

$$w_m = \frac{(B_{m||} - B_r)^2}{2\mu_\circ\mu_{r||}} + \frac{B_{m\perp}^2}{2\mu_\circ\mu_{r\perp}} \tag{2.25}$$

$\mathbf{B}_m$ and $\mathbf{H}_m$ may vary within the PM region. Each unit volume within the PM region, v_m, may have a different amount of stored energy. Each unit volume of the PM region has an associated amount of stored energy in the linear region, which also varies according to $\mathbf{B}_m$ and $\mathbf{H}_m$, as shown by eqn. 2.11. For the sake of simplicity, the PM flux density will be assumed to be parallel to the direction of magnetisation, such that $B_{m\perp} = 0$. The stored energy of the PM system per unit volume of the PM material is then given by

$$w = \int_{\mathbf{B}_\circ}^{\mathbf{B}_m} \mathbf{H}_m \cdot d\mathbf{B}_m \, v_m - \frac{1}{2}\mathbf{B}_m \cdot \mathbf{H}_m \, v_m = \frac{(B_{m||} - B_r)^2}{2\mu_\circ\mu_{r||}} v_m - \frac{B_{m||}(B_{m||} - B_r)}{2\mu_\circ\mu_{r||}} v_m \tag{2.26}$$

The first term in eqn. 2.26 gives the stored energy of the magnet, per unit volume of the magnet. The second term gives the stored energy of the linear region or airgap, per unit volume of the magnet.

The coenergy in the PM material is calculated from eqn. 2.16. Assuming that the PM flux density is parallel to the direction of magnetisation, the coenergy density function of the PM material is given by

$$w'_m = \frac{B_{m||}^2 - B_r^2}{2\mu_\circ\mu_{r||}} \tag{2.27}$$

The coenergy of the PM system per unit volume of the PM material is therefore given

by

$$w' = \int_0^{\mathbf{H}_m} \mathbf{B}_m \cdot d\mathbf{H}_m \, v_m - \frac{1}{2}\mathbf{B}_m \cdot \mathbf{H}_m \, v_m = \frac{B_{m\|}^2 - B_r^2}{2\mu_o \mu_{r\|}} v_m - \frac{B_{m\|}(B_{m\|} - B_r)}{2\mu_o \mu_{r\|}} v_m \tag{2.28}$$

The first term in eqn. 2.28 gives the coenergy of the magnet, per unit volume of the magnet. The second term gives the coenergy of the linear region or airgap, per unit volume of the magnet.

Inspection of eqn.s 2.26 and 2.28 shows that $w + w' = 0$ for any unit volume of the PM material. By then integrating over the entire volume of the permanent magnet, the sum of the total stored energy and coenergy is zero, as required by eqn. 2.19. The total stored energy and coenergy per unit volume of the magnet given by eqn.s 2.26 and 2.28 are plotted in Fig. 2.4.

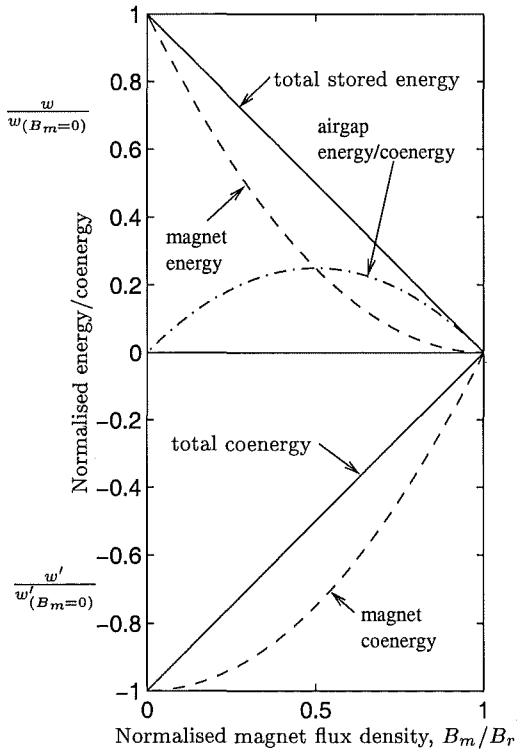

Figure 2.4 PM system comprising of PM material having a major linear demagnetisation characteristic, and an airgap or linear region: Normalised stored energy and coenergy per unit volume of the PM material plotted against the normalised PM flux density. The magnet, airgap, and total stored energies per unit volume of magnet are obtained by normalising eqn. 2.26. The magnet, airgap, and total coenergies per unit volume of magnet are obtained by normalising eqn. 2.28.

Fig. 2.4 shows that the stored energy is a linearly decreasing function of the PM flux density. $B_m = B_r$ corresponds to zero airgap length and volume, and the stored energy is zero. At $B_m = B_r/2$, the airgap stored energy peaks and is equal to $\frac{1}{2}(BH)_{max}$. At $B_m = 0$, the airgap volume is infinite but the airgap flux density is

zero. At $B_m = 0$, the energy stored in the PM is four times greater than the maximum energy that can be stored in the airgap. In practice, B_m is unlikely to reduce to zero if the PM is being subject to only its own demagnetising field. At low flux densities, the stored energy available to generate reluctance torque is relatively high.

The prediction of cogging torque in PM motors has been performed by only determining the coenergy in the rotor airgap [Li and Slemon 1988]. Unless the stator teeth are heavily saturated, the coenergy contribution from the stator teeth may be ignored. The error in neglecting the coenergy contribution of the magnet is shown by Fig. 2.4. The total coenergy is negative but the coenergy of the airgap is positive. Therefore, the sign of the coenergy is incorrect. This results in the sign of the calculated torque being incorrect. However, the error in the magnitude of the reluctance torque is the same as that if the torque is calculated by using only the airgap stored energy. This is because the airgap energy and coenergy both have the same sign and magnitude.

If the PM reluctance torque is calculated by determining only the stored energy in the airgap, then the error in the stored energy is the difference between the magnitude of the total stored energy and the airgap stored energy in Fig. 2.4. At high values of B_m, this error is small, but increases substantially as B_m decreases. For example, at $B_m = B_r/2$, the airgap energy only accounts for half of the total stored energy. [Li and Slemon 1988] show that the variation in field energy near the stator teeth at the two ends of a rotor magnet are largely responsible for the generation of PM reluctance torque. Significant variation in the PM flux density at the ends of the rotor magnet is to be expected and the flux density is likely to be low. In this case, the results of this section suggest that the stored energy or coenergy of the magnet should not be neglected in the calculation of reluctance torque.

2.4 ELECTROMECHANICAL COUPLING

2.4.1 Classical Electromechanical Coupling

In this section electromechanical energy conversion theory is briefly reviewed with respect to magnetic fields established by only winding currents. Energised windings and permanent magnets are introduced in the following sections. Thorough treatments of electromechanical energy conversion theory, which exclude permanent magnets, are found in references [White and Woodson 1959], [Woodson and Melcher 1968], and [Fitzgerald *et al.* 1983]. By applying the principle of conservation of energy (the first law of thermodynamics), the balance of energy in a lossless magnetic electromechanical system may be written as:

$$\begin{bmatrix}\text{Energy input from}\\ \text{electrical source}\end{bmatrix} = \begin{bmatrix}\text{Mechanical energy}\\ \text{output}\end{bmatrix} + \begin{bmatrix}\text{Change in energy stored}\\ \text{in magnetic field}\end{bmatrix} \tag{2.29}$$

where the magnetic field acts as a coupling field between electrical and mechanical systems. Eqn. 2.29 is represented by terminal pairs for the case of a single mechanical terminal pair, and a single electrical terminal pair in Fig. 2.5. λ and e represent respectively the flux linkage and induced voltage created by the magnetic field across the electrical terminals. The current i is supplied from an electrical source external to the coupling field. At the mechanical terminal, a torque of magnetic origin T acts at a mechanical angle θ. λ, i, T, and θ are the electrical and mechanical terminal variables. Any dissipative effects such as resistive, frictional, and hysteresis losses are modelled

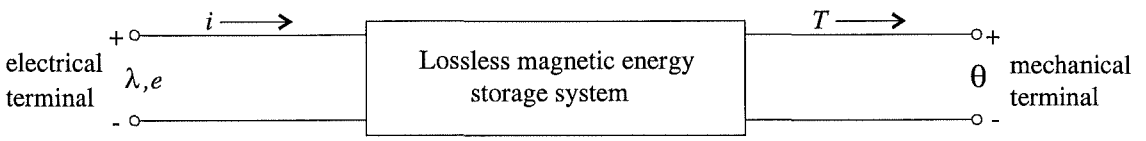

Figure 2.5 Terminal pair representation of a lossless magnetic field coupling system.

externally to the coupling field. For example, the resistance of the winding may be represented as a lumped parameter connected to the electrical terminal. In doing this, the magnetic coupling field is defined as being lossless, and is therefore conservative. Mechanical energy storage is also excluded from the coupling field. With $e = d\lambda/dt$, eqn. 2.29 can be rearranged and written in the form of conservation of power by

$$\frac{dW}{dt} = i\frac{d\lambda}{dt} - T\frac{d\theta}{dt} \tag{2.30}$$

By multiplying eqn. 2.30 by dt, the differential energy is given by

$$dW(\lambda, \theta) = id\lambda - Td\theta \tag{2.31}$$

As incremental changes in λ and θ yield an incremental change in W, it appears reasonable to use λ and θ as variables of integration to obtain W. The stored energy is found by evaluating the line integral:

$$W(\lambda, \theta) = \int_{0,0}^{\lambda,\theta} id\lambda - Td\theta \tag{2.32}$$

In eqn. 2.32, W is described as being a function of λ and θ. As the coupling field has been defined as being conservative, W is described as being a function of the *states* of λ and θ. As a state function, the change in stored energy between any two points in the variable space of λ and θ is independent of the path of integration. This allows any path of integration to be taken, where all paths yield the same result. If the flux linkage is held at zero, and the mechanical variable is raised to its final value, the stored energy integrated is zero because the torque of magnetic origin T is zero. By first raising the

mechanical variable to its final value, eqn. 2.32 is integrated more conveniently as

$$W(\lambda,\theta) = \int_0^{\lambda} i(\lambda,\theta)\, d\lambda \tag{2.33}$$

As a state function, $W(\lambda,\theta)$ is a single-valued function of the independent state variables λ and θ. Of particular interest is the torque obtained as a function of the stored energy. The total differential of $W(\lambda,\theta)$ is

$$dW(\lambda,\theta) = \frac{\partial W}{\partial \lambda} d\lambda + \frac{\partial W}{\partial \theta} d\theta \tag{2.34}$$

where the partial derivatives are each taken holding the other state variable constant. Since λ and θ are independent variables, eqn.s 2.31 and 2.34 must be equal for all values of $d\lambda$ and $d\theta$. Therefore, by equating the respective coefficients of $d\lambda$ and $d\theta$:

$$i = \frac{\partial W(\lambda,\theta)}{\partial \lambda} \tag{2.35}$$

where the partial derivative is taken with θ held constant, and

$$T = -\frac{\partial W(\lambda,\theta)}{\partial \theta} \tag{2.36}$$

where the partial derivative is taken with λ held constant. Eqn.s 2.35 and 2.36 show that the current and the torque can be obtained from the partial derivative of the stored field energy using flux linkage and mechanical angle as independent variables.

The electrical terminal variables are related by an electrical terminal relation expressible in the form

$$i = i(\lambda,\theta) \tag{2.37}$$

which shows that the current is obtained as a function of the flux linkage and mechanical angle. This is demonstrated by eqn. 2.35. Solving eqn. 2.37 for λ alternatively yields

$$\lambda = \lambda(i,\theta) \tag{2.38}$$

which shows that the flux linkage may be obtained as a function of the current and mechanical angle. Since flux linkage can be expressed as a function of current and mechanical angle, it seems reasonable that $W = W(\lambda,\theta)$ can also be expressed in the form $W = W(i,\theta)$, where i replaces λ as an independent state variable. This selection of independent variables may be described as being more convenient as the terminal variable i is easily measured and the solutions may also be simpler. To obtain an equation for torque in terms of (i,θ), eqn. 2.31 can be written in a form that involves

di and $d\theta$ by first applying the rule of differentiation:

$$id\lambda = d(\lambda i) - \lambda di \tag{2.39}$$

to eqn. 2.31 to yield the differential coenergy

$$dW'(i,\theta) = \lambda di + Td\theta \tag{2.40}$$

where

$$W' = \lambda i - W \tag{2.41}$$

The coenergy $W'(i,\theta)$ is defined in relation to stored energy by eqn. 2.41. This manipulation, which represents conservation of energy in terms of new independent variables, is called a Legendre transformation [Woodson and Melcher 1968]. To obtain the coenergy by integrating eqn. 2.40, the mechanical angle is again conveniently raised first to its final value to give

$$W'(i,\theta) = \int_0^i \lambda(i,\theta)\, di \tag{2.42}$$

$W'(i,\theta)$ can also be expressed in total differential form. Equating the total differential to eqn. 2.40 yields

$$\lambda = \frac{\partial W'(i,\theta)}{\partial i} \tag{2.43}$$

where the partial derivative is taken with θ held constant, and

$$T = \frac{\partial W'(i,\theta)}{\partial \theta} \tag{2.44}$$

where the partial derivative is taken with i held constant. A second useful form of the torque equation with the independent variables (i,θ) is obtained by substituting eqn. 2.41 into eqn. 2.44 to express the torque in terms of energy:

$$T = i\frac{\partial \lambda(i,\theta)}{\partial \theta} - \frac{\partial W(i,\theta)}{\partial \theta} \tag{2.45}$$

Similarly, by rearranging eqn. 2.41 and substituting into eqn. 2.36, the torque is expressed with independent variables (λ,θ) by coenergy:

$$T = \frac{\partial W'(\lambda,\theta)}{\partial \theta} - \lambda\frac{\partial i(\lambda,\theta)}{\partial \theta} \tag{2.46}$$

2.4.2 Permanent Magnets and Single Energised Winding

Fig. 2.1 is now extended to include a mechanical terminal like Fig. 2.5 such that simultaneous electrical and mechanical energy conversion may occur. If current and flux linkage are now assumed to be state functions then hysteresis is excluded, the functional relationship between these variables is single-valued, and the system is conservative. The conservation of power is then given by eqn. 2.30:

$$\frac{dW}{dt} = i\frac{d\lambda}{dt} - T\frac{d\theta}{dt}$$

and the differential energy is given by eqn. 2.31:

$$dW(\lambda,\theta) = id\lambda - Td\theta$$

whereby the torque is obtained in terms of stored energy by the classical result of eqn. 2.36:

$$T = -\frac{\partial W(\lambda,\theta)}{\partial\theta}$$

where the partial derivative is taken with λ held constant. The key point is that the differential energy $dW(\lambda,\theta)$ must have the properties of a state function for eqn. 2.31, and thus eqn. 2.36, to hold. However, this does not imply that $dW(\lambda,\theta)$ or $W(\lambda,\theta)$ are required to have the properties of state functions for all values of independent variables λ and θ. This imposes the constraint that if any of the independent variables are outside of a range where $W(\lambda,\theta)$ has the properties of a state function, then the torque cannot be obtained using eqn. 2.36 for those values of the independent variables.

Following classical procedure, the stored energy is obtained by integration of eqn. 2.31. The line integral of eqn. 2.32 is simplified by first mechanically assembling the system as described in sections 2.2 and 2.4.1. The energy transferred to the system in raising the flux linkage to a final value is then given by eqn.s 2.4 and 2.5. To determine the stored component of transferred energy, eqn. 2.5 must be used. In raising the flux density of the magnet from zero to $\mathbf{B}_o$, the system is not conservative. However, because the magnetisation history is known, the stored energy can be calculated within these limits, and is found to be zero. The stored energy is therefore obtained by raising the flux density of the magnet from $\mathbf{B}_o$ to $\mathbf{B}_m$, through which the stored energy is regarded to have the properties of a state function and is given by eqn. 2.7. The stored energy is regarded to have the properties of a state function if the demagnetising field $\mathbf{H}_m$ remains within limits such that the demagnetising characteristic remains single-valued. The state function requirement of eqn. 2.31 is therefore satisfied allowing the torque of the permanent magnet system to be given by eqn. 2.36.

In a conservative system which does not contain permanent magnets but has an

energised winding, the relationship between energy and coenergy is given by eqn. 2.41. This relationship is necessarily shown in section 2.7.3 (by setting $J = 1$) to also hold for a permanent magnet system having an energised winding. This relationship allows the torque to be equivalently expressed by the remaining classical results given by eqn.s 2.46, 2.44, and 2.45. The coenergy W' for a permanent magnet system is obtained by eqn. 2.17. Eqn.s 2.36, 2.46, 2.44, and 2.45 each allow the torque to be obtained for a permanent magnet system. For these equations, it is essential to hold the independent variable λ or i constant while taking the partial derivative analytically or numerically. Note that eqn.s 2.36 and 2.44 are more general forms of eqn.s 2.13 and 2.20.

2.4.3 Permanent Magnets and Multiple Energised Windings

Fig. 2.1 is now extended to include J electrical and K mechanical terminal pairs. The energy differential is then given by

$$dW = \sum_{j=1}^{J} i_j d\lambda_j - \sum_{k=1}^{K} T_k d\theta_k \tag{2.47}$$

whereby the torque obtained at the kth mechanical terminal is obtained in terms of stored energy by

$$T_k = -\frac{\partial W(\lambda, \theta)}{\partial \theta_k} \tag{2.48}$$

where (λ, θ) is now an abbreviation for $(\lambda_1, \ldots, \lambda_J; \theta_1, \ldots, \theta_K)$. If the system is assembled in an analogous manner to that described in section 2.2, the energy transferred to the system in raising the flux linkages to their final values is given by eqn. 2.5 and also by

$$\vartheta = \int_{0,\ldots,0}^{\lambda_1,\ldots,\lambda_J} \sum_{j=1}^{J} i_j d\lambda_j \tag{2.49}$$

where $i_j = i_j(\lambda_1, \ldots, \lambda_J; \theta_1, \ldots, \theta_K)$. If there is no hard magnetic material in the system and the functional relationships between between variables is single-valued, eqn. 2.49 obtains the stored energy as a state function given that independence of path is demonstrated by satisfying the following equalities:

$$\frac{\partial i_1}{\partial \lambda_2} = \frac{\partial i_2}{\partial \lambda_1}, \quad \frac{\partial i_1}{\partial \lambda_3} = \frac{\partial i_3}{\partial \lambda_1}, \quad \frac{\partial i_2}{\partial \lambda_3} = \frac{\partial i_3}{\partial \lambda_2}, \ldots \tag{2.50}$$

For example, in the absence of iron saturation, a two winding system may be represented using inductance coefficients by

$$\lambda_1(i_1, i_2, \theta) = L_{11} i_1 + L_{12} i_2 \tag{2.51}$$

$$\lambda_2(i_1, i_2, \theta) = L_{21} i_1 + L_{22} i_2 \tag{2.52}$$

It is shown experimentally that $L_{21} = L_{12}$ [Jones 1967], and these two coefficients will be replaced by mutual inductance M. Inverting eqn.s 2.51 and 2.52 obtains the currents, with flux linkages as independent variables:

$$i_1(\lambda_1, \lambda_2, \theta) = \frac{L_{22}\lambda_1 - M\lambda_2}{B} \tag{2.53}$$

$$i_2(\lambda_1, \lambda_2, \theta) = \frac{-M\lambda_1 + L_{11}\lambda_2}{B} \tag{2.54}$$

where $B = L_{11}L_{22} - M^2$. Eqn.s 2.53 and 2.54 are shown to demonstrate independence of path:

$$\frac{\partial i_1}{\partial \lambda_2} = -\frac{M}{B} = \frac{\partial i_2}{\partial \lambda_1} \tag{2.55}$$

Substitution of eqn.s 2.53 and 2.54 into 2.49 then yields the stored energy which is obtained by following any path of integration:

$$W(\lambda_1, \lambda_2, \theta) = \frac{1}{2B} L_{11}\lambda_2^2 - \frac{M}{B}\lambda_1\lambda_2 + \frac{1}{2B} L_{22}\lambda_1^2 \tag{2.56}$$

Alternatively, the coenergy of the two winding system may be obtained by integrating eqn.s 2.51 and 2.52. By then taking the partial derivative with respect to a linear displacement, eqn. 2.1 is obtained.

If a permanent magnet is present, the stored energy is determined by eqn. 2.7. Section 2.7.3 shows that the relationship

$$W + W' = \sum_{j=1}^{J} \lambda_j i_j \tag{2.57}$$

holds for a permanent magnet system with multiple energised windings. Application of eqn. 2.57 allows the torque to be equivalently expressed by:

$$T_k = \frac{\partial W'(\lambda, \theta)}{\partial \theta_k} - \sum_{j=1}^{J} \lambda_j \frac{\partial i_j(\lambda, \theta)}{\partial \theta_k} \tag{2.58}$$

$$T_k = \frac{\partial W'(i, \theta)}{\partial \theta_k} \tag{2.59}$$

$$T_k = \sum_{j=1}^{J} i_j \frac{\partial \lambda_j(i,\theta)}{\partial \theta_k} - \frac{\partial W(i,\theta)}{\partial \theta_k} \tag{2.60}$$

where (i,θ) is an abbreviation for $(i_1,\ldots,i_J;\theta_1,\ldots,\theta_K)$. With CAD packages on electromagnetics, it is known that values of torque can be accurately determined from the rate of change of the total coenergy computed by integrating the coenergy density over the volume of the system, as demonstrated by [Brauer *et al.* 1984]. This confirms the validity of eqn. 2.59. The validity of torque eqn.s 2.48, 2.58, and 2.60[4] are demonstrated by mathematical equivalence to eqn. 2.59, resulting from the proof of eqn. 2.57 given in section 2.7.3.

In many CAD packages, a representation of permanent magnets described in section 2.6 is useful for numerical computation. This representation is shown in section 2.6 to give an identical rate of change of permanent magnet coenergy to that of the second quadrant representation of coenergy given in section 2.3 by eqn. 2.16. Thus coenergy, as defined by eqn. 2.17, is also shown by equivalence to yield accurate values of torque.

2.5 TORQUE EQUATIONS FOR A LINEAR PERMANENT MAGNET SYSTEM

In the absence of iron saturation, where a single winding is energised, the flux linkage of the winding may be given by

$$\lambda = \lambda_m(\theta) + L(\theta)i \tag{2.61}$$

where λ_m is the flux linkage due to the magnet, and L is the inductance of the winding. Substituting eqn. 2.61 into eqn. 2.45 yields

$$T = i\frac{d\lambda_m}{d\theta} + i^2\frac{dL}{d\theta} - \frac{\partial W(i,\theta)}{\partial \theta} \tag{2.62}$$

The stored energy $W(i,\theta)$ is determined by eqn. 2.7. Fig. 2.2(a) shows that if $\mathbf{B}_m$ increases towards $\mathbf{B}_o$ due to, for example, a winding current increase, the stored energy of the magnet decreases. A corresponding increase in $\mathbf{B}$ in a region surrounding the magnet yields an increase in the stored energy in that region. Eqn. 2.62 can be simplified by approximating the energy stored to correspond to mutually exclusive components provided by the winding and the magnet, whereby

$$W = W(i=0,\theta) + 1/2\, L(\theta)i^2 \tag{2.63}$$

[4]The 'work function' formulation in [Marinescu and Marinescu 1988] is equivalent to eqn. 2.60, and is supported numerically by comparison to Maxwell stress results.

and the torque is approximated by

$$T = i\frac{d\lambda_m}{d\theta} + \frac{1}{2}i^2\frac{dL}{d\theta} - \frac{dW(i=0,\theta)}{d\theta} \tag{2.64}$$

which is given in [Kamerbeek 1973] and is shown to model the motion of a single phase permanent magnet motor sufficiently accurately in [Schemmann 1971]. The first term in eqn. 2.64 is used to calculate the torque due to the coupling between a magnet and an energised winding in brushless permanent magnet machines. The remaining two terms describe the torques obtained due to reluctance variation with rotational displacement. Eqn. 2.64 is particularly useful for experimental purposes because all of the quantities can be measured from electrical and mechanical terminals. All torque equations for single phase PM motors examined in this Thesis are derived from eqn. 2.64.

2.6 CURRENT SHEET MODEL OF A PERMANENT MAGNET

In a permanent magnet material the relation of $\mathbf{B}$ to $\mathbf{H}$ may be expressed in the form of [Stratton 1941, p.13, 129]:

$$\mathbf{B} = \mu_o[\mathbf{H} + \mathbf{M}(\mathbf{H}, \mathbf{M}_o) + \mathbf{M}_o] \tag{2.65}$$

$\mathbf{M}$ is the induced polarisation defined by $\mathbf{M} = \chi_m\mathbf{H}$ where magnetic susceptibility χ_m is defined by $\chi_m = \partial\mathbf{M}/\partial\mathbf{H}$. $\mathbf{M}_o$ is the residual magnetisation which is non-zero in permanent magnet regions such that $\mathbf{B}$ is non-zero when $\mathbf{H} = 0$. $\mathbf{M}_o$ is interpreted as a source of the field. $\mathbf{M}_o$ may be replaced by a stationary volume distribution of current throughout the volume of the magnet of density

$$\mathbf{J} = \text{curl } \mathbf{M}_o \tag{2.66}$$

and with a current distribution on the surface bounding the magnet volume of density

$$\mathbf{K} = \mathbf{M}_o \times \mathbf{n} \tag{2.67}$$

where $\mathbf{n}$ is the unit outward normal to the surface [Stratton 1941, p. 129]. With $\mathbf{M}_o$ replaced by an equivalent current sheet, eqn. 2.65 reduces to $\mathbf{B} = \mu_o[\mathbf{H} + \mathbf{M}]$ which describes a $\mathbf{B} - \mathbf{H}$ characteristic of the first quadrant passing through the origin. The shifted curve representation is shown in Fig. 2.6(b).

CAD packages on electromagnetics use the technique of shifting the second quadrant demagnetisation curve to the origin and introduce a suitable current carrying coil for modelling a permanent magnet [Gupta *et al.* 1990]. The torque may be obtained from the current sheet model using Maxwell stress [Gupta *et al.* 1990] or some other

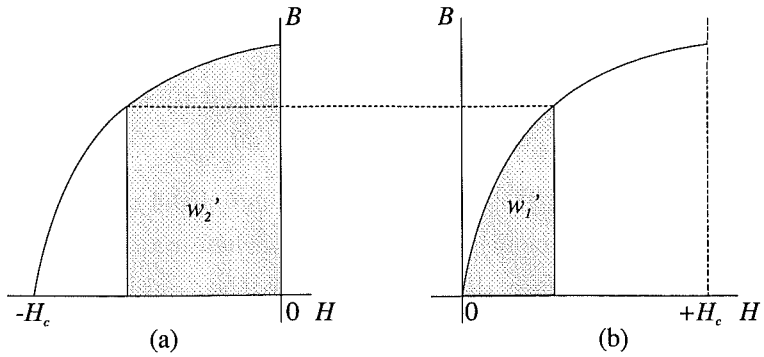

Figure 2.6 Representations of permanent magnet coenergy density. (a) Second quadrant demagnetisation curve. (b) Curve shifted to first quadrant.

method.

With CAD packages, it is known that values of torque can be accurately determined from the rate of change of the total coenergy using the first quadrant representation of permanent magnet coenergy, as demonstrated by [Brauer *et al.* 1984]. Coenergy density for the first quadrant representation of a permanent magnet is shown by the shaded region in Fig. 2.6(b). The relationship between first and second quadrant coenergy representations is given by

$$w_1' = w_2' + w_{1\,H_c}' \tag{2.68}$$

where w_2' is a negative coenergy density. The term $w_{1\,H_c}'$ is the area under the shifted curve from 0 to H_c and is a constant. The rate of change of coenergy is therefore the same for both representations, thus yielding identical values of torque. This relationship provides first: a supporting theoretical basis for the first quadrant representation; and secondly supporting evidence for the experimental validity of the second quadrant representation.

However caution must be observed, if stored energy rather than coenergy is used, as the respective first and second quadrant rates of change of stored energy are different. In this case, only a second quadrant representation has a theoretical basis.

2.7 ENERGY-COENERGY RELATIONSHIP

Magnetic field equations are briefly introduced in the section 2.7.1, before the energy-coenergy relationship is derived from these field equations in sections 2.7.2 and 2.7.3.

2.7.1 Quasistatic Electromagnetic Equations

A quasistatic system may be described as one in which the electric or magnetic field, although varying with time, has the spatial forms of a static (time invariant) field

[Ramo *et al.* 1994]. Nearly all electromechanical systems of technical importance are described as being quasistatic [Woodson and Melcher 1968]. In this quasistatic case, Maxwell's equations can be written in two quasistatic limits. These describe either a magnetic field system or an electric field system. A quasistatic system is either magnetic or electric, but it is not practical for a quasistatic system to have both magnetic and electric fields [Woodson and Melcher 1968, pp. B23-B25]. A quasistatic permanent magnet system is a magnetic field system. The magnetic field equations are therefore applicable, and are given in partial differential form by:

$$\text{curl}\,\mathbf{H} = \mathbf{J}_f \tag{2.69}$$

$$\text{div}\,\mathbf{B} = 0 \tag{2.70}$$

$$\text{div}\,\mathbf{J}_f = 0 \tag{2.71}$$

$$\text{curl}\,\mathbf{E} = -\frac{\partial \mathbf{B}}{\partial t} \tag{2.72}$$

where $\mathbf{J}_f$ is the free current density, and $\mathbf{E}$ is electric field intensity. Eqn.s 2.69 and 2.70 are used in the following sections.

2.7.2 Zero Currents

A quasi-static permanent magnet system with all windings de-energised satisfies curl $\mathbf{H} = 0$ and div $\mathbf{B} = 0$, from which it can be shown that [Zijlstra 1982, Brown Jr. 1962]

$$\int_V \mathbf{H} \cdot \mathbf{B}\, dv = 0 \tag{2.73}$$

where V is volume of the permanent magnet system. By applying the rule of differentiation, whereby $d(\mathbf{H} \cdot \mathbf{B}) = \mathbf{H} \cdot d\mathbf{B} + \mathbf{B} \cdot d\mathbf{H}$, eqn. 2.73 is expressed as

$$\int_V \left[\int \mathbf{H} \cdot d\mathbf{B} + \int \mathbf{B} \cdot d\mathbf{H} \right] dv = 0 \tag{2.74}$$

which according to eqn.s 2.7 and 2.17 may be written as

$$W(i = 0) + W'(i = 0) \; = 0 \tag{2.75}$$

where the magnetisation characteristics of regions within the system are arbitrary.

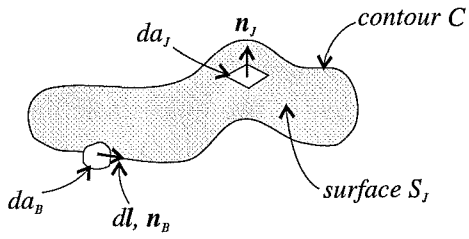

Figure 2.7 A contour of flux.

2.7.3 Non-Zero Currents

The permanent magnet system of section 2.7.2 is now extended to the case where curl $\mathbf{H} = \mathbf{J}_f$ and div $\mathbf{B} = 0$, where the free current density $\mathbf{J}_f$ will be attributed to winding currents. The integral forms of the field equations described above are respectively given by

$$\oint_C \mathbf{H} \cdot d\mathbf{l} = \int_{S_J} \mathbf{J}_f \cdot \mathbf{n}_J \, da_J \tag{2.76}$$

and

$$\oint_S \mathbf{B} \cdot \mathbf{n} \, da = 0 \tag{2.77}$$

These integral forms enable the circuit quantities λ and i to be deduced. Contour C is chosen so as to follow any single contour of flux, where $\mathbf{H}$ is related to $\mathbf{B}$ by eqn. 2.65. In any non permanent magnet region through which the contour may pass, $\mathbf{M}_o$ is zero in which case eqn. 2.65 shows that $\mathbf{H}$ and $\mathbf{B}$ are in the same direction. However, within a permanent magnet material $\mathbf{H}$ and $\mathbf{B}$ are not in the same direction, as discussed by [Cullity 1972]. Eqn. 2.77 will be written in the modified form of

$$\mathbf{B} \cdot \mathbf{n}_B \, da_B = \phi \tag{2.78}$$

where da_B may be any surface element of near infinitesimal area which is orthogonal to an element of length $d\mathbf{l}$ and bisects C once and only once, as shown in Fig. 2.7. Unit normal vector $\mathbf{n}_B$, $\mathbf{B}$, and $d\mathbf{l}$ are parallel. ϕ is the integrated flux which will be required to remain constant wherever eqn. 2.78 is evaluated over contour C. The path chosen for C ensures that $\mathbf{B} \cdot \mathbf{n} \neq 0$ such that $\phi \neq 0$. Multiplying eqn. 2.76 by eqn. 2.78 gives

$$\mathbf{B} \cdot \mathbf{n}_B \, da_B \oint_C \mathbf{H} \cdot d\mathbf{l} = \phi \int_{S_J} \mathbf{J}_f \cdot \mathbf{n}_J \, da_J \tag{2.79}$$

The LHS of eqn. 2.79 is transformed as follows. Let $\oint_C \mathbf{H} \cdot d\mathbf{l} = \sum_{i=1}^{\infty} \mathbf{H}_i \cdot d\mathbf{l}_i = \sum_{i=1}^{\infty} \mathbf{H}_i \cdot \mathbf{n}_{B_i} \Delta l_i$, giving

$$\mathbf{B} \cdot \mathbf{n}_B \, da_B \oint_C \mathbf{H} \cdot d\mathbf{l} = \sum_{i=1}^{\infty} \Big(\mathbf{H}_i \cdot \mathbf{n}_{B_i} \Delta l_i \Big) \Big(\mathbf{B}_i \cdot \mathbf{n}_{B_i} \Delta a_{B_i} \Big) \tag{2.80}$$

which is equal to

$$\sum_{i=1}^{\infty} \Big(|\mathbf{H}_i| |\mathbf{n}_{B_i}| \cos \gamma_{H_i} \Big) \Big(|\mathbf{B}_i| |\mathbf{n}_{B_i}| \cos \gamma_{B_i} \Big) \Delta v_i \tag{2.81}$$

where $\Delta v_i = \Delta l_i \Delta a_{B_i}$ is an element of volume. Eqn. 2.81 is simplified by letting $|\mathbf{n}_{B_i}| = 1$ and $\cos \gamma_{B_i} = 1$ to yield

$$\sum_{i=1}^{\infty} |\mathbf{H}_i| |\mathbf{B}_i| \cos \gamma_{H_i} \Delta v_i \tag{2.82}$$

γ_{H_i} is also the angle between $\mathbf{H}_i$ and $\mathbf{B}_i$, therefore

$$\sum_{i=1}^{\infty} |\mathbf{H}_i| |\mathbf{B}_i| \cos \gamma_{H_i} \Delta v_i = \sum_{i=1}^{\infty} \mathbf{H}_i \cdot \mathbf{B}_i \, \Delta v_i = \int_{V_C} \mathbf{H} \cdot \mathbf{B} \, dv_C \tag{2.83}$$

V_C is the filament volume corresponding to contour C. The RHS of eqn. 2.79 is transformed as follows. The integral $\int_{S_J} \mathbf{J}_f \cdot \mathbf{n}_J \, da_J$ may be expressed as a sum of contributions from winding currents crossing surface S_J by $\sum_{j=1}^{J} \nu_j i_j$ where i_j is the current of the jth winding and ν_j is a coefficient corresponding to the jth winding which may for some values of j be a fractional number or zero. The RHS of eqn. 2.79 may then be expressed by

$$\phi \sum_{j=1}^{J} \nu_j i_j = \sum_{j=1}^{J} \lambda_{Cj} i_j \tag{2.84}$$

where $\lambda_{Cj} = \phi \nu_j$. The flux ϕ is a function of the currents and $\mathbf{M}_o$ such that $\phi = \phi(i_1, \ldots, i_J, \mathbf{M}_o)$ and $\lambda_{Cj} = \lambda_{Cj}(i_1, \ldots, i_J, \mathbf{M}_o)$. Eqn. 2.79 is then expressed as

$$\int_{V_C} \mathbf{H} \cdot \mathbf{B} \, dv_C = \sum_{j=1}^{J} \lambda_{Cj} i_j \tag{2.85}$$

By then summing the contributions from all the filaments into which the field has been resolved yields

$$W + W' = \sum_{j=1}^{J} \lambda_j i_j$$

2.8 CONCLUSIONS

Stored energy and coenergy have been defined for a permanent magnet system. It has been shown that either stored energy or coenergy may be used to determine permanent magnet reluctance torque where the magnetisation characteristics of regions within the system are arbitrary. A specific example of the energy to coenergy relationship in a PM system using a linear PM demagnetisation characteristic and a linear magnetisation characteristic external to the PM has been demonstrated. It has also been shown how residual magnetism may be incorporated into classical electromechanical coupling theory. It has therefore been shown how general equations for torque can be derived for nonlinear permanent magnet systems from classical electromechanical coupling theory. In doing this it has been shown that the relationship $W + W' = \lambda i$ holds for a permanent magnet system. The approximation made in deriving a simplified equation for torque in a linear system has been described. Finally, the validity of the first quadrant representation of the rate of change of coenergy within a permanent magnet material, relevant to CAD systems, has been demonstrated.

Chapter 3

A PM MOTOR WITH TRIANGULAR RELUCTANCE TORQUE

3.1 INTRODUCTION

This chapter examines the concept of the triangular motor introduced in section 1.5. This concept involves the use of two types of torques produced in PM motors, which are the phase-magnet and PM reluctance torques, to obtain a constant instantaneous torque in a single phase PM motor. The concept requires a PM reluctance torque of triangular shape. An experimental triangular motor is built with the aim of verifying the concept.

3.2 A PHYSICAL IMPLEMENTATION OF THE TRIANGULAR MOTOR

The triangular motor is implemented for the purpose of experimentation as an axial flux machine. This choice is made given the following considerations; the first being the selection of magnets. Ideally a squarewave EMF is required. For an axial flux geometry a near squarewave or trapezoidal EMF may be achieved using parallel magnetised magnets. Parallel magnetisation is easily achieved. If, alternatively, a radial flux geometry is selected, radially magnetised magnets are required to achieve the desired EMF waveform. A radial magnetisation is more difficult to achieve, and such magnets may be more difficult to obtain, particularly for a prototype motor. Secondly, from the point of view of analysis, an elementary expression for the flux density is more easily obtained from a parallel magnetic field obtained using parallel magnetised magnets and axial airgaps. An expression which satisfies zero divergence of the magnetic flux density (div $B = 0$) is more easily obtained in this case.

Fig. 3.1 shows a drawing of the stator viewed from the airgap end. The airgap surface consists of four pole arcs, each arc extending nearly 90°. The poles are constructed out of concentrically wound silicon steel lamination. Slots are cut out of the stator surface using electro-discharge machining (EDM). The width of each slot opening is $2q$.

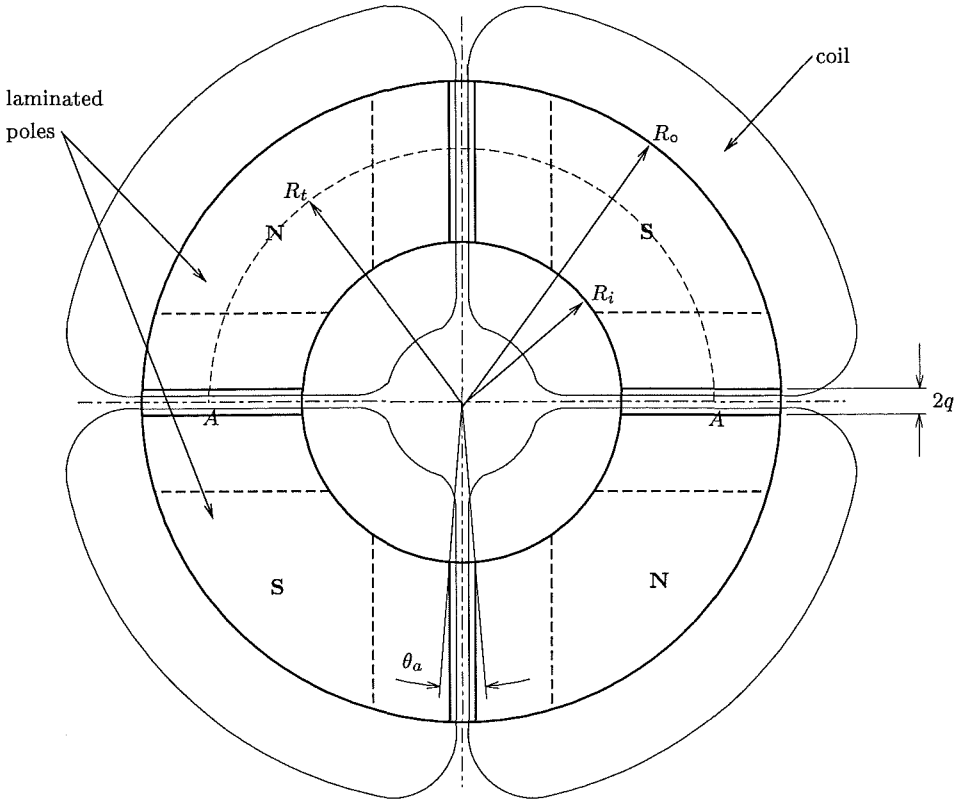

Figure 3.1 Airgap end view drawing of the triangular motor stator.

Fig. 3.2 shows a rolled out view of the stator, and the rest of the triangular motor, corresponding to the semicircular section AA marked in Fig. 3.1. Two out of four poles are shown, and the mechanical supporting structure is not shown. The stator poles house concentrated coils and the slot/pole ratio is one. Two coilsides share each slot, and there are a total of four stator coils which are connected in series. To maximise PM flux linkage, the magnets are surface mounted adjacent to the stator poles. The magnet poles have the same pitch and shape as the stator poles. The surface mounting of the magnets also reduces stator winding inductance due to the larger airgap reluctance resulting from the thickness and the low permeability of the magnets [Miller 1989, p. 77]. Assuming that the flux density across the magnets is uniform, the EMF induced in the stator windings, and the EMF/torque function, are ideally squarewave. This is demonstrated by hypothetically removing the stator iron and applying the *flux cutting rule*. If conductor velocity u, flux density B, and conductor length l are mutually perpendicular, then the EMF induced in a conductor by its motion in the magnetic field is given by [Edwards 1986]:

$$e = Blu \tag{3.1}$$

According to eqn. 3.1, if the magnitude of the flux density is constant, and alternates in direction according to the polarity of the PM poles, a squarewave EMF is obtained.

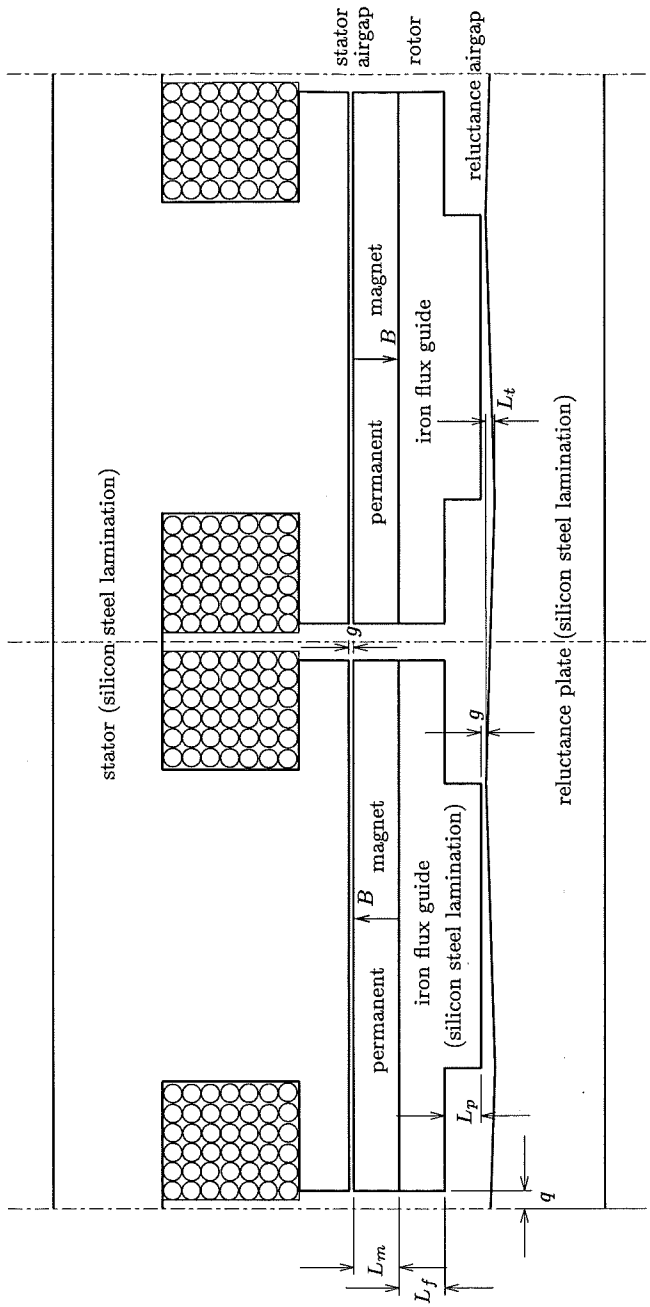

Figure 3.2 Rolled out view of the triangular motor corresponding to the semicircular section AA marked in Fig. 3.1.

In practice, the induced EMF is trapezoidal. In section 3.8.5, a trapezoidal EMF is not shown to present a problem regarding the torque quality of the triangular motor. This stator/rotor design therefore satisfies the EMF/torque function characteristic required for the triangular motor. In order to extend the plateau region of the trapezoidal EMF within each half cycle as far as possible, the rotor PM and stator pole arcs are made as full pitched as possible. Interpolar flux leakage, of the rotor in particular, and mechanical considerations, restrict the pitch of the rotor and stator poles.

The second characteristic to be implemented is a triangular reluctance torque. This requires

1. A PM reluctance geometry which can provide a reluctance torque of satisfactory triangular shape and sufficient magnitude, completing two cycles per electrical cycle.

2. An implementation of the reluctance torque geometry which preferably does not require a second separate set of magnets and an additional flux circuit. The reluctance torque and EMF/torque function characteristic are therefore to be obtained using the same magnets and flux circuit. This single flux circuit requirement creates the following problem. As mentioned, the desired EMF/torque function requires poles ideally extending a full electrical pole pitch. The triangular reluctance torque is required to complete a full cycle per half electrical cycle. A corresponding airgap reluctance cycle must therefore also be completed within an electrical pole pitch. To produce a triangular reluctance torque with axial parallel magnetised magnets, the PM poles are required to extend over only a half electrical pole pitch. However, if the PM poles are shortened to half a pole pitch, eqn. 3.1 shows that the induced EMF is shortened by a corresponding amount. The plateau width then extends no more than 90° per electrical half cycle. Such shortening of the plateau width is unacceptable in this design where only a single phase is used.

3. A design which enables a PM reluctance torque displacement angle of $\gamma_m = 45°$ electrical. This establishes the correct alignment of the reluctance torque and the EMF/torque function, as shown by Fig. 1.7. This angle is limited in the conventional motor designs, as described in section 1.2.2.

These requirements are achieved by the rotor and reluctance plate configuration shown in Fig. 3.2. An iron *flux guide* is attached to the underside of each magnet. Each magnet and flux guide form part of the rotor. Each fluxguide reduces in width to a half pole pitch. Underneath each flux guide, the PM flux crosses a second airgap to link the iron *reluctance plate*. The reluctance plate remains stationary. The reluctance plate is triangularly modulated, completing a modulation cycle every electrical pole pitch. The conflicting rotor pole pitch requirements for EMF/torque function shape and reluctance torque generation are satisfied by using two sets of airgaps, each side having a different pole pitch. The experimental triangular motor is therefore described as a *double airgap* machine. The rotor has the tendency to align itself at the stable detent reluctance torque position. This occurs where the rotor/reluctance plate airgap length underneath the half pitch pole of the iron flux guide is minimised. Section 3.6 describes how the triangular reluctance torque is obtained.

In this design, the reluctance plate airgap, rather than the stator airgap, is modulated to produce a reluctance torque. If slotting is ignored, the stator airgap flux density is uniform across the magnets at any given rotor position. As rotation occurs, the reluctance airgap modulation causes the uniform flux density across the entire width of each magnet to be gradually modulated. This causes some modulation of the EMF/torque function waveform, and this is analysed in section 3.6.2.1.

The design allows any PM reluctance torque displacement angle to be obtained. This is achieved by rotating the reluctance plate relative to the stator to achieve the desired displacement angle. The stator and reluctance plate are then fixed mechanically together at this angle.

3.3 SELECTION OF MAGNETIC MATERIALS

3.3.1 Non Grain Oriented Silicon Steel

The stator, flux guides, and reluctance plate are all constructed out of laminated coils of non grain oriented (NGO) silicon steel sheet. NGO steel is used mainly in rotating electrical machinery because of its isotropic magnetism in the sheet plane [Ervens and Wilmesmeier 1985-1994]. NGO steel is therefore ferromagnetic at right angle directions in the plane of the sheet.

All machining, shearing, and stamping operations on electrical steel sheet produce stresses which extend for some distance from the strained area and have an adverse effect on the magnetic characteristics. For example, stamping the airgap surface of a lamination creates magnetic hardening to a depth corresponding approximately to the thickness of the lamination. The coiling of the laminations also produces mechanical stresses and possible hardening. Stress relief annealing removes the stresses and improves the magnetic properties. The lamination thickness is 0.5 mm. The steel lamination[1] is covered with a coat of organic insulation and another coat of inorganic insulation. After the lamination is coiled, it is annealed in a non-oxidising and non-carburising Argon atmosphere. During the annealing process the organic insulation layer perishes but the inorganic insulation remains to maintain an inter-lamination resistance.

3.3.2 Permanent Magnet Materials

In this section, the three main groups of PM materials are briefly described. Section 3.3.2.1 describes in more detail the PM material selected for the triangular motor.

[1]The NGO silicon steel used is SG13CP4 from BHP Steel. At a flux density of 1.55 Tesla (T), this steel requires a magnetising force of 564 A/m, but can also be magnetised to at least 1.8 T. At 1.5 T, core loss is typically 6.5 W/Kg.

Alnicos have a relatively high remanence and low coercive force [Hamdi 1994]. They are hard and brittle, and can only be machined by grinding. Use of Alnicos in motors is diminishing [Hamdi 1994]. The second group, *hard ferrites*, are in widespread use. They have a low remanence but fairly high coercivity. Ferrites are also hard and brittle. Ferrites are very cheap and have a plentiful supply of raw material.

The third group consists of the rare earth compositions of Samarium Cobalt and Neodymium-Iron-Boron (Nd-Fe-B). The coercivities and remanences of these materials are much higher, and less material is required. However, the rare earths, and the Samarium Cobalt magnets in particular, are more expensive than the ferrites.

Rare earths and ferrites can be manufactured in plastic bonded form [Ervens and Wilmesmeier 1985-1994]. *Plasto-ferrites*, for example, have lower magnetic values than their unbonded counterparts, but they offer much better mechanical properties. This enables production costs to be held down [Ervens and Wilmesmeier 1985-1994]. Machining and fabrication of these materials are simple.

3.3.2.1 Bonded Nd-Fe-B Permanent Magnets

Bonded Nd-Fe-B permanent magnets are selected for the triangular motor. This choice is based on the ease to which these magnets can be prototyped. Similar advantages exist for plastoferrites, but the remanences are much lower. *Isotropic* material, which has the same magnetic properties in all directions, is used. The bonded isotropic form has the advantage for prototyping of: first, being able to be machined as required; and secondly, being able to be magnetised as desired in either a simple or complex manner. The magnets were machined and then magnetised by the manufacturer. A significant advantage of the bonded Nd-Fe-B magnets in relation to the unbonded form, is substantially increased resistance to corrosion. The bonded Nd-Fe-B material has a major linear demagnetisation characteristic, which is convenient for modelling. Table 3.1 lists the properties of the bonded Nd-Fe-B magnets used in the design.

property	unit	value
Remanence B_r	T	0.68
Inductive coercive force H_{cB}	kA/m	450
Intrinsic coercive force H_{cJ}	kA/m	820
Energy product $(BH)_{max}$	kJ/m^3	80
Relative recoil permeability μ_r		1.25
Maximum operating temperature	°C	150
Temperature coefficient	%/°C	-0.10
Density	g/cm^3	6.0
Compressive strength	MPa (cylindrical h/d=2)	220

Table 3.1 Properties for Bremag 10N bonded Nd-Fe-B permanent magnets.

3.4 MECHANICAL DESIGN

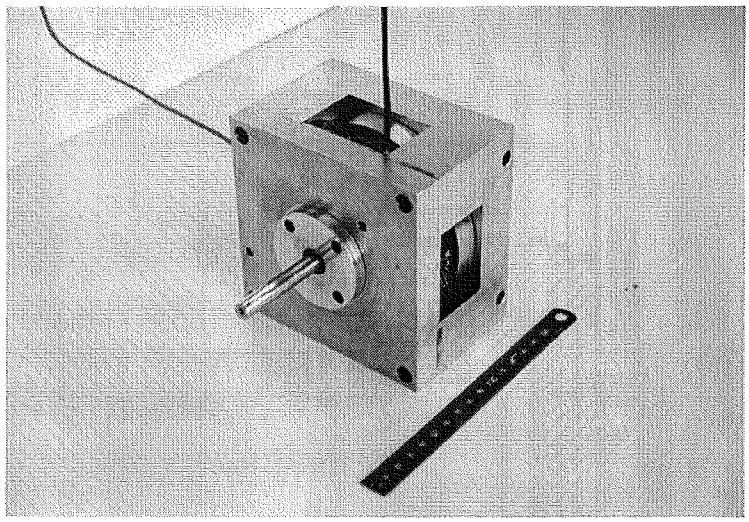

Figure 3.3 Experimental triangular motor

Fig. 3.3 shows a photograph of the fully assembled experimental triangular motor. Stator windings and the rotor are visible within the aluminium housings. The stator, rotor, and reluctance plate are contained within two aluminium housings. Fig. 3.4 shows a drawing of a cross-section of the triangular motor. In this design, the structural components such as the housings, are non-ferromagnetic.

The bearing arrangement of a rotating shaft requires two bearings to support and locate the shaft radially and axially with respect to the stationary housing. These are a locating bearing and a non-locating bearing which are both identified in Fig. 3.4. The locating ball bearing accommodates combined radial and axial loads, and is fixed in position on the shaft and in the stator housing. The non-locating bearing is only required to provide radial support. It permits axial displacement so that the bearings do not mutually stress each other. The mutual stress can be caused by the differential thermal expansion of the stainless steel shaft and the aluminium housings, where both materials have different coefficients of thermal expansion. Deep groove ball bearings were found to be the most suitable type of ball bearing in terms of cost, compactness, and performance requirements. These ball bearings have their own seals which simplifies the design of the ball bearing housings. Deep groove ball bearings are capable of withstanding axial as well as radial loadings. Axial, as well as radial loading, is expected in this design. Deep groove ball bearings require accurate alignment of the bearing bores through both aluminium housings. Incidentally, this ensures that the rotor and stator airgaps have a high degree of parallelism.

With reference to Fig. 3.4, the motor is assembled from the three major components as follows. The locating bearing is placed in the stator housing and the shaft is placed inside the bearing. The lock nut is then tightened over the washer and lo-

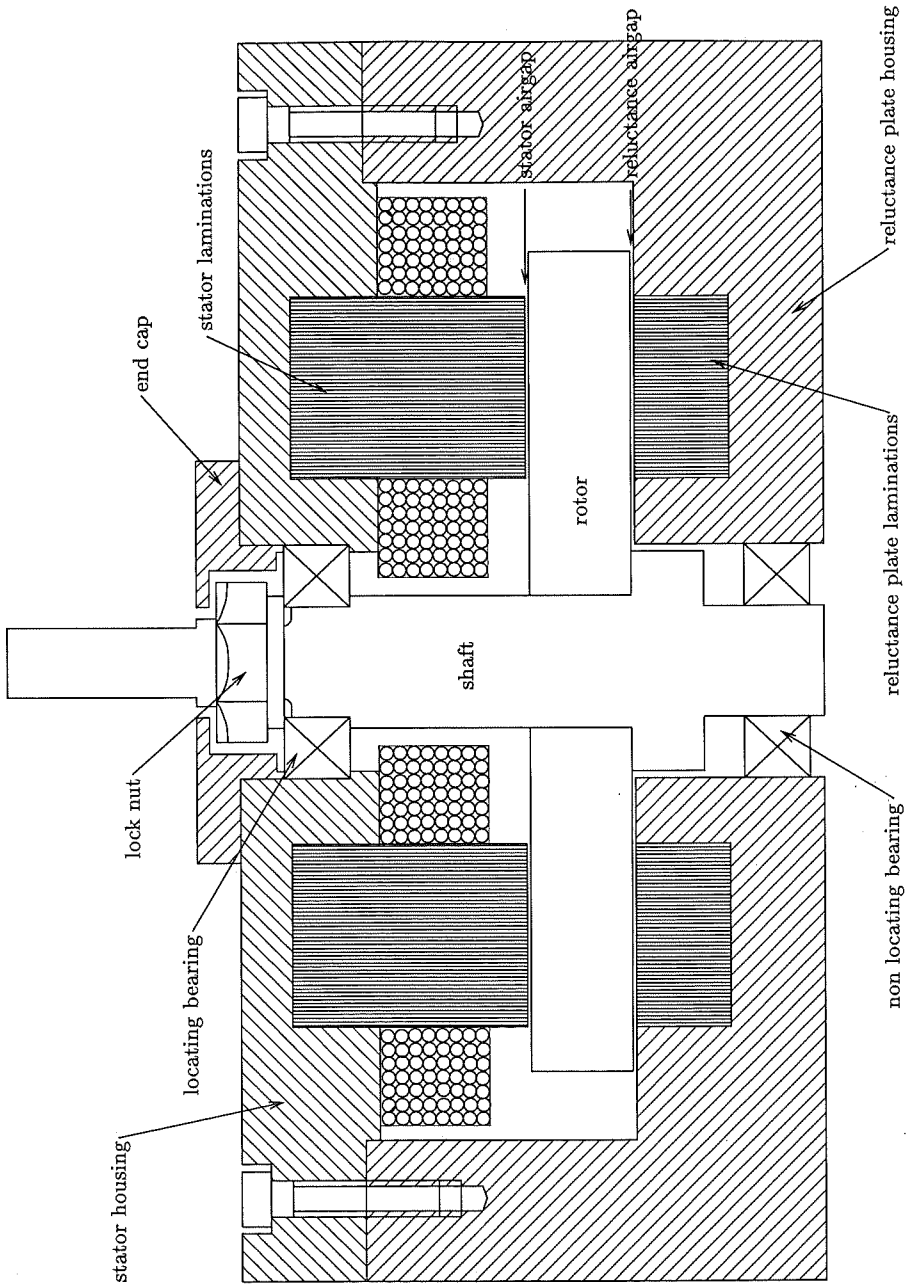

Figure 3.4 Cross-section of the triangular motor showing structural detail.

cating bearing. The end cap is then fastened over the bearing with capscrews. This fixes the stator airgap. The non-locating bearing is then placed inside the reluctance plate housing, and the reluctance plate and stator housings are fastened together using capscrews.

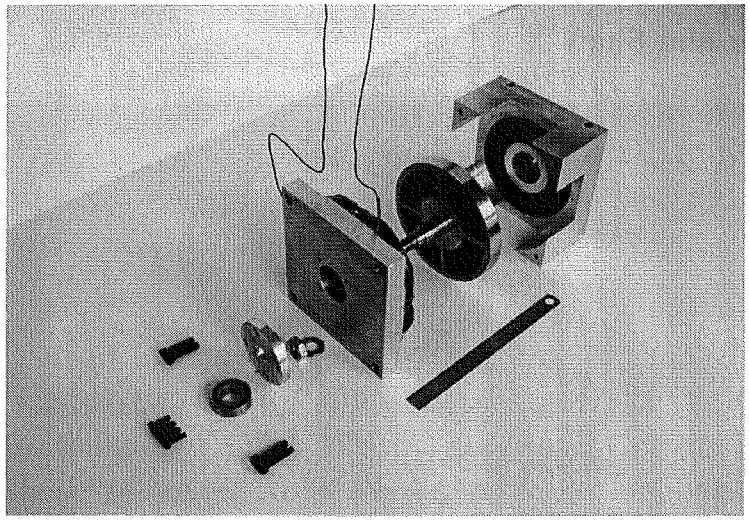

Figure 3.5 Disassembled triangular motor

Fig. 3.5 shows a photograph of the motor disassembled into its three major components. From left to right: stator/stator housing, rotor/shaft, and reluctance plate/reluctance housing.

3.4.1 Stator and Stator Housing

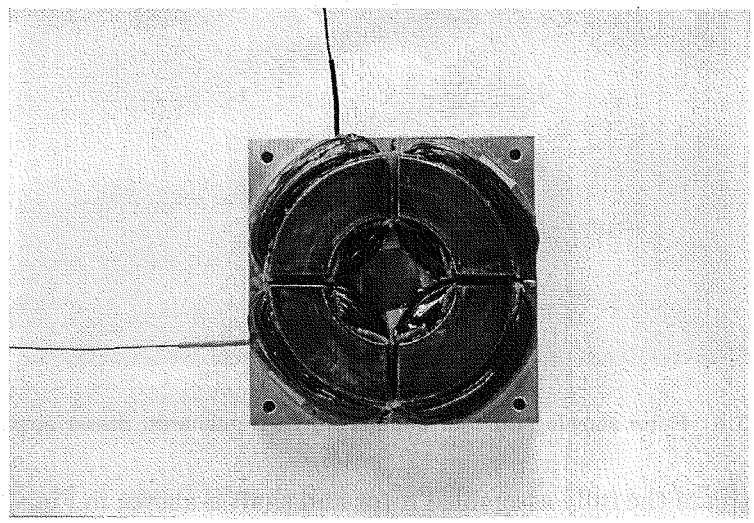

Figure 3.6 Stator and stator housing.

Fig. 3.6 shows the poles of the fully completed stator/stator housing. The stator poles are constructed from coiled laminations. The stator is constructed as follows:

a silicon steel coil is wound and then annealed to relieve mechanical stress. The four slots in the coil are cut out by EDM. The stator coil is then sealed into the aluminium stator housing with epoxy resin. The four copper stator windings are then hand wound into the stator, and coated with epoxy resin for protection.

3.4.2 Rotor and Shaft

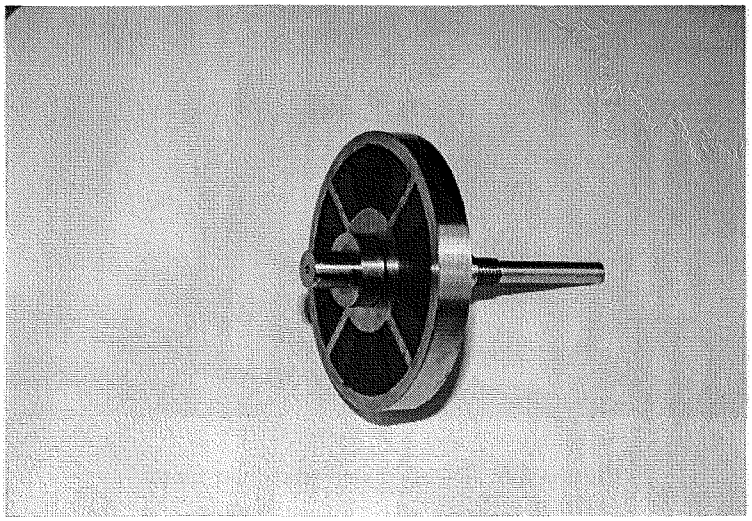

Figure 3.7 Assembled rotor.

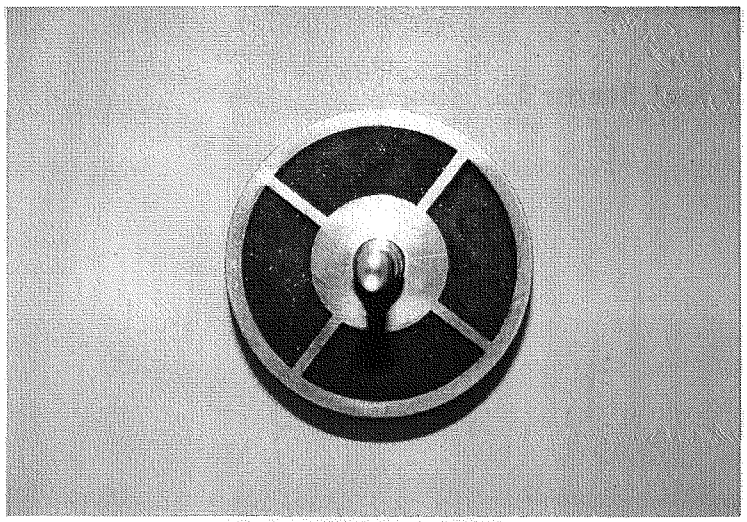

Figure 3.8 Rotor showing the four bonded Nd-Fe-B pole arcs. Stator airgap side.

A photograph of the fully assembled rotor and shaft is shown in Fig. 3.7. The shaft is made from stainless steel. The four bonded Nd-Fe-B pole arcs are shown in Fig. 3.8. These poles face the stator airgap. The four PM pole arcs are held inside a stainless steel spider and ring. Fig. 3.9 shows the flux guide poles on the other side of the rotor. These poles face the reluctance plate airgap. These poles each extend a half electrical

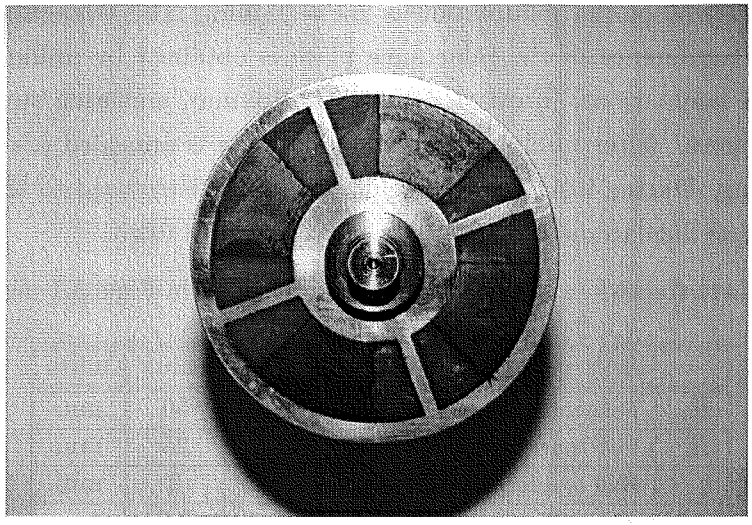

Figure 3.9 Rotor showing the four fluxguide poles. Reluctance plate airgap side.

pole pitch. The fluxguides are milled out from coiled laminations, before annealing and insertion into the rotor spider and ring behind the magnets. The cavities adjacent to the flux guide poles are filled in with epoxy resin. The fluxguides are laminated as a precautionary measure to protect against eddy currents caused by flux modulation, resulting from the reluctance plate airgap modulation.

3.4.3 Reluctance Plate and Housing

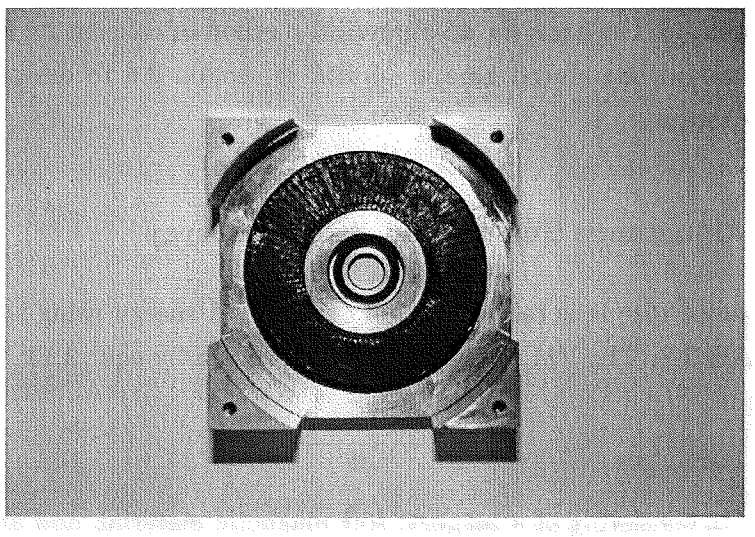

Figure 3.10 Reluctance Plate and Housing.

The airgap surface of the reluctance plate, and the aluminium reluctance plate housing, are shown in Fig. 3.10. The coiled laminations of the reluctance plate are imbedded in the aluminium housing. Although not clearly visible, the height of the reluctance plate is modulated triangularly, completing four cycles around the circum-

ference. The height of the modulation is $L_t = 1$ mm. The triangular modulation around the circumference of the reluctance plate is obtained by milling radial steps into the coiled laminations. Each step height is 0.1 mm, and each step extends 4.5 mechanical degrees. After milling, the reluctance plate is annealed prior to insertion into the housing. During insertion, the reluctance plate is rotated to the correct PM reluctance torque displacement angle γ_m, relative to the stator.

Table 3.2 lists the values of the dimensions identified in Fig.s 3.1 and 3.2.

	description	value	units
R_o	Pole outer radius	50	mm
R_i	Pole inner radius	25	mm
q	Half of interpolar airgap	2	mm
g	Airgap clearances	0.5	mm
L_m	Magnet thickness	5	mm
L_f	Fluxguide feed height	5	mm
L_p	Fluxguide pole height	4	mm
L_t	Reluctance airgap modulation height	1	mm

Table 3.2 Selected values of mechanical dimensions identified in Fig.s 3.1 and 3.2.

3.5 AN ANALYTICAL METHOD OF CALCULATING PM RELUCTANCE TORQUE

This section describes the basis for an analytical method of calculating PM reluctance torque. The method introduced here is applied in section 3.6 to design a triangular PM reluctance torque.

3.5.1 PM Reluctance Torque and Stored Energy

The PM reluctance torque is calculated from the stored energy using the method described in section 2.2. The PM reluctance torque is given by eqn. 2.13:

$$T_r = -\frac{dW(i=0)}{d\theta}$$

For a PM system consisting of a magnet, soft magnetic material, and an air or linear material, the stored energy is given by eqn. 2.7. For air, the linear relationship between $\mathbf{B}$ and $\mathbf{H}$ is given by $\mathbf{B} = \mu_o \mathbf{H}$. As a function of the airgap flux density, the energy density of the air is

$$w_a = \frac{B_a^2}{2\mu_o} \tag{3.2}$$

The magnetic field may also permeate iron regions. For the purpose of illustration, if the iron is assumed to be linear, the energy density of the iron is given by $w_s = B_s^2/(2\mu_o\mu_{rs})$. μ_{rs} is the relative permeability of the iron and is usually large. Unless the iron is heavily saturated, thus yielding a low relative permeability, the iron energy density is unlikely to be large. For the purpose of simplification, the energy density contribution due to the iron is approximated to be zero. For a PM material having a major linear demagnetisation characteristic, the stored energy density function w_m is given by eqn. 2.25. By neglecting the contribution from the iron, eqn. 2.7 may be simplified to

$$W(i=0) = \int_{V_m} w_m \, dv_m + \int_{V_a} w_a \, dv_a \tag{3.3}$$

3.5.2 Approximation of the Direction and Magnitude of the Magnetic Flux Density

To obtain an analytical expression for the reluctance torque, an analytical expression for the magnetic field is first required. All stationary magnetic fields in a uniform medium are described by Poisson's equation or, its particular form, Laplace's equation [Binns and Lawrenson 1963]. Poisson's equation applies within current regions and Laplace's equation applies in all other regions of the field. PM regions may be represented by a magnetisation vector or an equivalent current sheet, as described in section 2.6. [Binns and Lawrenson 1963] describe a number of methods which are used to obtain analytical solutions for the field. However, these analytical methods lead to highly idealised solutions to a relatively small number of problems, and a large proportion of practical problems must be solved using numerical methods [Silvester 1968].

In this section, an analytical expression for the reluctance torque over a reluctance cycle is required. Therefore an expression for the field is required which includes the angle of rotation. The geometry of the problem is not fixed. This makes an analytical solution to Poisson's and Laplace's equations even more difficult, if not impossible. An elementary expression for the flux density is obtained without finding solution to Poisson's and Laplace's equations. This is possible because reasonable approximations regarding the direction and magnitude of the flux density can be made because of the simple nature of the configurations examined.

Magnetic fields are three dimensional. However, solutions of sufficient accuracy may be obtained in electrical machines by only considering two dimensions. For a two dimensional treatment, the flux density in any element of area consists of normal and tangential components, as shown by Fig. 3.11(a). The directions of the flux density in the magnet and the airgap are required to be determined. Fig. 3.11(b) shows a generalised magnet and airgap configuration which can represent an axial rotary magnet and iron structure which is laid out linearly. Flux lines link a magnet, an airgap, and an iron return path of infinite permeability. Flux lines have been drawn

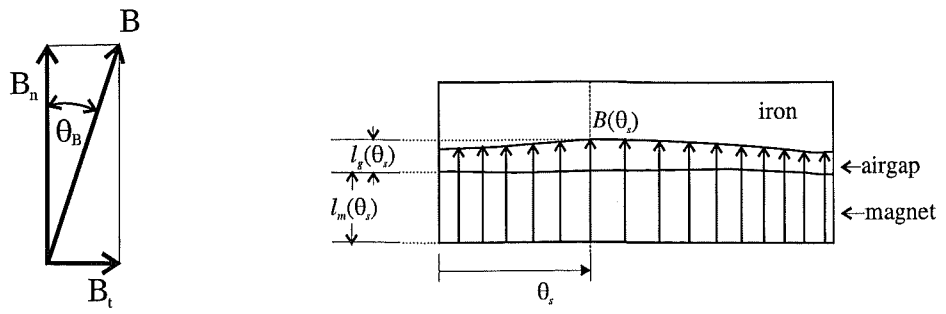

(a) Components of flux density.

(b) Normal lines of flux.

Figure 3.11

only in regions where the stored energy is calculated. In both the airgap and magnet regions, the flux density is approximated to lie in the normal direction only (up the page), given the presence of the following requirements:

1. The magnet is magnetised in the normal direction. The significance of the direction of the residual magnetisation is explained as follows. The principle of minimum potential energy may be applied to many physical systems [Hamdi 1994]. Minimisation of the energy of the system then leads to an approximate solution. By applying this principle to the PM system, inspection of eqn. 2.25 shows that the magnet energy density is minimised if the flux density is parallel to the direction of magnetisation. The second RHS term of eqn. 2.25 vanishes, and the first RHS term is minimised. The magnet energy density function reduces to

$$w_m = \frac{(B_{m||} - B_r)^2}{2\mu_o\mu_{r||}} \tag{3.4}$$

2. The ratio of airgap area to airgap length is large. This reduces the influence of end effects which improves the uniformity of the flux density.

3. The modulation of the airgap length is small.

This last requirement ensures that the modulation of the iron airgap surface is small. This, in turn, ensures that an airgap flux line directed normally intercepts the iron airgap surface at an angle which is approximately normal to the iron surface. This requirement becomes apparent by considering the iron/airgap boundary conditions. Any magnetic field problem is solved by finding solutions which satisfy the magnetic field equations 2.69-2.72. Because these are partial differential equations, an infinite number of possible solutions exist. If there are regions containing distinct media, the additional requirement that certain conditions must be satisfied at all the boundaries that separate these regions, is necessary to obtain the correct solution. For a magnetic

field system, there are two boundary conditions which are required to be specified. These are obtained from the integral forms of eqn.s 2.69 and 2.70, which are eqn.s 2.76 and 2.77, respectively. From eqn. 2.77, the boundary condition

$$B_{n1} - B_{n2} = 0 \tag{3.5}$$

is obtained. Subscript n denotes the normal component to the boundary surface, and the numerical subscripts identify two different media. Eqn. 3.5 states that the normal component of $\mathbf{B}$ must be continuous at the boundary. The second boundary condition is obtained from eqn. 2.76, in the absence of current sheets, as

$$H_{t1} - H_{t2} = 0 \tag{3.6}$$

where subscript t denotes the tangential component to the boundary surface. Eqn. 3.6 states that the tangential component of $\mathbf{H}$ must be continuous at the boundary. Solutions at media boundaries, in which the relative permeabilities are different, are discontinuous. This may result in the magnitude and direction of the flux density changing abruptly at the boundary. An iron/airgap boundary, in which the iron is assumed to be infinitely permeable, is an example of a limiting case. If the iron permeability is infinite, $\mathbf{B}$ within the iron is infinite unless $\mathbf{H}$ is zero, since $\mathbf{B} = \mu\mathbf{H}$. An infinite flux density is prohibited by the requirement that the divergence of $\mathbf{B}$ is zero. $\mathbf{H}$ must therefore be zero within the iron. The boundary condition of eqn. 3.6 requires that the tangential component of $\mathbf{H}$ be continuous at the boundary. The tangential component of $\mathbf{H}$ on the airgap boundary must also be zero. As a result, only a normal component of airgap flux density exists, and airgap flux lines intersect the iron at angles normal to the boundary surface [Silvester 1968]. This iron/airgap boundary solution serves the purpose of determining the correct direction of the airgap flux lines at the iron/airgap surface in Fig. 3.11(b). It shows that the directions of the airgap flux lines into the iron/airgap surface drawn in Fig. 3.11(b) are approximations of the correct solution, if the iron surface is modulated.

The specification that flux lines cross the boundary at a normal angle is known as a Neumann boundary condition [Brauer 1988]. [Silvester 1968, pp. 179-182] demonstrates that even with a relative permeability of only ten, airgap flux lines will meet an iron/air interface very nearly at right angles.

In Fig. 3.11(b), the direction of the airgap flux density at the airgap/magnet boundary also requires examination. Given the assumptions that the flux density in the magnet is parallel to the residual magnetisation, the demagnetising field in the magnet is obtained from eqn. 2.65 as

$$H_m = \frac{B_m}{\mu_o \mu_r} - \frac{M_o}{\mu_r} \tag{3.7}$$

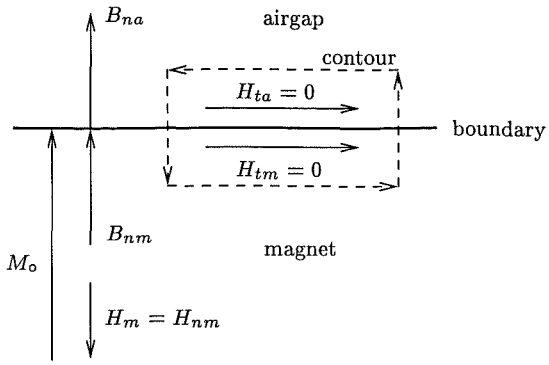

Figure 3.12 Direction of the flux density at the airgap/magnet boundary. The contour is used for determining the continuity in the tangential components of the field intensity.

Eqn. 3.7 shows that H_m is negative, or antiparallel in relation to B_m and M_o. Fig. 3.12 shows the field components at the airgap/magnet boundary where the boundary surface is normal to the magnetisation. To satisfy eqn. 3.5, the normal component of the magnet flux density B_{nm}, and the normal component of the airgap flux density B_{na}, are equal. Since H_m is antiparallel to B_{nm}, the tangential component of H_m is zero. There is no current sheet at the boundary surface and eqn. 3.6 holds. The tangential component of $\mathbf{H}$ at the boundary must be continuous, and as $H_{tm} = 0$, so must $H_{ta} = 0$. Only a normal component of airgap flux density can exist, and airgap flux lines are parallel to magnet flux lines at the boundary.

In Fig. 3.11(b), if the modulation of the PM surface is small, then the situation described by Fig. 3.12 may be assumed, and the airgap flux density remains parallel to the magnet flux density at the boundary surface. In all the magnet and airgap configurations selected for analysis in this Thesis, the airgap/magnet boundary surface is always normal to the magnetisation, as shown in Fig. 3.12.

Given the normal direction of the airgap flux density at the magnet/airgap and airgap/iron boundaries, and the small airgap modulation, the airgap flux lines are assumed to traverse the airgap in straight lines parallel to the magnet flux density.

An approximation of the magnitude of the flux density can be made now that the direction of the flux density has been established. The flux density is obtained using eqn.s 2.76 and 2.77. In the absence of currents, eqn. 2.76 reduces to

$$\oint_C \mathbf{H} \cdot d\mathbf{l} = 0 \tag{3.8}$$

Contour C is chosen to follow a single contour of flux. Because $\mathbf{H} = 0$ in the iron return path, contour C is only required to be integrated through the magnet and airgap. Given that $\mathbf{H}$ remains constant within each of the airgap and magnet mediums

along the contour, eqn. 3.8 is evaluated as

$$H_m l_m + H_g l_g = 0 \tag{3.9}$$

where l_m and l_g are respectively the magnet and airgap lengths defined in Fig. 3.11(b). Eqn. 2.77 may be written in the modified form of

$$B_m \, dA_m - B_g \, dA_g = 0 \tag{3.10}$$

where dA_m and dA_g may be any surface elements, in the magnet and airgap respectively, of near infinitesimal area which are orthogonal to C. Using eqn.s 3.9, 3.10, and the constitutive relations $B_g = \mu_o H_g$ for the airgap, and $B_m = \mu_o \mu_r H_m + B_r$ for the magnet, the flux density of contour C within the magnet is obtained as

$$B_{m_C} = \frac{B_r}{1 + \frac{dA_m}{dA_g}\frac{l_g}{l_m}\mu_r} \tag{3.11}$$

In Fig. 3.11(b), $dA_m/dA_g = 1$ for all contours, and so from eqn. 3.10, $B_m = B_g$. The magnitude of the flux density for all contours is then given by

$$B(\theta_s) = \frac{B_r}{1 + \frac{l_g(\theta_s)}{l_m(\theta_s)}\mu_r} \tag{3.12}$$

3.5.3 A Comparison to the Maxwell Stress Tensor Method

In this section, the approach to calculating reluctance torque developed in the previous sections is compared to the method of torque calculation using Maxwell stress. The Maxwell stress method is selected for comparison because it is popularly used. Both methods are compared in relation to obtaining analytical, rather than numerical solutions. Comparison of energy, Maxwell stress, and other methods in numerical computation are described in depth in the literature.

To begin, the Maxwell stress method is briefly described. For a two dimensional problem, the force and torque are evaluated by integrating the force density or *stress* over a contour surrounding the part of interest. The stresses are represented by field *tensors* [Hamdi 1994]. For a two dimensional flux density distribution and a contour C enclosing a body, the force acting on the body is given by

$$\mathbf{F} = \int_C \left[\frac{1}{\mu_o}\mathbf{B}(\mathbf{B}\cdot\mathbf{n}) - \frac{1}{2\mu_o}B^2 \cdot \mathbf{n}\right] dC \tag{3.13}$$

where $\mathbf{n}$ is a unit normal vector to the contour. The contour must be placed entirely in the air, and the contour must enclose the part on which the force is exerted. The shape of the contour is chosen arbitrarily. Of particular interest are the components of

stress normal and tangential to the contour, which are respectively given by

$$df_n = \frac{1}{2\mu_o}\left(B_n^2 - B_t^2\right)dC \tag{3.14}$$

and

$$df_t = \frac{1}{\mu_o} B_n B_t \, dC \tag{3.15}$$

Eqn.s 3.14 and 3.15 show that the Maxwell stress method requires the flux density to be accurately resolved into its normal and tangential components in the *local* vicinity of the contour. The unresolved flux density approximation of section 3.5.2 provides an example in which a meaningless result would be obtained: for a contour of integration following a path perpendicular to the flux density in Fig. 3.11(b), $B_t = 0$ and the tangential force is zero. Only the normal force is accounted for. An accurate field solution is clearly required. The difficulty in obtaining such a solution analytically has been noted in section 3.5.2.

In contrast, the energy method allows for greater approximation of the local flux density. This is because stored energy is a *global* quantity. This allows an elementary expression for the flux density to be used which is simple enough to allow an analytical expression for the reluctance torque to be obtained. Because the stored energy is an analytical expression, the error in taking the derivative with respect to rotational displacement θ is zero. A powerful analytical result is obtained in a simple manner. This is demonstrated by the example of section 3.6.1. This analytical method yields a fast solution of the reluctance torque waveform, whilst also providing ready insight into the influence of parameters.

The application of this analytical energy method is limited to problems where the airgap is reasonably smooth. This probably excludes cogging torque problems due to stator slotting because the requirements of section 3.5.2, particularly requirements 2 and 3, are unlikely to be met. The field is therefore unlikely to be described with sufficient accuracy by the approximation made.

In more complicated magnet and airgap geometries where the field approximation is still reasonable, the expression for the stored energy may not be integrable in closed form. The examples of section 4.8, and section V in the paper 'Effects of Airgap and Magnet Shapes on Permanent Magnet Reluctance Torque' in Appendix A, are such cases. To obtain the stored energy, numerical evaluation of the integral is required. Powerful numerical techniques are available [Forsythe *et al.* 1977] which allow fast and accurate evaluation of the integral. Because the computation is not intensive, the energies corresponding to a large number of rotor positions may be evaluated. Numerical differentiation is then required to obtain the reluctance torque waveform. Because the evaluation of the stored energy is accurate, the difference between the

energies at adjacent rotor positions also remains accurate. Therefore, the error in the numerical differentiation is reduced to a desirable level by increasing the number of rotor positions for which the stored energy is evaluated. Fast and accurately evaluated reluctance torque waveform solutions are still obtainable.

3.6 DESIGN OF A TRIANGULAR PM RELUCTANCE TORQUE

This section develops analytical models for the PM reluctance torque of selected magnet and airgap configurations. The analytical energy method of section 3.5 is used. These configurations are shown to produce reluctance torques which approximate triangular waveforms. These configurations are selected on the assumption that the shape of the reluctance torque is related to the shape of the airgap, for these particular configurations. The results of the analysis support this assumption for these examples. To support the validity of the analytical models, finite element analysis (FEA) results are presented in section 3.7 for the experimental triangular motor.

3.6.1 Rectangular Magnet and Triangular Airgap

(a) Stable detent position, $\theta = 0$.

(b) Unstable detent position, $\theta = \pi$.

Figure 3.13 Rectangular magnet and triangular airgap.

Fig. 3.13(a) shows a rectangular magnet/triangular airgap configuration where a rotary permanent magnet and iron structure is laid out linearly. The triangular iron shape modulates the airgap in a triangular manner, repeating a cycle every 2π reluctance radians. The magnet is rectangular, uniformly magnetised in the normal direction (up the page), and extends over half an airgap cycle. In Fig. 3.13(a), the magnet is aligned at the stable detent position coresponding to rotational angle $\theta = 0$. In Fig. 3.13(b) the magnet is aligned at the unstable detent position one half reluctance cycle later.

Fig. 3.14(a) shows the three dimensional depiction of the rectangular magnet and triangular airgap configuration. In this axial configuration the direction of magnet magnetisation and the flux density are parallel to the axis of rotation. The airgap is perpendicular to the axis of rotation. Cylindrical coordinates are used. Fig. 3.14(b) shows a rolled out view of Fig. 3.14(a) from which an analytical equation for the reluctance torque is obtained. The angles are specified in reluctance radians, which in

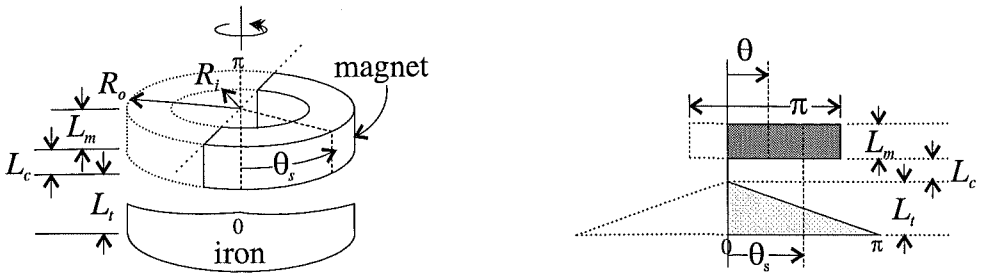

(a) Axial configuration.

(b) Rolled out view of Fig. 3.14(a).

Figure 3.14 Axial configuration, and two dimensional model.

Fig.s 3.14(a) and 3.14(b), are also equal to mechanical radians. Only the stored energy in the magnet, and in the airgap directly beneath the magnet, are calculated. Return paths for the flux are assumed to be infinitely permeable. From eqn.s 3.2, 3.3, and 3.4, the stored energy is obtained by

$$\mathcal{W} = \int \frac{(B_r - B)^2}{2\mu_o \mu_r} dV_m + \int \frac{B^2}{2\mu_o} dV_a \tag{3.16}$$

where B is given by eqn. 3.12. With reference to Fig. 3.14(b), $l_m(\theta_s) = L_m$ along the angular width of the magnet, and $l_g(\theta_s) = (\theta_s/\pi)L_t + L_c$ where $0 \leq \theta_s \leq \pi$. With reference to Fig. 3.14(a), the volume of the magnet from zero up to angle θ_s is given by $V_m(\theta_s) = \frac{1}{2}(R_o^2 - R_i^2)\theta_s L_m$ where the magnet is an arc of π radians, with an outer radius R_o, and an inner radius R_i. Then, for eqn. 3.16

$$dV_m = \frac{1}{2}(R_o^2 - R_i^2)L_m \, d\theta_s \tag{3.17}$$

Up to angle θ_s the volume of the airgap is given by $V_a(\theta_s) = (R_o^2 - R_i^2)\theta_s^2 L_t/4\pi + (R_o^2 - R_i^2)\theta_s L_c/2$, and

$$dV_a = \frac{(R_o^2 - R_i^2)}{2}\left(\frac{L_t\theta_s}{\pi} + L_c\right)d\theta_s \tag{3.18}$$

Substitution of eqn.s 3.12, 3.17, and 3.18 into eqn. 3.16 yields

$$\mathcal{W} = \int \frac{B_r^2 k_a (L_t\theta_s + L_c\pi)L_m}{4\mu_o(\pi L_m + \theta_s L_t \mu_r + \pi\mu_r L_c)} d\theta_s \tag{3.19}$$

where

$$k_a = R_o^2 - R_i^2 \tag{3.20}$$

For the case described by Fig. 3.14(b) where the magnet extends π radians, the airgap symmetry about $\theta_s = 0$ allows the total stored energy to be given over an angle of

rotation of $-\pi/2 \leq \theta \leq \pi/2$ by

$$W = \mathcal{W}\Big|_0^{\pi/2+\theta} + \mathcal{W}\Big|_0^{\pi/2-\theta} \tag{3.21}$$

Because the airgap modulation is discontinuous, mathematically the angle of rotation is restricted to $\theta = -\pi/2 \ldots \pi/2$, and W is a piecewise function. Integrating eqn. 3.19 yields

$$\mathcal{W} = \frac{k_a L_m B_r^2}{4\mu_o \mu_r}\left[\theta_s - \frac{L_m \pi \ln(\pi L_m + \theta_s L_t \mu_r + \mu_r \pi L_c)}{\mu_r L_t}\right] \tag{3.22}$$

From eqn.s 2.13 and 3.21, the PM reluctance torque is then obtained as

$$T_r = \frac{-\pi k_a B_r^2 L_m^2}{2\mu_o \mu_r} \frac{\theta}{\left(\frac{\pi L_m}{L_t \mu_r} + \frac{\pi L_c}{L_t} + \frac{\pi}{2} + \theta\right)\left(\frac{\pi L_m}{L_t \mu_r} + \frac{\pi L_c}{L_t} + \frac{\pi}{2} - \theta\right)} \tag{3.23}$$

where $-\pi/2 \leq \theta \leq \pi/2$. If $|\theta| \ll \frac{\pi L_m}{\mu_r L_t} + \frac{\pi L_c}{L_t} + \frac{\pi}{2}$, eqn. 3.23 is approximated by

$$T_r \approx \frac{-\pi k_a B_r^2 L_m^2}{2\mu_o \mu_r} \frac{\theta}{\left(\frac{\pi L_m}{\mu_r L_t} + \frac{\pi L_c}{L_t} + \frac{\pi}{2}\right)^2} \tag{3.24}$$

and $T_r(\theta)$ approximates a straight line. A second piece-wise function, similar to that of eqn. 3.23, can be obtained for the second half of the cycle to demonstrate a triangular reluctance torque. Eqn. 3.23 suggests that if $L_m > L_t \mu_r$, a high quality triangular reluctance torque waveform can be obtained with triangular airgap modulation.

3.6.2 A Magnetic Reluctance Model of the Triangular Motor

This section describes a magnetic reluctance model of the triangular motor. The magnet and airgap configuration of the triangular motor differs from that of Fig. 3.14, in that the iron flux guide separates the magnet and the reluctance airgap. The reluctance airgap is thus bounded by two iron surfaces. The reluctance model is used to obtain an estimate of the shape and magnitude of the PM reluctance torque. In section 3.6.2.1, this reluctance model is also used to obtain an estimate of the EMF/torque function.

The concept of the magnetic reluctance circuit is useful for the estimation of inductance [Silvester 1968, pp. 199-207], but it may also be used to estimate the fluxes and flux densities in a PM circuit. This, in turn, allows estimation of the stored energy. The application of the magnetic reluctance circuit concept to a PM system is demonstrated by simple manipulation of eqn. 3.11. By assuming uniform flux densities throughout

areas A_g and A_m, eqn. 3.10 may be written in the modified form of

$$\phi = B_m A_m \tag{3.25}$$

where ϕ is the magnetic flux. Substitution of eqn. 3.11 into 3.25 yields

$$\phi = \frac{\dfrac{B_r l_m}{\mu_o \mu_r}}{\dfrac{l_m}{\mu_o \mu_r A_m} + \dfrac{l_g}{\mu_o A_g}} \tag{3.26}$$

which is of the form

$$\phi = \frac{\mathcal{F}}{\mathcal{R}} \tag{3.27}$$

where $\mathcal{F}$ is the MMF and $\mathcal{R}$ is the magnetic reluctance. $\mathcal{F} = \phi\mathcal{R}$ is referred to as the *magnetic Ohm's law*. $\mathcal{F}$ is defined by $\mathcal{F} = \int \mathbf{H} \cdot d\mathbf{l}$, and is the dual to the EMF, $e = \int \mathbf{E} \cdot d\mathbf{l}$. In eqn. 3.26, $\mathcal{F} = \frac{B_r l_m}{\mu_o \mu_r}$. Setting $H_m = 0$ in eqn. 3.7 shows that $\mathcal{F}$ is related to the residual magnetisation by $\mathcal{F} = M_o \frac{l_m}{\mu_r}$. If the demagnetisation characteristic of the PM material remains linear down to zero induction, $\mathcal{F}$ is related to the inductive coercivity H_{cB} by $\mathcal{F} = -H_{cB} l_m$.

Both terms in the denominator of eqn. 3.26 represent magnetic reluctances. Magnetic reluctance is analogous to electric resistance. A magnet reluctance $\mathcal{R}_m = \frac{l_m}{\mu_o \mu_r A_m}$ is specified by the physical dimensions and permeability of the magnet. Similarly, an airgap reluctance is given by $\mathcal{R}_g = \frac{l_g}{\mu_o A_g}$. Reluctances in magnetic circuits are additive in the same manner as resistances in electric circuits. Reluctances $\mathcal{R}_m$ and $\mathcal{R}_g$ are therefore connected in series across the MMF source, $\mathcal{F}$. For more complicated magnetic circuits, extra series or parallel reluctances may be included.

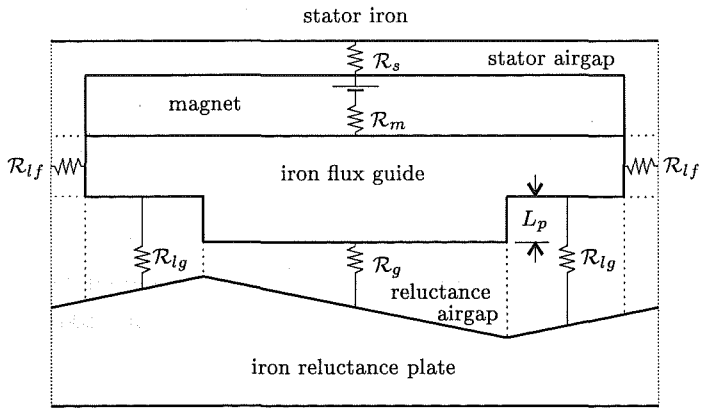

Figure 3.15 Triangular motor magnetic reluctance circuit.

Fig. 3.15 illustrates a simple reluctance circuit for one pole of the triangular motor.

The reluctances are identified using resistance symbols. The iron components of the circuit are assumed to be infinitely permeable and only the reluctances of the airgaps and magnet are considered. Reluctance $\mathcal{R}_{lf}$ represents leakage paths between adjacent iron flux guides which shunts flux away from the reluctance airgap. The reluctance of the reluctance airgap is crudely approximated by two components, $\mathcal{R}_{lg}$ and $\mathcal{R}_g$. Estimation of the direction and magnitude of the flux density in the reluctance airgap is difficult because of the discrete step in the airgap modulation caused by the iron flux guide. Estimation is also difficult because the reluctance airgap is bounded by two iron surfaces. Unlike the configuration of section 3.6.1, the flux across the reluctance airgap is not distributed by the uniform residual magnetisation of a magnet bordering the airgap surface. The directions of all flux densities are assumed to be parallel to the vertical or horizontal orientation of their respective reluctance symbols. Within each reluctance region, the magnitude of the flux density is assumed to remain constant. Reluctances $\mathcal{R}_{lg}$ and $\mathcal{R}_g$ are proportional to the average airgap length in each of their respective regions. These average airgap lengths vary as the rotor moves across the reluctance plate. For example, as the rotor begins to move to the right from the position shown in Fig. 3.15, the average airgap length of reluctance $\mathcal{R}_g$ increases, and $\mathcal{R}_g$ increases. At the same time, the average airgap length of $\mathcal{R}_{lg}$ decreases, and $\mathcal{R}_{lg}$ decreases. Without the extra airgap length L_p, $\mathcal{R}_{lg}$ would be of similar magnitude to $\mathcal{R}_g$. No net airgap reluctance modulation would occur yielding no net reluctance torque. The modulations of $\mathcal{R}_{lg}$ and $\mathcal{R}_g$ may then be considered to be in antiphase. $\mathcal{R}_{lg}$ is considered to be a leakage reluctance because it reduces the magnitude of the reluctance torque. The reluctance torque is increased by increasing iron flux guide dimension L_p, but this also increases the size and inertia of the rotor. To obtain a satisfactory design, a balance of dimensional values is obtained using the reluctance model.

Because of the high permeability of the iron flux guide and the uniform residual magnetisation of the magnet, the flux is uniformly distributed along the boundary of the flux guide and the magnet. Therefore, the magnet flux density and the energy density across the pitch of the magnet are almost constant at a given rotor position. Accordingly, a single flux path through the magnet of reluctance $\mathcal{R}_m$ is used. This is clearly different from the configuration of section 3.6.1 where the flux and energy densities across the pitch of the magnet varies at a given rotor position. The total magnetic circuit reluctance is given by

$$\mathcal{R}(\theta) = \mathcal{R}_s + \mathcal{R}_m + \frac{\mathcal{R}_{lf}}{2} \left\| \frac{\mathcal{R}_{lg}(\theta)}{2} \right\| \mathcal{R}_g(\theta) \tag{3.28}$$

The total magnetic flux is given by

$$\phi = \frac{B_r L_m}{\mu_o \mu_r \mathcal{R}} \tag{3.29}$$

from which the flux densities and stored energies of individual reluctance paths may then be calculated. The reluctance model is applied to calculate the reluctance torque over a half reluctance torque cycle. The half cycle from the stable to unstable detent torque positions is selected. The rotor moves from the minimum reluctance airgap position to the maximum airgap position, in the manner illustrated by Fig. 3.13. With reference to Fig. 3.2, within this half reluctance cycle, the stator slots remain covered by the magnets. *Cogging* torque will be referred to as the PM reluctance torque caused by stator slotting in the stator airgap. Cogging torque occurs in the triangular motor because there is slotting. However, no cogging torque effects are present due to slotting within this half reluctance torque cycle. This is because it is the ends of the magnets which are responsible for causing cogging torque [Li and Slemon 1988], and the magnet ends experience a uniform reluctance in the stator airgap while the stator slots are covered. No cogging torque components are therefore produced. Both cogging torque (due to the stator airgap) and reluctance torque (due to the reluctance airgap) are present in the other half of the reluctance cycle. Calculation of the reluctance torque in the second half cycle is excluded because the reluctance model does not include the effects of slotting. The experimental torque measurements of section 3.8.1 confirm that no cogging components are present while the stator slots are completely covered by the magnets.

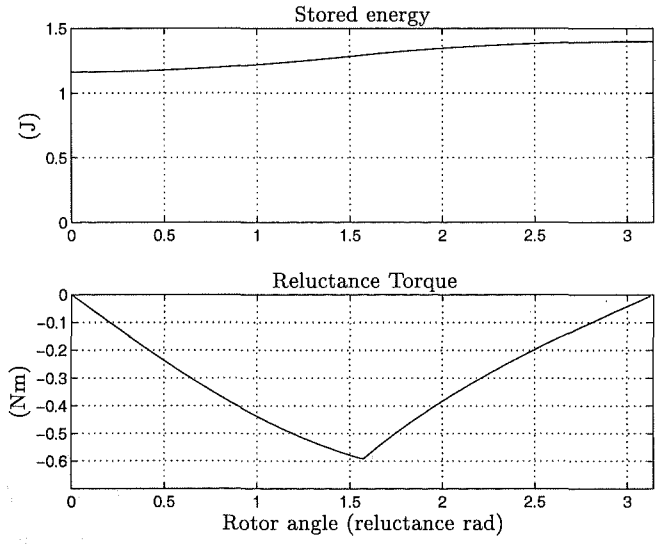

Figure 3.16 Stored energy and PM reluctance torque computed using the magnetic reluctance model of the triangular motor. Energy and torque are plotted over the negative half cycle of the reluctance torque.

Because the reluctance airgap modulation is a piecewise function, and because

multiple parallel reluctance paths exist, an analytical expression for the reluctance torque is not derived. The stored energy within each reluctance path is computed numerically. Fig. 3.16 plots the stored energy and reluctance torque for all four poles of the final triangular motor design. The stored energy is shown to increase as the rotor moves from the stable detent to the unstable detent position: mechanical work is required to be done on the rotor. The reluctance torque approximates a triangular waveform. In the other half reluctance cycle the reluctance torque is positive and has cogging torque components superimposed upon it. Unlike the magnet and airgap configuration of section 3.6.1, the torque waveform is not symmetrical about its peak values.

3.6.2.1 The EMF/Torque Function

In section 3.2, the flux cutting rule is applied. It is shown that if the magnitude of the stator airgap flux density is constant, and alternates in direction according to the polarity of the PM poles, a squarewave EMF is obtained. In practice, a trapezoidal EMF and EMF/torque function are obtained. With regard to this trapezoidal function, the purpose of the analysis in this section is twofold: first, to obtain a quantitative estimate of the magnitude of the EMF/torque function plateau within each half electrical cycle; and secondly, to determine the effect of the modulation of the reluctance airgap on this plateau region.

Applying the flux cutting rule to achieve these aims, or application of the flux cutting rule in general, requires care. In applying the flux cutting rule, incorrect results can be obtained when parts of the magnetic structure, such as the stator iron, move with the conductors relative to the source of the field [Edwards 1986]. To obtain a correct result, the source of the magnetic field must not be affected by the relative motion of the rotor and stator. To achieve this, either the stator iron must be removed, or the stator slots must be filled in such that there is no modulation of the stator airgap surface. To obtain the correct magnitude of the flux density, the slots are hypothetically filled in, and the conductors are concentrated on the stator surface. By neglecting the effect of stator slotting, the solution to the problem becomes idealised.

Faraday's law may be used to determine the correct EMF and EMF/torque function in all situations. The stator surface may be modulated in any manner. The PM flux linking a closed turn is given by

$$\phi_m = \int_S \mathbf{B} \cdot \mathbf{n}\, da \tag{3.30}$$

where S is any surface spanning the boundary of the closed turn. The EMF/torque function for a machine having N series connected turns linked by the same flux is then

given by

$$\frac{d\lambda_m}{d\theta} = N\frac{d\phi_m}{d\theta} \tag{3.31}$$

Eqn.s 3.30 and 3.31 are used in this section to obtain the EMF/torque function with the aid of Fig. 3.17. In Fig. 3.17, stator slotting is omitted, and the rotor poles are full pitched. With the removal of the stator slots, the flux cutting rule could also be used. In applying Faraday's law, the surface of integration is taken along the airgap surface

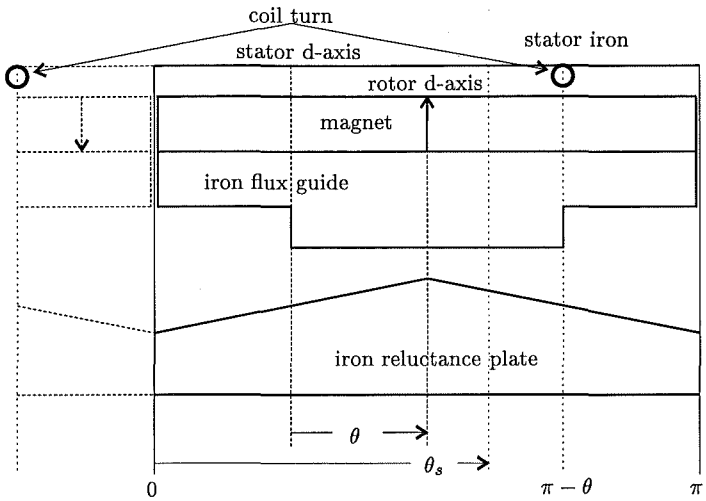

Figure 3.17 Flux linkage model for the triangular motor.

of the magnet pole lying between angles $\theta_s = 0$ and $\theta_s = \pi$. By setting appropriate integration limits, integrating over this surface is equivalent to integrating over a surface spanning the stator turn. θ_s is defined relative to the rotor pole and lies within the limits $0 \leq \theta_s \leq \pi$. The flux linkage is integrated with respect to θ_s. θ is the angle of rotation defined as the angle between the stator d-axis and the rotor d-axis. Because the flux density is normal to the integration surface, $\mathbf{B} \cdot \mathbf{n} = |\mathbf{B}| = B_m$. Using the reluctance circuit model, the flux density is obtained from

$$B_m = \frac{\phi_m}{A_m} \tag{3.32}$$

where A_m is the airgap surface area of a magnet pole. For the surface of integration spanning the airgap surface of the magnet pole, the integration limits are

$$\phi_m = \int_0^{\pi-\theta} B_m \, da - \int_{\pi-\theta}^{\pi} B_m \, da \qquad 0 \leq \theta \leq \pi \tag{3.33}$$

Fig. 3.18 shows the EMF/torque function computed using the reluctance circuit model. The plateau regions of the computed waveform extend a full half electrical cycle because the effects of pole saliency and flux fringing are not modelled. The reluctance

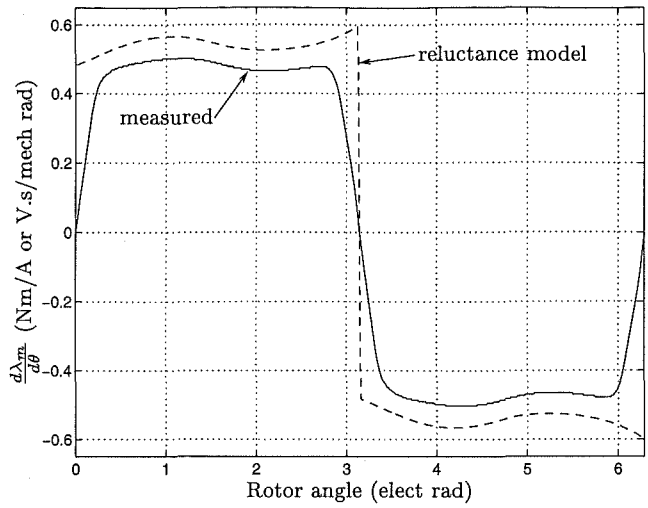

Figure 3.18 EMF/torque function, $\frac{d\lambda_m}{d\theta} = N\frac{d\phi_m}{d\theta}$, computed using the reluctance circuit model. $N = 600$ series connected stator turns. The experimental measurement of the EMF/torque function is also plotted.

model shows that the reluctance airgap causes modulation of the plateau regions. This is confirmed by the experimental measurement of the EMF/torque function which is also shown in Fig. 3.18. A modulation of the measured waveform is also clearly discernible. The measured waveform is trapezoidal in nature. The angular width of the plateau regions of the measured waveform extend approximately the rotational angle swept out while the stator slots are completely covered by the magnet poles. The magnitude of the computed waveform is larger than the measured waveform because the reluctance model does not account for PM flux leakage at the stator airgap. Neither does the reluctance model account for effects such as MMF drop in the iron, which if present, would lower the flux density.

3.7 FINITE ELEMENT ANALYSIS

In this section computational results obtained using finite element analysis are presented for a two dimensional model of the triangular motor. These results correspond to several selected rotor positions. At these positions, solutions are computed for both zero and nonzero stator winding currents. The FEA results are compared to the results obtained using the reluctance circuit model.

3.7.1 The Finite Element Method

The finite element method provides a powerful tool in the CAD design of electrical machines. It can allow accurate calculation of flux distribution, flux density, winding inductance, EMF, forces, and torques, under conditions of iron saturation. The method can also be applied to the structural and thermal analysis of the machine design.

The finite element method applied to electromagnetic problems is well documented in the literature [Lowther and Silvester 1986, Brauer 1988, Hamdi 1994]. In the finite element method, the field problem is divided into a number of subdomains, or *finite elements*. The magnetic potential distribution within each element is then approximated by a polynomial. A numerical solution to the field problem is then obtained with respect to some optimal criterion [Hamdi 1994]. Principal element types are the triangle, the quadrilateral, and curvilinear shapes. Element types are defined in terms of the element shape and the *order* of the polynomial interpolation. An element contains a number of *nodes*, the number of which is related to the type of the element.

After the magnetic potential distribution has been solved, the flux density can be obtained, and forces or torques can be calculated. The Maxwell stress method is used in this analysis. The analysis is performed using a commercial FEA software package[2].

3.7.2 Formulation of a Two Dimensional Linear Model

In machines with radial airgap flux, flux paths are generally restricted to the two dimensional planes of the laminations. For the triangular motor having axial airgap flux, the laminations are curved, therefore occupying three dimensional space. The flux within the laminations therefore also follows three dimensional paths. For example, with reference to Fig. 3.2, the flux paths crossing the airgaps into the laminations are in the axial direction. With reference to Fig. 3.1, the flux paths in the stator yoke between poles follow circular arcs in the plane perpendicular to the axis. In order to avoid a more complicated three dimensional analysis, the triangular motor is rolled out to form an equivalent two dimensional linear motor model. This is achieved by rolling the axial motor out at a radius corresponding to where the net tangential force acts. An appropriate pole width is then calculated. The original axial height and axial dimensions of the motor remain unchanged. The radius at which the tangential force acts is assumed to lie where the pole areas inside and outside the radius are equal. With reference to Fig. 3.1, this radius is given by

$$R_t = \sqrt{\frac{R_o^2 + R_i^2}{2}} \tag{3.34}$$

The pole pitch for the four pole motor is then given by

$$L_{pole} = \frac{2\pi R_t}{4} \tag{3.35}$$

The width of a pole is then selected such that the pole area remains unaltered. The relative dimensions of the linear motor model corresponding to radius R_t are shown in Fig. 3.2. Interpolar airgap lengths and slot dimensions remain unaltered. Due to

[2]The finite element analysis has been performed by Dr J. D. Edwards of the University of Sussex using the [MagNet 5.2 1996] software package.

the periodic nature of the magnetic field, only one pole is needed to be analysed in the FEA. The force calculated by the linear two dimensional model is converted to an equivalent axial motor torque by

$$T = 4F_t R_t \tag{3.36}$$

where F_t is the tangential force per pole for the linear model. The iron regions in the linear model are represented using the magnetisation curve of the silicon steel laminations used. The bonded Nd-Fe-B material is modelled by its remanence and linear recoil permeability.

3.7.3 Flux Plots

In this section, flux or equipotential plots corresponding to several rotor positions are shown. About 3000 elements are used to produce each plot, and the solutions are third order. Boundary conditions are applied to confine the field problem solution to a finite two dimensional region. The Neumann boundary condition is introduced in section 3.5.2. Two other types of boundary conditions are also used to solve magnetic field problems. These are known as *Dirichlet* and *interconnection* boundary conditions [Brauer 1988]. The latter two boundary condition types are applied to the linear motor model.

In Fig.3.19(a), the upper and lower boundaries mark the outer edges of the iron laminations. Because of the high permeability of the iron, most of the flux does not cross the boundary into the air. The reasonably accurate approximation that all the flux lines are contained within the boundaries can be made. This is implemented by specifying a constant magnetic potential along the boundary known as the Dirichlet boundary condition. A flux line is a line of constant magnetic vector potential. Flux lines are therefore contained with the boundary. The magnetic potential A may be set to a constant value, or to zero as shown in Fig. 3.19(a).

Interconnection boundary conditions are applied to the left and right sides in Fig. 3.19(a). In the case of a single pole, the magnetic potential is half periodic at the side boundaries. In this type of boundary, only one of two nodal magnetic potentials separated by a pole pitch is independently specified.

The flux plot of Fig. 3.19(a) corresponds to a rotor position of 0° electrical and zero stator current. The force is entirely due to PM reluctance caused by the modulation of the reluctance airgap. The reluctance force due to the reluctance airgap is at its peak value at this position. The cogging reluctance force is zero because the rotor and stator poles are aligned. The force on the rotor is directed in the forward direction (to the right), and enables the rotor to move to a startable position. All the flux lines drawn link the stator slots suggesting a high flux linkage. Fig. 3.19(b) shows the normal

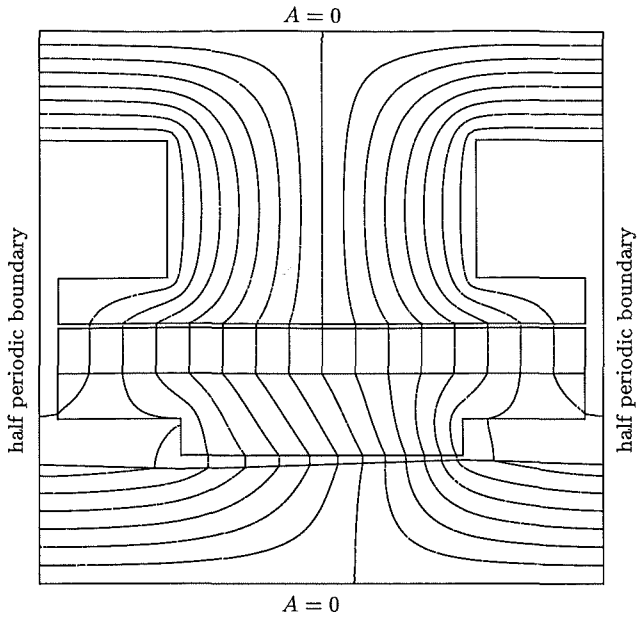

(a) Flux plot.

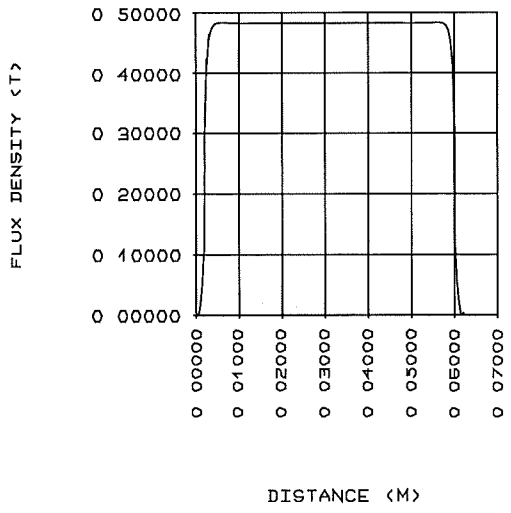

(b) Stator airgap normal flux density.

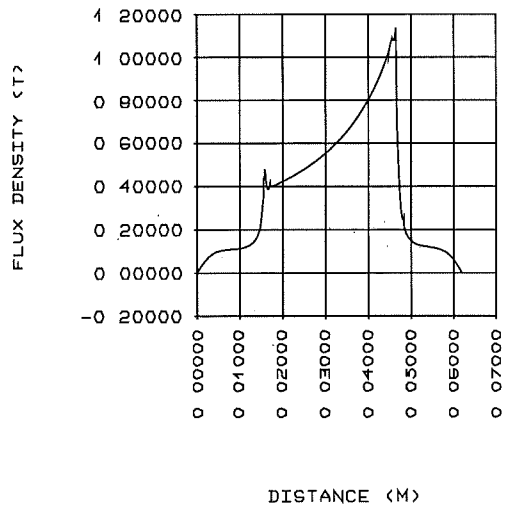

(c) Reluctance airgap normal flux density.

Figure 3.19 Rotor position: 0°. Rotor magnetisation: upwards. Stator current: 0. Tangential force on rotor per pole: +3.82 N.

flux density taken along a line through the middle of the stator airgap. Fig. 3.19(c) shows the normal flux density taken along a line through the middle of the reluctance airgap. The flux density remains very uniform along the magnet surface, whereas it varies considerably underneath the flux guide.

Fig. 3.20 shows the flux plot for the starting position of 45° electrical. This is the stable detent position where the reluctance airgap directly beneath the pole of the

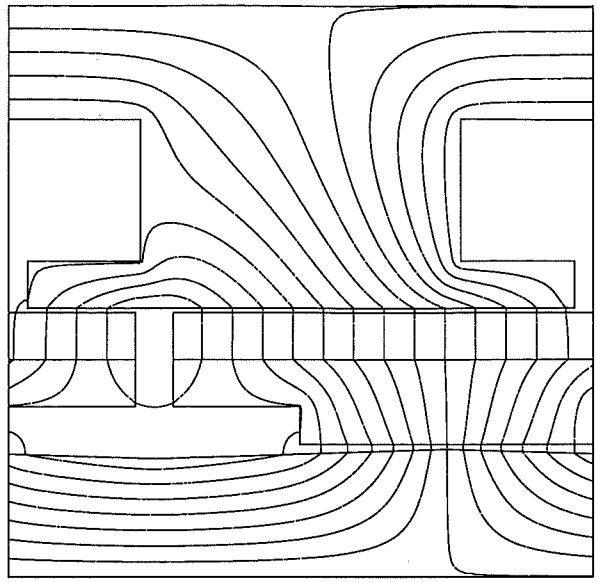

Figure 3.20 Rotor position: 45°. Rotor magnetisation: left downwards, right upwards. Stator current: 0. Tangential force on rotor per pole: +0.12 N.

iron flux guide is minimised. The nonzero tangential force is assumed to provide an indication of the size of the FEA error.

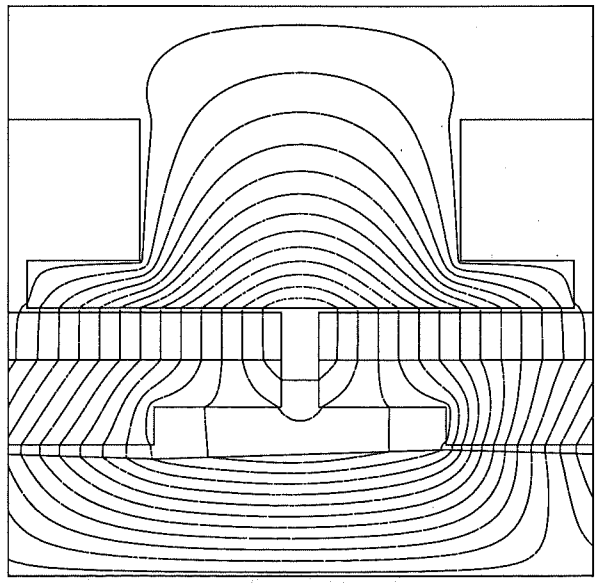

Figure 3.21 Rotor position: 90°. Rotor magnetisation: left downwards, right upwards. Stator current: 0. Tangential force on rotor per pole: -3.77 N.

Fig. 3.21 shows the flux plot for 90° electrical. The rotor and stator d-axes are in quadrature. The PM flux linkage is clearly zero because no flux lines link the stator slots. A half reluctance cycle has been completed and the reluctance force peaks, pulling the rotor in the reverse direction.

Fig. 3.22 shows the flux plot for 90° electrical with the stator windings energised.

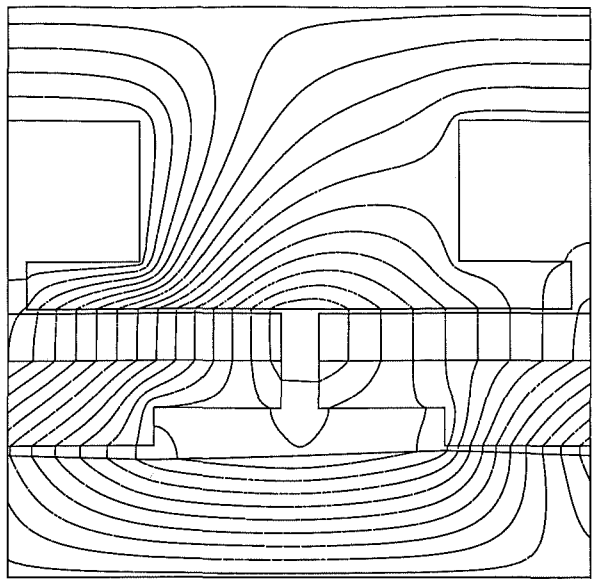

Figure 3.22 Rotor position: 90°. Rotor magnetisation: left downwards, right upwards. Stator current left: -3.1 A, right + 3.1 A. Tangential force on rotor per pole: +7.62 N.

The ideal current waveform is triangular and peaks in amplitude at this position. A current amplitude of 3.1 A is used as a test value. The direction of current specified produces a N-pole on the stator. The left side magnet is an S-pole and the MMF's of these two poles combine. This increases the flux density where these poles overlap. The right side magnet pole is a N-pole and the MMF's of this and the stator pole oppose each other. These decreases the flux density where these poles overlap. The resulting phase-magnet force pulls the rotor in the forward direction to the right. The net tangential force on the rotor pole of +7.62 N is the result of the phase-magnet force and the opposing PM reluctance force.

Fig. 3.23 shows the flux plot for the unstable detent position of 135° electrical. Again, the nonzero tangential force is assumed to provide an indication of the size of the FEA error.

3.7.4 Comparison of FEA and Reluctance Model Results

The FEA is performed for four rotor positions spanning a half electrical cycle or a full PM reluctance cycle. Table 3.3 shows finite element and reluctance circuit model results for the PM reluctance torque at these four rotor positions. The values of the FEA equivalent and reluctance model torques are very close. At these positions, cogging torque contributions due to stator slotting are zero. The nonzero FEA results at 45° and 135° are assumed to give an indication of the magnitude of the FEA error. The small number of FEA values do not enable a detailed picture of the reluctance torque waveform to be obtained, but they do support the reluctance circuit model results in suggesting that the torque waveform is triangular.

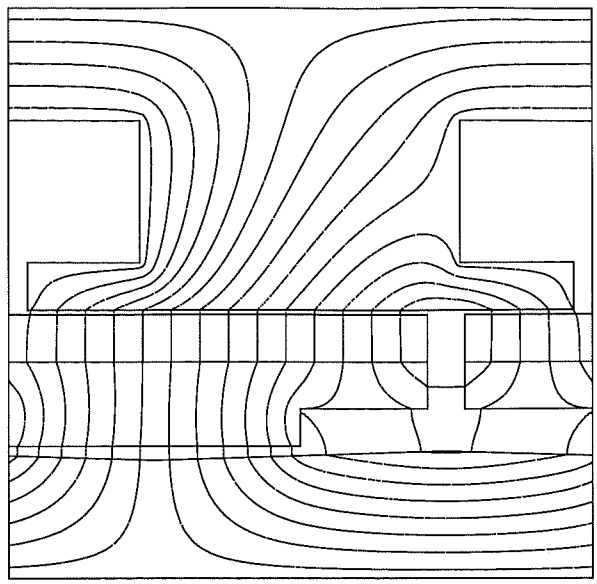

Figure 3.23 Rotor position: 135°. Rotor magnetisation: left downwards, right upwards. Stator current: 0. Tangential force on rotor per pole: +0.06 N.

Position (elect)	FEA force per pole F_t (N)	FEA equivalent torque $T_r = 4F_tR_t$ (Nm)	Reluctance model torque T_r (Nm)
0°	+3.82	+0.604	+0.59
45°	+0.12	+0.019	0
90°	-3.77	-0.596	-0.59
135°	+0.06	+0.009	0

Table 3.3 PM reluctance torque results.

A value of $\hat{T}_r \approx 0.6$ Nm is selected as the triangular reluctance torque amplitude. With reference to Fig. 1.7, $\hat{T}_r$ is also the rated torque for constant instantaneous torque. The reluctance circuit model shows that the value of $\hat{T}_r$ is strongly dependent on the size of the triangular airgap modulation depth L_t. A value of $\hat{T}_r = 0.6$ Nm corresponds to $L_t = 1$ mm. It is possible to increase the value of L_t by several millimetres. This significantly increases the reluctance torque and the rated torque. The reluctance circuit model shows that increasing L_t also increases the modulation of the EMF/torque function. Increasing the modulation in the EMF/torque function results in an increasing departure from the ideal EMF, current, and voltage waveforms of Fig. 1.7 required to produce a constant torque. The current and voltage waveforms required to produce constant instantaneous torque for the experimental motor are calculated in section 3.8.5. The value of L_t is restricted to a value of 1 mm in the design. This is for the purpose of demonstrating reasonably ideal experimental waveforms.

FEA results for the energised motor at rotor positions of 45°, 90°, and 135° electrical are shown in Table 3.4. No analysis for energised stator windings is performed at 0° and 180° because the current is ideally zero at these positions, as illustrated by

Position (elect)	Net force per pole F_t (N)	Current i (A)	Force phase/magnet $F_{ph-m} = F_t - F_r$ (N)	FEA EMF/force function $\frac{d\lambda_m}{dx} = \frac{F_{ph-m}}{i}$ (N/A)	FEA EMF/torque function $\frac{d\lambda_m}{d\theta} = \frac{T_{ph-m}}{i}$ (Nm/A)	Reluctance model $\frac{d\lambda_m}{d\theta}$ (Nm/A)
0°	+3.82	0	-	-	-	-
45°	+5.82	+1.55	+5.70	3.68	0.58	0.54
90°	+7.62	+3.1	+11.39	3.67	0.58	0.52
135°	+5.27	+1.55	+5.21	3.36	0.53	0.50
180°	+3.82	0	-	-	-	-

Table 3.4 Net force per pole using a triangular test current waveform, and comparison of the EMF/torque function estimated from the FEA and the reluctance circuit model.

Fig. 1.7. Eqn. 2.64 identifies the three types of torque producing mechanisms which may all simultaneously contribute to the net torque in a PM machine when the stator is energised. These torques are the phase-magnet torque $T_{ph-m} = i\frac{d\lambda_m}{d\theta}$, the inductive reluctance torque $T_{ind} = \frac{1}{2}i^2\frac{dL}{d\theta}$, and the PM reluctance torque $T_r = -\frac{dW(i=0,\theta)}{d\theta}$. The phase-magnet and PM reluctance torques are explicitly used in the triangular motor concept. The inductive reluctance torque may provide an unintentional contribution. The inductive reluctance torque is proportional to the variation of the stator winding inductance with respect to rotor position. The nature and effect of the stator winding inductance is examined in section 3.8.3, where it is shown that the inductive reluctance torque is not significant. If the inductive reluctance contribution is assumed to be zero for nonzero stator current, the force per pole F_t is the net result of the phase-magnet force F_{ph-m} and PM reluctance force F_r. Given the correct triangular current amplitude, the net forces at the various rotor positions in Table 3.4 should all be the same and equal to the amplitude of the reluctance force. The increase in the net force as the current increases suggests that the amplitude of the test current used in the FEA is too large.

The FEA results for the energised motor also allow an estimate of the EMF/torque function to be obtained. The phase-magnet force is obtained by subtracting the reluctance force from the net force. The values for the reluctance force F_r are obtained from the zero current results of Table 3.3. This assumes that the PM reluctance force is not affected by non-zero stator winding current. A comparison of the flux plots of Fig.s 3.21 and 3.22 shows a considerable change in the flux distribution occurring as a result of energising the stator. Though not shown, plots of the stator airgap normal flux density also show considerable differences. However, the plots of the reluctance airgap normal flux density for the same zero and non-zero currents are hardly distinguishable. These results are observed to occur at the 45° and 135° rotor positions as well. The triangular reluctance force is due to the tangential Maxwell stress in the reluctance airgap, and is calculated from the normal and the tangential flux density components. Since the normal flux density distribution is shown to remain constant, it is likely that

the tangential distribution also remains unchanged. The conclusion can therefore be made that the triangular PM reluctance force is not affected to any significant extent by energising the stator in this double airgap motor. Therefore the PM reluctance and phase-magnet forces may be assumed to superimpose linearly. The EMF/force function and the equivalent EMF/torque function can then be obtained as shown in Table 3.4. These values are compared to those calculated using the reluctance circuit model in Table 3.4.

In summary, the FEA and reluctance circuit model estimates of the PM reluctance torque, and the EMF/torque function, are quite close. For larger values of reluctance airgap modulation, it is expected that the differences in these estimates will increase. For these larger values, the reduced accuracy of the reluctance circuit model will cause the expected increase. Both the FEA and reluctance circuit model results suggest that the required triangular motor characteristics are fulfilled by the experimental design.

3.8 EXPERIMENTAL RESULTS

In this section, the characteristics of the experimental triangular motor are measured. These measured characteristics are then used to validate an electrical model of the triangular motor. A mechanical model is also described, from which an optimal current waveform for motoring is obtained.

3.8.1 Measurement of the PM Reluctance Torque

The PM reluctance torque is measured with the stator winding de-energised using a torque lever. The torque lever consists of a long thin rod which is bisected by the rotor shaft. The protrusion of equal lengths of the rod from either side of the shaft ensures that the lever is counter-balanced. A lightweight cradle is suspended from one end of the rod, into which lead pellets of known mass are placed. The torque exerted due to the lead pellets counteracts the PM reluctance torque. The torque is measured when the lever reaches a horizontally marked position, such that the lever is perpendicular to the force due to gravity acting on the lead pellets. The reluctance torque is then given by

$$T_r = mgx \tag{3.37}$$

where

m = mass of the lead pellets

g = acceleration due to gravity (9.81 m/s^2)

x = length along the rod between the centre of the rotor shaft and the cradle

The rotor position at which the torque is exerted is measured using a protractor attached to the rotor shaft.

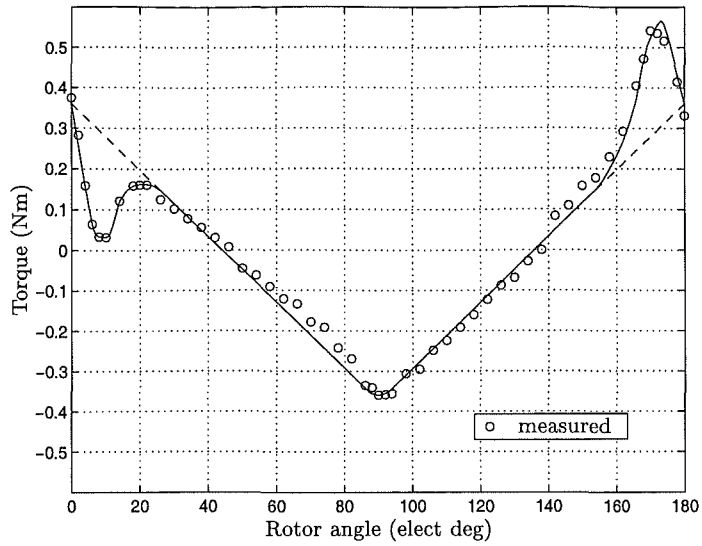

Figure 3.24 Measured PM reluctance torque.

Fig. 3.24 plots the measured PM reluctance torque over an electrical cycle. The solid line provides an estimate of the waveform shape. A PM reluctance torque cycle is completed in the half electrical cycle. The dip in the waveform within $0° - 20°$, and the spike within $160° - 180°$, are due to cogging torque caused by stator slotting. Although the cogging torque cycle spans 180°, the cogging torque is active over an effective cycle of about $40 - 45°$. Each effective half cycle, corresponding to either the dip or the spike, extends just over 20°. This is a little larger than the rotational angle swept out while a stator slot is not completely covered by a magnet pole. This geometrical angle is the angle between the inner edges of the stator poles identified by θ_a in Fig. 3.1, and is given by

$$\theta_a = 4 \arctan\left(\frac{q}{R_i}\right) \tag{3.38}$$

where θ_a is specified in electrical units. For the experimental design, $\theta_a = 18.3°$. Fringing effects extend the width of the dip or the spike to the measured value of just over 20°.

The cogging torque waveform differs from that found in conventional PM machines in that the torque waveform remains positive over the angles in which the cogging torque is active. This occurs because the cogging torque is superimposed upon the torque produced by the reluctance airgap. The dashed lines extrapolate the shape of the reluctance torque with the cogging torque removed. By omitting the cogging torque, a triangular PM reluctance torque is clearly discernible. The stable detent position occurs at approximately 45°, and the unstable detent position occurs at approximately 135°. The estimate of the PM reluctance torque plotted in Fig. 3.16 using the reluctance circuit model corresponds to the half reluctance cycle spanning $45° - 135°$ in Fig. 3.24.

The measured amplitude of the triangular reluctance torque of $\hat{T}_r = 0.36$ Nm is well below the predicted value of $\hat{T}_r = 0.60$ Nm. The cause of this reduced amplitude was found to be the permeability of the stainless steel spider shown in Fig.s 3.7-3.9. This spider supports the magnet poles and the iron flux guides. The effect of the stainless steel permeability is explained with reference to the reluctance circuit model of Fig. 3.15. The interpolar space between adjacent rotor poles and iron flux guides is occupied by the stainless steel spider. The reluctance between adjacent flux guides is modelled by reluctance $\mathcal{R}_{lf}$. If the relative permeability of the stainless steel is greater than one, the value of $\mathcal{R}_{lf}$ is decreased. Decreasing $\mathcal{R}_{lf}$ has the effect of shunting flux away from the reluctance airgap. This reduces the amplitude of the triangular reluctance torque. Using a value of only $\mu_r = 3$ for the relative permeability of the stainless steel was found to reduce the magnitude of the reluctance torque calculated using the reluctance circuit model to that of the measured reluctance torque. A value of $\mu_r = 3$ reduces $\mathcal{R}_{lf}$ by a factor of three, and is equivalent to reducing the interpolar airgaps by the same factor.

A force of attraction between the Nd-Fe-B magnets and the stainless steel was noticed after the stainless steel spider had been manufactured. The force of attraction, and thus also the relative permeability, was found to increase as a magnet was moved towards the centre of the bar from which the spider was machined. The 304 grade of austenitic steel is used, which has a theoretical relative permeability of $\mu_r = 1.008$ [Peckner and Bernstein 1977]. Enquiries were made by the steel supplier regarding the apparent ferromagnetism in this particular grade of stainless steel. It was discovered that ferrite impurities form in the stainless rod during manufacturing, increasing in concentration towards the centre of the rod, giving rise to some ferromagnetism.

The variation of the stainless steel permeability makes measurement and incorporation of the stainless steel permeability into the finite element and reluctance models very difficult. An attempt was made to measure the relative permeability using the ring and fluxmeter method described by [Hughes 1960, pp. 74-75]. A ring was machined out of the rod used to make the stainless steel spider. Most of the rotor interpolar leakage through the stainless steel between flux guides occurs between radii R_o and R_i in Fig. 3.1. As the permeability of the stainless steel decreases with increasing radius, choosing the radius of the test ring is not straight forward. A test ring with an inner diameter equal to R_i (25 mm) was selected. A primary coil is wound uniformly around the circumference of the test ring to provide a uniform MMF per unit length. A secondary coil, connected to the fluxmeter, is wound over the primary. Reversing the current in the primary coil induces an EMF in the secondary coil which is integrated by the fluxmeter. Given the magnitude of the current, the number of primary turns, and the mean circumference of the test ring, H around the mean circumference can be calculated. B is calculated from the value of the integrated flux, and the cross-sectional area of the ring. The value of H in a toroid varies from a maximum at the inner pe-

riphery to a minimum at the outer periphery, and the flux density varies accordingly. H at the mean diameter is the average value for the ring; and if the radial thickness of the ring does not exceed about one-tenth of the mean diameter, the average value of B may, without appreciable error, be assumed to be the density at the mean diameter, which is due to the mean value of H. This corresponds to setting the ratio of outer to inner diameters of the test ring to a value no greater than $d_o/d_i = 11/9$. The outer diameter of the test ring was set to the maximum value of 30.5 mm. The relative permeability of the ring was found to be $\mu_r = 2.6 - 2.8$ over a range of $H = 3.6$ to 36 kA/m.

The permeability measurement supports using the value of $\mu_r = 3$ for the reluctance path $\mathcal{R}_{lf}$ in the reluctance circuit model. The slightly larger value of μ_r used in the model compensates for other leakage paths in the stainless steel spider which are not modelled.

In summary, the PM reluctance torque measurements qualitatively support the finite element and reluctance circuit model results in demonstrating that the experimental design produces a triangular reluctance torque waveform. The estimated results are also quantitatively supported by the measurement of the stainless steel permeability.

3.8.2 Measurement of the EMF/Torque Function

The back EMF is measured by driving the motor as a generator under no load. The measured EMF/torque function of Fig. 3.18 is obtained from the back EMF. The plateau region within each half cycle extends for approximately 140°. As noted in section 3.6.2.1, the width of the plateau region extends approximately the rotational angle swept out in which the stator slots are completely covered by the magnet poles. This angle, calculated with respect to the pole geometry, is given by

$$\theta_{plateau} = 180^\circ - 2\theta_a \qquad \text{(elect deg)} \tag{3.39}$$

and is slightly larger than the measured plateau width.

The permeability of the stainless steel affects mainly the reluctance airgap flux. The effect of the stainless steel on the stator airgap is to reduce the total magnetic circuit reluctance, which increases the stator airgap flux density and the EMF/torque function by a small amount. For the reluctance model calculation of the EMF/torque function shown in Fig. 3.18, a value of $\mu_r = 3$ is used for the stainless steel permeability.

3.8.3 Measurement of the Stator Winding Inductance

3.8.3.1 Method of Inductance Measurement

The DC method of inductance measurement described by [Jones 1967] is used to measure the self-inductance of the stator winding. The more well known alternating current method, which is described in section 5.5.5.1, can also be used.

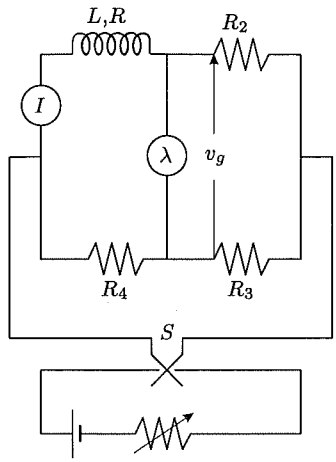

Figure 3.25 DC self-inductance bridge.

The stator winding self-inductance is measured with the use of the bridge circuit shown in Fig. 3.25. (L, R) represents a machine winding of self-inductance L and resistance R, and R_2, R_3, and R_4 are non-inductive resistors. Using a direct current source the bridge is balanced by adjusting the non-inductive resistors so that v_g is zero. When the switch S is opened, the current through the inductor will remain instantaneously at I and then fall exponentially to zero. The transient voltage is integrated by the voltage integrator, obtaining flux λ. The self-inductance is given by

$$L = \left(\frac{R + R_2}{R_2}\right)\frac{\lambda}{I} \tag{3.40}$$

and is derived in [Jones 1967]. The bridge serves the purpose of compensating for integration of the IR voltage drop across the winding as the current decays. In the experiment, the current I is reversed. This averages the saturating effect of the magnet poles on the inductance measurement which is discussed in section 3.8.3.2. The current change is then $2I$ and the correct value of inductance is then obtained by dividing L in eqn. 3.40 by a factor of two.

The DC inductance bridge circuit was practically implemented as follows. Batteries were used to supply current I. Resistors R_4 and R_3 consisted of a single length of nichrome wire which was bisected by a slidable contactor connected to one terminal of the fluxmeter. Resistors R_4 and R_3 and the slidable contactor were part of a prebuilt resistive divider bridge. Instead of balancing the bridge by adjusting R_2 and then

measuring the R/R_2 ratio, the bridge was balanced by sliding the contactor to adjust R_4 and R_3. Once the bridge was balanced the R_4/R_3 ratio was measured. Rather than requiring to measure the resistances, the ratio could simply be determined by measuring how far along the nichrome wire the slidable contactor was positioned. The contactor was able to be moved along a rule imbedded in the resistive divider bridge. The slider distance and thus the R_4/R_3 ratio were able to be determined to an accuracy greater than one part in three thousand. A fluxmeter was used as a voltage integrator. To enable the bridge to be finely balanced a long length (three meters) of nichrome wire was used in the resistive divider, and a voltmeter was placed in parallel with the fluxmeter to balance the bridge voltage (to within tens of micro-volts). A non-inductive nichrome resistor was used for R_2. Factors limiting inductance measurement accuracy were thermal resistive drift which unbalances the bridge, and the accuracy to which the fluxmeter could be read.

The DC inductance method is particularly useful for measuring the inductance of machines containing solid steel. For example, the field windings of a synchronous machine carry direct currents in normal operation, in which case the field poles may be constructed out of solid steel. The AC method cannot be applied because the large eddy currents in the solid steel render the results inapplicable to normal operation. The DC method also allows the winding resistance to be accurately excluded from being a source of error, unlike the AC method where the winding resistance must also be measured. In AC measurements, hysteresis and eddy current core losses are functions of the number of electrical cycles per second, and affect the measurement. The empirical relationships describing these losses are documented in the standard texts. In the DC method, the inductance measurement is unaffected by the induced current of a short-circuited secondary winding [Jones 1967, p. 22], and is thus similarly unaffected by induced eddy current in the iron. This makes the DC method less prone to errors caused by core losses.

3.8.3.2 Measurement Results

Fig. 3.26 shows the stator winding inductance for a current of 0.5 A. A cycle of inductance modulation is completed in a half electrical cycle. The waveform changes little over the range of 0-2 A, suggesting that the current does not saturate the stator over this current range. The modulation in the inductance is caused by the magnet poles, and the saliency of the iron flux guides. At 90° the magnet poles are in quadrature with the rotor poles. At this rotor position, the stator yoke is less saturated by magnet flux than when the poles are aligned, as is seen by comparing Fig.s 3.19(a) and 3.21. The stator yoke permeability, and therefore the stator winding inductance are higher at 90°. At the quadrature position the iron flux guides provide a lower reluctance path for stator winding flux crossing the stator airgap, adding to the quadrature inductance.

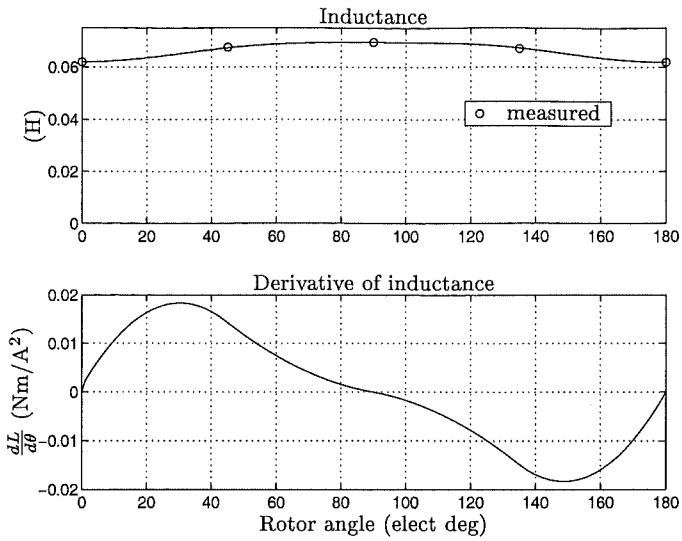

Figure 3.26 Measured stator winding inductance.

The effect of the saliency of the rotor fluxguide is lessened by the relatively large effective airgap separation between the fluxguides and the stator poles, provided by the magnet thickness.

Fig. 3.26 also shows the derivative of the inductance with respect to rotor position. The shape of the inductive reluctance torque waveform is proportional to this characteristic, and also to the square of the current waveform. For a triangular current waveform peaking at 90°, the rate of change of inductance is smallest when the current is largest. Therefore, the production of inductive reluctance torque is retarded by the ideal triangular current waveform shape. For a triangular test current having an amplitude of 2 A, the maximum reluctance torque is 7.3 mNm, or 2% of the measured reluctance torque amplitude.

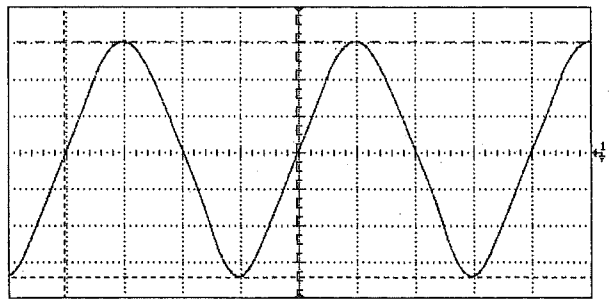

Figure 3.27 50 Hz alternating current waveform demonstrating differing levels of saturation with respect to current polarity. Scale: 2 A/div.

If the inductance is measured without reversing the stator winding current, for both positive and negative directions of current, it is found that two different values of inductance are obtained at the same rotor position. This is caused by the presence of the rotor magnets. If the rotor is positioned such that the PM and armature MMF's

superimpose to produce a larger resultant MMF, the armature iron is driven towards saturation. This results in a lower inductance. Alternatively, if the PM and armature MMF's superimpose to produce a smaller resultant MMF, the stator iron is driven away from saturation. This results in a higher inductance. If an alternating voltage is applied to the stator, two different peak values of current will be produced corresponding to the differences in inductance. The degree to which the inductance differs depends upon the rotor position and whether the magnitude of the applied voltage is high enough to induce sufficient saturation. This is demonstrated in Fig. 3.27 where the amplitude of the lower half cycles of current is larger. The rotor is at the stable detent starting position which may be either 45° or 225°. To start in the forward direction, the MMF's of the magnet and stator poles must be in opposite directions along the regions of greatest mutual rotor/stator pole overlap. This corresponds to lower net saturation and higher inductance. It follows that the correct current energisation is in the direction of the lower current amplitude. This effect may be used to ensure correct starting in a sensorless scheme where no rotor position sensors are used to drive the motor. The exploitation of magnetic saturation has been used in polyphase PM motors to determine the rotor position prior to starting [Lee and Pollock 1992, Feucht 1993, Matsui and Takeshita 1994].

	value	units	comment
L_{av}	65.5	mH	Average stator winding inductance
R	2.21	Ω	Stator winding resistance (cold)
J_r	1.36×10^{-3}	Kg.m^2	Moment of inertia of the rotor. Measured using the torsional pendulum method [Bevan 1962]

Table 3.5 Experimental measurements.

Table 3.5 lists remaining experimental measurements.

3.8.4 Verification of an Electrical Equation of Motion

In this section, an electrical equation of motion is derived, which allows the terminal voltage and current to be calculated for the triangular motor. This equation is validated by comparing simulated and experimental results of voltage regulation tests.

The motor terminal voltage is given by

$$v = iR + \frac{d\lambda(i,\theta)}{dt} \tag{3.41}$$

where $\lambda(i,\theta)$ is the flux linkage of the stator winding. The second RHS term in 3.41, being a function of both current and rotor position, expands to

$$\frac{d\lambda(i,\theta)}{dt} = \frac{\partial\lambda}{\partial i}\frac{di}{dt} + \frac{\partial\lambda}{\partial\theta}\frac{d\theta}{dt} \tag{3.42}$$

In the absence of iron saturation, or if the saturation is constant, the flux linkage may be given by eqn. 2.61:

$$\lambda = \lambda_m(\theta) + L(\theta)i$$

Substitution of eqn. 2.61 into 3.42 yields

$$\frac{d\lambda(i,\theta)}{dt} = \frac{\partial\lambda_m}{\partial i}\frac{di}{dt} + L\frac{di}{dt} + \frac{\partial\lambda_m}{\partial\theta}\frac{d\theta}{dt} + i\frac{\partial L}{\partial\theta}\frac{d\theta}{dt} \tag{3.43}$$

Since λ_m and L have not been defined to be functions of i in eqn. 2.61, $\partial\lambda_m/\partial i$ becomes zero, and the remaining partial derivatives become derivatives of a single variable. Eqn. 3.41 then becomes

$$v = iR + \frac{d\lambda_m}{d\theta}\dot{\theta} + L(\theta)\frac{di}{dt} + i\frac{dL}{d\theta}\dot{\theta} \tag{3.44}$$

where $\dot{\theta} = d\theta/dt$. The second RHS term of eqn. 3.44 is the EMF, e, induced by the field of the magnets. The third and fourth RHS terms represent induced EMF's due to the self-induction of the stator winding, referred to respectively as the *transformer* and *speed* voltages [Woodson and Melcher 1968, pp. 19-20].

For generation, the terminal voltage is equal to the voltage across the electrical load. For a purely resistive load, $v = iR_l$, where R_l is the resistive load. The EMF induced by the magnets, $e = \frac{d\lambda_m}{d\theta}\dot{\theta}$, energises the armature and the load. To simulate generation under a resistive load, eqn. 3.44 is presented in state equation form:

$$\frac{di}{dt} = \frac{1}{L(\theta)}\left[\frac{d\lambda_m}{d\theta}\dot{\theta} - i\left(R + R_l + \frac{dL}{d\theta}\dot{\theta}\right)\right] \tag{3.45}$$

where the variables describing the state of the system are i and θ. Eqn. 3.45 is a nonlinear ordinary differential equation because $L(\theta)$, $\frac{d\lambda_m}{d\theta}$, and $\frac{dL}{d\theta}$ are nonlinear functions. The shaft speed is held constant for generation, and θ is obtained from the state equation given by

$$\frac{d\theta}{dt} = \dot{\theta} = \text{constant} \tag{3.46}$$

Eqn.s 3.45 and 3.46 form a set of equations which must be solved numerically. The simulations are performed using the SIMNON simulation package [Elmqvist *et al.* 1990], which applies the Runge-Kutta-Fehlberg integration method. $L(\theta)$ and $\frac{dL}{d\theta}$ are modelled using the measured waveforms of Fig. 3.26. $\frac{d\lambda_m}{d\theta}$ is modelled using the measured waveform of Fig. 3.18. The value of R given in Table 3.5 is used.

Voltage regulation tests were performed running the triangular motor as a generator under constant speed, using a resistive load. Under no load, the terminal voltage waveform is simply the induced EMF, $e = \frac{d\lambda_m}{d\theta}\dot{\theta}$, shown in Fig. 3.18. With a load across

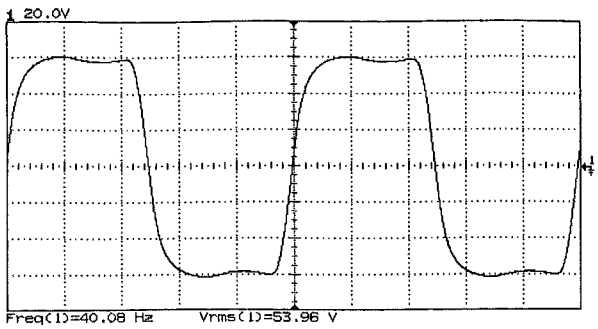

Figure 3.28 Resistive voltage regulation test showing the terminal voltage waveform corresponding to a current of 0.5 A RMS. $R_l = 107.9\ \Omega$.

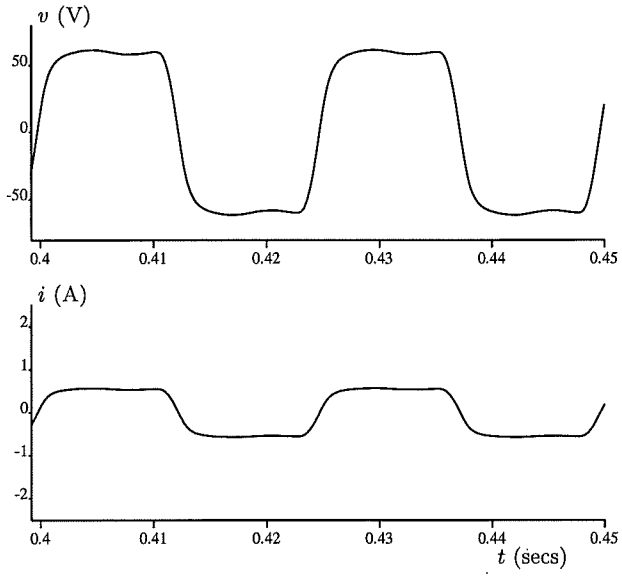

Figure 3.29 Simulated terminal voltage and current waveforms for $R_l = 107.9\ \Omega$, at an electrical frequency of 40.08 Hz.

the generator terminals, the steady state voltage waveform of Fig. 3.28 is obtained. The contribution of the self-induced voltage of the stator winding slightly rounds the corners of the terminal voltage waveform. Fig. 3.29 plots the simulated steady state voltage and current waveforms for this value of the load. The initial values of the state variables used in the simulation are $[i_\emptyset = 0, \theta_\emptyset = 0]$. At the beginning of the simulation, an interval occurs in which a transient solution decays to reveal the steady state solution. At about $t = 0.4$ seconds, the transient response is sufficiently decayed to show the steady state waveforms. The measured and simulated voltage waveforms are in close agreement.

Fig. 3.30 shows the terminal voltage waveform for an increased resistive load. Fig. 3.31 plots the simulated voltage and current waveforms for this load. The measured and simulated waveforms are in reasonably close agreement. Simulations demonstrate that the $L(\theta)\frac{di}{dt}$ component of the energised stator winding is predominantly responsible for rounding the corners and attenuating the magnitudes of the terminal voltage

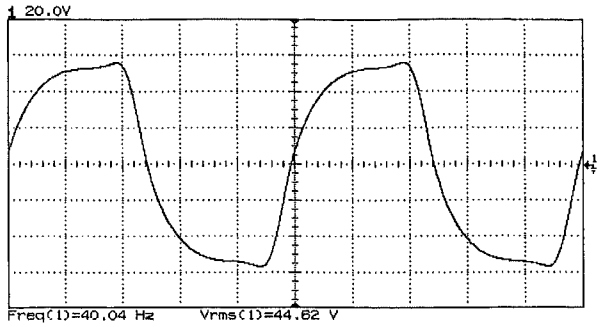

Figure 3.30 Resistive voltage regulation test showing the terminal voltage waveform corresponding to a current of 1.5 A RMS. $R_l = 29.7\ \Omega$.

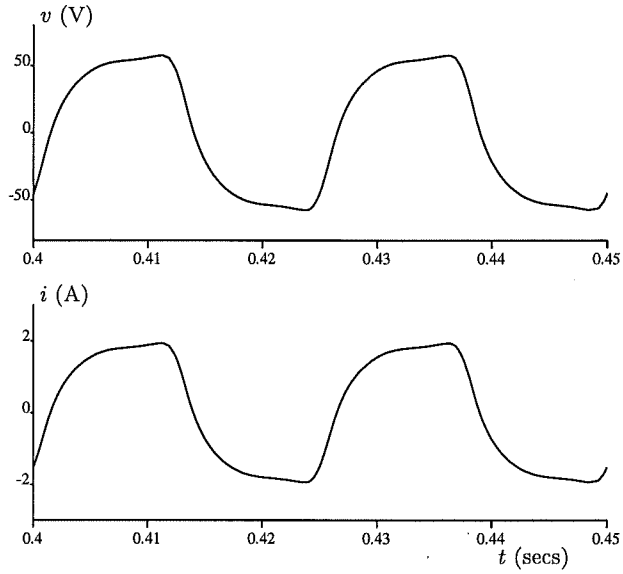

Figure 3.31 Simulated terminal voltage and current waveforms for $R_l = 29.7\ \Omega$, at an electrical frequency of 40.04 Hz.

waveforms.

The agreement between experimental and simulated results suggests that eqn. 3.44 provides a good electrical representation of the triangular motor. The accuracy of the simulation results are dependent on the accuracy to which $L(\theta)$, $\frac{d\lambda_m}{d\theta}$, and R can be measured for the conditions required to be simulated. With regard to the effect of saturation on inductance, simulation results remain reasonable if the magnitude of the current remains within the range over which the inductance is measured.

3.8.5 Current and Voltage Waveform Calculation for Motoring

In this section, current and voltage waveforms for constant or near constant instantaneous torque are calculated, using the measured characteristics of the triangular motor. These waveforms are obtained from mechanical and electrical equations used to model the motor.

Eqn. 2.64 is used to model the motor airgap torque. By applying d'Alembert's law, the following equation of motion describing the complete mechanical system is obtained:

$$J\frac{d\dot{\theta}}{dt} + T_l = i\frac{d\lambda_m}{d\theta} + \frac{1}{2}i^2\frac{dL}{d\theta} + T_r(\theta) \tag{3.47}$$

where

J = moment of inertia of the rotor and the load
T_l = load torque
T_r = PM reluctance torque $-dW(i=0,\theta)/d\theta$

The shape and magnitude of the current waveform required to deliver a specified torque to the load is obtained by solving eqn. 3.47 for i, whereby a quadratic solution is obtained. The measured inductance characteristic shows that $dL/d\theta$ is small. Thus without losing significant accuracy, the inductive reluctance torque may be assumed to be zero. If the motor airgap and load torques are assumed to remain matched, $d\dot{\theta}/dt = 0$ and the speed is constant. By applying these simplifications, the solution for the current waveform is obtained as

$$i = \frac{T_l - T_r(\theta)}{\frac{d\lambda_m}{d\theta}} \tag{3.48}$$

At rated load, the amplitude of the PM reluctance torque is equal to the load, such that $T_l = \hat{T}_r$. This ensures that the current remains finite at all rotor positions. In theory, a constant instantaneous airgap torque may be obtained at the rated load, as demonstrated by Fig. 1.7. In practice, undesirable effects produce characteristics which are less than ideal. The cogging torque is an undesirable effect which acts over a $40° - 45°$ interval producing speed ripple. If $\frac{d\lambda_m}{d\theta}$ is large enough through the interval in which the cogging torque acts, a current may be injected into the stator winding to produce a phase-magnet torque $T_{ph-m} = i\frac{d\lambda_m}{d\theta}$ in antiphase to the cogging torque, thereby eliminating the speed ripple. However, in a single phase PM motor, $\frac{d\lambda_m}{d\theta}$ is small within this interval, crossing zero when poles are aligned together. This causes the rate of change of the current required for cancellation of the cogging torque to be very high. As a brushless motor requiring a non-sinusoidal terminal voltage, the triangular motor cannot be connected directly to an AC mains supply. The triangular motor is required to be connected to a single phase inverter. A finite inverter DC bus voltage is available which restricts the maximum rate of change of current because of the nonzero stator winding inductance. Therefore, because of the high rate of change of current required, the cancellation of the cogging torque through current injection is difficult in practice. Because of this difficulty, the cogging torque components of the reluctance torque are not included in the calculation of the current waveform. Speed ripple will be produced by the cogging components, but averages to zero over the $40° - 45°$ interval in which the cogging torque acts every half electrical cycle. The measured reluctance torque

characteristic of Fig. 3.24 is used, where the cogging components are neglected by extrapolating along the dashed lines.

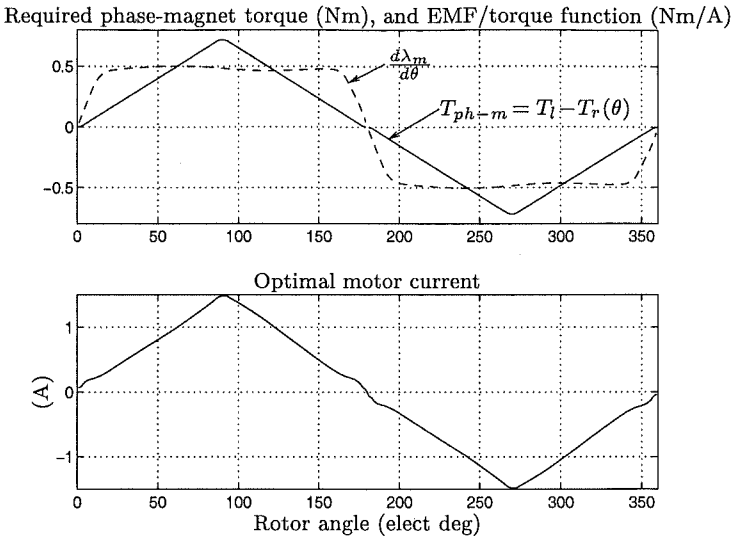

Figure 3.32 Optimal current waveform for the experimental triangular motor, calculated for near constant instantaneous torque using measured characteristics. Rated load $T_l = \hat{T}_r = 0.36$ Nm.

Fig. 3.32 shows the optimal current waveform, and the waveforms from which it is calculated. In the upper figure, the required phase-magnet torque waveform is calculated from $T_{ph-m} = T_l - T_r(\theta)$, and is a quasi-triangular waveform which does not compensate for cogging torque. The current waveform is obtained by dividing the phase-magnet torque waveform by the EMF/torque function, point by point according to eqn. 3.48. The current waveform deviates from the ideal triangular waveform in several respects. The peak of the waveform is rounded. This occurs because the peaks of the reluctance torque are rounded. The current waveform rises quickly over short intervals at the ends and beginnings of each half cycle. This is caused by the trapezoidal nature of the EMF/torque function, which reduces in magnitude within these intervals. The current waveform is not perfectly linear within the intervals of $20° - 80°$ and $100° - 160°$, and also within similar intervals in the second half cycle. This is caused by the modulation across the plateau region of the EMF/torque function. The falling away of the EMF/torque function about 0° and 180°, and the modulation of the plateau region, are unwanted effects which result from the motor design. However, these effects do not present problems because torque quality can still be preserved: the current waveform remains finite, and is quasi-triangular.

The method of current waveform calculation using eqn. 3.48 is similar to the method of *back EMF Inversion* [Jahns and Soong 1996] which optimises current waveforms for eliminating torque ripple in polyphase PM motors. The back EMF inversion method recognises that the optimised current is proportional to the reciprocal of the back EMF. This is demonstrated by setting $T_r(\theta)$ to zero in eqn. 3.48, and multiplying

both the numerator and the denominator by the speed $\dot{\theta}$. The calculation of the current for the triangular motor is unique in that a designed PM reluctance torque $T_r(\theta)$ is used to provide a key torque contribution. Like the back EMF inversion method, the calculation of the current for the triangular motor is reliant upon the accuracy of measured characteristics. Both methods are sensitive to parameter variation.

Three phase brushless PM motors with trapezoidal EMF's are prone to *commutation* ripple. The ideal current waveforms contain discrete steps. Because the phase inductances are nonzero, and because the inverter bus voltage is finite, the current cannot change levels instantaneously. This produces torque ripple. The triangular motor current waveform of Fig. 3.32 is not discrete. The waveform is continuous, and the rate of change of current is spread out across each entire half cycle, in a near linear manner from peak to peak. The triangular motor, whilst having a trapezoidal EMF, is similar to a PM motor having a sinusoidal EMF, in that it is not afflicted by commutation torque ripple because the optimal current waveform is continuous.

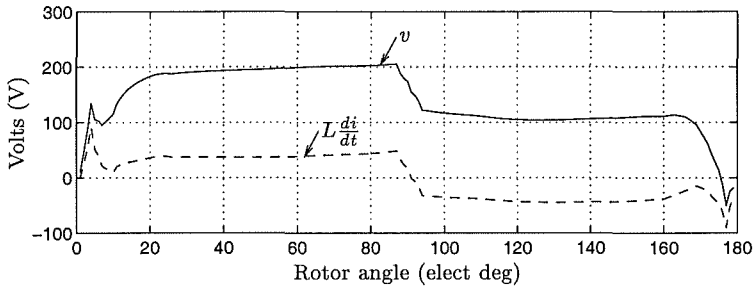

Figure 3.33 Terminal voltage waveform of the experimental triangular motor shown over a half electrical cycle, corresponding to a rotor speed of 3000 RPM.

The optimal terminal voltage waveform can be calculated, having calculated the optimal current waveform, by using eqn. 3.44. This calculation allows the suitability of connecting the triangular motor to an inverter to be determined for torque ripple minimising operation. For example, the ideal alternating output voltage for a full bridge inverter [Mohan *et al.* 1989] is a squarewave of amplitude equal to the DC bus voltage. No modulation of the output voltage is required within each half cycle. Therefore, no turning on or off (switch mode), or linear mode operation, of the switches are required within these cycles. This minimises switching losses and switch voltage ratings. Fig. 3.33 shows the calculated terminal voltage waveform of the experimental triangular motor over a half electrical cycle, corresponding to a speed of 3000 RPM. The voltage waveform is approximately squarewave with two steps per half cycle. The dominant voltage components from which the waveform is composed are the back EMF, and the reactive voltage due to the inductance, which is plotted by the dashed line. The reactive voltage yields a significant step in the waveform. The reactive volt-seconds are distributed across the entire half cycle. The inductance of the experimental motor is relatively large, perhaps too large for an effective motor design. For a DC bus voltage

of approximately 200 V, the optimal torque ripple minimising voltage and current waveforms can be achieved. For a hypothetical three phase brushless motor of similar rotor design having similar values of per phase inductance, significant commutation ripple is likely to result. In order for the current to change levels quickly to maintain reasonable torque quality, similar reactive volt-seconds are required to be distributed over much shorter intervals. In this case, a higher DC bus voltage would be required to accommodate the volt-sconds.

A triangular motor drive consisting of a current regulated inverter, and a current reference waveform generator, is recommended. The current reference generator uses eqn. 3.48 to convert the required torque into a current reference. This scheme does not require calculation of the terminal voltage, as in the case of a voltage regulated inverter, and is thus not prone to further errors created by the measurement or estimation of the electrical equation parameters. Rotor position feedback is required to synchronise i and θ. The selection of the type of rotor position sensors is dependent on the required resolution. This, in turn, is dependent on the required quality of the torque. For a basic position sensing scheme, a Hall effect sensor is required to detect the rotor position every half electrical cycle where the current changes direction. A second sensor may also be required to detect rotor position at the middle of every half electrical cycle, where the current peaks.

3.9 CONCLUSIONS

This chapter has provided two contributions: the first is the description of an analytical method of calculating PM reluctance torque; the second is the examination of the triangular motor concept.

The analytical method of calculating PM reluctance torque uses an elementary expression for the magnetic field to obtain the stored energy. It is shown that the method does not require the magnetic field to be accurately resolved into its normal and tangential components, unlike the Maxwell stress method where similar approximation is intolerable. This allows the use of an elementary expression for the field. Because the stored energy is an analytical expression, the error in taking the derivative with respect to rotational displacement to obtain the torque is zero. The method has been demonstrated to provide a powerful and fast design tool. The method can be generally applied to reluctance torque problems where the airgap is reasonably smooth. Further examples of the application of the method are found in the paper 'Effects of Airgap and Magnet Shapes on Permanent Magnet Reluctance Torque' in Appendix A, and in Chapter 4. However, application of the method is likely to exclude cogging torque problems due to stator slotting because the field is unlikely to be described with sufficient accuracy.

An experimental motor has been built to verify the concept of the triangular motor.

This requires the implementation of an ideally square-wave EMF/torque function, and a triangular PM reluctance torque waveform. It is shown that the implementation of each of these characteristics requires conflicting PM pole pitches. Full pitched poles are required for the desired EMF/torque function, and poles of half an electrical pitch are required for the production of the triangular reluctance torque. To successfully accommodate both of these characteristics using a single magnetic circuit, a double set of airgaps, and the magnet/iron flux guide rotor construction, have been implemented.

Unwanted effects are shown to be present in the measurements of these characteristics. The EMF/torque function is trapezoidal in shape, rather than squarewave. The plateau region of the EMF/torque function is shown to be modulated by the triangular modulation of the reluctance airgap. The PM reluctance torque is triangular in shape, but has cogging torque components due to stator slotting superimposed upon it. The non ideal characteristics of the EMF/torque function are shown not to create significant difficulty, in that the optimal current waveform calculated using the measured characteristics remains quasi-triangular, or close to the ideal triangular waveform. The cogging torque is shown to be difficult to eliminate, but it is noted that the cogging torque acts over only a short interval of every half electrical cycle. The experimental results demonstrate that the required EMF/torque function and reluctance torque characteristics can be adequately implemented in a real motor. This demonstrates that it is possible to produce a high quality torque in a brushless single phase PM motor.

The concept of the magnetic reluctance circuit has been used to model the triangular motor. Both the PM reluctance torque and the EMF/torque function are successfully modelled using a simple reluctance circuit model. The results of the model are supported by results obtained using finite element analysis. The measured amplitude of the PM reluctance torque is significantly lower than the value estimated using the methods described above. This was found to be caused by ferromagnetism in the stainless steel structure supporting the rotor poles. Even though the permeability of the stainless steel was shown to be low, the reluctance circuit model demonstrates that the reluctance torque is sensitive to the permeability, or effective interpolar distance, between the iron flux guides of the rotor.

The axial flux construction, employing double rotor airgaps and concentrically wound laminations, made the experimental motor difficult to build. Whilst serving the purpose of demonstrating the triangular motor concept, the experimental design is unlikely to be manufacturable for any other purpose. As a brushless PM motor which cannot be connected directly to an AC supply, an electronic drive is required: an inverter is necessary to inject the required triangular current into the stator winding; and rotor position sensing is required to maintain synchronism. The need for an electronic drive increases the cost and complexity of the motor. The performance of the motor is limited. The triangular motor is not designed to run in the reverse direction because the PM reluctance and phase-magnet torques superimpose to yield a large pulsating

torque. For rotation in the forward direction, torque ripple results if the load torque is not equal to the amplitude of the PM reluctance torque. For example, for rotor positions of stator and rotor pole alignment (0° or 180°), the triangular PM reluctance torque is the only motor airgap torque acting. At these positions the magnitude of the reluctance torque is equal to its amplitude. If the magnitude of the load is not the same, acceleration must occur at these positions. The amplitude of the reluctance torque remains fixed, and cannot be adjusted to match the load. The amount of acceleration occurring at these positions is proportional to the difference between the two torques. At other rotor positions, it is possible to match the load torque by injection of the appropriate current to modulate the phase-magnet torque as required. This, however, increases the complexity of the controller, and requires high resolution position sensing.

In contrast, three-phase brushless PM motors have similar drive complexity, but in addition offer reversibility and a wider torque-speed range. Therefore, the triangular motor is unlikely to be able compete in general brushless PM motor applications. If an application is to be proposed for the triangular motor, it must be one that only requires capabilities that the triangular motor can perform well. Performance requirements must still remain high, or else cheaper motors which do not require drives such as single phase induction motors, could be used. A computer hard disk drive motor [Jabbar *et al.* 1992] is a possible application. Three phase brushless PM motors with electronic drives are generally used in this application. The application requires rotation in one direction only, the running load torque and speed remain fixed, and a high quality motor torque is required. These performance requirements are met by the triangular motor, but a manufacturable design is required. A radial flux design having a single airgap has been proposed for this purpose. A single phase triangular motor design has both advantages and disadvantages in comparison to the conventional three-phase motor designs. For such an application, a large number of issues are required to be considered in comparing the proposed motor and existing three-phase disk drive motors.

Chapter 4

THE UNIDIRECTIONAL SINGLE PHASE SYNCHRONOUS PM MOTOR

4.1 INTRODUCTION

This chapter examines in more detail the concept of the unidirectional motor introduced in section 1.4. Like the motor tested in the Chapter 3, the unidirectional motor also uses PM reluctance torque to obtain constant instantaneous torque. However, in contrast the unidirectional motor employs a sinusoidal back EMF and sinusoidal PM reluctance torque. This chapter covers the theoretical development of the unidirectional motor. The scope of this development is to produce two 'ballpark' designs which provide a starting point for experimental investigation.

4.2 THEORY OF THE SINGLE PHASE SYNCHRONOUS PM MOTOR

This section reviews a selection of equations and characteristics corresponding to the conventional single phase synchronous PM motor. *Conventional* is used in this context to mean the common designs demonstrated, for example, by Fig.s 1.1 and 1.2. The final direction of rotation is not predetermined for the conventional motors. Much of the material in the review is based on the thesis of [Schemmann 1971], but all the equations are extended from the single pole pair case to an arbitrary number of pole pairs.

The unidirectional motor is designed to operate at a specific mechanical loading associated with a specific load angle under synchronous operation. This specific load angle corresponds to the EMF/torque function and the current being in phase with each other. The load angle is defined later in this section. However, the load angle varies as a function of mechanical loading. Therefore, if the load deviates from the ideal value, the load angle of the unidirectional motor also deviates from the design value. The conventional theory provides for a variable load, and thus an arbitrary load angle. In respect to load angle, the unidirectional motor loading may be described as a single

and special example within the wider range of conventional motor loading. Therefore the conventional theory can provide a general framework in which the unidirectional motor may be analysed. As such, this review of the conventional motor is important because its equations and characteristics are also applicable to the unidirectional motor.

The PM flux linkage of single pole pair and multiple pole pair single phase motors is determined in section 4.7. In this present section, the PM flux linkage, or its fundamental component at least, is assumed to be given by

$$\lambda_m = -\hat{\lambda}_m \cos(p\theta) \tag{4.1}$$

where

$\hat{\lambda}_m$ = peak PM flux linkage (flux-turns)
p = number of pole pairs
θ = mechanical rotor angle

The EMF/torque function is then given by

$$d\lambda_m/d\theta = p\hat{\lambda}_m \sin(p\theta) \tag{4.2}$$

and the induced EMF is given by

$$e = \dot{\theta}\frac{d\lambda_m}{d\theta} = p\dot{\theta}\hat{\lambda}_m \sin(p\theta) \tag{4.3}$$

where $\dot{\theta} = d\theta/dt$ is the instantaneous mechanical angular rotor speed.

The following analysis corresponds to perfect synchronous motion in which the speed ripple is zero and the instantaneous speed $\dot{\theta}$ is constant. The electrical rotor angle may therefore be expressed by

$$p\theta = p\,\dot{\theta}\,t + \theta'_o \tag{4.4}$$

where θ'_o is the electrical rotor angle at $t = 0$.

Furthermore, the mechanical rotor speed and the electrical angular speed, ω_e, are related by

$$p\dot{\theta} = \omega_e \tag{4.5}$$

Substitution of eqn.s 4.4 and 4.5 into eqn. 4.3 yields the synchronous EMF:

$$e = \omega_e\hat{\lambda}_m \sin(\omega_e t + \theta'_o) \tag{4.6}$$

The current may be obtained from:

$$i = \frac{\hat{v}\sin(\omega_e t + \epsilon - \alpha) - \omega_e \hat{\lambda}_m \sin(\omega_e t + \theta'_o - \alpha)}{Z} \tag{4.7}$$

where $\alpha = \arctan(\omega_e L/R)$, and Z is given by eqn. 1.14.

The peak value of the induced EMF is given by

$$\hat{e} = \omega_e \hat{\lambda}_m \tag{4.8}$$

If ϵ is set to zero, comparison of the voltage terms in eqn. 4.7 show that θ'_o then gives the phase angle between $\hat{v}$ and $\hat{e}$. θ_o will be defined to be the angle between $\hat{v}$ and $\hat{e}$ with $\epsilon = 0$. The current may then be expressed by

$$i = \frac{\hat{v}\sin(\omega_e t - \alpha) - \hat{e}\sin(\omega_e t + \theta_o - \alpha)}{Z} = \hat{i}_1 \sin(\omega_e t + \varphi) \tag{4.9}$$

where φ is the phase angle between $\hat{v}$ and $\hat{i}_1$.

The average torque produced by the motor is given by

$$\overline{T} = \frac{1}{\tau}\int^{\tau} i\frac{d\lambda_m}{d\theta}dt \tag{4.10}$$

where τ is the electrical period.

Substitution of eqn.s 4.2 and 4.7 into eqn. 4.10 with $\epsilon = 0$ and $p\theta = \omega_e t + \theta_o$ yields

$$\overline{T} = \frac{p\hat{v}\hat{\lambda}_m}{2Z}\cos(\alpha + \theta_o) - \frac{p\omega_e \hat{\lambda}_m^2}{2Z}\cos\alpha \tag{4.11}$$

Eqn. 4.11 shows that the average torque is composed of two components: one which varies as a sinusoidal function of θ_o, and another which is constant and negative. The torque cannot be controlled by adjusting $\hat{\lambda_m}$ because the PM excitation is fixed. The motor torque is determined by the mechanical load, and θ_o will thus be referred to as the *load angle*. The winding resistance of single phase synchronous PM motors is relatively large and cannot be neglected in the calculation of torque. The torque cannot be approximated to be a linear function of θ_o for small load angles where α is not large. This differs from three phase synchronous machines where the winding resistance is relatively small, and α approaches 90°. In this case, with a large value of α, eqn. 4.11 simplifies to a single term where the torque is proportional to $-\sin\theta_o$.

Positive (motoring) pullout torque occurs when $\cos(\alpha+\theta_o) = 1$. The pullout torque is given by

$$\overline{T} = \frac{p\hat{\lambda}_m}{2Z}(\hat{v} - \omega_e \hat{\lambda}_m \cos\alpha) \tag{4.12}$$

and the corresponding load angle is

$$\theta_o = -\alpha \tag{4.13}$$

If bearing friction and windage are ignored, the average output power and pullout power may be obtained by multiplying eqn.s 4.11 and 4.12 by $\dot{\theta}$, respectively. Output power may be expressed as

$$P_{out} = \frac{\hat{e}\hat{v}}{2Z}\cos(\alpha + \theta_o) - \frac{\hat{e}^2}{2Z}\cos\alpha \tag{4.14}$$

The input power is obtained from

$$P_{in} = \frac{1}{\tau}\int^{\tau} vi\,dt \tag{4.15}$$

Substitution of eqn.s 1.6 and 4.9 into 4.15 yields

$$P_{in} = \frac{\hat{v}^2}{2Z}\cos\alpha - \frac{\hat{e}\hat{v}}{2Z}\cos(\alpha - \theta_o) \tag{4.16}$$

The efficiency is then given by

$$\eta = \frac{P_{out}}{P_{in}} == \frac{\hat{e}\hat{v}\cos(\alpha + \theta_o) - \hat{e}^2\cos\alpha}{\hat{v}^2\cos\alpha - \hat{e}\hat{v}\cos(\alpha - \theta_o)} \tag{4.17}$$

The maximum efficiency [Schemmann 1971, p. 28] is given by

$$\eta_{max} = \frac{(\hat{e}/\hat{v})\cos\alpha + 1}{(\hat{e}/\hat{v}) + \cos\alpha}\,\frac{\hat{e}}{\hat{v}}, \qquad \frac{\hat{e}}{\hat{v}} \leq 1 \tag{4.18}$$

and the corresponding value of θ_o is given by

$$\tan(-\theta_o) = \frac{1 - \eta_{max}}{1 + \eta_{max}}\tan\alpha \tag{4.19}$$

4.2.1 Unperturbed Motion

In practice, speed ripple about the mean synchronous value is characteristic of single phase synchronous PM motors. The motion of the motor is governed by eqn.s 1.5 and 1.7. These are a set of nonlinear differential equations which are not integrable in closed form [Bertram and Schemmann 1976]. However, approximate solutions to the synchronous motion may be obtained without fully solving these equations.

By applying the method of successive approximation, an *unperturbed* solution of the differential equations may be obtained. The unperturbed motion is characterised by a nearly sinusoidal current with a synchronous speed modulated at twice the electrical frequency. A detailed derivation of the unperturbed solution is given in [Schem-

mann 1971, pp. 21-25]. A shortened description of this derivation is given in this section. The solution is extended to include an arbitrary number of pole pairs.

A first approximation of the current is provided by eqn. 4.9. By assuming the instantaneous speed to be constant as a first approximation, the instantaneous torque produced by the motor is obtained by the product of eqn.s 4.9 and 4.2, with $p\theta = \omega_e t + \theta_o$:

$$T = \hat{i}_1 \sin(\omega_e t + \varphi) p\hat{\lambda}_m \sin(\omega_e t + \theta_o) \tag{4.20}$$

For convenience, the no load case is obtained. Substitution of $\varphi = 3\pi/2 + \theta_o$ into eqn. 4.20 yields the no load torque:

$$T = -\frac{\hat{i}_1 p\hat{\lambda}_m}{2} \sin 2(\omega_e t + \theta_o) \tag{4.21}$$

With reference to eqn. 4.53, with the load torque T_l set to zero, the mechanical angular acceleration is obtained as

$$\frac{d\dot{\theta}}{dt} = \frac{1}{J}\Big[-\frac{\hat{i}_1 p\hat{\lambda}_m}{2} \sin 2(\omega_e t + \theta_o) - 2p\hat{W}_r \sin 2(\omega_e t + \theta_o - p\gamma_r)\Big] \tag{4.22}$$

In eqn. 4.22, the acceleration is the result of contributions from both the phase-magnet torque and the PM reluctance torque. $\hat{W}_r$ is the amplitude of stored energy modulation when the current is zero. Generally γ_r is small, and a reasonably accurate simplification of eqn. 4.22 is achieved by setting $\gamma_r = 0$. Application of this simplification followed by integration with respect to time yields the following speed modulation:

$$\dot{\theta}_\sim = \frac{\hat{i}_1 p\hat{\lambda}_m + 4p\hat{W}_r}{4\omega_e J} \cos(2\omega_e t + 2\theta_o) \tag{4.23}$$

The amplitude of the speed modulation may be normalised as follows:

$$a = \frac{p\hat{\dot{\theta}}}{\omega_e} = p^2 \frac{(\hat{i}_1 \hat{\lambda}_m + 4\hat{W}_r)}{4\omega_e^2 J} \tag{4.24}$$

Eqn. 4.24 shows that increasing the number of pole pairs exacerbates the speed ripple. An improved approximation of the speed is obtained by

$$p\dot{\theta} = \omega_e + a\omega_e \cos(2\omega_e t + \delta_1) \tag{4.25}$$

Integration of the speed yields an improved approximation of the rotor position. The improved approximations of speed and position allow a more complicated approximation of the induced EMF to be obtained. A further approximation of the current is then obtained by a calculation similar to eqn. 4.9. Odd current harmonics are obtained

yielding

$$i = \hat{i}_1 \sin(\omega_e t + \varphi_1) - \hat{i}_3 \sin(3\omega_e t + \varphi_3) + \ldots \tag{4.26}$$

Expressions for the amplitudes of the harmonic currents show that the higher order harmonics are very small. This is supported by the steady state water-pumping test results of the Siemens motor presented in section 5.5.4.3. In these test results, current harmonics above the third are negligible.

Use of eqn. 4.26 allows further improved approximation of the acceleration and speed to be obtained. Even speed harmonics are found. The fourth harmonic is relatively small and may be neglected. Schemmann describes eqn.s 4.25 and 4.26 as good approximations. These equations are defined as the unperturbed solutions to the differential equations. Single phase synchronous PM motors are designed to exhibit the unperturbed motion during running [Schemmann 1973]. The unperturbed motion must be maintained within the expected spread of the parameters of the motor.

4.2.2 Perturbed Motion

Other harmonic solutions are also shown to exist for synchronous motion. Other harmonic solutions for the rotor speed are derived in [Schemmann 1971] and [Schemmann 1973]. These solutions are described in this section.

For synchronous motion, the average speed of the rotor must correspond to the angular speed of the electrical supply in accordance with eqn. 4.5. This means that the speed variations over a long time must be zero. Periodic speed variations may be written as the sum of a number of simple harmonic motions given by

$$p\dot{\theta} - \omega_e = \sum_{\nu=1}^{n} A_\nu \sin(a_\nu \omega_e t + \psi_\nu) \tag{4.27}$$

The integral of each harmonic averages to zero over a time extending the period, τ_ν, of each harmonic. This is expressed mathematically by

$$A_\nu \int^{\tau_\nu} \sin(a_\nu \omega_e t + \psi_\nu) dt = 0 \tag{4.28}$$

For the unperturbed motion described by eqn. 4.25, the harmonic has a frequency exactly double that of the electrical frequency. The period of this harmonic may be written as $\tau_1 = \pi/\omega_e$. Subharmonic possibilities may occur when the period is an integral multiple of τ_1, such that $\tau_\nu = k\tau_1 = k\pi/\omega_e$, where $k = 1, 2, 3 \ldots$. The integral may be rewritten as

$$\int_0^{k\pi/\omega_e} \sin(a_\nu \omega_e t + \psi_\nu) dt = 0 \tag{4.29}$$

which evaluates to

$$\cos(a_\nu k\pi + \psi_\nu) = \cos(\psi_\nu) \tag{4.30}$$

Eqn. 4.30 is satisfied if $a_\nu = 2\nu/k$, where $\nu = 1, 2, 3, \ldots$. The following values may therefore be calculated for a_ν:

$k = 1$	$a_1 = 2,$	$a_2 = 4,$	$a_3 = 6, \ldots$
$k = 2$	$a_1 = 1,$	$a_2 = 2,$	$a_3 = 3, \ldots$
$k = 3$	$a_1 = 2/3,$	$a_2 = 4/3,$	$a_3 = 6/3, \ldots$

Values of a_ν for higher values of k may also be calculated. Substitution of the values of a_ν corresponding to $k = 1$ into eqn. 4.27 yields the unperturbed motion:

$$p\dot{\theta} = \omega_e + A_1 \sin(2\omega_e t + \alpha_1) + A_2 \sin(4\omega_e t + \alpha_2) + A_3 \sin(6\omega_e t + \alpha_3) + \ldots \tag{4.31}$$

Larger values of k describe what are referred to as periodic *perturbed* motions. For $k = 2$, for a 50 Hz supply frequency, there is a 50 Hz perturbation:

$$p\dot{\theta} = \omega_e + B_1 \sin(\omega_e t + \beta_1) + B_2 \sin(2\omega_e t + \beta_2) + B_3 \sin(3\omega_e t + \beta_3) + \ldots \tag{4.32}$$

Likewise, $k = 3$ yields a $33\frac{1}{3}$ Hz perturbation:

$$p\dot{\theta} = \omega_e + C_1 \sin(2/3\omega_e t + \gamma_1) + C_2 \sin(4/3\omega_e t + \gamma_2) + C_3 \sin(6/3\omega_e t + \gamma_3) + \ldots \tag{4.33}$$

These perturbations are illustrated in Table 1.1. Perturbations are possible for larger values of k resulting in more complicated motion. Schemmann describes these perturbed motions as subharmonic resonances of a periodic driving torque with a frequency equal to twice the electrical frequency. This torque occurs due to the backward field which rotates around the surface of the rotor at this frequency.

The unidirectional motor presents a special case where, under appropriate conditions, the PM reluctance torque cancels out the torque modulation created by the backward rotating field. The instantaneous motor torque is constant and the speed ripple is zero. In this case, the synchronous motion is simply described by

$$p\dot{\theta} = \omega_e$$

4.3 STEADY STATE THEORY OF THE UNIDIRECTIONAL MOTOR

In this section, the theory introduced in section 1.3.2 is extended. Equations specific to the unidirectional motor are developed corresponding to running at constant instantaneous synchronous speed.

For a unidirectional motor having p pole pairs, the instantaneous current required is obtained as a function of the torque requirement from eqn. 4.53. For zero mechanical angular acceleration, the current is given by

$$i = \frac{T_l + 2p\hat{W}_r \sin[2p(\theta - \gamma_r)]}{p\hat{\lambda}_m \sin(p\theta)} \tag{4.34}$$

For forward rotation, the PM reluctance displacement angle is set to $p\gamma_r = 45°$(electrical). To allow constant instantaneous torque to be applied to the load, the magnitude of the load torque is set to the amplitude of the PM reluctance torque:

$$T_l = \overline{T} = 2p\hat{W}_r \tag{4.35}$$

The required current is then obtained as a function of the rotor position by

$$i = \frac{4\hat{W}_r}{\hat{\lambda}_m} \sin(p\theta) \tag{4.36}$$

where the amplitude of the current is $\hat{i} = 4\hat{W}_r/\hat{\lambda}_m$. Substitution of $\hat{W}_r = \overline{T}/2p$ into this expression for $\hat{i}$ gives an alternative equation for the unidirectional motor torque:

$$\overline{T} = p\frac{\hat{i}\hat{\lambda}_m}{2} \tag{4.37}$$

Comparison of eqn.s 4.3 and 4.36 shows that the current and induced EMF are in phase. The phase angle between the current and the supply voltage is therefore the same as the angle between the induced EMF and the supply voltage, such that $\varphi = \theta_o$. For synchronous motion, with $\epsilon = 0$ and $p\theta = \omega_e t + \theta_o$, the current may be given by

$$i = \hat{i} \sin(\omega_e t + \theta_o) \tag{4.38}$$

The instantaneous terminal voltage of the motor is given by

$$v = L\, di/dt + iR + e \tag{4.39}$$

Substitution of eqn. 4.38 and its derivative with respect to time, as well as eqn.s 1.6 and 4.6, into 4.39, with $\epsilon = 0$ yields

$$\hat{v} \sin(\omega_e t) = \frac{4\omega_e L\hat{W}_r}{\hat{\lambda}_m} \cos(\omega_e t + \theta_o) + \left[\frac{4R\hat{W}_r}{\hat{\lambda}_m} + \omega_e\hat{\lambda}_m\right] \sin(\omega_e t + \theta_o) \tag{4.40}$$

Eqn. 4.40 shows that the terminal voltage is the sum of orthogonal components. There-

fore $\hat{v}$ is given by

$$\hat{v} = \sqrt{\left(\frac{4\omega_e L\hat{W}_r}{\hat{\lambda}_m}\right)^2 + \left(\frac{4R\hat{W}_r}{\hat{\lambda}_m} + \omega_e\hat{\lambda}_m\right)^2} \tag{4.41}$$

The RMS value of the reactive voltage is given by

$$\jmath IX = \frac{4\hat{W}_r}{\sqrt{2}\hat{\lambda}_m}\omega_e L \tag{4.42}$$

and the RMS values of the induced EMF and resistive voltage are given by, respectively

$$E = \omega_e\hat{\lambda}_m/\sqrt{2} \tag{4.43}$$

$$IR = \frac{4\hat{W}_r}{\sqrt{2}\hat{\lambda}_m}R \tag{4.44}$$

Fig. 4.1(b) shows the phasor diagram corresponding to eqn. 4.41. For a unidirectional motor, the load angle corresponds to ripple free torque. E and I are in phase with each other and lag V by $\theta_o = \varphi$. A conventional motor may also operate at this load angle but torque ripple will occur because the PM reluctance torque is not suitably modified. I_m is a fictitious current which is proportional to the MMF produced parallel to the d-axis of the rotor by the permanent magnet. I_m is in phase with the rotor d-axis and lags E by 90°.

The remaining phasor diagrams represent the no load and pullout cases. These phasor diagrams are also applicable to both the conventional and unidirectional motors, being the result of mechanical loading. Fig. 4.1(a) corresponds to no load. E and I are at right angles to each other yielding zero average power output. The stator winding and rotor MMFs are in phase, which is shown by the alignment of I and I_m. The resultant MMF is therefore large which results in higher stator saturation [Schemmann 1971, pp. 38-40][Thees 1965].

Fig. 4.1(c) shows the case corresponding to pullout torque. A comparison of Fig.s 4.1(b) and (c) shows that pullout cannot occur when E and I are in phase. This is because, in Fig. 4.1(c) at pullout, $\theta_o = -\alpha$, whilst in Fig. 4.1(b), $|\theta_o| < \alpha$. This allows the unidirectional motor a torque buffer for starting and for load variation. The phase angle between I and I_m is largest, resulting in lower stator saturation at pullout.

For ripple free torque, the magnitude of unidirectional motor torque is given by eqn. 4.35. The torque may alternatively be expressed solely as a function of electrical parameters by substituting $\hat{W}_r = \overline{T}/2p$ into eqn. 4.41, and then solving for $\overline{T}$ to get:

$$\overline{T} = \frac{p\hat{\lambda}_m}{2Z}\sqrt{\hat{v}^2 - (\omega_e\hat{\lambda}_m\sin\alpha)^2} - \frac{p\omega_e\hat{\lambda}_m^2}{2Z}\cos\alpha \tag{4.45}$$

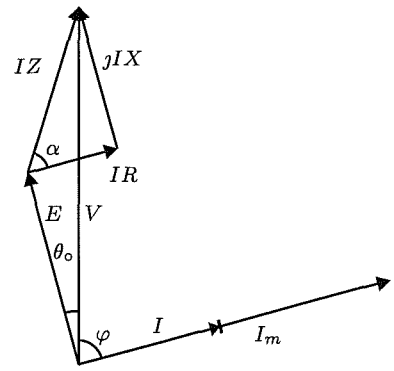

(a)

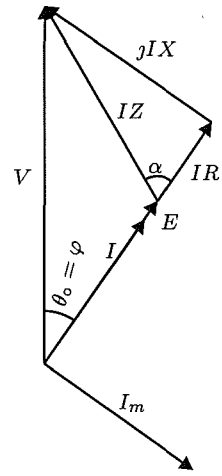

(b)

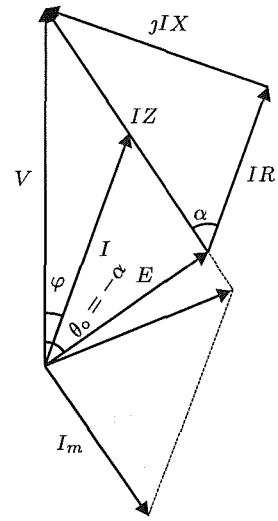

(c)

Figure 4.1 Phasor diagrams for the single phase synchronous PM motor.(a) No load. (b) Unidirectional motor load. (c) Pullout.

Eqn. 4.10 gives the same value for $\overline{T}$ as eqn. 4.45 for the unidirectional load. Therefore, by equivalence

$$\hat{v}\cos(\alpha+\theta_o) = \sqrt{\hat{v}^2 - (\omega_e\hat{\lambda}_m \sin\alpha)^2} \tag{4.46}$$

and the unidirectional load angle, at which E and I are in phase, is

$$\theta_o = \arcsin\left(\frac{\hat{e}}{\hat{v}}\sin\alpha\right) - \alpha \tag{4.47}$$

The electromagnetic power is obtained by multiplying eqn. 4.45 by $\dot{\theta}$ to get

$$P_{out} = \frac{\hat{e}}{2Z}\sqrt{\hat{v}^2 - (\hat{e}\sin\alpha)^2} - \frac{\hat{e}^2}{2Z}\cos\alpha \tag{4.48}$$

Expressing the unidirectional motor torque as a fraction of the pullout torque is useful for the purpose of design. This *pullout ratio* is obtained by dividing eqn. 4.45 by eqn. 4.12:

$$\Gamma = \frac{\overline{T}}{\overline{T}_p} = \frac{\sqrt{\hat{v}^2 - (\omega_e\hat{\lambda}_m\sin\alpha)^2} - \omega_e\hat{\lambda}_m\cos\alpha}{\hat{v} - \omega_e\hat{\lambda}_m\cos\alpha} \tag{4.49}$$

4.4 SIMULATION OF THE UNIDIRECTIONAL MOTOR

In this section, the principle of the unidirectional motor is demonstrated by simulation. The PM reluctance torque of a conventional motor is modified for the simulation. This modification allows the conventional motor to be simulated as a unidirectional motor.

4.4.1 Derivation of the PM Reluctance Torque

The PM reluctance torque for a single pole pair motor is given in Chapter 1 by eqn. 1.8. In this section, an equation for the PM reluctance torque for a motor having an arbitrary number of pole pairs is developed. The stored energy of single pole pair and multiple pole pair motors is determined in section 4.8. It is shown that a reasonable approximation of the stored energy is given by

$$W(i=0) = W_{ro} - \hat{W}_r\cos[2p(\theta-\gamma_r)] \tag{4.50}$$

where

W_{ro} = DC component of the stored field energy (when $i=0$)
$\hat{W}_r$ = amplitude of the stored energy modulation (when $i=0$)

γ_r is measured in mechanical units. The stored energy is modulated at twice the rate

of the PM flux linkage. The PM reluctance torque is given by

$$T_r = -\frac{dW(i=0)}{d\theta} = -2p\hat{W}_r \sin[2p(\theta - \gamma_r)] \tag{4.51}$$

which is identical to eqn. 1.8 for $p = 1$. The amplitude of the reluctance torque is given by

$$\hat{T}_r = 2p\hat{W}_r \tag{4.52}$$

4.4.2 State Equations

The electrical and mechanical equations of motion given in Chapter 1 by 1.5 and 1.7 may be presented in state equation form for the purpose of motor simulation. These equations are extended here to accommodate an arbitrary number of pole pairs. With the EMF/torque function given by eqn. 4.2, and the PM reluctance torque given by eqn. 4.51, the state equations become

$$\frac{d\dot{\theta}}{dt} = \frac{1}{J}\left[ip\hat{\lambda}_m \sin(p\theta) - 2p\hat{W}_r \sin[2p(\theta - \gamma_r)] - T_l\right] \tag{4.53}$$

$$\frac{di}{dt} = \frac{1}{L}\left[\hat{v}\sin(\omega_e t + \epsilon) - \dot{\theta}p\hat{\lambda}_m \sin(p\theta) - iR\right] \tag{4.54}$$

$$\frac{d\theta}{dt} = \dot{\theta} \tag{4.55}$$

where $\dot{\theta}$, i, and θ are the state variables. These equations form a set of nonlinear ordinary differential equations which must be solved numerically. For $p = 1$, these equations are identical to those given by [Schemmann 1971, p. 52] for motor simulation. [Schemmann 1973] compares the simulation results of these equations to experimental results for a single pair pole motor. Schemmann shows that

> ... the equations represent a behaviour completely analogous to that of the motor. Not only do the equations reproduce the details of the motion observed in the motor but there are no extraneous effects, i.e. effects not observed in the motor.

These equations are used to test the design of single pole pair motors [Diefenbach and Schemmann 1989][Altenbernd 1991]. A unidirectional motor having a single pole pair is simulated by setting appropriate values for T_l, $\hat{T}_r$, and γ_r. The form of the equations remains unaltered. Therefore, if the parameters of the unidirectional motor can be accurately calculated, it is assumed that the simulation results will accurately predict the motion of the unidirectional motor prior to its construction.

The extension of these equations to the form above which accommodates an arbitrary number of pole pairs is considered to be valid if the PM flux linkage and the PM reluctance torque do not have significant higher order harmonics. Therefore if this is the case, for a set of accurately calculated multiple pole pair motor parameters, these equations are also expected to give accurate results.

The simulations are performed using Matlab software[Matlab 1994] which implements computational algorithms by [Forsythe *et al.* 1977]. These algorithms apply Runge-Kutta-Fehlberg integration methods.

4.4.3 A Simulation Example

The parameters of the water-pump motor produced by Siemens are used in this example. Table 4.1 lists the parameters of the Siemens motor. The motor is rated at

	value	units	comment
$\hat{v}$	$\sqrt{2}\ 220$	V	
f	50	Hz	
p	1		
$\hat{\lambda}_m$	0.355	V.sec	Measured in section 5.5.3
R	119	Ω	Cold (room temp.) measurement
L	1.655	H	Measured in section 5.5.5 corresponding to steady state current during water-pumping
J	22×10^{-7}	Kg.m^2	
$\hat{T}_r$	0.03	Nm	Approximate value
γ_r	7°	deg.	Measured in section 5.5.1.2

Table 4.1 Conventional Siemens motor parameters

220/230 V RMS. The lower value of 220 V RMS is used in the simulation. The moment of inertia of the rotor and load is estimated for the water-pumping application[1]. The estimation of the inertia is difficult because it is a combination of two parts. The first part includes the PM rotor and the impeller of the pump, both of which are rigidly coupled together. This inertia is approximately $14-20\times10^{-7}$ Kg.m^2. The second part is the inertia of the ring of water in the impeller chamber. This ring of water must accelerate to synchronous speed during start-up. The inertia is a function of the rotor speed and its estimation is a hydrodynamic problem. An estimate of the inertia of the ring of water is $2-8\times10^{-7}$ Kg.m^2. An estimate of the combined rotor and load inertia is therefore between $16-28\times10^{-7}$ Kg.m^2. A value of $J=22\times10^{-7}$ Kg.m^2 is used in the simulation.

The load torque of the pump is a quadratic function of the rotor speed, and is

[1]These estimates are provided by Dr G. Altenbernd

modelled by

$$T_l = \mathrm{sgn}(\dot{\theta}) K_{lq}\, \dot{\theta}^2 \tag{4.56}$$

where K_{lq} is the quadratic load coefficient.

For the Siemens motor[2], the rated load is $T_l = 0.048$ Nm. Table 4.2 shows some performance parameters calculated using this value of load torque. For simulation

	value	units	comment
$\overline{T}$	0.048	Nm	
P_{in}	24.3	W	Calculated using eqn. 4.16. The nameplate rating is 25 W
P_{out}	15	W	Power delivered to the shaft, $P_{out} = \omega_e T_l$
$\overline{T}_p$	0.095	Nm	From eqn. 4.12
η	0.62		From eqn. 4.17

Table 4.2 Siemens motor performance parameters.

as a unidirectional motor, the value of motor torque at which E and I are in phase must first be calculated. The new value of motor torque calculated using eqn. 4.45 is $\overline{T} = 0.0887$ Nm. Table 4.3 identifies the simulation parameters which are modified to allow simulation as a unidirectional motor. Fig. 4.2 shows how the Siemens motor and

parameter	value	units	comment
$\hat{T}_r$	0.0887	Nm	$\hat{T}_r = \overline{T}$
γ_r	45°	deg.	
K_{lq}	2.82×10^{-4}	$\frac{\text{Nm.sec}^2}{\text{rad}^2}$	Corresponds to $T_l = \overline{T}$

Table 4.3 Parameters modified for unidirectional simulation.

its unidirectional equivalent compare in terms of torque, current amplitude, resistive power loss, and efficiency, as a function of the load angle. The range of operation for motoring extends from no load, at $\theta_o = 0.14$ radians, to the pullout torque at $\theta_o = -1.31$ radians.

Fig. 4.3 shows a simulation of the Siemens motor with the unidirectional modifications to parameters. The simulation corresponds to starting with $\epsilon = 0$. The initial values of the state variables are $[i_\emptyset = 0, \dot{\theta}_\emptyset = 0, \theta_\emptyset = \gamma_r = 45°]$. The rotor speed characteristic shows that the rotor successfully accelerates to synchronous speed in the forward direction. The speed ripple decays to zero as steady state motion is established. The lower plots provide a breakdown of the torques produced by the motor. The motor torques characteristics show the phase-magnet torque, $i\frac{d\lambda_m}{d\theta}$, and the PM reluctance torque, T_r. In the steady state, the instantaneous sum of these two components is constant and equal to the load torque. Speed ripple is thereby eliminated.

[2]Siemens model with nameplate number 710.600 00/1

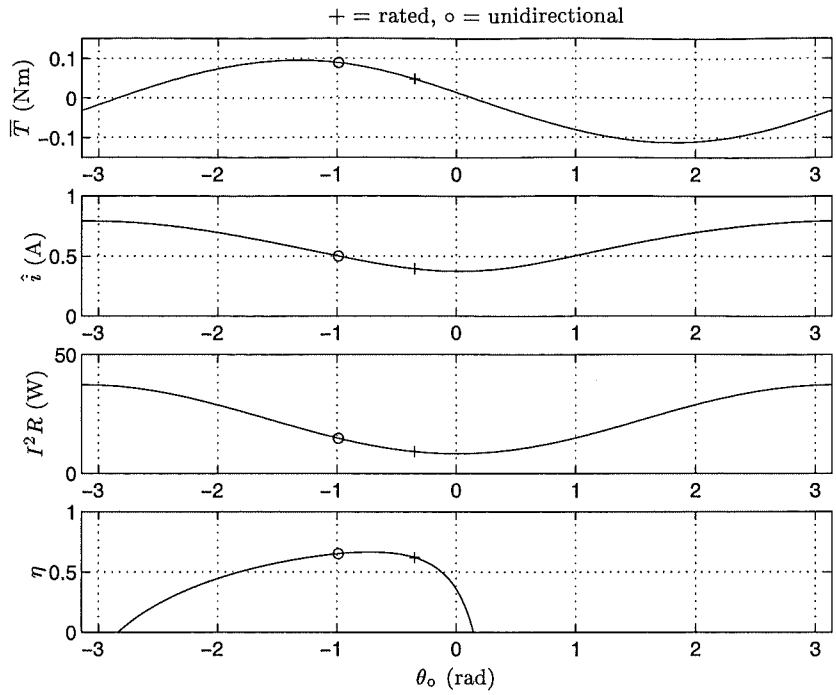

Figure 4.2 Siemens motor characteristics plotted as a function of load angle.

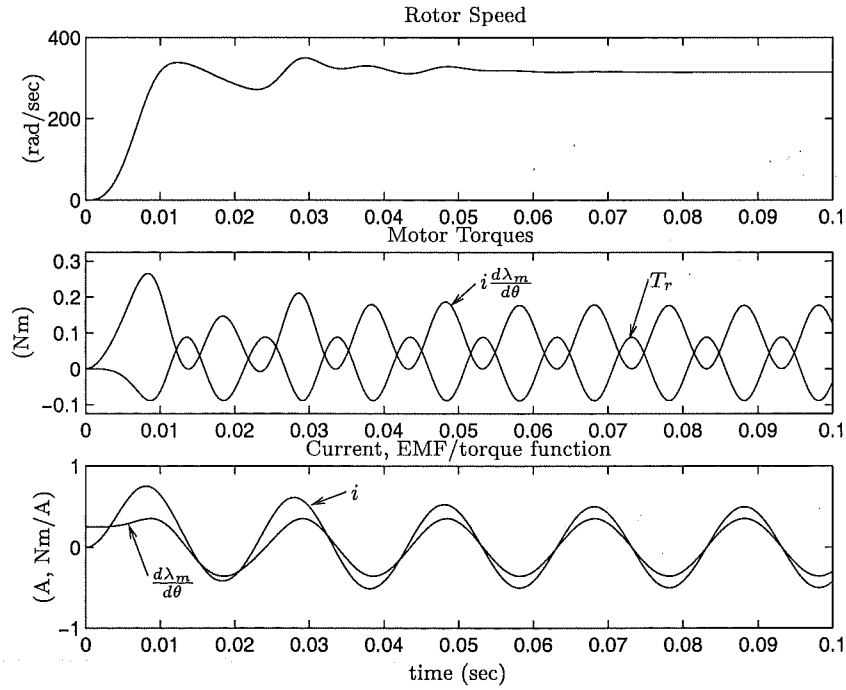

Figure 4.3 Simulation of starting of the Siemens motor using unidirectional parameters. $\epsilon = 0$, the initial values of the state variables are $[i_\emptyset = 0, \dot{\theta}_\emptyset = 0, \theta_\emptyset = \gamma_r = 45°]$, and $J = 22 \times 10^{-7}$ Kg.m^2.

The current and EMF/torque function characteristics plot i and $\frac{d\lambda_m}{d\theta}$, respectively. The product of these two characteristics yields the phase-magnet torque, $i\frac{d\lambda_m}{d\theta}$. These two characteristics fall into phase with each other as steady state motion is established.

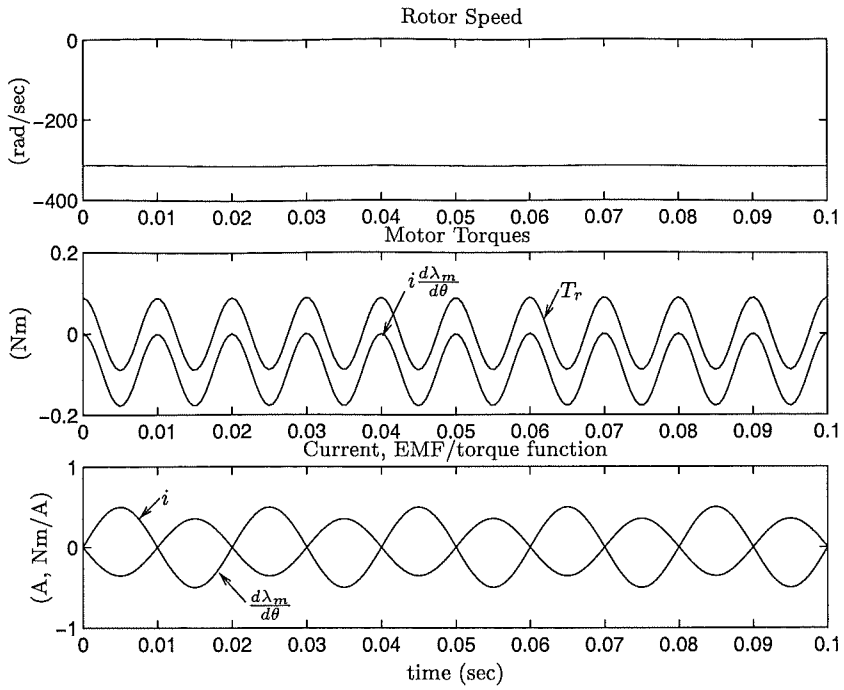

Figure 4.4 Simulation of synchronous motion in the backward direction. $\epsilon = -\theta_o$, $[i_\emptyset = 0, \dot{\theta}_\emptyset = -\omega_e, \theta_\emptyset = 0]$, and the moment of inertia is increased to $J = 22 \times 10^{-4}$ Kg.m^2 to smooth out speed ripple.

To simulate synchronous forward motion from the beginning of the simulation, the initial values of the state variables may be conveniently set to $[i_\emptyset = 0, \dot{\theta}_\emptyset = \omega_e, \theta_\emptyset = 0]$ with $\epsilon = -\theta_o$. θ_o is calculated from eqn. 4.47. In an analogous manner, to simulate synchronous motion in the backward direction, the initial values of the state variables are set to $[i_\emptyset = 0, \dot{\theta}_\emptyset = -\omega_e, \theta_\emptyset = 0]$ with $\epsilon = -\theta_o$. Backward synchronous motion is simulated in Fig. 4.4. Backward synchronous motion requires that the phase-magnet torque be negative in sign. This occurs if i and $d\lambda_m/d\theta$ are in anti-phase. This is illustrated in Fig. 4.4. The current and induced EMF, $\dot{\theta}\frac{d\lambda_m}{d\theta}$, still remain in phase. The phase angle of the PM reluctance torque also remains unchanged. This results in the PM reluctance torque accentuating the twice electrical frequency torque pulsation of the phase-magnet torque. The resultant of these torques has an amplitude of modulation equal to twice the magnitude of the load torque. This causes a large modulation of the rotor speed, unless the rotor inertia is very large. In the simulation of Fig. 4.4, J has been increased to smooth out the speed ripple. This allows synchronous backward motion at constant instantaneous speed to be demonstrated.

Fig. 4.5 shows the resulting motion when the initial conditions of the previous simulation are applied, but the inertia is reduced to its original value. Within the first 0.04 seconds, backward synchronous motion is observed. Within this interval, the rotor speed modulates at twice the electrical frequency because of the motor torque modulation. At the end of this interval, the rotor falls out of backward synchronism.

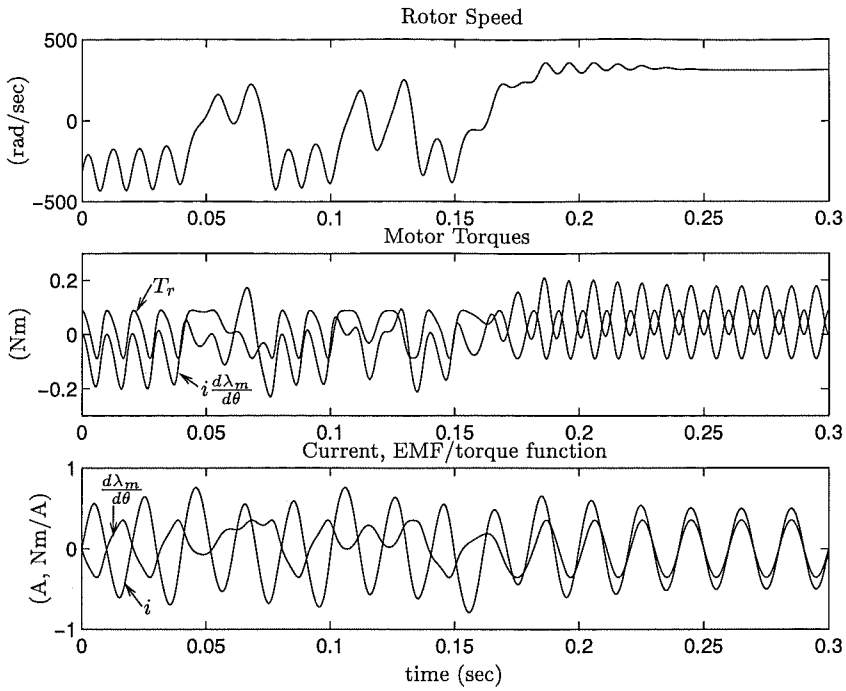

Figure 4.5 Identical simulation to that of Fig. 4.4, but with the moment of inertia reduced to its original value. $\epsilon = -\theta_o$, $[i_\emptyset = 0, \dot{\theta}_\emptyset = -\omega_e, \theta_\emptyset = 0]$, and $J = 22 \times 10^{-7}$ Kg.m^2.

An asynchronous interval then follows where the rotor attempts to synchronise alternatively in the forward and backward directions. At approximately 0.2 seconds, the rotor achieves synchronism in the forward direction. Stable motion is established.

This simulation demonstrates the ability of the motor to self correct the direction of rotation. This is achieved without using mechanical devices to exclude rotation in one direction. These simulations also demonstrate how speed ripple is eliminated.

However, this particular unidirectional design based on the Siemens motor will not be developed further because of the following reasons. First, the ability of the motor to self correct its direction of rotation is not strong enough. Backward synchronous motion easily becomes stable at lower load torques. The final direction of rotation then becomes undetermined from start up. Secondly, the unidirectional torque is too close to the pullout torque, or $\Gamma = \overline{T}/\overline{T}_p$ is too high. This does not allow for overload situations, and simulations results with values of ϵ other than zero show that the motor has trouble starting. Thirdly, the design is not physically realisable using the construction of the Siemens motor. It is neither possible to phase shift the PM reluctance torque from $\gamma_r = 7°$ to $\gamma_r = 45°$, nor increase its amplitude from $\hat{T}_r = 0.03$ to $\hat{T}_r = 0.088$ Nm, using the single slot stator.

4.5 INVESTIGATION OF THE SELF CORRECTING CHARACTERISTIC

This section investigates what causes the unidirectional motor to self correct its direction of rotation. An understanding of this characteristic is important for the purpose of design, if no mechanical self correcting device is used.

4.5.1 Power Series Solution

The power series method [Kreyszig 1988] yields an analytical solution to eqn.s 4.53 and 4.54 in open form: the solution consists of an infinite power series. A power series solution to these equations is obtained below for a specific set of initial values of the state variables. The initial values of the state variables correspond to forward motion at synchronous speed given by $[i_\emptyset = 0, \dot{\theta}_\emptyset = \omega_e/p, \theta_\emptyset = 0]$. The first three terms of the solution for the rotor speed are:

$$\dot{\theta} = \frac{\omega_e}{p} + \frac{2p\hat{W}_r \sin(2p\gamma_r) - T_l}{J} t - \frac{2p\hat{W}_r \cos(2p\gamma_r)\omega_e}{J} t^2 + \ldots \tag{4.57}$$

Inspection of eqn. 4.57 shows that substitution of $p\gamma_r = \pi/4$, and $T_l = 2p\hat{W}_r$ sets the coefficients of the first and second powers of t to zero. These substitutions describe requirements necessary for ripple free motion for the unidirectional motor, as shown in section 4.3. With these substitutions the coefficients of higher powers of t are simplified. The solution up to the fifth power of t is then simplified to

$$\dot{\theta} = \frac{\omega_e}{p} - \frac{1}{3}\frac{p\omega_e(4\hat{W}_r\omega_e L - \hat{v}\hat{\lambda}_m \sin\epsilon)}{LJ} t^3 - \frac{1}{8}\frac{p\omega_e\hat{\lambda}_m(R\hat{v}\sin\epsilon - \omega_e L\hat{v}\cos\epsilon + \hat{\lambda}_m\omega_e^2 L)}{L^2 J} t^4 + \ldots \tag{4.58}$$

All the motor parameters are finally introduced into the coefficients at the fourth power of t. The last parameter to be introduced is resistance R. The coefficient of the third power of t equates to zero if

$$\sin\epsilon = \frac{4\hat{W}_r\omega_e L}{\hat{v}\hat{\lambda}_m} \tag{4.59}$$

Eqn. 4.36 identifies $4\hat{W}_r/\hat{\lambda}_m$ as the amplitude of the currrent $\hat{i}$ for the unidirectional motor. Therefore eqn. 4.59 is equivalently expressed in terms of RMS voltages by

$$\sin\epsilon = \frac{IX}{V} \tag{4.60}$$

Fig. 4.1(b) shows that eqn. 4.60 defines the relationship between the supply voltage and the reactive voltage for the unidirectional motor, where $\epsilon = -\theta_\circ$.

The coefficient of the fourth power of t equates to zero if

$$\omega_e L\hat{v}\cos\epsilon = R\hat{v}\sin\epsilon + \hat{\lambda}_m\omega_e^2 L \tag{4.61}$$

Substitution of eqn. 4.59 into eqn. 4.61 allows eqn. 4.61 to be solved as

$$V\cos\epsilon = IR + E \tag{4.62}$$

Fig. 4.1(b) shows that eqn. 4.62 describes the relationship between the supply voltage, the resistive voltage, and the induced EMF for the unidirectional motor, where $\epsilon = -\theta_o$. All of the requirements and relationships between motor parameters for the unidirectional motor have been defined above. This has been achieved by setting to zero and solving the coefficients of the first four powers of t in the power series. The analysis of section 4.3 shows that the rotor speed is constant if these requirements and initial conditions are in place. Therefore all power series terms corresponding to higher powers of t must equate to zero. In this case the power series converges to $\dot{\theta} = \omega_e/p$ for all values of t.

This specific power series solution yields neither insight into the self correcting characteristic nor the motor parameters which may have a predominant role. Power series solutions corresponding to other combinations of initial states do not yield any clearer insight into the self correcting characteristic.

4.5.2 Approximate Condition for Failure of Backward Synchronous Motion

Fig. 4.5 illustrates an example of a unidirectional motor simulation where loss of backward synchronism occurs over multiple electrical cycles. However, loss of backward synchronism within an electrical cycle, corresponding to a stronger self correcting characteristic, is desirable. In this section, a condition corresponding to loss of backward synchronism within an electrical cycle is determined. An analytical expression which identifies key motor parameters is obtained.

Fig. 4.6 plots the PM reluctance torque, T_r, and the EMF/torque function, $d\lambda_m/d\theta = p\hat{\lambda}_m \sin p\theta$, for the unidirectional motor. These characteristics are plotted over half an electrical cycle centred at $\theta = 0$. The PM stored energy $W(i = 0)$ is also shown. Within the quadrant $\theta = -\frac{\pi}{4p} \ldots \frac{\pi}{4p}$, the magnitude of $d\lambda_m/d\theta$ is significantly smaller than it is in the quadrant spanning $\theta = -\frac{\pi}{2p} \ldots -\frac{\pi}{4p}, \frac{\pi}{4p} \ldots \frac{\pi}{2p}$. Within the former quadrant, $d\lambda_m/d\theta$ diminishes to zero, and T_r peaks, towards $\theta = 0$. Therefore, within this quadrant, and particularly near $\theta = 0$, the magnitude of the phase-magnet torque $i\frac{d\lambda_m}{d\theta}$ is reduced. This reduction is significant regardless of the magnitude of the current. In contrast, near $\theta = 0$, T_r is not reduced and has a large amplitude for a unidirectionally designed motor. Therefore the following simplifying approximations

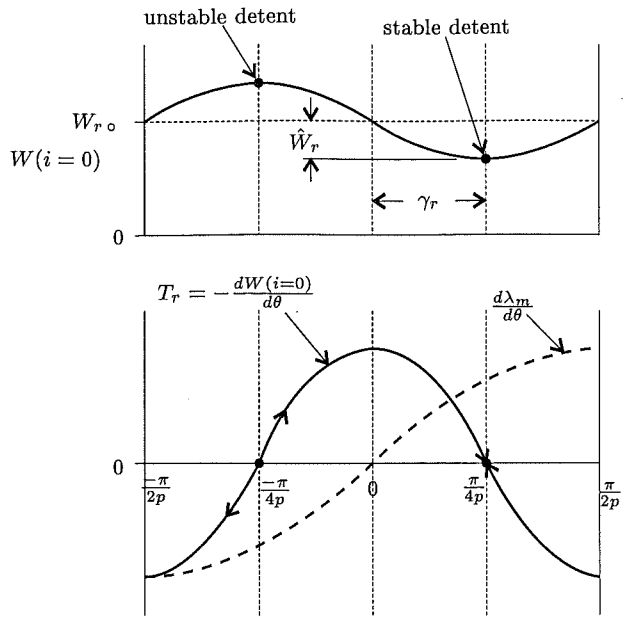

Figure 4.6 PM reluctance torque T_r, EMF/torque function $d\lambda_m/d\theta$, and PM stored energy $W(i=0)$, about $\theta = 0$ for the unidirectional motor.

may be made to the mechanical equation of motion about $\theta = 0$. The phase-magnet torque $i\frac{d\lambda_m}{d\theta}$ may be omitted from eqn. 4.53. The angular acceleration is then determined without requiring calculation of i. By also neglecting the load torque T_l, eqn. 4.53 is approximated about $\theta = 0$ for a unidirectional motor by

$$J\frac{d\dot{\theta}}{dt} \approx 2p\hat{W}_r \cos(2p\theta) \tag{4.63}$$

With reference to Fig. 4.6, eqn. 4.63 shows that over the interval $\theta = -\frac{\pi}{4p} \ldots \frac{\pi}{4p}$, the PM reluctance torque yields an angular acceleration in the forward direction of rotation. It may then be supposed that if the rotor is running at synchronous speed in the backward direction at $\theta = \pi/4p$, it is possible for the rotor to de-accelerate and come to rest on or before $\theta = -\pi/4p$. The rotor may then be accelerated in the forward direction from $\theta = -\frac{\pi}{4p}$ to $\frac{\pi}{4p}$. This describes a self correcting process.

In the interval $\theta = \frac{\pi}{4p} \ldots \frac{\pi}{2p}, -\frac{\pi}{2p} \ldots -\frac{\pi}{4p}$, the PM reluctance torque will be unsuccessful at reversing synchronous motion in the forward direction, in an analogous manner to that described above. This is because, in this quadrant, torques $i\frac{d\lambda_m}{d\theta}$ and T_r superimpose to yield a constant net torque and zero acceleration.

Synchronous motion in the backward direction is still be possible. In this case the torques $i\frac{d\lambda_m}{d\theta}$ and T_r align in the manner shown by Fig. 4.4. Speed ripple is present. Through each middle quadrant corresponding to $\theta = -\frac{\pi}{4p} \ldots -\frac{\pi}{2p}, \frac{\pi}{2p} \ldots \frac{\pi}{4p}$, both torques add to provide sufficient acceleration to allow the rotor to carry through the de-accelerating quadrant, $\theta = \frac{\pi}{4p} \ldots -\frac{\pi}{4p}$. However, the backward motion becomes less stable as speed ripple increases.

Eqn. 4.63 describes a conservative system where energy is transferred between rotational stored energy and PM stored energy. The balance of energy corresponding to the de-acceleration from backward synchronous speed to zero speed may be obtained from eqn. 4.63 by

$$\int_{-\dot{\theta}}^{0} J\dot{\theta}\, d\dot{\theta} \approx \int_{\frac{\pi}{4p}}^{-\frac{\pi}{4p}} 2p\hat{W}_r \cos(2p\theta)\, d\theta \tag{4.64}$$

which evaluates to

$$-\frac{1}{2}J\dot{\theta}^2 \approx -2\hat{W}_r \tag{4.65}$$

For backward synchronous speed to be reduced to zero over the interval $\theta = \frac{\pi}{4p} \ldots -\frac{\pi}{4p}$, the amount of energy able to be stored magnetically by the PM must be at least as great as the rotational energy required to be transferred to reduce the speed to zero. In this case eqn. 4.65 may be expressed in the form of the inequality:

$$\frac{4\hat{W}_r p^2}{J\omega_e^2} > 1 \tag{4.66}$$

where the substitution $\dot{\theta} = \omega_e/p$ relates the mechanical speed to the electrical angular speed. Eqn. 4.66 defines an approximate condition required for failure of backward synchronism. This ideally occurs over a quarter of an electrical cycle, but is possible over a number of cycles. The ratio $4\hat{W}_r p^2/J\omega_e^2$ will be referred to as the *backward instability ratio*. Simulation results have shown that eqn. 4.66 provides, in general, a useful indication of whether a unidirectional design is likely to have a sufficient self correcting characteristic. For the example of the Siemens motor using unidirectional parameters, the self correcting characteristic is not strong, and the backward instability ratio is only 0.82. Simulation results show that if the backward instability ratio is high enough, backward synchronous motion will in general be unstable, within a useful range of motor parameter variation.

The influence of the load torque has been neglected in the formulation of eqn. 4.66. The effect of the load torque is to extract stored energy as the rotor de-accelerates and accelerates. This is explained with reference to Fig. 4.6. During de-acceleration from $\theta = \pi/4p$, rotational energy is transferred into PM stored energy, and is also transferred to the load. This aids de-acceleration such that the rotor may come to rest before reaching $\theta = -\pi/4p$. The PM reluctance torque then accelerates the rotor in the forward direction. However, the amount of PM stored energy available to accelerate the rotor to synchronous speed is reduced because the rotor starts accelerating forward closer to the stable detente at $\theta = \pi/4p$. During acceleration, the available energy is transferred into rotational stored energy, and is also transferred to the load. This further reduces the amount of energy available to be converted into rotational energy. The available

energy may then be insufficient to bring the rotor up to forward synchronous speed by $\theta = \pi/4p$.

The influence of the load torque requires that the backward instability ratio be higher than unity to compensate for stored energy lost to the load.

4.6 FORMULATION OF TWO UNIDIRECTIONAL MOTOR DESIGNS

In this section, two unidirectional motor designs are formulated. The aim of the designs is for each motor to be able to self correct its direction of rotation. This is to be achieved without the requirement of a mechanical self correcting device.

Eqn. 4.66 may be used as a design tool for the development of these unidirectional motor designs. Achieving the design aim requires the backward instability ratio to be maximised. The motor parameters ω_e, J, $\hat{W}_r$, and p feature in this ratio. The electrical angular speed ω_e cannot be varied if the motor is directly connected to the electrical AC supply. Therefore ω_e may be considered to be a constant. The moment of inertia of the PM rotor is given by

$$J_r = \frac{\pi}{2} \varrho L_r \left(\frac{D_r}{2}\right)^4 \tag{4.67}$$

where

ϱ = rotor mass density
L_r = length of rotor
D_r = rotor diameter

The inertia of the rotor J_r is generally larger than that of the load, and contributes most significantly to the total inertia J. Eqn. 4.67 shows that decreasing the rotor diameter strongly decreases the rotor inertia. Therefore, the total inertia is also strongly decreased. A physical limit to the rotor diameter exists at which further increases in diameter and inertia inhibit adequate acceleration to synchronous speed [Bertram and Schemmann 1976]. This illustrates why the size and power rating of the conventional motor is small. For the unidirectional motor, decreasing the rotor diameter very significantly increases the backward instability ratio. However, doing this reduces the power rating of the motor. In each of the two designs, an attempt is made to maximise power rating, thereby maximising rotor diameter and inertia. Reduction of the rotor diameter will only be used as a last design option to raise the backward instability ratio to a sufficiently high value. Each of the motor designs is based on maximising one of the two remaining parameters in the backward instability ratio. These designs are introduced in sections 4.6.1 and 4.6.2.

4.6.1 A Single Pole Pair Design

This design maximises the amplitude of the PM stored energy modulation $\hat{W}_r$. The results obtained from the analysis of section 3.6 show that $\hat{W}_r$ increases as the amplitude of airgap modulation is increased. Dimension L_t is maximised for both designs. The example of section 3.6.1 shows clearly that W and $\hat{W}_r$ are proportional to the square of the PM remanent flux density B_r. For the single pole pair design, $\hat{W}_r$ is increased by increasing B_r. This is achieved by using a higher grade of magnet. The bonded Nd-Fe-B grade of magnet specified in section 3.3.2.1 is used. The increased magnitude of $\hat{W}_r$, in relation to J, permits a single pole pair design to be implemented. This design is developed in section 4.9.

4.6.2 A Multiple Pole Pair Design

This design implements multiple pole pairs to allow ferrite grade magnets to be used. With ferrite magnets, the magnitude of $\hat{W}_r$ in relation to J is lower. This is compensated for by increasing the number of pole pairs. The ferrite material has the economic attraction of being a cheap PM material. This enables conventional 2-pole motors of this type to be economically feasible in the low performance and low power applications in which they are used. This design uses three pole pairs and is developed in section 4.10. The rotor speed of this motor connected to a 50 Hz supply is 1000 RPM.

4.6.3 Physical Implementation

This section explains how the single and multiple pole pair designs may be physically realised. Each unidirectional design requires:

1. A sinusoidal EMF/torque function, $d\lambda_m/d\theta$.
2. A sinusoidal PM reluctance torque of amplitude equal to the rated torque, displaced to a phase angle of $p\,\gamma_r = 45°$ electrical.
3. The above characteristics implemented in a manufacturable design.

A conventional 2-pole synchronous PM motor has a single set of airgaps. The airgap around the stator iron is modulated by the asymmetric steps. Experimental measurement of the induced EMF in section 5.5.3 shows that the fundamental component is dominant. The third harmonic has a range of 3-5% and higher order harmonics are negligible. This implies that the asymmetric airgap modulation has little distorting effect on the EMF/torque function. This demonstrates that the 2-pole parallel magnetised rotor design of the conventional motor enables a sinusoidal EMF/torque function to be obtained, even with modulation of the airgap to allow a PM reluctance torque to be obtained. The parallel magnetised rotor of the conventional motor will be used

in the unidirectional designs. The mechanisms influencing EMF/torque function shape are examined in section 4.7.

The PM reluctance torque of the conventional 2-pole motor is approximated by a sinusoid, as described in section 1.2.1. A remaining requirement is to establish the $p\gamma_r = 45°$ (electrical) displacement angle. In the conventional single slot design, the slot is predominantly responsible for the magnitude and phase of the PM reluctance torque. If the asymmetric stator steps are removed, the PM reluctance torque remains present with a displacement angle of $p\gamma_r = 0$. The asymmetric steps, or alternative saturating notches, act to phase shift this torque by a small angle which is sufficient for starting. To establish a large displacement angle, the slots must be eliminated altogether. This is achieved in the slotless 2-pole design of Fig. 1.2(b). A displacement angle of $\gamma_r = 90°$ is obtained. However, unidirectional synchronous motion requires that $\gamma_r = 45°$. The stator construction of the motor of Fig. 1.2(b) will be adopted. But a suitable airgap modulation will be employed to achieve the desired displacement angle. In the paper "Effects of Airgap and Magnet Shapes on Permanent Magnet Reluctance Torque" in Appendix A, the shape of the reluctance torque appears to correlate to the shape of the airgap modulation for the examples analysed. For the unidirectional motor a sinusoidal reluctance torque containing minimal harmonics is required. A sinusoidal airgap modulation is employed. The displacement angle $p\gamma_r = 45°$ is achieved by rotating the axis of the airgap modulation an appropriate angle from the stator d-axis. The PM reluctance torques of parallel magnetised rotors with sinusoidally modulated airgaps are examined analytically in section 4.8.

A stator design based on that of the motor of Fig. 1.2(b) also satisfies the requirement of a manufacturable design. A motor of this small size connected directly to the mains supply typically requires thousands of turns. This stator design permits the turns to be prewound onto formers, before being slotted onto the pole shanks. The stator ring or yoke is then fitted over the pole shanks.

The multiple pole pair design solution is to duplicate the single pole pair design. An example of this design is shown in Fig. 4.50. The rotor consists of alternately parallel magnetised PM sectors. In section 4.7, it is shown that this multiple pole pair design is more prone than the single pole pair design to harmonics in the EMF/torque function. As already mentioned, a limit on the rotor inertia places a limit on the rotor diameter. This limit makes the rotor diameter too small for the multiple slots per pole designs of larger electrical machines to be applied. Concentrated coils are necessary. This precludes the use of standard space harmonic suppression techniques such as distributed, chorded, and skewed coils [McPherson 1981, pp. 79-87] to improve the EMF/torque function.

4.7 ANALYSIS OF THE EMF/TORQUE FUNCTION

This section develops analytical equations for the EMF/torque functions of several machines having radial airgap flux. This allows the induced EMF and the phase-magnet torque to then be obtained for these machines. The analysis provides insight into the mechanisms which shape the EMF/torque function. In all the machines analysed, the coils are concentrated and full pitched. Each coil is represented by a single turn. The rotor poles are full pitched but the analysis may also be extended to short pitched PM poles. PM flux leakage is assumed to be zero. Faraday's law is again applied. The PM flux linking a closed turn is given by eqn. 3.30:

$$\phi_m = \int_S \mathbf{B} \cdot \mathbf{n}\, da$$

where S is any surface spanning the boundary of the closed turn. The EMF/torque function for a machine having N series connected turns is then given by eqn. 3.31:

$$\frac{d\lambda_m}{d\theta} = N\frac{d\phi_m}{d\theta}$$

This section concludes with an analysis of the EMF/torque functions of the proposed single and multiple pole pair unidirectional motors.

4.7.1 Radial Magnetisation

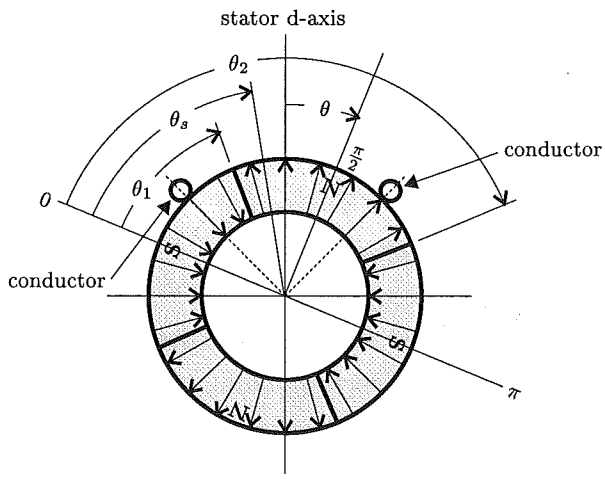

Figure 4.7 Radially magnetised PM arcs and a full pitched stator turn.

This section determines the EMF/torque function obtained using radially magnetised PM arcs and an arbitrary number of pole pairs. Fig. 4.7 shows a transverse section of a cylindrical rotor having radially magnetised PM arcs. The surface of inte-

gration S is taken along the surface of the rotor pole lying between angles θ_1 and θ_2. By setting appropriate integration limits, integrating over this surface is equivalent to integrating over a surface spanning the stator turn. Because the flux density is normal to the integration surface, $\mathbf{B} \cdot \mathbf{n} = |\mathbf{B}| = B$. The arcs are uniformly magnetised and B is assumed to be constant around the arcs. End effects are ignored such that B is also assumed to be uniform through the rotor in the axial direction.

Angles θ_1 and θ_2 determine the pitch of a PM pole in mechanical radians. These angles are defined relative to the rotor as shown by Fig. 4.7 and may have arbitrary values corresponding to an arbitrary PM pole pitch. For full pitched PM poles, θ_1 and θ_2 are defined such that

$$\theta_1 = \frac{\pi}{2} - \frac{\pi}{2p} \tag{4.68}$$

$$\theta_2 = \frac{\pi}{2} + \frac{\pi}{2p} \tag{4.69}$$

θ_s is defined relative to the rotor and lies within the limits $\theta_1 \leq \theta_s \leq \theta_2$. The flux linkage is integrated with respect to θ_s. θ is the angle of rotation defined as the angle between the stator d-axis and the rotor d-axis. The active magnetic surface area of the rotor cylinder is assumed to be:

$$a = 2\pi R_m L_{stk} \tag{4.70}$$

where

R_m = rotor radius $(D_r/2)$
L_{stk} = axial length of the stator lamination stack

The differential area is given by

$$da = L_{stk} R_m d\theta_s \tag{4.71}$$

Integration limits similar to eqn. 3.33 are applied to determine the flux linkage. For an arbitrary number of poles, the limits corresponding to the surface of integration lying between angles $theta_1$ and θ_2 are

$$\phi_m = \int_{\theta_1}^{\theta_2 - \theta} \mathbf{B} \cdot \mathbf{n}\, da - \int_{\theta_2 - \theta}^{\theta_2} \mathbf{B} \cdot \mathbf{n}\, da \qquad 0 \leq \theta \leq \pi/p \tag{4.72}$$

After substitution of eqn.s 4.68, 4.69, and 4.71 into eqn. 4.72, with $\mathbf{B} \cdot \mathbf{n} = B =$ constant, the PM flux linkage per turn is evaluated as

$$\phi_m = B L_{stk} R_m (\pi/p - 2\theta) \qquad 0 \leq \theta \leq \pi/p \tag{4.73}$$

and the EMF/torque function per turn is

$$\frac{d\phi_m}{d\theta} = -2BL_{stk}R_m \qquad 0 \leq \theta \leq \pi/p \tag{4.74}$$

Eqn.s 4.73 and 4.74 are piecewise functions extending π electrical radians. These

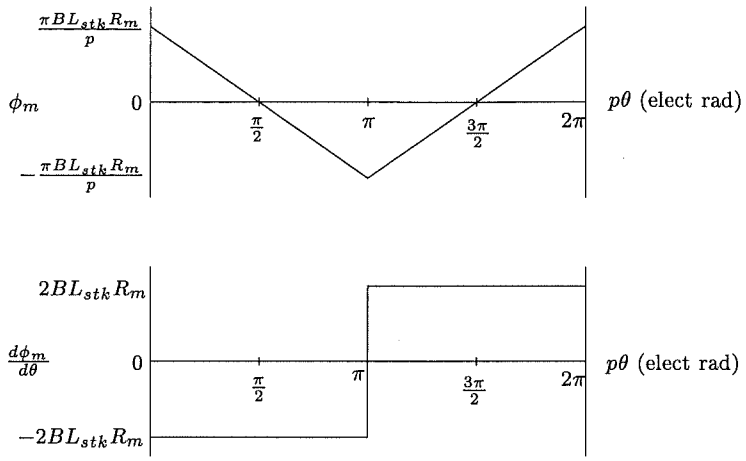

Figure 4.8 Flux linkage per turn ϕ_m, and EMF/torque function per turn $d\phi_m/d\theta$, plotted over an electrical cycle corresponding to a motor with radially magnetised PM arcs and an arbitrary number of pole pairs.

idealised functions are drawn extending over an electrical cycle in Fig. 4.8. The EMF/torque function per turn is a squarewave. It maintains constant shape and amplitude as a function of pole pair number. Therefore, if the total number of series turns and the angular speed remain constant, the amplitude of the induced EMF, $\hat{e} = \dot{\theta}N\frac{d\phi_m}{d\theta}$, also remains constant.

4.7.2 Parallel Magnetisation

This section determines the EMF/torque function obtained using parallel magnetised PM arcs. The flux linkage of a single pole turn is determined with reference to Fig. 4.9. The surface of integration is again taken around the rotor pole surface between angles θ_1 and θ_2. Because $\mathbf{B}$ is parallel to the rotor d-axis, $\mathbf{B}$ and $\mathbf{n}$ are collinear only along the d-axis. This is illustrated with reference to Fig. 4.10 where

$$\mathbf{B} \cdot \mathbf{n} = |\mathbf{B}||\mathbf{n}| \cos\alpha = |\mathbf{B}||\mathbf{n}| \sin\theta_s \tag{4.75}$$

For this example, the flux density within the PM perpendicular to the d-axis of the rotor pole is assumed to be constant such that $|\mathbf{B}| = B = \text{constant}$. da is again defined by eqn. 4.71, then

$$\int_S \mathbf{B} \cdot \mathbf{n}\, da = \int_S L_{stk}R_m B \sin\theta_s\, d\theta_s \tag{4.76}$$

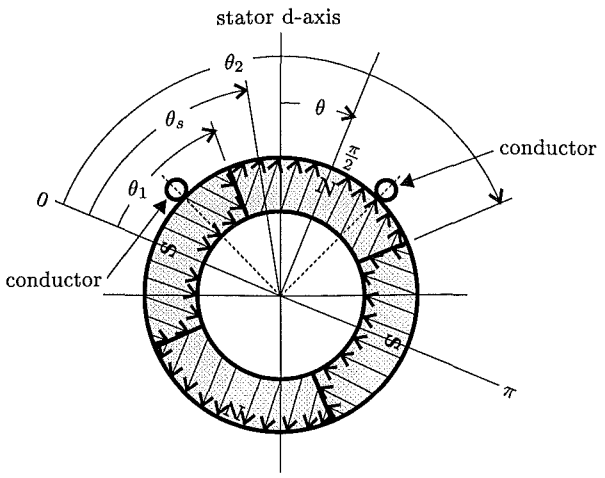

Figure 4.9 Parallel magnetised PM arcs and a stator turn.

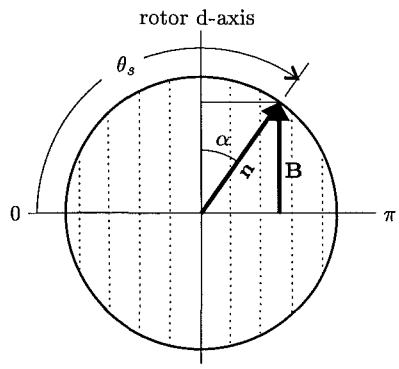

Figure 4.10 Relationship between **B** and **n** corresponding to parallel magnetisation.

By applying the integration limits of eqn. 4.72, the PM flux linkage per turn is given by

$$\phi_m = 2BL_{stk}R_m \sin(\pi/2p - \theta) \qquad 0 \leq \theta \leq \pi/p \tag{4.77}$$

and the EMF/torque function per turn is

$$\frac{d\phi_m}{d\theta} = -2BL_{stk}R_m \cos(\pi/2p - \theta) \qquad 0 \leq \theta \leq \pi/p \tag{4.78}$$

With $p = 1$, eqn. 4.78 simplifies to

$$\frac{d\phi_m}{d\theta} = -2BL_{stk}R_m \sin\theta \tag{4.79}$$

Eqn. 4.79 shows that the EMF/torque function for a parallel magnetised rotor having a single pole pair and constant B is sinusoidal. Using a parallel magnetisation is identified as an effective method of creating a sinusoidal EMF/torque function in a single pole pair motor.

For $p = 2$, eqn. 4.78 becomes

$$\frac{d\phi_m}{d\theta} = -2BL_{stk}R_m \cos(\pi/4 - \theta) \qquad 0 \leq \theta \leq \pi/2 \tag{4.80}$$

and for $p = 3$, eqn. 4.78 becomes

$$\frac{d\phi_m}{d\theta} = -2BL_{stk}R_m \cos(\pi/6 - \theta) \qquad 0 \leq \theta \leq \pi/3 \tag{4.81}$$

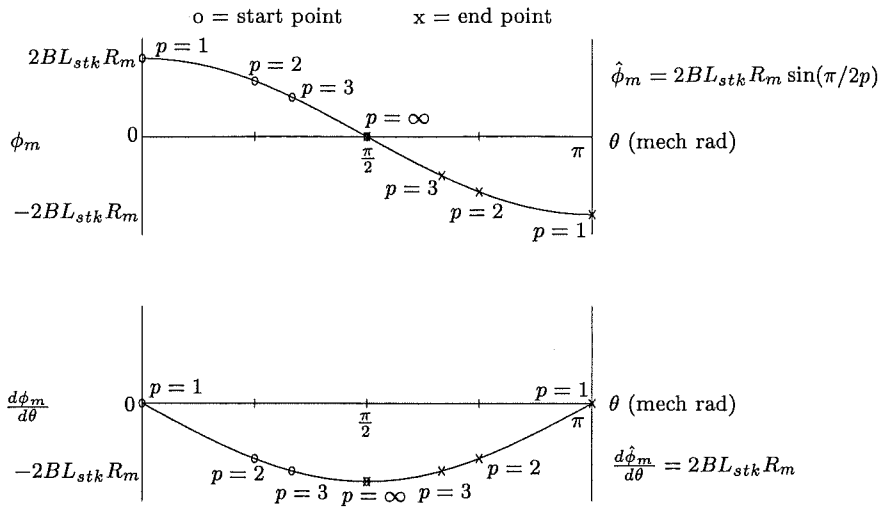

Figure 4.11 Waveforms for parallel magnetised rotor having an arbitrary number of pole pairs and constant flux density. PM flux linkage per turn ϕ_m, and EMF/torque function per turn $d\phi_m/d\theta$, are plotted over half a cycle.

Fig. 4.11 illustrates how the ϕ_m and $d\phi_m/d\theta$ waveforms change as the pole pair number p is increased. The waveforms are plotted over π mechanical radians. If p is doubled, the angular distance in mechanical radians between start and end points is halved. The angular distance between each respective start and end point corresponds to half an electrical cycle. As p increases, the ϕ_m waveform becomes less sinusoidal and more linear. The $d\phi_m/d\theta$ waveform becomes less sinusoidal and more rectangular. ϕ_m and $d\phi_m/d\theta$ corresponding to $p = 3$ are plotted in Fig. 4.16.

For large p, $d\phi_m/d\theta$ is approximated by a square-wave:

$$\frac{d\phi_m}{d\theta} \approx -2BL_{stk}R_m \frac{4}{\pi}\left(\sin p\theta + \frac{1}{3}\sin 3p\theta + \frac{1}{5}\sin 5p\theta + \ldots\right) \tag{4.82}$$

Comparison of eqn.s 4.79 and 4.82 shows that higher order odd harmonics emerge as p increases. A comparison of the analysis of this section and the previous section shows that a parallel magnetisation approximates a radial magnetisation with increasing precision as the number of pole pairs increases. This increasing similarity is noted by [Jahns and Soong 1996].

4.7.3 EMF/Torque Function of the Unidirectional Motor

The EMF/torque function of the unidirectional motor is derived the same way as that of section 4.7.2 except that B cannot be assumed to be constant. The airgap of the unidirectional motor is modulated sinusoidally. The length of the parallel magnetisation also varies across a rotor pole. Therefore B is not constant across a rotor pole pitch. End effects are still ignored such that B is assumed to be uniform in the axial direction. Sections 4.7.3.1 and 4.7.3.2 examine the direction and magnitude of the PM flux density.

4.7.3.1 Approximation of the Direction of the PM Flux Density

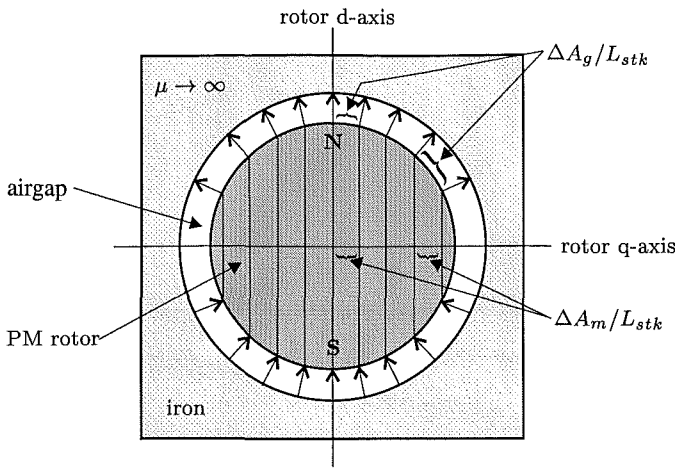

Figure 4.12 Directions of the PM flux density within the PM rotor and the airgap.

The assumed directions of the PM flux density are shown in Fig. 4.12. Within the PM, the flux density is parallel to the direction of the magnetisation. It is radial in the airgap. This follows the assumption that the magnetic field is set up in a manner which minimises the stored energy. The energy density within a PM material having a linear major demagnetisation characteristic is given by eqn. 2.25:

$$w_m = \frac{(B_r - B_{m||})^2}{2\mu_o\mu_{r||}} + \frac{B_{m\perp}^2}{2\mu_o\mu_{r\perp}}$$

Eqn. 2.25 shows that the PM energy density is minimised when B_m is parallel to the magnetisation. Both the bonded Nd-Fe-B and hard ferrite materials used in the proposed designs have major linear demagnetisation characteristics and near unity values of $\mu_{r||}$.

The energy density in the air is given by eqn. 3.2:

$$w_a = \frac{B_a^2}{2\mu_o}$$

The energy density in the airgap is minimised if the airgap flux density B_a is minimised. This occurs if the distance between flux lines is maximised. If end effects and leakage are ignored, the distance between flux lines in a radial airgap are maximised if the direction is radial. If the airgap length is modulated, and the modulation is not large relative to the mean airgap length, then the assumption of a radially directed airgap flux is considered a reasonable approximation. The finite element solution of the PM field for a conventional motor is shown in Fig. 4.13. The flux lines within the PM are essentially parallel to the direction of the magnetisation. The flux lines are essentially radial in the airgap. The finite element solution supports the assumptions made above.

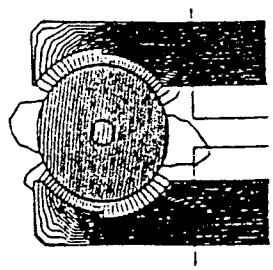

Figure 4.13 Finite element solution of the PM field for a conventional 2-pole motor (reproduced form Fig. 6(b) of [Altenbernd 1991]).

4.7.3.2 Approximation of the Magnitude of the PM Flux Density

Following the assumptions made in section 3.5.2, the magnitude of the PM flux density corresponding to a contour of flux linking both PM and airgap regions is given by eqn. 3.11:

$$B_{m_C} = \frac{B_r}{1 + \frac{dA_m}{dA_g}\frac{l_g}{l_m}\mu_r}$$

Fig. 4.12 shows that the ratio dA_m/dA_g varies around the rotor surface. At the rotor d-axis $dA_m/dA_g = 1$, but this ratio reduces to zero at the rotor q-axis. The assumption that $dA_m/dA_g = 1$ around the whole surface of the rotor is made. This assumption results in the lowering of the flux density near the q-axis because the ratio l_g/l_m is large near the q-axis. In the vicinity of the q-axis region, a significant proportion of the PM flux does not link the stator winding. This leakage flux may not follow a radial path and leaks from the N-pole to the S-pole. The assumption that $dA_m/dA_g = 1$ reduces the flux linkage contribution from this region. With this assumption, the magnitude of the flux density for all contours is

$$B_m = \frac{B_r}{1 + \frac{l_g}{l_m}\mu_r} \tag{4.83}$$

4.7.3.3 A Model of the PM Flux Linkage

Fig. 4.14 shows a representation of the unidirectional motor used for the calculation of the PM flux linkage. PM sectors rather than arcs are drawn. In practice, arcs are used because space is required for the rotor shaft. However, the error in using sectors is typically small. This is because the difference in B is very small due to the typically large ratios of PM to airgap length in practical designs.

In an analogous manner to the example of section 4.7.2, the surface of integration extends around the surface of a rotor pole. Angles θ_1, θ_2, and θ_s are similarly referenced to the rotor. The PM displacement angle γ_r is referenced to the d-axis of the stator turn. γ_r is the angle between the d-axis of the stator turn and the minimum of the

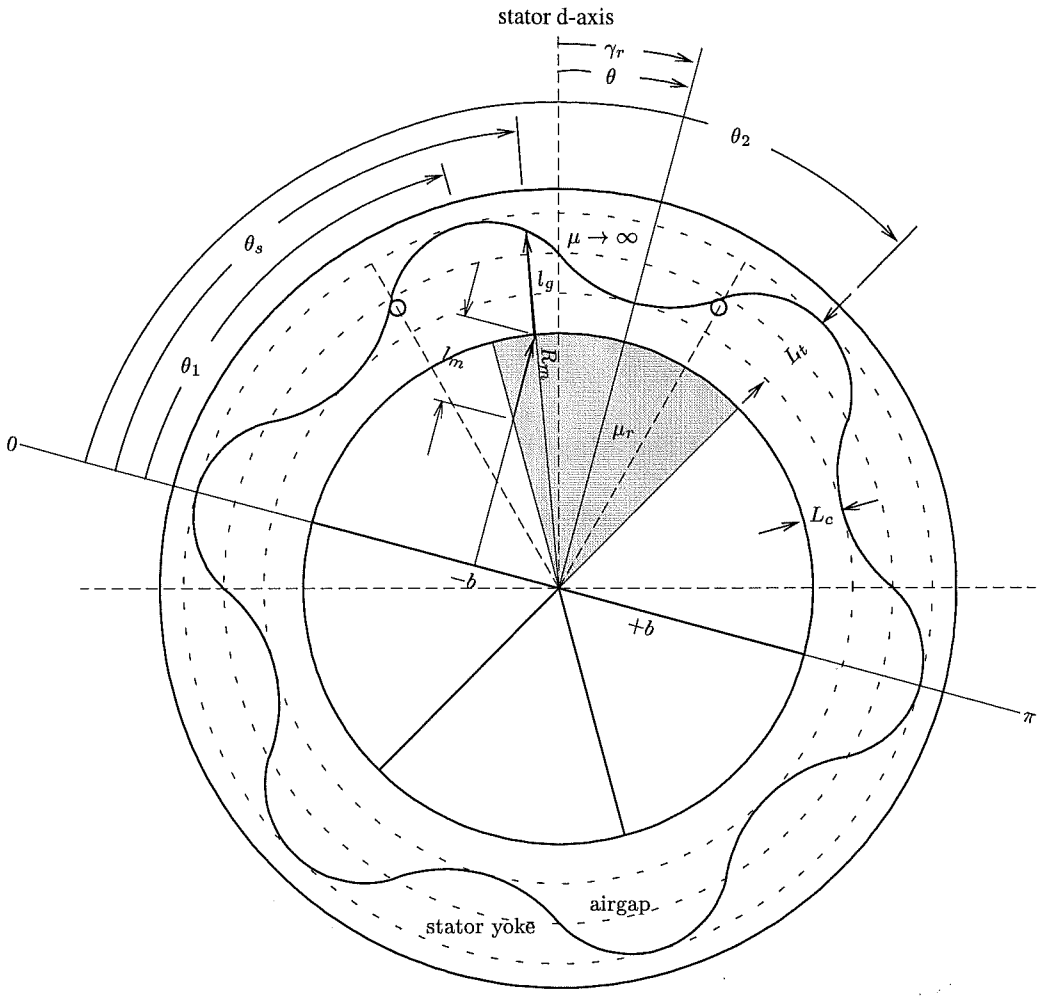

Figure 4.14 Representation of the unidirectional motor for the calculation of the PM flux linkage. (In this drawing, $p = 3$, $\gamma_r = \pi/4p$, and $\theta = \pi/4p$.)

airgap modulation, as shown in Fig. 4.14. γ_r has an arbitrary value.

With reference to Fig. 4.14, the airgap modulation is given by

$$l_g = L_c + L_t/2\Big[1 - (-1)^p \cos 2p(\theta_s + \theta - \gamma_r)\Big] \tag{4.84}$$

and the PM length parallel to the magnetisation within a sector is given by

$$l_m = R_m\Big(\sin\theta_s - \tan(\theta_1)|\cos\theta_s|\Big) \tag{4.85}$$

The flux density across the sector is determined by substitution of eqn.s 4.84 and 4.85 into eqn. 4.83. $\mathbf{B}\cdot\mathbf{n}$ is given by eqn. 4.75, and da is given by eqn. 4.71. $\mathbf{B}\cdot\mathbf{n}\,da$ is then given by

$$L_{stk}R_m B_m \sin\theta_s d\theta_s = B_r L_{stk} R_m \left(\frac{l_m}{l_m + l_g\mu_r}\right)\sin\theta_s\, d\theta_s \tag{4.86}$$

The flux linkage per turn is obtained by applying the integration limits of eqn. 4.72:

$$\phi_m = B_r L_{stk} R_m \left[\int_{\theta_1}^{\theta_2-\theta} \left(\frac{l_m}{l_m + l_g \mu_r} \right) \sin\theta_s \, d\theta_s - \int_{\theta_2-\theta}^{\theta_2} \left(\frac{l_m}{l_m + l_g \mu_r} \right) \sin\theta_s \, d\theta_s \right] \quad 0 \leq \theta \leq \pi/p \tag{4.87}$$

After the substitution of eqn.s 4.84, 4.85, 4.68, and 4.69, eqn. 4.87 cannot be integrated analytically and is integrated numerically.

4.7.3.4 Numerical Analysis

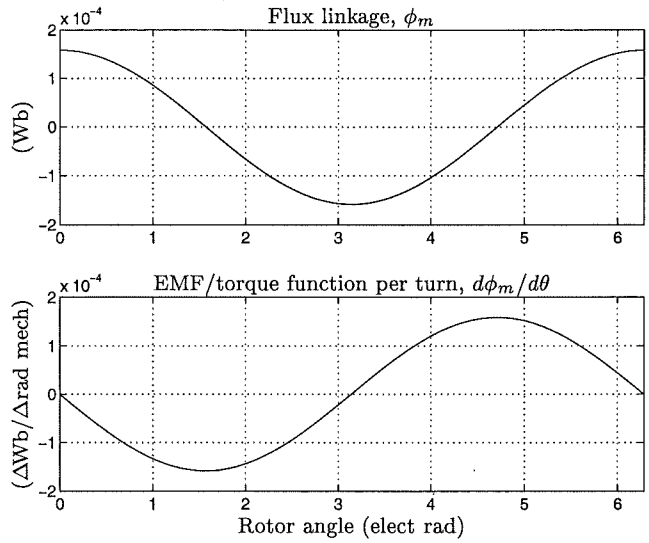

Figure 4.15 ϕ_m and $\frac{d\phi_m}{d\theta}$ for constant flux density and $p = 1$. ($B_m = B_r = 0.66$ T, $R_m = 6$ mm, $L_{stk} = 20$ mm).

This section presents an analysis of the flux linkage of the parallel magnetised motor using eqn. 4.87. A single set of motor parameters is used corresponding to the single pole pair unidirectional motor design. This design uses bonded Nd-Fe-B magnets. The pole pair number is varied to demonstrate its influence on the flux linkage.

Fig. 4.15 plots the flux linkage per turn ϕ_m, and the EMF/torque function per turn $\frac{d\phi_m}{d\theta}$, for the single pole pair case where the PM flux density is constant. The PM flux density is set to the value of the remanence. The waveforms are sinusoidal and contain no harmonics. The amplitudes correspond to $\hat{\phi}_m = 2BL_{stk}R_m \sin(\pi/2p)$ and $\frac{d\hat{\phi}_m}{d\theta} = 2BL_{stk}R_m$, as given in Fig. 4.11.

Fig. 4.16 plots ϕ_m and $\frac{d\phi_m}{d\theta}$ for a pole pair number of three. The waveforms vary over the first half cycle in shape and amplitude in accordance with Fig. 4.11. $\frac{d\hat{\phi}_m}{d\theta}$ is the same as for $p = 1$. $\frac{d\phi_m}{d\theta}$ closely approximates a square-wave. The frequency spectrum of $\frac{d\phi_m}{d\theta}$ is plotted up to the 10th harmonic. The magnitude of each harmonic is normalised to the magnitude of the fundamental. Even harmonics are zero and the

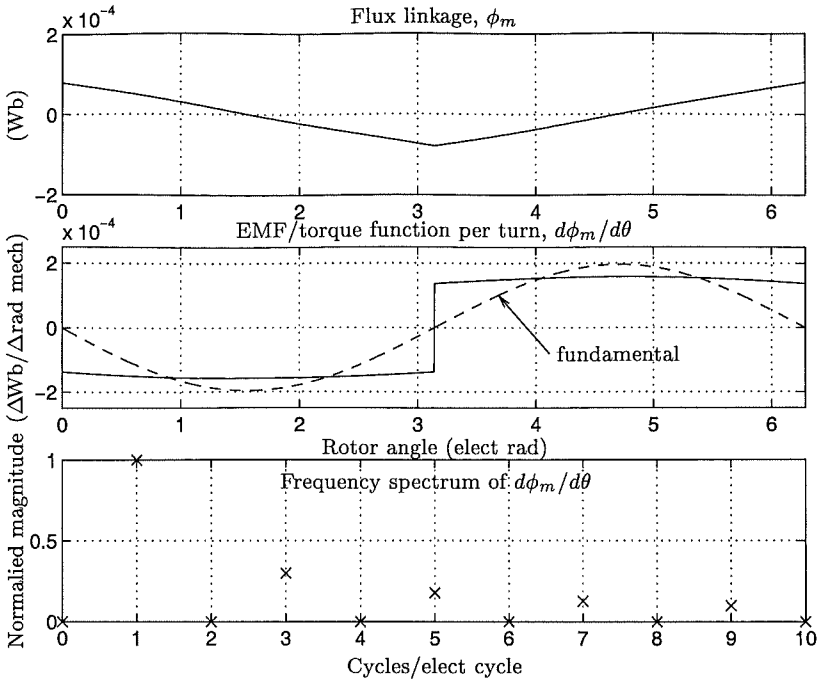

Figure 4.16 ϕ_m and $\frac{d\phi_m}{d\theta}$ for constant flux density and $p = 3$. ($B_m = B_r = 0.66$ T, $R_m = 6$ mm, $L_{stk} = 20$ mm).

spectrum closely approximates the square-wave spectrum of eqn. 4.82. For example, the normalised magnitude of the third harmonic is 0.3. For a square-wave, this value is 1/3.

The fundamental component of the EMF/torque function, $d\phi_{m1}/d\theta$, is also plotted. Amplitude $\frac{d\hat{\phi}_{m1}}{d\theta}$ is larger than it is for $p = 1$ by the ratio $\frac{d\hat{\phi}_{m1}}{d\theta_{(p=3)}} / \frac{d\hat{\phi}_m}{d\theta_{(p=1)}} = 1.24$. This is very close to the maximum theoretical ratio. The maximum theoretical ratio corresponds to a square-wave where $p = \infty$ and is $\frac{d\hat{\phi}_{m1}}{d\theta_{(p=\infty)}} / \frac{d\hat{\phi}_m}{d\theta_{(p=1)}} = \frac{4}{\pi}$. The effect of the increase of $\frac{d\hat{\phi}_{m1}}{d\theta}$ as a function of p is demonstrated by the following example. The phase-magnet torque corresponding to the fundamental components of the current and the EMF/torque function is given by

$$T^1_{ph-m} = i_1 N \frac{d\hat{\phi}_{m1}}{d\theta} \tag{4.88}$$

If the total number of turns N and current i_1 remain constant, and the pole pair number is increased, the phase-magnet torque increases by up to a factor of $4/\pi$. This increase is a result of the parallel magnetisation becoming a better approximation of a radial magnetisation as the number of pole pairs increases.

In practice, the PM flux density is not constant. Fig.s 4.17 to 4.19 demonstrate how variation in the PM flux density affects the shape of the EMF/torque function for a parallel magnetisation. In these Figures, the airgap length is constant and corresponds to the airgap clearance. Fig. 4.17 plots the PM flux densities corresponding to $p = 1$

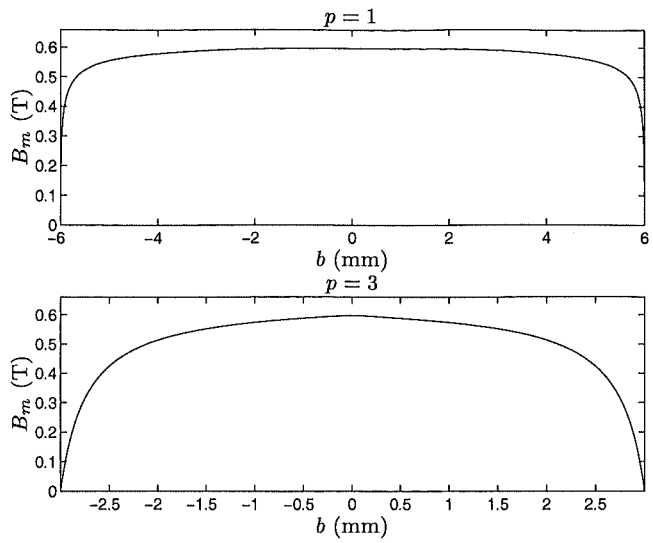

Figure 4.17 PM flux density perpendicular to the magnetisation for constant airgap length. (B_r = 0.66 T, R_m = 6 mm, L_{stk} = 20 mm, L_c = 0.5 mm, μ_r = 1.25).

and $p = 3$. The PM flux density B_m is plotted across the rotor pole perpendicular to the magnetisation. b is defined in Fig. 4.14 and is perpendicular to the magnetisation. $B_m(\theta_s)$ is obtained using eqn. 4.83 by setting $l_g = L_c$, and by substituting eqn. 4.85 for l_m. To plot B_m versus b, θ_s and b are related by

$$b = -R_m \cos\theta_s \tag{4.89}$$

In both plots B_m is lower than B_r. The reduction in B_m is most significant for $p = 3$. The PM length parallel to the magnetisation, l_m, is defined in Fig. 4.14. For $p = 3$, l_m decreases more rapidly towards each end of the PM pole. This causes the greater fall off in B_m towards each side of the pole.

Fig. 4.18 shows how the variation in the flux density for a pole pair number of one affects ϕ_m and $\frac{d\phi_m}{d\theta}$. In comparison to Fig. 4.15, the amplitudes of ϕ_m and $\frac{d\phi_m}{d\theta}$ are reduced. The variation in B_m has the effect of adding a small harmonic content. This comprises a small contribution from the third harmonic and almost negligible contributions from higher order harmonics.

Fig. 4.19 shows how the variation in B_m for a pole pair number of three affects ϕ_m and $\frac{d\phi_m}{d\theta}$. With non constant B_m, higher order harmonics are significantly reduced in comparison to Fig. 4.16. The third harmonic is reduced from a normalised magnitude of 0.3 to 0.2. In this multiple pole pair example, the variation of the PM flux density through the pole is identified as a significant means of improving the sinusoidal shape of the EMF/torque function.

For the unidirectional motors, the influence of the airgap modulation must also be examined. The airgap modulation is described by parameters L_t and γ_r. The effect of increasing L_t is to decrease $\frac{d\phi_m}{d\theta}$. This occurs because increasing L_t increases the

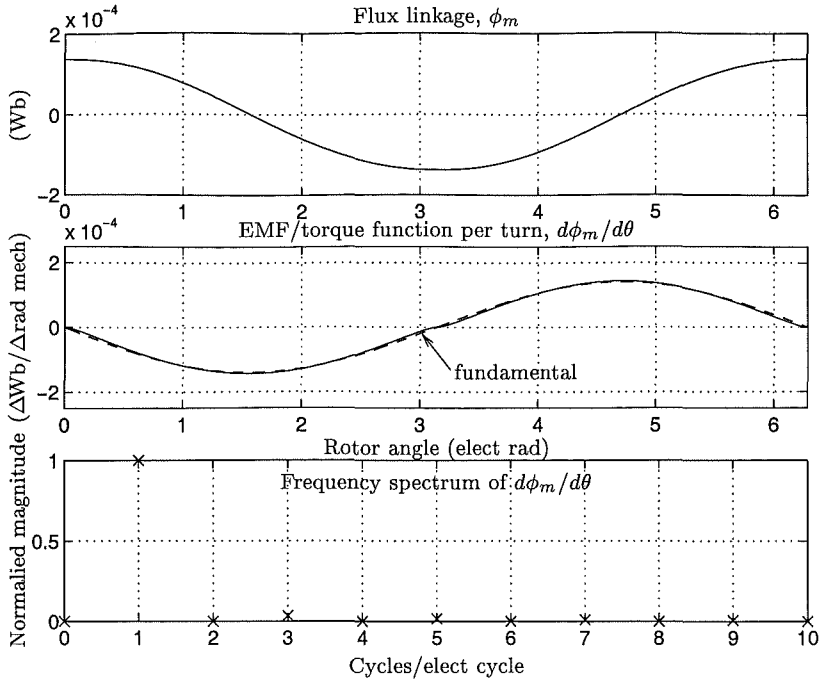

Figure 4.18 ϕ_m and $\frac{d\phi_m}{d\theta}$ for constant airgap length and $p = 1$. ($B_r = 0.66$ T, $R_m = 6$ mm, $L_{stk} = 20$ mm, $L_c = 0.5$ mm, $\mu_r = 1.25$).

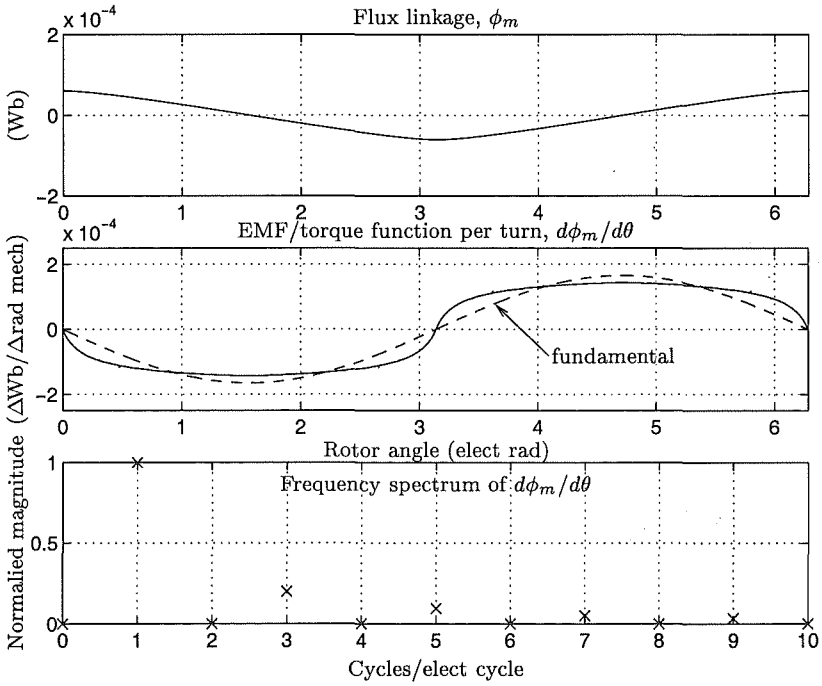

Figure 4.19 ϕ_m and $\frac{d\phi_m}{d\theta}$ for constant airgap length and $p = 3$. ($B_r = 0.66$ T, $R_m = 6$ mm, $L_{stk} = 20$ mm, $L_c = 0.5$ mm, $\mu_r = 1.25$).

average airgap relative to the stator d-axis.

Fig. 4.20 illustrates how γ_r affects the airgap relative to the d-axis of the stator turn. Fig. 4.21 shows ϕ_m and $\frac{d\phi_m}{d\theta}$ for a single pole pair motor having a large airgap

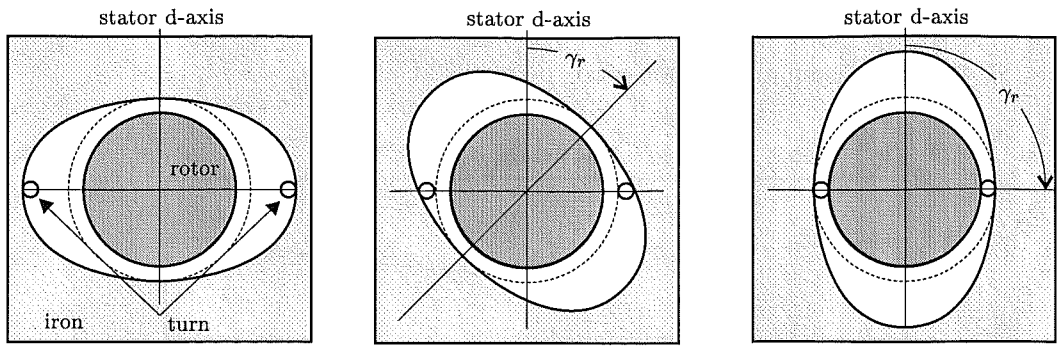

(a) $\gamma_r = 0$ (b) $\gamma_r = \pi/4$ (c) $\gamma_r = \pi/2$

Figure 4.20 Sinusoidal airgap modulation corresponding to various values of γ_r for a single pole pair motor.

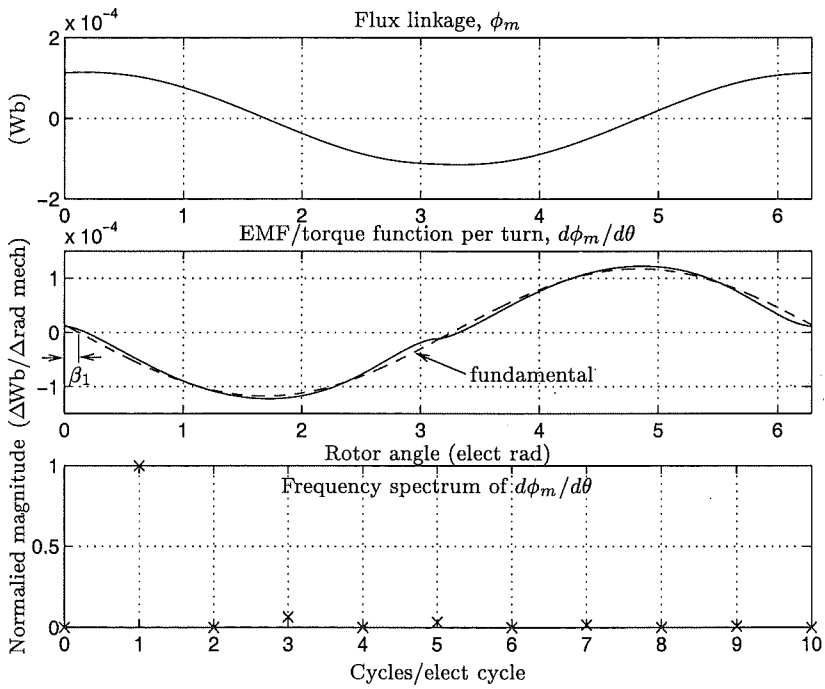

Figure 4.21 ϕ_m and $\frac{d\phi_m}{d\theta}$ for airgap modulation and $p = 1$. ($B_r = 0.66$ T, $R_m = 6$ mm, $L_{stk} = 20$ mm, $L_c = 0.5$ mm, $\mu_r = 1.25$, $L_t = 2$ mm, $\gamma_r = \pi/4$).

modulation where $\gamma_r = \pi/4$ and $L_t/R_m = 1/3$. $\hat{\phi}_m$ is reduced due to the larger airgap. Comparison of Fig. 4.21 to Fig. 4.18 shows that the shape of $\frac{d\phi_m}{d\theta}$ is largely unaffected by the airgap modulation. However, a phase shift of both $\frac{d\phi_m}{d\theta}$ and its fundamental component occurs. Because higher order harmonics are small, the EMF/torque function for the single pole pair unidirectional motor is modelled by only its fundamental component. The fundamental component is described by its amplitude $\frac{d\hat{\phi}_{m1}}{d\theta}$ and phase angle β_1.

For the single pole pair motor, $\frac{d\phi_m}{d\theta}$ remains closely sinusoidal over the range

$0 \leq \gamma_r \leq \pi/2$. The parallel magnetisation remains the dominant waveform shaping mechanism. At $\gamma_r = 0$ and at $\gamma_r = \pi/2$, phase angle β_1 is zero. Within the range $0 < \gamma_r < \pi/2$, β_1 is small but non-zero. β_1 peaks at about $\gamma_r = \pi/4$.

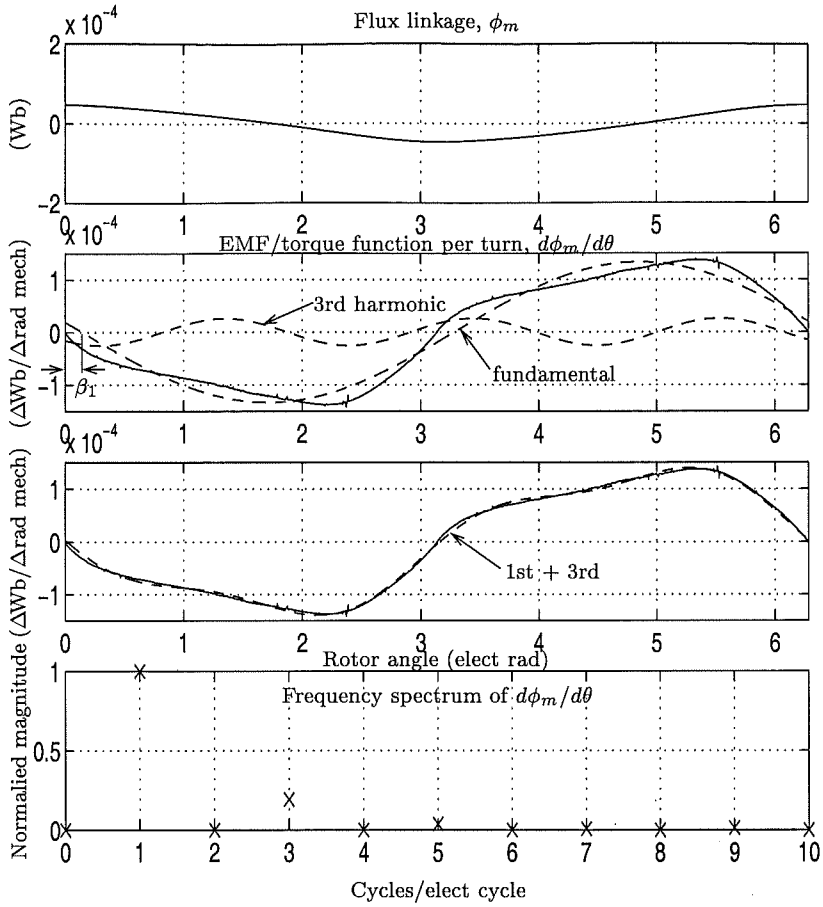

Figure 4.22 ϕ_m and $\frac{d\phi_m}{d\theta}$ for airgap modulation and $p = 3$. ($B_r = 0.66$ T, $R_m = 6$ mm, $L_{stk} = 20$ mm, $L_c = 0.5$ mm, $\mu_r = 1.25$, $L_t = 2$ mm, $\gamma_r = \pi/4$).

Fig. 4.22 shows ϕ_m and $\frac{d\phi_m}{d\theta}$ for a pole pair number of three and airgap modulation. The fundamental and third harmonic components of $\frac{d\phi_m}{d\theta}$ are also plotted. The harmonic spectrum shows that harmonics above the third are almost negligible. The third harmonic remains significant. Therefore $\frac{d\phi_m}{d\theta}$ for the multiple pole unidirectional motor is modelled by its fundamental and third harmonic components. These components are described by $\frac{d\hat{\phi}_{m1}}{d\theta}$, β_1, $\frac{d\hat{\phi}_{m3}}{d\theta}$, and phase angle β_3. A reconstructed waveform consisting of the fundamental and the third harmonic components is plotted along with $\frac{d\phi_m}{d\theta}$. The reconstructed waveform provides a good approximation of $\frac{d\phi_m}{d\theta}$.

For pole pair numbers higher than one, variation in the PM flux density across the pole becomes a dominant waveform shaping mechanism. This is due predominantly to the airgap modulation. γ_r has a strong influence on the shape of $\frac{d\phi_m}{d\theta}$ over the range $0 \leq \gamma_r/p \leq \pi/2p$. The harmonic content increases as γ_r increases. For $p = 3$ and $\gamma_r = 0$, for example, $\frac{d\phi_m}{d\theta}$ is closely triangular but has curved peaks. As γ_r increases,

$\frac{d\phi_m}{d\theta}$ transforms into a flat topped trapezoid with rounded edges occurring at $\gamma_r = \pi/2p$.

For the unidirectional motor, only a value of about $\gamma_r = \pi/4p$ is of use. Only this value achieves the desired PM reluctance torque displacement. The effects of the phase shift and harmonics in $\frac{d\phi_m}{d\theta}$ are addressed in sections 4.9 and 4.10.

4.8 ANALYSIS OF THE PM RELUCTANCE TORQUE

This section determines the PM reluctance torque of a unidirectional motor having an arbitrary number of pole pairs. The aim of the analysis is to provide a fast 'ball-park' estimate of the reluctance torque. In an identical manner to section 4.7.3.3, the rotor poles consist of PM sectors and the airgap is modulated sinusoidally.

The energy method of section 3.5 is used to determine the PM reluctance torque. The reluctance torque is calculated after first obtaining the stored field energy with all windings de-energised, $W(i = 0)$. The PM reluctance torque is given by eqn. 2.13:

$$T_r = -\frac{dW(i=0)}{d\theta}$$

The stator iron is again assumed to be infinitely permeable such that the energy stored in this region is negligible. The stored energy is then obtained from contributions from the PM rotor and the airgap. These contributions are integrated over the respective PM rotor and airgap volumes according to eqn. 3.3:

$$W(i=0) = \int_{V_m} w_m \, dv_m + \int_{V_a} w_a \, dv_a$$

where w_m and w_a are the energy density functions of the PM material and the airgap, respectively. As discussed in section 4.7.3.1, the flux density within the PM material is assumed to be parallel to the magnetisation. For a PM material modelled by a linear major demagnetisation characteristic, the stored energy density is then given as a function of the flux density by eqn. 3.4:

$$w_m = \frac{(B_m - B_r)^2}{2\mu_o\mu_r}$$

The approximations of the direction and magnitude of the PM flux density, described in sections 4.7.3.1 and 4.7.3.2, allow an elementary expression for B_m to be obtained.

The stored energy density within the airgap is given by eqn. 3.2:

$$w_a = \frac{B_a^2}{2\mu_o}$$

End effects are ignored such that the flux and energy densities are assumed to remain constant in the axial direction. This allows the volume integration of the stored

energy to be simplified to a double integration over a transverse section of the rotor and the airgap. Cylindrical coordinates are used and the stored energy is given, in general, by

$$W = z \int \int w(r, \theta_s) r \, dr \, d\theta_s \tag{4.90}$$

The cylindrical coordinates are r, θ_s, and z. $w(r, \theta_s)$ is the energy density function. The active magnetic length of the rotor is assumed to correspond to the length of the stator stack. The axial coordinate z is therefore constant and is set equal to the stack length.

Equations for the stored energy in the airgap and the PM rotor are derived separately in sections 4.8.1 and 4.8.2.

4.8.1 Airgap Energy

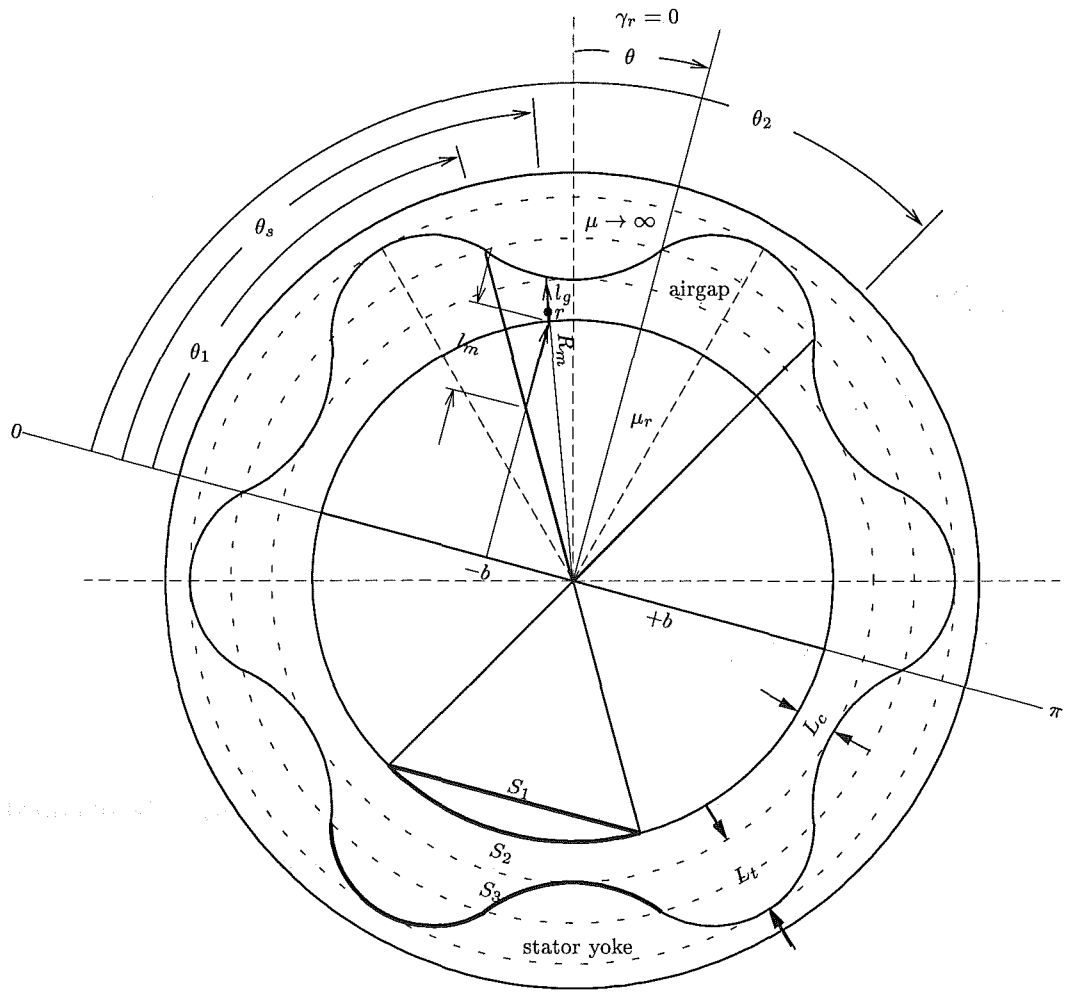

Figure 4.23 Representation of the unidirectional motor for the calculation of the stored airgap energy. (In this drawing, $p = 3$, and $\theta = \pi/4p$.)

The stored energy corresponding to the airgap of the unidirectional motor is derived with reference to Fig. 4.23. Fig. 4.23 is almost identical to Fig. 4.14 except that the PM reluctance torque displacement angle γ_r is set to zero and the stator conductors are not shown. The simplification obtained by setting $\gamma_r = 0$ does not effect the magnitude nor the shape of the PM reluctance torque. The integration of the airgap energy is performed in the airgap region above a single PM rotor pole sector. The total airgap energy is then obtained by multiplying the integrated energy by the number of poles. First, airgap densities B_a and w_a are derived as a function of coordinates r and θ_s. At the rotor pole surface the airgap flux density is given according to eqn. 4.75 by

$$B_a(r=R_m, \theta_s) = B_m \sin\theta_s \tag{4.91}$$

The flux density within the PM sector lying parallel to the magnetisation, B_m, is derived identically to section 4.7.3. B_m is obtained from eqn.s 4.83, 4.84, and 4.85 with $\gamma_r = 0$.

Expressions for the flux density throughout the airgap and PM rotor volumes, and therefore also the corresponding energy densities, are more accurate if div $\mathbf{B} = 0$. Cross-sections of surfaces S_1, S_2, and S_3 are drawn in Fig. 4.23. Each surface spans the pitch of the pole. Surface S_1 spans the surface of the PM sector perpendicular to the PM flux density B_m. S_2 spans the airgap surface of the PM sector perpendicular to the airgap flux density B_a. S_3 spans the airgap surface of the stator yoke. If

$$\int_S \mathbf{B} \cdot \mathbf{n}\, da = \text{constant} \tag{4.92}$$

for each of these surfaces, div $\mathbf{B} = 0$ is likely to be satisfied in the PM sector and in the airgap. Substitution of eqn.s 4.91 and 4.71 into eqn. 4.92 demonstrates that eqn. 4.91 satisfies div $\mathbf{B} = 0$ at the airgap surface of the PM sector: the pole surface flux is equal to the flux within the PM sector.

An expression for $B_a = B_a(r, \theta_s)$ corresponding to any coordinate within the airgap must also satisfy div $\mathbf{B} = 0$. For the element of airgap area defined by

$$da = L_{stk} r\, d\theta_s \qquad\qquad r \geq R_m, \tag{4.93}$$

the radial flux density is parallel to the unit normal vector such that $\mathbf{B} \cdot \mathbf{n} = B_a(r, \theta_s)$. $\mathbf{B} \cdot \mathbf{n}\, da$ is then equal to $B_a(r, \theta_s) L_{stk} r\, d\theta_s$. If θ_s and $d\theta_s$ are held constant, div $\mathbf{B} = 0$ is satisfied if

$$B_a(r, \theta_s) L_{stk} r\, d\theta_s = B_a(r=R_m, \theta_s) L_{stk} R_m\, d\theta_s \tag{4.94}$$

or, by substitution of eqn. 4.91 into eqn. 4.94:

$$B_a(r,\theta_s) = B_m \sin\theta_s \frac{R_m}{r} \tag{4.95}$$

After substitution for B_m, the airgap flux density is given by

$$B_a = \left(\frac{B_r \sin\theta_s}{1 + \dfrac{L_c + L_t/2\Big(1-(-1)^p \cos\left[2p(\theta_s+\theta)\right]\Big)}{R_m\Big(\sin\theta_s - \tan\theta_1 |\cos\theta_s|\Big)}\mu_r} \right) \frac{R_m}{r} \tag{4.96}$$

The total airgap energy is obtained from

$$W_a = 2pL_{stk} \int_{\theta_1}^{\theta_2} \int_{R_m}^{R_m+L_c+L_t/2\left(1-(-1)^p\cos[2p(\theta_s+\theta)]\right)} w_a(r,\theta_s) r\, dr\, d\theta_s \tag{4.97}$$

The values of the integration limits θ_1 and θ_2 are arbitrary and may correspond to either a short pitched or full pitched PM pole. For the unidirectional motor, the rotor poles are full pitched and θ_1 and θ_2 are given by eqn.s 4.68 and 4.69, respectively:

$$\theta_1 = \frac{\pi}{2} - \frac{\pi}{2p}$$

$$\theta_2 = \frac{\pi}{2} + \frac{\pi}{2p}$$

Eqn. 4.97 cannot be integrated analytically, and is integrated numerically.

4.8.2 PM Rotor Energy

With reference to Fig. 4.24, the PM flux density at coordinate (r,θ_s) is given by

$$B_m(r,\theta_s) = \frac{B_r}{1 + \dfrac{l'_g}{l'_m}\mu_r} \qquad 0 \le r \le R_m, \quad \theta_1 \le \theta_s \le \theta_2 \tag{4.98}$$

where

$$l'_g = L_c + L_t/2\Big(1-(-1)^p \cos\left[2p(\theta'_s+\theta)\right]\Big) \tag{4.99}$$

$$l'_m = \sqrt{R_m^2 - r^2\cos^2\theta_s} - r|\cos\theta_s|\tan\theta_1 \tag{4.100}$$

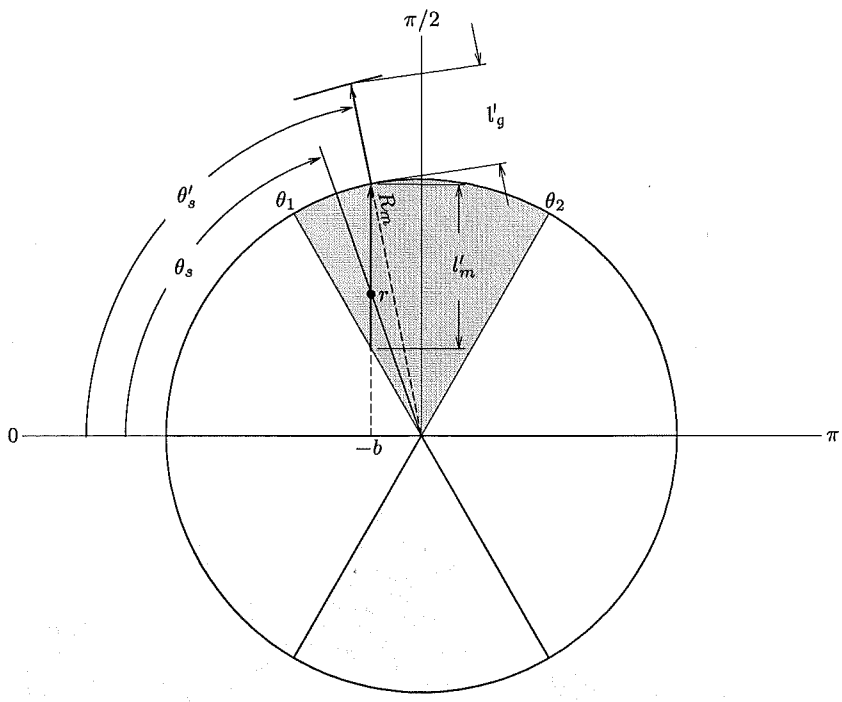

Figure 4.24 Representation of a rotor pole sector for the calculation of the stored rotor energy. (In this drawing, $p = 3$.)

and

$$\theta'_s = \arccos\left(\frac{r}{R_m}\cos\theta_s\right) \tag{4.101}$$

For any line parallel to the magnetisation within the pole sector, the PM flux density, obtained by eqn. 4.98 corresponding to any coordinate (r, θ_s) on the line, remains constant. Substitution of eqn.s 4.98 -4.101 into eqn. 3.4 obtains the energy density function $w_m(r, \theta_s)$. The total rotor airgap energy is then given by

$$W_m = 2pL_{stk}\int_{\theta_1}^{\theta_2}\int_0^{R_m} w_m(r, \theta_s) r\, dr\, d\theta_s \tag{4.102}$$

The values of the integration limits θ_1 and θ_2 are the same as those used for determining the airgap energy. Eqn. 4.102 cannot be integrated analytically, and is integrated numerically.

4.8.3 Numerical Analysis

For the analysis of the PM reluctance torque, a single set of motor parameters is used. The set of motor parameters corresponds to the single pole pair unidirectional motor design. This design uses bonded Nd-Fe-B magnets. The pole pair number is varied to demonstrate its influence on the PM reluctance torque.

Fig.s 4.25 -4.27 illustrate examples of how the flux density and the stored energy

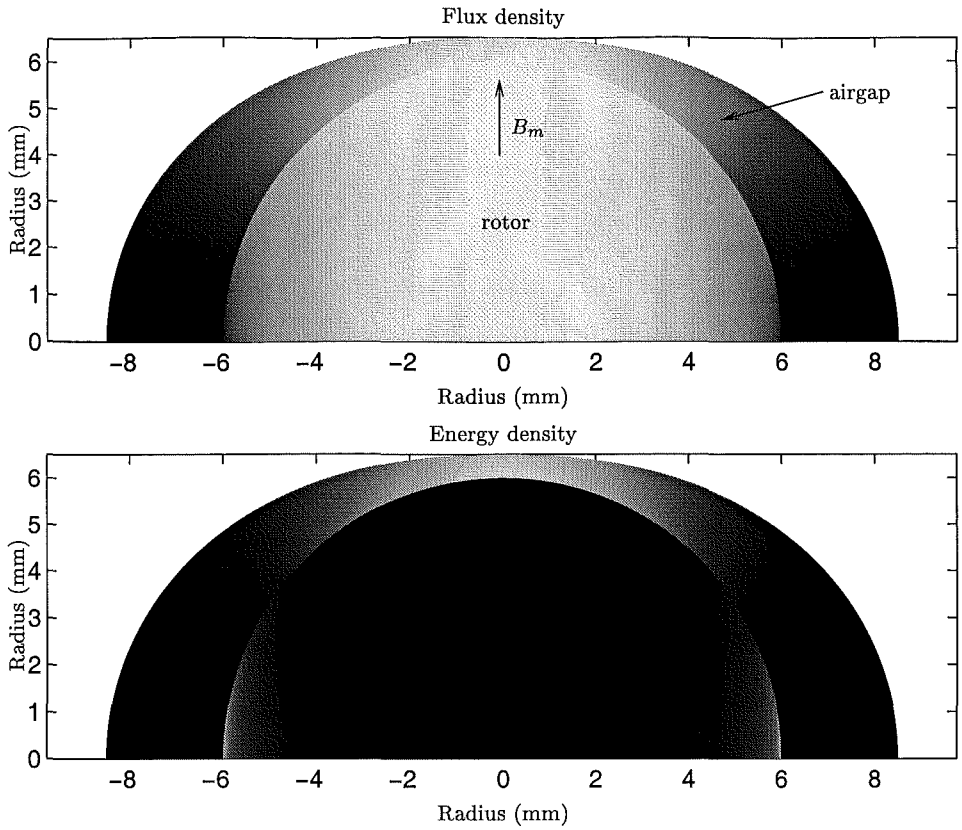

Figure 4.25 Flux and stored energy densities plotted in greyscale over a pole sector, corresponding to $p = 1$ and $\theta = 0$. [Flux density greyscale: linear scaling from black to white corresponds to $B = 0$ to $B = B_r$. Energy density greyscale: black to white corresponds to $W = 0$ to $W = B_r^2/2\mu_o$]. The motor parameter values are $B_r = 0.66$ T, $\mu_r = 1.25$, $R_m = 6$ mm, $L_c = .5$ mm, $L_t = 2$ mm.

density vary across the rotor pole sector and the airgap according to the model developed. Fig. 4.25 plots the flux density and energy density for the single pole pair unidirectional motor corresponding to rotor position $\theta = 0$ defined in Fig. 4.23. Half the rotor and half the airgap are plotted corresponding to a single pole sector. The airgap flux density is plotted using eqn. 4.96. The PM flux density is plotted using eqn. 4.98. The flux densities in the airgap and in the PM are normalised to the maximum possible flux density corresponding to the PM remanence B_r. Pure white corresponds to $B = B_r$ and pure black corresponds to $B = 0$. The outline of the PM rotor is clearly discernible around most of its half circle circumference. This is due to the difference in the PM and airgap flux densities. This difference is caused by the sinusoidal variation of the airgap flux density around the rotor circumference, which is required to satisfy div $\mathbf{B} = 0$. About the angle of $\theta_s = \pi/2$, the difference is not clearly discernible because $\sin\theta_s$ is approximately unity. The PM flux density is constant parallel to the magnetisation. The PM flux density is greatest at $\theta_s = \pi/2$ where the PM length is longest and the airgap length is shortest. The airgap flux density decreases in inverse proportion to the radial airgap distance.

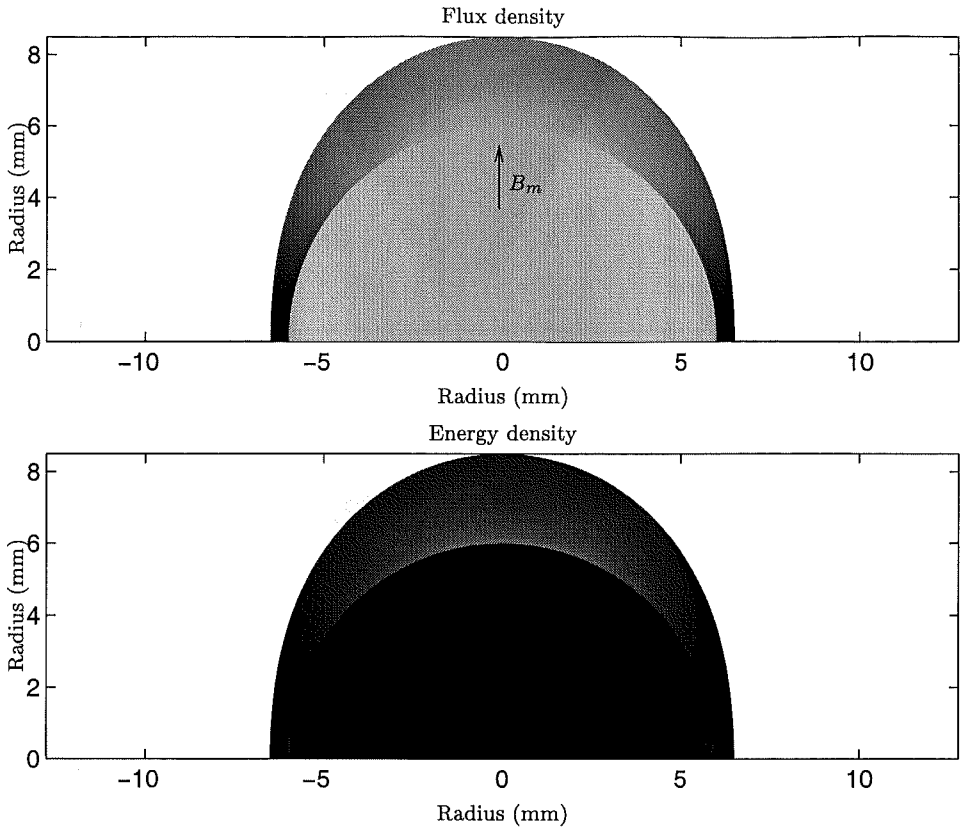

Figure 4.26 Flux and stored energy densities corresponding to $p = 1$ and $\theta = \pi/2$. The greyscaling and parameter values of Fig. 4.25 are used.

The stored energy density is normalised to the maximum theoretical value of $B_r^2/2\mu_o$. This energy density cannot be exceeded in neither the airgap nor the PM. In most regions the energy density is considerably lower than this value. Pure white corresponds to $W = B_r^2/2\mu_o$ and pure black corresponds to $W = 0$. The airgap/rotor boundary is clearly discernible. This is due to the contrary nature of the airgap and PM energy density functions: the PM energy density is high if the flux density is low, but the airgap energy density remains low if the flux density is low. A sharper contrast also occurs within each of the PM and airgap regions due to the quadratic nature of both energy density functions.

Fig. 4.26 plots the flux and energy densities for the single pole pair example corresponding to $\theta = \pi/2$. The flux density within the PM is reduced by the larger airgap and remains reasonably uniform. Most of the stored energy is concentrated in the airgap.

Fig. 4.27 plots the flux and energy densities corresponding to a pole pair number of three and rotor position $\theta = 0$. The flux and energy density distributions are similar to those of the single pole pair example of Fig. 4.25. The PM flux density towards each end of the pole decreases more rapidly than the single pole pair example because of the greater decrease in the PM sector length parallel to the magnetisation. This yields

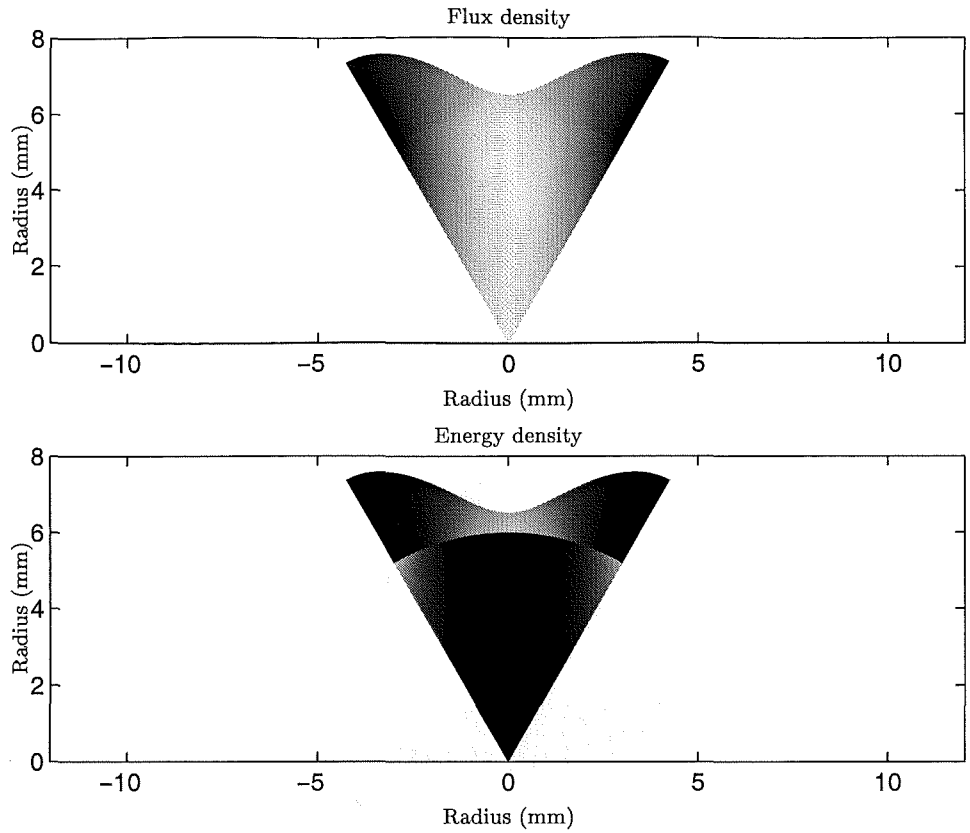

Figure 4.27 Flux and stored energy densities corresponding to $p = 3$ and $\theta = 0$. The greyscaling and parameter values of Fig. 4.25 are used.

correspondingly higher energy densities at the ends.

As the pole pair number is increased above one, the model may become less accurate. This is demonstrated by a comparison of the flux density plots of Fig.s 4.25 and 4.27. If the airgap clearance is maintained constant, the ratio of the airgap area to the airgap length decreases. In both Figures, the airgap clearance remains fixed, and the ratio decreases for $p = 3$. The effect of the decrease of this ratio is to increase the influence of the edge effects at the rotor N-S pole interfaces. This reduces the uniformity of the flux density distribution and a greater proportion of the flux is leakage between poles.

The stator iron is modelled as being infinitely permeable. Therefore, flux lines correctly intercept the stator pole surface at a normal angle. Without airgap modulation, normal vectors to the stator pole surface are parallel to radial flux lines. The assumption of radial airgap flux lines is accurate in this case. With airgap modulation, most of the normal vectors are not parallel to radially directed flux lines. The angles between the normal vectors and the radial flux lines are typically small for the $p = 1$ case. The approximation of radial airgap flux lines still remains reasonable.

If the number of pole pairs is increased, the pole pitch decreases. The pitch over

which the airgap modulation occurs decreases by the same amount. The effect of decreasing the pitch is to increase the angle between the normal vectors to the stator pole surface and the radial airgap flux lines, if the amplitude of the airgap modulation remains constant. For the airgap shape of Fig. 4.27, significant curvature of most airgap flux lines is required to allow the flux lines to intercept the stator pole surface at a normal angle. Therefore, if the amplitude of the airgap modulation remains constant, the approximation of a radial airgap flux distribution becomes poorer as the pole pair number increases.

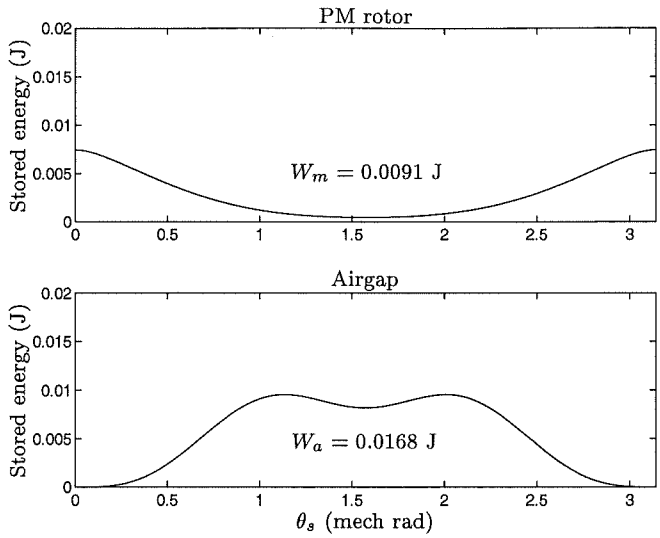

Figure 4.28 PM rotor pole and airgap stored energies, for $p = 1$ and $\theta = 0$. The combined PM and airgap energy per pole is $W(\theta = 0) = 0.0260$ J. ($B_r = 0.66$ T, $R_m = 6$ mm, $L_{stk} = 20$ mm, $L_c = 0.5$ mm, $\mu_r = 1.25$, $L_t = 2$ mm).

Fig. 4.28 plots the stored energy density of Fig. 4.25 after integration over coordinate r. The energy is plotted as a function of angle θ_s across the pole pitch. The PM and airgap energy distributions are plotted separately. The area under each curve corresponds to the total PM or airgap energy for a single pole. The energies corresponding to these areas are specified. At $\theta = 0$, the energy stored in the airgap is greater than that stored in the PM pole sector.

Fig. 4.29 plots the stored energy density of Fig. 4.26 after integration over r. At $\theta = \pi/2$, the energy stored in the airgap is also greater than the energy stored in the PM rotor. A comparison of Fig.s 4.28 and 4.29 shows that the energies stored in the PM rotor and the airgap both increase from $\theta = 0$ to $\theta = \pi/2$. At $\theta = 0$, the stored energy is minimised corresponding to the stable detent rotor position. At $\theta = \pi/2$, the stored energy is maximised corresponding to the unstable detent position. One half of a PM reluctance torque cycle is completed over this interval.

Fig. 4.30 plots the stored energy W and the PM reluctance torque T_r with respect to rotor position, for a pole pair number of one. The stored energy corresponds to the contributions of all poles. The frequency spectrum of T_r shows that the PM reluc-

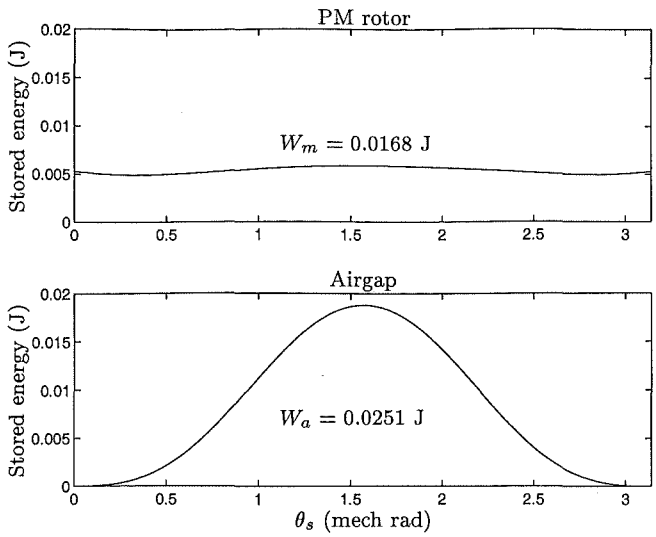

Figure 4.29 PM rotor pole and airgap stored energies, for $p = 1$ and $\theta = \pi/2$. The combined PM and airgap energy per pole is $W(\theta = \pi/2) = 0.0419$ J.

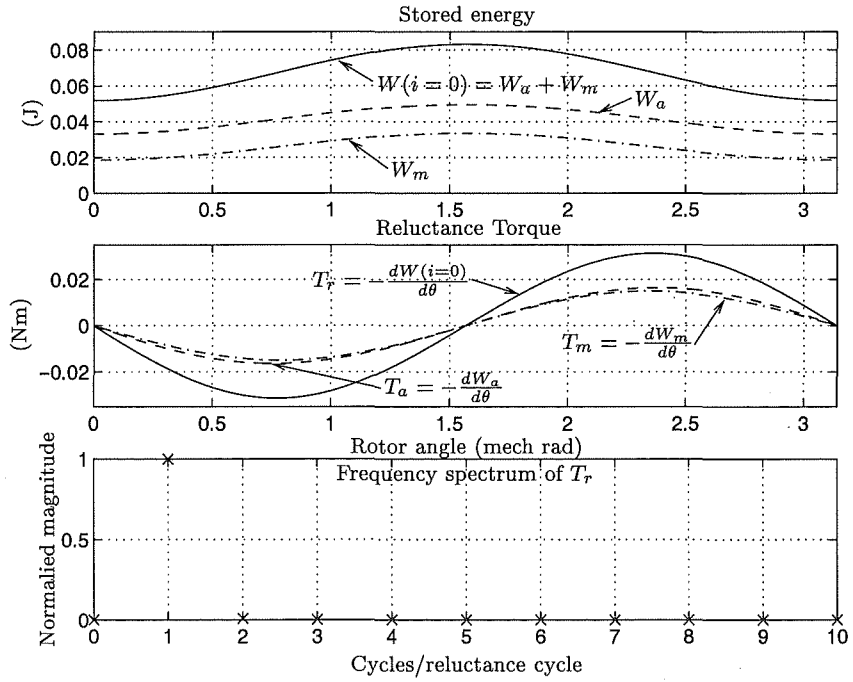

Figure 4.30 Stored energy and PM reluctance torque for $p = 1$. $\hat{W}_r = 0.0156$ J.

tance torque is an excellent approximation of a sinusoid. Higher order even and odd harmonics are present but these are negligible. The PM reluctance torque of the unidirectional motor for $p = 1$ is modelled by its fundamental component, and is given by eqn. 4.51. In this example, the airgap and the PM regions contribute similarly to the total reluctance torque. The airgap stores significantly more energy than the PM, but the differences in stored energy between $\theta = 0$ and $\theta = \pi/2$ for each region are similar. In Fig. 4.30, the amplitude of the total stored energy modulation is $\hat{W}_r = 0.0156$ J.

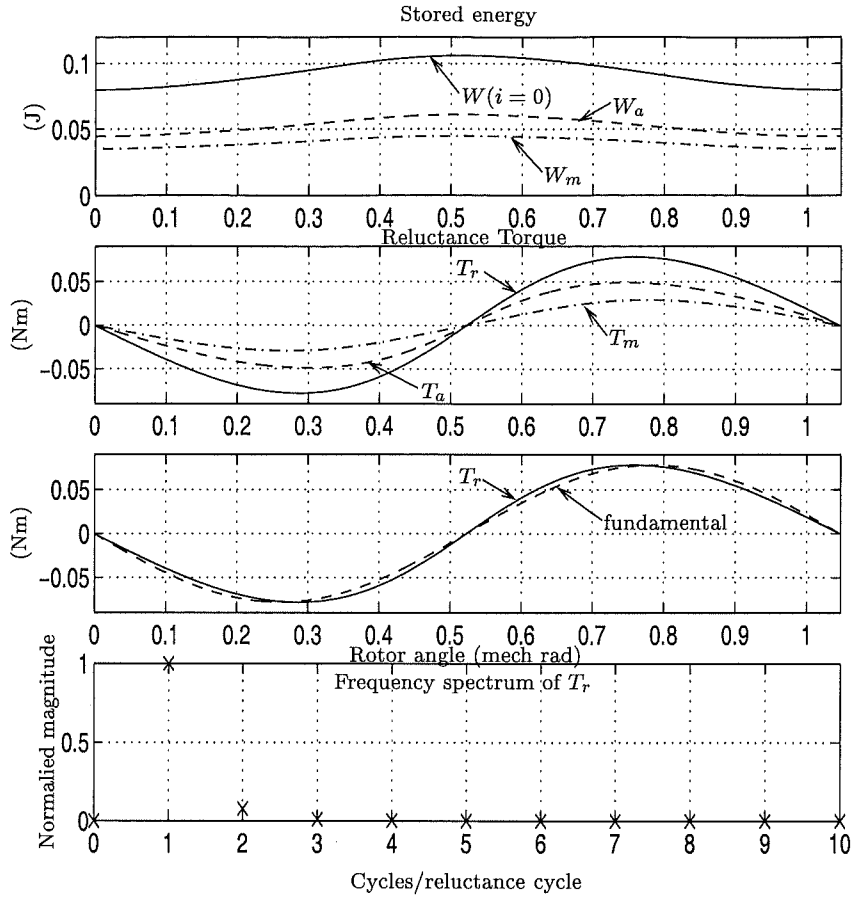

Figure 4.31 Stored energy and PM reluctance torque for $p = 3$. $\hat{W}_r = 0.0130$ J.

Fig. 4.31 plots the stored energy and PM reluctance torque for a pole pair number of three. The frequency spectrum of T_r shows that a small second harmonic is present. Higher order harmonics are negligible. T_r and its fundamental are also plotted. The torque is approximated reasonably well by the fundamental. Therefore, the PM reluctance torque for the multiple pole pair unidirectional motor is also modelled by eqn. 4.51.

4.9 A 2-POLE UNIDIRECTIONAL MOTOR DESIGN USING BONDED ND-FE-B MAGNETS

The previous sections of this chapter establish the theory of the unidirectional motor. A number of important design equations are developed. In section 4.6, a description of a manufacturable motor design is outlined. Theoretical models of the EMF/torque function and the PM reluctance torque, corresponding to this design, are developed in sections 4.7 and 4.8 respectively. These sections provide a foundation on which a unidirectional design can proceed.

In this section, the design of a 2-pole unidirectional motor using bonded Nd-Fe-

B rotor magnets is described. Estimates of performance parameters, and parameters required for simulation, are calculated. The motor is then simulated using the equations of motion to evaluate the success of the design. The aim is to produce a 'ballpark' design which provides a starting point for experimental investigation.

The design described in this section is the result of a number of design iterations. This began with a ferrite rotor design, which was then replaced with a Nd-Fe-B design. Various rotor diameters were tried for each of these PM materials. The success of each of these designs was determined by simulation. During this iterative design process, eqn. 4.66 emerged as a critical tool for estimating the success of a design in terms of attaining sufficient backward instability:

$$\frac{4\hat{W}_r p^2}{J\omega_e^2} > 1$$

The parameters of the backward instability ratio are obtained from only the design of the rotor and the rotor airgap. $\hat{W}_r$ is obtained by integrating the stored energy over only the volume of the rotor and the airgap. The moment of inertia of the rotor, J_r, contributes most significantly to the total inertia, J. An estimate of J can then be made by only considering the dimensions of the rotor and the density of the PM material used. Therefore, it is not necessary to begin the design of the stator until a satisfactory backward instability ratio has been obtained.

A 50 Hz supply frequency is selected, and $p = 1$. The selection of the rotor diameter D_r affects both J_r and $\hat{W}_r$. Eqn. 4.67 shows that $J_r \propto D_r^4$. $\hat{W}_r$ is proportional to the rotor volume, such that $\hat{W}_r \propto D_r^2$. The backward instability ratio is therefore proportional to the inverse square of the rotor diameter. A rotor diameter of $D_r = 12$ mm is selected for this design. The bonded Nd-Fe-B magnets specified in section 3.3.2.1 are used. A value of $B_r = 0.66$ T is used corresponding to an operating temperature of 60° C. As shown in section 3.6, $\hat{W}_r$ is proportional to the square of B_r. It then follows that

$$\frac{4\hat{W}_r p^2}{J\omega_e^2} \propto \frac{B_r^2}{D_r^2} \tag{4.103}$$

For single pole pair unidirectional motors with larger rotor diameters, higher grades of PM material may be required. An airgap modulation of $L_t = 2$ mm is selected with an airgap clearance of $L_c = 0.5$ mm. These values are selected such that the approximations made regarding the PM field remain reasonable. The shape and scale of the airgap relative to the rotor, corresponding to these values, is illustrated by Fig. 4.25. An axial rotor length of $L_r = 20$ mm is selected. The stack length is set equal to the rotor length, in accordance with the practice that rare earth magnets normally do not use overhang [Hendershot and Miller 1994, p. 3-23].

The PM reluctance torque corresponding to these parameters is plotted in Fig.

4.30. For this design, a value of $\hat{W}_r = 0.0163$ J is used. The amplitude of the PM reluctance torque, given by eqn. 4.52, is $\hat{T}_r = 2p\hat{W}_r = 0.0327$ Nm. Because the rated torque is set equal to the amplitude of the PM reluctance torque, $\overline{T} = 0.0327$ Nm. By neglecting friction and windage, the rated output power at 3000 RPM is $P_{out} = \overline{T}\omega_e = 10.3$ W. For $J = 2J_r$, the backward instability ratio is $\frac{4\hat{W}_r}{J\omega_e^2} = 1.36$.

4.9.1 The EMF/Torque Function

Ideally, for a unidirectional motor, $\gamma_r = \pi/4$ electrical radians. This establishes the phase relationship between T_r and $\frac{d\lambda_m}{d\theta}$ illustrated by Fig. 1.6. With $\gamma_r = \pi/4$, the orientation of the airgap modulation relative to the stator d-axis is shown by Fig. 4.20(b). With this airgap orientation, and for this design, the EMF/torque function per turn, $\frac{d\phi_m}{d\theta}$, is illustrated by Fig. 4.21. The fundamental component $\frac{d\phi_{m1}}{d\theta}$ is phase shifted by angle β_1. Simulation results show that with $\gamma_r = \pi/4$, the corresponding phase shifting of the fundamental component $\frac{d\lambda_{m1}}{d\theta}$ causes speed ripple at the rated load. This occurs because the phase-magnet torque $i\frac{d\lambda_{m1}}{d\theta}$ and the PM reluctance torque are also disaligned by angle β_1. The torque components no longer add to produce a constant instantaneous torque.

To eliminate this torque ripple requires the correct re-alignment of T_r and $\frac{d\lambda_{m1}}{d\theta}$. The correct phase relationship between T_r and $\frac{d\lambda_{m1}}{d\theta}$ is maintained if

$$\gamma_r - \beta_1 = \frac{\pi}{4} \tag{4.104}$$

Eqn. 4.104 is clearly not satisfied by the example of Fig. 4.21 because $\gamma_r = \pi/4$ and β_1 is non zero. However, the orientation of the airgap relative to the stator d-axis may be rotated. γ_r is not required to have a fixed value of $\pi/4$ radians. The β_1 versus γ_r characteristic is shown to provide a solution which satisfies eqn. 4.104.

Fig.s 4.32(a) and 4.32(b) plot $\frac{d\phi_m}{d\theta}$ for values of $\gamma_r = 0$ and $\gamma_r = \pi/2$, respectively. These Figures correspond to the airgap orientations of Fig.s 4.20(a) and 4.20(c). In both Figures, $\beta_1 = 0$. Fig. 4.21 demonstrates that β_1 is non zero at $\gamma_r = \pi/4$. Fig. 4.33 plots the β_1 versus γ_r characteristic over the range $0 \leq \gamma_r \leq \pi$. The airgap modulation is rotated a full cycle over this interval. In the second half cycle of the characteristic, the phase shift changes direction. β_1 is an odd function about $\gamma_r = \pi/2$. The first half cycle is of relevance to the motor design. The characteristic is not symmetrical about $\gamma_r = \pi/4$, and β_1 peaks at a value of $\gamma_r > \pi/4$. The peak value of β_1 corresponds to a phase shift of only a few electrical degrees, but this phase shift can produce significant torque ripple.

The solution to eqn. 4.104 is found by iteration. A nearly exact approximation is

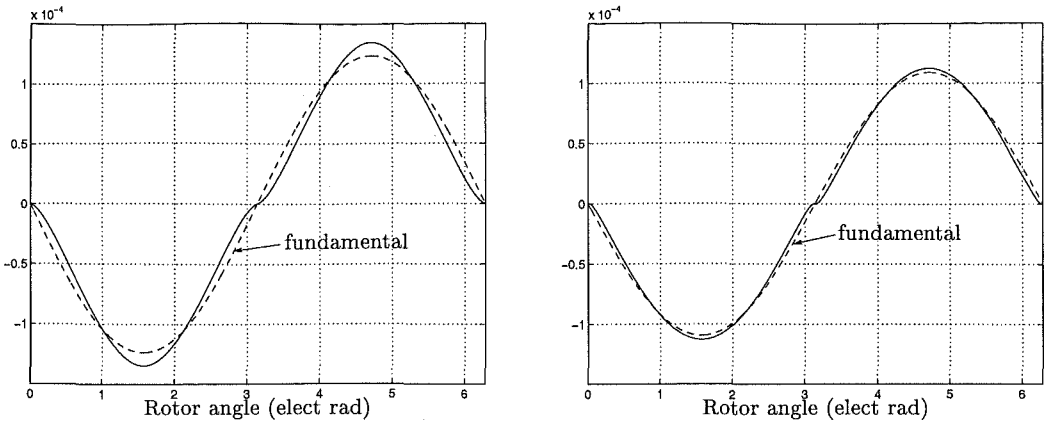

(a) $\gamma_r = 0$. (b) $\gamma_r = \pi/2$.

Figure 4.32 EMF/torque function per turn, $\frac{d\phi_m}{d\theta}$.

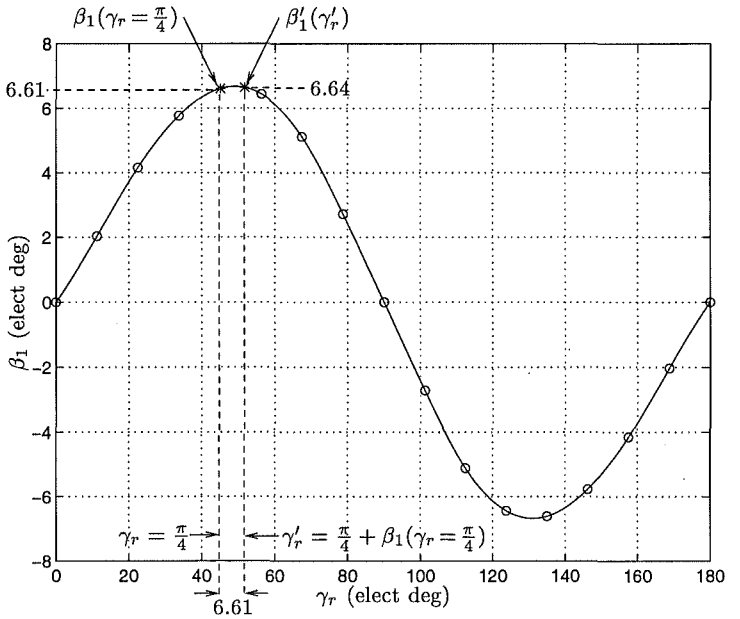

Figure 4.33 β_1 versus γ_r.

found using a single iteration. This first iteration is given by

$$\gamma_r' = \frac{\pi}{4} + \beta_1(\gamma_r = \tfrac{\pi}{4}) \tag{4.105}$$

where the phase shift β_1 occuring at $\gamma_r = \pi/4$ is added to γ_r. If the characteristic is nearly constant over the interval between γ_r and γ_r', then the new value of β_1 given by $\beta_1'(\gamma_r')$ is nearly the same as the old value $\beta_1(\gamma_r = \pi/4)$. This is demonstrated in Fig. 4.33. Therefore, the angle of the airgap modulation can be increased to correctly align the PM reluctance torque to the EMF/torque function, without causing further misalignment.

The new value γ_r' is used in the design. The magnitude of $\frac{d\phi_{m1}}{d\theta}$ decreases as γ_r increases over the range $0 \leq \gamma_r \leq \pi/2$. This occurs because the stator d-axis airgap length increases. Because $\gamma_r' > \gamma_r$, the magnitude of $\frac{d\phi_{m1}}{d\theta}$ is reduced. However, in this design the reduction in $\frac{d\phi_{m1}}{d\theta}$ is not significant. The original values of amplitude $\frac{d\hat{\phi}_{m1}}{d\theta}$ and β_1 are retained. However, the stable rotor rest position now occurs at $\theta = \gamma_r'$.

The amplitude of the fundamental component of the PM flux linkage is given by

$$\hat{\lambda}_{m1} = K_m n \tag{4.106}$$

where n = number of turns per pole.

K_m is referred to as the *PM flux linkage constant* and is defined by

$$K_m = 2\,\xi_m\, p\ \hat{\phi}_{m1} \tag{4.107}$$

where

ξ_m = PM flux linkage factor. This is defined as the fraction of the PM flux linking a stator turn.

$\hat{\phi}_{m1}$ = amplitude of the fundamental component of the PM flux linkage per turn (assuming no leakage)

In this analysis, $\hat{\phi}_{m1}$ is obtained from

$$\hat{\phi}_{m1} = \frac{1}{p}\,\frac{d\hat{\phi}_{m1}}{d\theta} \tag{4.108}$$

The fundamental amplitude $\frac{d\hat{\phi}_{m1}}{d\theta}$ is obtained from the frequency analysis of the EMF/torque function. The single pole pair motor is drawn in Fig. 4.34. In the designs of Fig.s 4.34 and 1.2(b), the PM flux leakage is exacerbated by the absence of slot openings. For these designs, the PM flux leakage is typically up to 20%. A corresponding value of $\xi_m = 0.8$ is used for the single pole pair design.

For a motor having an arbitrary number of pole pairs, the EMF/torque function is given by

$$\frac{d\lambda_m}{d\theta} = p\hat{\lambda}_{m1}\sin(p\theta - \beta_1) + 3p\hat{\lambda}_{m3}\sin(3p\theta - \beta_3) \tag{4.109}$$

where

$\hat{\lambda}_{m3}$ = amplitude of the third harmonic component of the PM flux linkage

β_3 = phase angle of the third harmonic

Angles β_1 and β_3 are specified in electrical units. A single pole pair motor is modelled by setting $\hat{\lambda}_{m3}$ to zero. To simulate a unidirectional motor, eqn. 4.109 is substituted into state eqn.s 4.53 and 4.54, replacing the term $p\hat{\lambda}_m \sin(p\theta)$.

4.9.2 Stator Design

The 2-pole unidirectional motor is drawn in Fig. 4.34. The PM rotor is located inside a stack of stator pole rings. Each stator pole ring is a single piece of silicon steel lamination. The two pole halves of the stator pole ring are joined by two narrow bridges of iron. These bridges are magnetically saturated by the energised stator winding and the PM rotor. Each of the two concentrated pole windings are pre-wound onto a winding former. The winding formers have a rigid construction and are designed to slip over each shank of the stator pole ring after pre-winding. The stator yoke rings, which are also of silicon steel lamination construction, are then fitted over the stator pole rings to complete the stator construction.

The iron parts are designed such that an iron flux density of 1.5 T is not exceeded due to the PM flux, excluding regions where saturation is required. Some dimensions are larger than magnetically necessary for mechanical reasons.

The coilside area per pole, A_w, is the slot area available for the winding minus the area taken up by the winding former. With reference to Fig. 4.35, A_w is approximated by

$$A_w \approx \frac{\theta_w}{2}\Big([D_{yi}/2 - l_f]^2 - [R_{so} + l_f]^2\Big) \tag{4.110}$$

where θ_w is specified in radians.

The copper area is estimated assuming that the conductors are stacked as they would be if each conductor had a square cross-section. In this case, no space between conductors is assumed. However, because the conductors actually have a circular cross-section, the fraction of the area that is utilised by the conductors is given by the ratio $\frac{\text{circle area}}{\text{square area}} = \frac{\pi R^2}{4R^2} = \frac{\pi}{4} = 0.785$. This ratio is referred to in this design as the stacking factor, sf. Provision is also made for the area taken up by the conductor insulation, by the insulation factor, $if = (D_c/D_i)^2$. D_c is the uninsulated diameter of the copper wire, and D_i is the insulated diameter. The copper coilside area per pole is then approximated by

$$A_c \approx sf \times if \times A_w = 0.785\,(D_c/D_i)^2 A_w \tag{4.111}$$

4.9.2.1 Winding Resistance

For all turns connected in series, the total stator winding resistance is given by

$$R = K_R\, n^2 \tag{4.112}$$

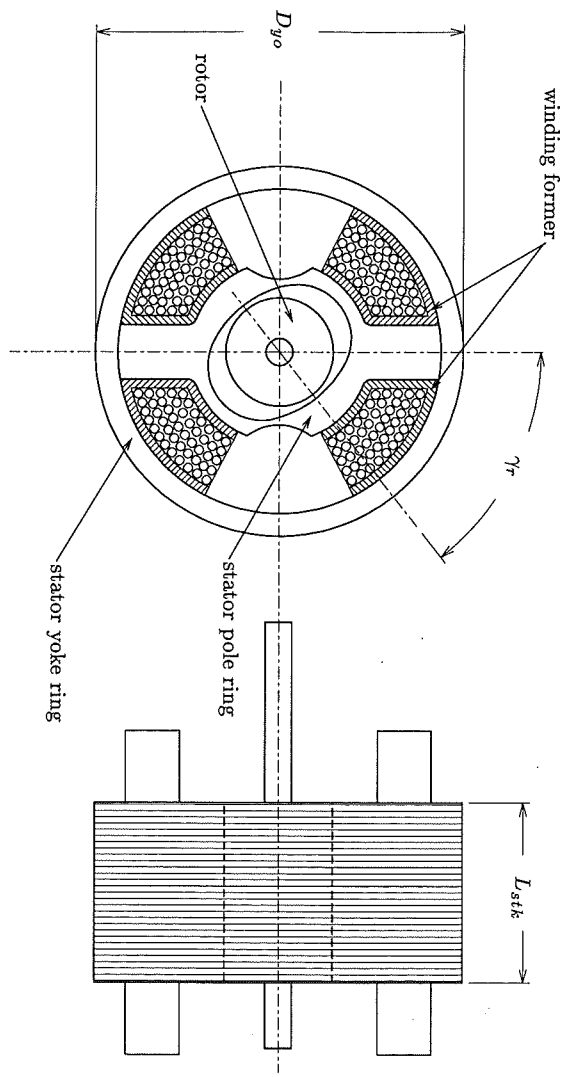

Figure 4.34 2-pole unidirectional motor.

K_R is referred to as the *winding resistance constant* and is defined by

$$K_R = 2pR_o \tag{4.113}$$

R_o is the resistance of one winding consisting of a single turn, occupying the entire coilside area per pole A_c. R_o is given by

$$R_o = \rho_c \frac{l_o}{A_c} \tag{4.114}$$

where

ρ_c = resistivity of copper
l_o = mean length per turn

Because the total length of wire is proportional to the number of turns, and the area per turn is inversely proportional to the number of turns, the total winding resistance is proportional to the square of the number of turns per pole, as shown by eqn. 4.112.

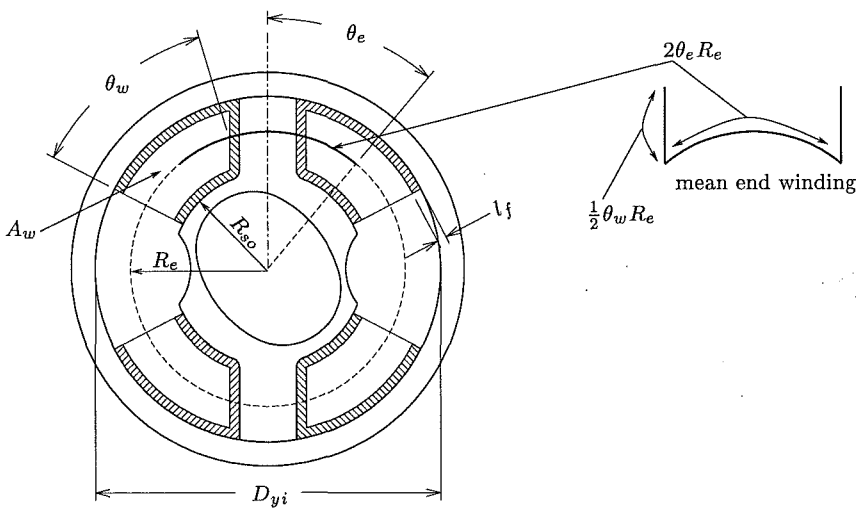

Figure 4.35 Estimation of the mean end winding length.

With reference to Fig. 4.35, an estimate of the mean length per turn is given by

$$l_o = 2L_{stk} + 2(2\theta_e R_e) + 2(\theta_w R_e) \tag{4.115}$$

The second and third RHS terms of eqn. 4.115 give contributions to the mean end winding length. $\theta_w R_e$ is an axial component of the end winding length due to the thickness of the winding. R_e is the mean turn radius and is given by

$$R_e = \sqrt{\frac{\left(D_{yi}/2 - l_f\right)^2 + \left(R_{so} + l_f\right)^2}{2}} \tag{4.116}$$

4.9.2.2 Winding Inductance

The winding inductance is estimated by summing contributions from the airgap, slot, and the end windings. The stator iron is assumed to be infinitely permeable such that the MMF due to the energised stator windings is dropped entirely across the airgaps.

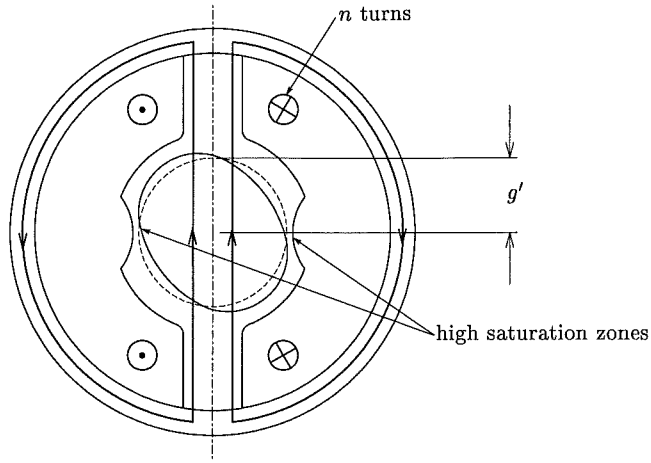

Figure 4.36 Airgap flux linkage for the calculation of airgap inductance

The flux linkage due to energised windings corresponding to the airgap inductance is identified in Fig. 4.36. Flux paths via the high saturation zones also exist, but these are accounted for later in this section. The field intensity across the airgap is given by

$$H_{air} = \frac{2ni}{2g'} = \frac{ni}{g'} \tag{4.117}$$

where g' is an effective airgap approximated by $g' = \frac{\pi}{4}\left(\frac{R_m}{\mu_r} + L_c + \frac{L_t}{2}\right)$. The airgap inductance per slot is calculated. The airgap flux linkage per slot corresponds to the flux crossing half the airgap pole area. This area is given by $A = (R_m + L_c + L_t/2)L_{stk}$. The airgap flux density is given by $B = \mu_o H$, and the airgap flux linkage of a single slot is given by

$$\lambda_{air} = 2nBA = \frac{8n^2\mu_o i\left(R_m + L_c + \frac{L_t}{2}\right)L_{stk}}{\pi\left(\frac{R_m}{\mu_r} + L_c + \frac{L_t}{2}\right)} \tag{4.118}$$

The airgap inductance per slot is then given by

$$L_{air} = \frac{\lambda_{air}}{i} = \frac{8\mu_o\left(R_m + L_c + \frac{L_t}{2}\right)L_{stk}}{\pi\left(\frac{R_m}{\mu_r} + L_c + \frac{L_t}{2}\right)}n^2 \tag{4.119}$$

The contribution of the slot inductance is typically of the same order as the airgap contribution [Hendershot and Miller 1994]. The method of slot inductance calculation

described by [Hendershot and Miller 1994, pp. 5.55-5.59] is applied.

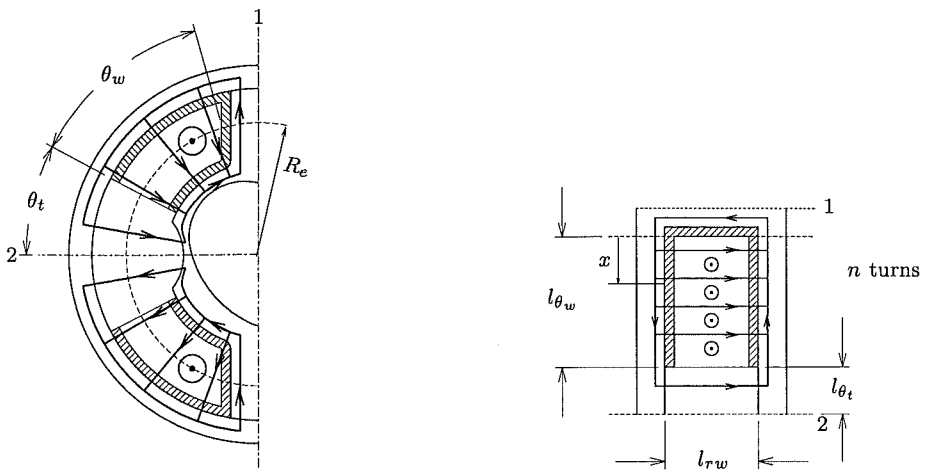

(a) Curved slot.

(b) Straightened approximation of the upper half of the slot.

Figure 4.37 Slot flux linkage for the calculation of the slot inductance.

Fig. 4.37(a) shows the distribution of the flux lines within a single stator slot. It is assumed, due to the geometry, that the flux lines do not link both coilsides in the slot. To calculate the inductance, the curved slot is approximated as being rectangular for each coilside as shown in Fig. 4.37(b). The effective slot depth per coilside is then given by $l_{\theta_w} + l_{\theta_t}$, where

$$l_{\theta_w} = \theta_w R_e \tag{4.120}$$

$$l_{\theta_t} = \theta_t R_e \tag{4.121}$$

The width of the slot is given by

$$l_{rw} = D_{yi}/2 - R_{so} \tag{4.122}$$

For the region of the slot spanning l_{θ_t}, the flux lines link all the turns of the coilside. This region is treated as being analogous to the 'tang' in [Hendershot and Miller 1994]. The field intensity is given by

$$H_{\theta_t} = \frac{ni}{l_{rw}} \tag{4.123}$$

such that

$$B_{\theta_t} = \frac{\mu_o ni}{l_{rw}} \tag{4.124}$$

The flux linkage corresponding to this region is given by

$$\lambda_{\theta_t} = n\, l_{\theta_t}\, L_{stk}\, B \tag{4.125}$$

and the inductance is given by

$$L_{\theta_t} = \mu_\circ L_{stk} \left(\frac{l_{\theta_t}}{l_{rw}} \right) n^2 \tag{4.126}$$

For the region of the slot spanning l_{θ_w}, the cross-slot flux density increases as x increases, and is given by

$$B_{\theta_w} = \mu_\circ H = \left(\frac{x}{l_{\theta_w}} ni \right) \frac{\mu_\circ}{l_{rw}} \tag{4.127}$$

The incremental flux linkage is given by

$$d\lambda_{\theta_w} = \left(\frac{x}{l_{\theta_w}} n \right) B_{\theta_w} L_{stk}\, dx \tag{4.128}$$

and the flux linkage is obtained by integration:

$$\lambda_{\theta_w} = \int_0^{l_{\theta_w}} d\lambda_{\theta_w} = \mu_\circ i L_{stk} \left(\frac{l_{\theta_w}}{3\, l_{rw}} \right) n^2 \tag{4.129}$$

and therefore

$$L_{\theta_w} = \frac{\lambda_{\theta_w}}{i} = \mu_\circ L_{stk} \left(\frac{l_{\theta_w}}{3\, l_{rw}} \right) n^2 \tag{4.130}$$

The inductance contributions from both coilsides of the slot is then given by

$$L_{slot} = 2L_{\theta_t} + 2L_{\theta_w} = 2\mu_\circ L_{stk} \left(\frac{l_{\theta_t}}{l_{rw}} + \frac{l_{\theta_w}}{3\, l_{rw}} \right) n^2 \tag{4.131}$$

A simple approximation of the end winding inductance is made following the method described by [Hendershot and Miller 1994, pp. 5.59-5.60]. Each end winding is treated as a half circle such that the contribution from both ends of a turn is equivalent to that of a single circular loop. The diameter of this loop is given by

$$D_e = 2\theta_e R_e \tag{4.132}$$

and the end winding inductance (per coil) is given by

$$L_{end} = \frac{\mu_\circ D_e}{2} \ln \left[\frac{4D_e}{GMD} - 2 \right] n^2 \tag{4.133}$$

where GMD is the geometric mean distance between conductors in the coil cross-

section. If the coil cross-section is assumed to be square, then $GMD = 0.477\sqrt{A_w}$.

The total inductance per pole is obtained by summing the contributions from the airgap , slot and end windings:

$$L_{pole} = \xi_L\Big(L_{air} + L_{slot} + L_{end}\Big) \tag{4.134}$$

ξ_L is referred to as the *stator flux linkage factor.* It is included to account for the increase in inductance due to the increase in flux linkage caused by the closed slot openings. For the single pole pair motor, a value of $\xi_L = 1.2$ is used. For a unidirectional motor with an arbitrary number of pole pairs, the total inductance is given by

$$L = 2pL_{pole} \tag{4.135}$$

If the number of turns per pole is not specified, the inductance is expressed by

$$L = K_L\, n^2 \tag{4.136}$$

where K_L is the *inductance constant.* K_L is obtained by dividing through eqn. 4.135 by n^2.

4.9.2.3 Turn Calculation

The load angle θ_o is a function of the number of stator winding turns. To obtain the unidirectional load angle, at which E and I are in phase, the correct number of turns must be specified. The correct number of turns per pole is calculated by substituting eqn.s 4.106, 4.112, and 4.136 into eqn. 4.41, and solving for n:

$$n = \sqrt{\frac{\hat{v}^2}{\left(\frac{4\omega_e K_L \hat{W}_r}{K_m}\right)^2 + \left(\frac{4K_R\hat{W}_r}{K_m} + \omega_e K_m\right)^2}} \tag{4.137}$$

The total number of stator winding turns is given by

$$N = 2pn \tag{4.138}$$

Both the single and multiple pole pair motors are designed to operate from a 220/230 V RMS, 50 Hz AC supply. In each case, the number of turns is calculated at 220 V RMS. This ensures that each motor can operate at the lowest supply voltage.

4.9.3 Design Synthesis

This section lists the design, performance, and simulation parameters of the single pole pair design. The values of the physical dimensions and angles defined in Fig. 4.34 are listed in Table 4.4.

	value	units	comment
D_{yo}	41	mm	Motor diameter
L_{stk}	20	mm	Stack length
D_r	12	mm	Rotor diameter ($D_r = 2R_m$)
L_r	20	mm	Rotor axial length
D_{yi}	36	mm	
l_f	1	mm	
R_{so}	10	mm	
L_t	2	mm	
L_c	0.5	mm	
γ_r	51.6	mech deg	γ_r is set to the value of γ_r'
θ_w	48	mech deg	
θ_e	40	mech deg	
θ_t	27.5	mech deg	

Table 4.4 Physical dimensions

	value	units	comment
ϱ	6000	$\mathrm{Kg/m^3}$	Density of bonded Nd-Fe-B rotor
ρ_c	2×10^{-8}	Ωm	Resistivity of copper at 60° C
B_r	0.66	T	Remanence of bonded Nd-Fe-B at 60° C
μ_r	1.25		Relative recoil permeability of bonded Nd-Fe-B
ξ_m	0.8		PM flux linkage factor
ξ_L	1.2		Stator flux linkage factor
sf	0.785		Stacking factor
D_c/D_i	0.9		Ratio of uninsulated to insulated wire diameters
f	50	Hz	Electrical supply frequency
V	220	V RMS	Terminal voltage for turn calculation

Table 4.5 Miscellaneous input parameters

Tables 4.4 and 4.5 list all the input parameters from which all remaining parameters are derived. Calculated parameters are listed in Table 4.6. In Table 4.6, the torque per unit rotor volume is given by

$$TRV = \frac{\overline{T}}{(\pi/4)D_r^2 L_{stk}} \tag{4.139}$$

The TRV provides an indication of the relative performance of the design. Comparison with the values of Table 4.8 shows that the design is well placed for its small size and the grade of PM used.

	value	units	comment
$\hat{T}_r$	0.0327	Nm	Amplitude of PM reluctance torque, eqn. 4.52
$\overline{T}$	0.0327	Nm	Rated torque, $\overline{T} = \hat{T}_r$
P_{out}	10.3	W	$P_{out} = \overline{T}\omega_e$
TRV	14.5	kNm/m^3	Torque per unit rotor volume, eqn. 4.139
m_r	0.0136	Kg	Rotor mass, $\varrho\,(\pi/4)\,D_r^2 L_r$
J_r	2.44×10^{-7}	Kg.m^2	Rotor inertia, eqn. 4.67
$\frac{4\hat{W}_r}{J\omega_e^2}$	1.36		Backward instability ratio, with $J = 2J_r$
K_m	1.88×10^{-4}	Wb	PM flux linkage constant, eqn. 4.107
A_w	70.4×10^{-6}	m^2	Coilside area per pole, eqn. 4.110
if	0.81		Insulation factor, $(D_c/D_i)^2$
A_c	44.7×10^{-6}	m^2	Copper coilside area per pole, eqn. 4.111
J_{RMS}	5.49	A/mm^2	RMS current density, eqn. 4.140
K_R	9.31×10^{-5}	Ω	Winding resistance constant, eqn. 4.113
P_R	5.63	W	Resistive power loss, eqn. 4.141
η	0.65		Efficiency, $\eta = P_{out}/(P_{out} + P_R)$
K_L	4.39×10^{-7}	H	Inductance constant, eqn. 4.136
n	3013	turns	Turns per pole, eqn. 4.137
N	6026	turns	Total stator turns, eqn. 4.138
L_{air}	0.69	H	Airgap inductance per pole, eqn. 4.119
L_{slot}	0.63	H	Slot inductance per pole, eqn. 4.131
L_{end}	0.33	H	End winding inductance per pole, eqn. 4.133
$\hat{i}$	0.116	A	Amplitude of rated current, $\hat{i} = 4\hat{W}_r/\hat{\lambda_m}$
D_c	0.138	mm	Minimum diameter of copper wire required, $D_c = \sqrt{4A_c/n\pi}$
α	56.0	elect deg	Eqn. 4.142
Γ	0.82		Pullout ratio, $\Gamma = \overline{T}/\overline{T}_p$, eqn. 4.49

Table 4.6 Calculated output parameters, excluding simulation parameters.

	value	units	comment
$\hat{v}$	$\sqrt{2}\,220/\sqrt{2}\,230$	V	
f	50	Hz	
p	1		
$\hat{\lambda}_{m1}$	0.566	V.sec	Eqn. 4.106
R	845	Ω	Eqn. 4.112
L	3.98	H	Eqn. 4.136
$\hat{W}_r$	0.0163	J	
γ_r	51.6	mech/elect deg	
β_1	6.6	mech/elect deg	

Table 4.7 A selection of simulation parameters for the single pole pair unidirectional motor design.

The RMS current density for the unidirectional value of the load is given by

$$J_{RMS} = \frac{\sqrt{2}\hat{T}_r}{pK_m A_c} \tag{4.140}$$

PM motor type	TRV (kNm/m^3)
Small, totally enclosed motors (Ferrite)	7-14
Totally enclosed motors (Sintered rare earth or Nd-Fe-B)	14-42
Totally enclosed motors (Bonded Nd-Fe-B)	21 typical
Integral hp industrial motors	7-30

Table 4.8 Guide values for TRV taken from [Hendershot and Miller 1994, p. 12.4].

The resistive power loss is given by

$$P_R = K_R(J_{RMS}A_c)^2 \tag{4.141}$$

The motor design has a current density of $J_{RMS} = 5.49$ A/mm^2 and a resistive power loss of $P_R = 5.63$ W. Table 4.9 enables this current density to be compared to typical current densities.

Type of cooling	J_{RMS} (A/mm^2)
Totally enclosed	1.5-5
Air over Fan cooled	5-10
Liquid cooled	10-30

Table 4.9 Typical current densities taken from [Hendershot and Miller 1994, p. 12.5].

In addition to the backward instability ratio, the pullout ratio Γ is also a critical design parameter. The pullout ratio must be low enough to allow a sufficient accelerating torque during starting, and must also allow for overloading. Simulation results for starting are unlikely to be successful unless a low enough value of Γ is obtained. The design value of $\Gamma = 0.82$ is considered to be at the upper limit. A specified value of Γ is obtained by designing the stator in accordance with eqn. 4.49:

$$\Gamma = \frac{\sqrt{\hat{v}^2 - (\omega_e\hat{\lambda}_m \sin\alpha)^2} - \omega_e\hat{\lambda}_m \cos\alpha}{\hat{v} - \omega_e\hat{\lambda}_m \cos\alpha}$$

The pullout ratio reduces as α increases towards 90°. α is obtained in terms of the stator inductance and resistance constants by

$$\alpha = \arctan\left(\frac{\omega_e K_L}{K_R}\right) \tag{4.142}$$

and increases by reducing K_R. K_R is reduced effectively by increasing the coilside area per pole, A_w. This is most likely to require the diameter of the stator to be increased. The pullout ratio is also increased by increasing $\hat{\lambda}_m$. $\hat{\lambda}_m$ is expressed in terms of the

stator constants by

$$\hat{\lambda}_m = K_m n = K_m \sqrt{\frac{\hat{v}^2}{\left(\frac{4\omega_e K_L \hat{W}_r}{K_m}\right)^2 + \left(\frac{4K_R \hat{W}_r}{K_m} + \omega_e K_m\right)^2}} \tag{4.143}$$

Eqn. 4.143 shows that decreasing K_R increases the number of turns and therefore also $\hat{\lambda}_m$. Increasing the winding area is therefore shown to be an effective design method for reducing Γ. However, there is a practical limit to the maximum motor diameter and the amount of copper and iron that can be used. The requirement to obtain a satisfactory value of Γ may result in a larger winding area and lower current density than initially anticipated.

4.9.4 Simulation

Simulation results corresponding to the 2-pole unidirectional motor design are presented in this section. Initial values of the state variables corresponding to starting are used. These initial states are $[i_\emptyset = 0, \dot{\theta}_\emptyset = 0, \theta_\emptyset = \gamma_r]$. For each simulation, it is determined first, whether synchronisation followed by steady state motion occurs, and secondly, whether the steady state motion is in the forward or backward direction. The motor has not been designed for a specific application. The motor is simulated for two different types of mechanical loads which are both functions of the rotor speed. These are purely quadratic and purely linear loads. The linear load is modelled by

$$T_l = K_{ln}\,\dot{\theta} \tag{4.144}$$

where K_{ln} is the linear load coefficient.

The quadratic load is modelled using eqn. 4.56. Even with these simple models of the load, the state equations describing the motion are a function of eleven simulation parameters. Given the high number of parameters, and the general approach to the application of the motor, only a limited number of parameter combinations are practical to simulate. For the purpose of limiting the number of simulations, a hierarchy of parameters considered to have the greatest variability is established. These parameters, in order of increasing variability are:

1. Mechanical load type (linear or quadratic)
2. Moment of inertia, J.
3. Supply voltage (220 or 230 V RMS)
4. Load magnitude (ranging from pullout to no load)
5. Supply voltage angle at switch-on, ϵ.

For every load magnitude tested, starting simulations of at least four switch-on angles, spanning the switch-on cycle, are completed. These values are $\epsilon = 0$, $\epsilon = \pi/2$, $\epsilon = \pi$, and $\epsilon = 3\pi/2$ radians. The simulation parameters which are not listed above are held constant.

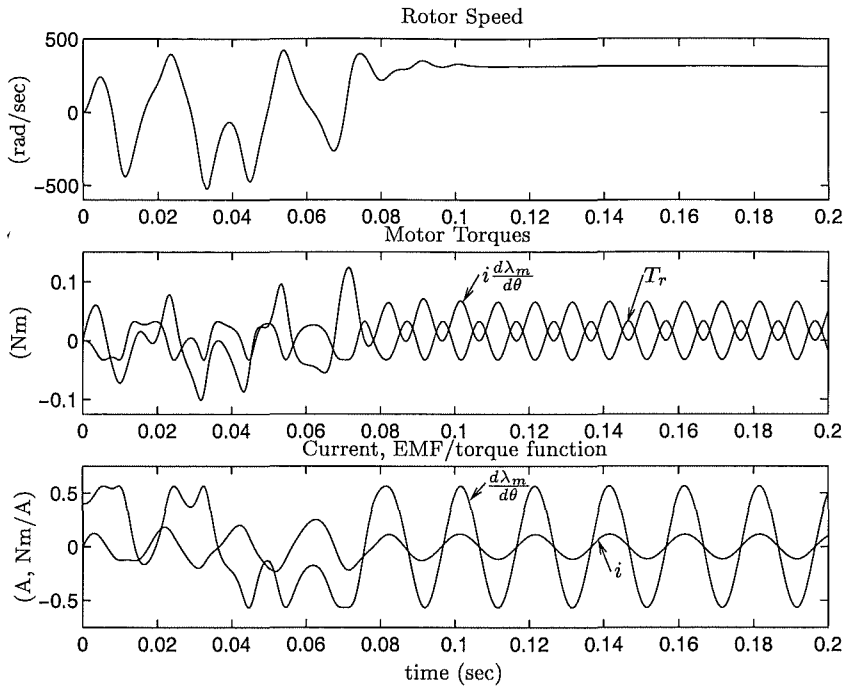

Figure 4.38 Simulation of starting for the rated quadratic load. $T_l = \hat{T}_r$, $J = 2J_r$, 220 V RMS, and $\epsilon = \pi/2$.

Fig. 4.38 shows the starting characteristic for the rated quadratic load at 220 V RMS with $\epsilon = \pi/2$. After a brief transient, unidirectional motion is established and the speed ripple is zero.

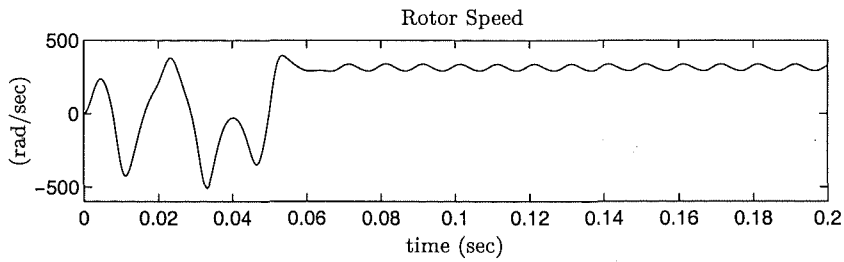

Figure 4.39 Simulation of starting for $T_l = 1.1\,\hat{T}_r$. The remaining parameters are the same as those of Fig. 4.38.

Fig. 4.39 shows the speed characteristic where the magnitude of the quadratic load is increased to $T_l = 1.1\hat{T}_r$. The steady state speed modulation is unperturbed and has a frequency of 100 Hz. The speed modulation is caused by i and $\frac{d\lambda_m}{d\theta}$ being out of phase with each other, corresponding to a load angle which is greater than the unidirectional load angle and closer to the pullout load angle.

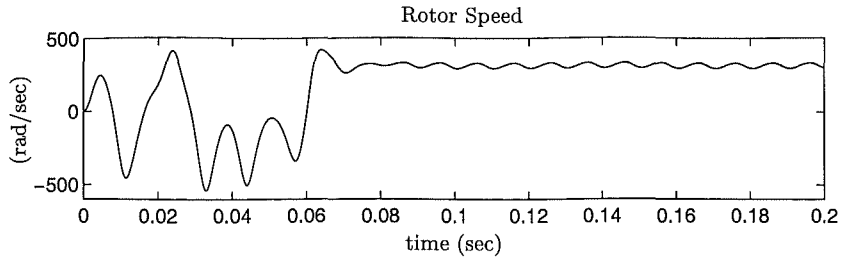

Figure 4.40 Simulation of starting for $T_l = 0.9\hat{T}_r$. The remaining parameters are the same as those of Fig. 4.38.

Fig. 4.40 shows the speed characteristic where the load is decreased to $T_l = 0.9\hat{T}_r$. Steady state speed modulation also occurs, and the load angle is smaller than the unidirectional load angle.

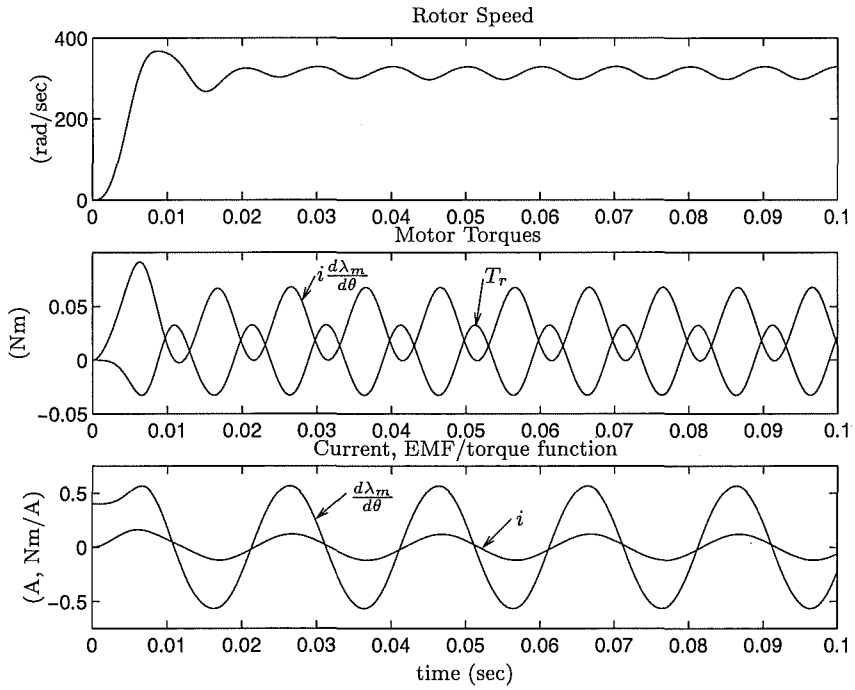

Figure 4.41 Simulation of starting for the rated quadratic load at 230 V RMS. $T_l = \hat{T}_r$, $J = 2J_r$, and $\epsilon = 0$. $a = \hat{\dot{\theta}}/\omega_e = 0.05$.

Fig. 4.41 shows the starting characteristic for the rated quadratic load at 230 V RMS. Steady state speed modulation occurs because a new load angle is established by the higher supply voltage. To eliminate speed ripple at this voltage, the number of stator winding turns must be increased. The normalised amplitude of the speed modulation is $a = \hat{\dot{\theta}}/\omega_e = 0.05$. For a conventional motor, a generally has a value within the range of 0.2 to 0.4 [Schemmann 1971].

Fig. 4.42 shows the speed characteristic where the load is decreased to $T_l = 0.1\hat{T}_r$ at 220 V RMS. The load may be considered to be an approximate no load value. Even at no load, significant frictional loading may still be present because of the low

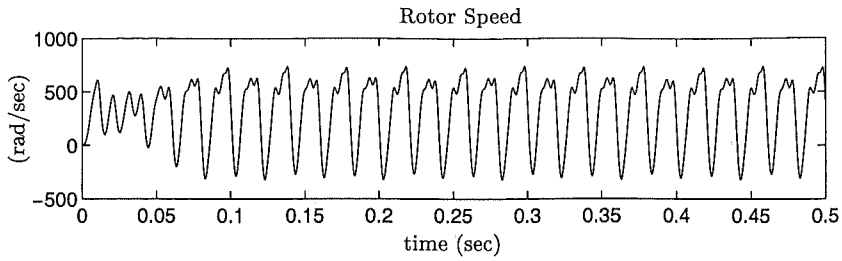

Figure 4.42 Simulation of starting for a quadratic load of $T_l = 0.1\,\hat{T}_r$ showing a 25 Hz perturbation. $J = 2J_r$, 220 V RMS, and $\epsilon = 0$.

performance types of bearing systems used. For example, the bearing system of the Siemens motor described in section 5.5.2.1 uses water lubricated cavities into which the ends of the stainless steel shaft are located. In Fig. 4.42, the steady state speed modulation is very large and significant rotor reversal occurs. However, the average speed established is synchronous. The speed modulation is periodic and has a frequency of 25 Hz. This is a perturbed motion. Acoustic noise and resistive power loss are expected to be substantially increased by this behaviour. The RMS resistive power loss for the simulation interval is 13.8 W. This is 77% of the locked rotor resistive power loss.

Table 4.10 shows the quadratic load simulation results for starting. The first set of results are for a total inertia equal to twice the rotor inertia. The load torque ranges are specified as fractions of the amplitude of the PM reluctance torque. Forward synchronous motion is required to be obtained after starting for values of the load torque which are near the rated value $T_l = \hat{T}_r$. This is satisfactory achieved. At 220 V RMS, the upper limit for the starting load is $T_l = 1.13\,\hat{T}_r$. At this value, synchronisation occurs within 0.5 seconds for all test values of ϵ. The theoretical steady state pullout torque is higher and is given by $\overline{T}_p = \hat{T}_r/\Gamma = 1.21\,\hat{T}_r$. Speed ripple reduces the actual steady state pullout torque to a value below the theoretical value $\overline{T}_p$. The actual steady state value lies close to $1.21\,\hat{T}_r$. For all simulation results in Table 4.10, the maximum value of the load torque corresponds to successful forward synchronisation within 0.5 seconds of switch-on, and is referred to as the *maximum starting load.*

For the mid-range of loads at 220 V RMS, stable backward synchronous motion, as well as forward synchronous motion, is possible depending on the value of ϵ. As the load is reduced, speed oscillation increases. At $T_l = 0.3\,\hat{T}_r$, a 50 Hz perturbation occurs for both directions of rotation. As the load is reduced further, only forward synchronous motion is obtained and the speed modulation increases. At $T_l = 0.1\,\hat{T}_r$, the 25 Hz perturbation shown in Fig. 4.42 occurs.

At 230 V RMS, the maximum starting load is increased because the starting transient current and the pullout torque are higher. Stable backward synchronous motion is again observed for mid-range loads, and is unperturbed. Only forward synchronous motion is observed for lower loads with a 50 Hz perturbation. At $T_l = 0.1\,\hat{T}_r$, perturbed

$J = 2J_r$

220 V RMS		
Type of motion		Load range
Forward unperturbed		$0.7\hat{T}_r \leq T_l \leq 1.13\hat{T}_r$
Backward stable (Bidirectional)	unperturbed	$0.4\hat{T}_r \leq T_l \leq 0.6\hat{T}_r$
	perturbed 50 Hz	$T_l = 0.3\hat{T}_r$
Forward perturbed	50 Hz	$T_l = 0.2\hat{T}_r$
	25 Hz	$T_l = 0.1\hat{T}_r$

230 V RMS	
Forward unperturbed	$0.7\hat{T}_r \leq T_l \leq 1.18\hat{T}_r$
Backward stable unperturbed	$0.4\hat{T}_r \leq T_l \leq 0.6\hat{T}_r$
Forward perturbed 50 Hz	$0.2\hat{T}_r \leq T_l \leq 0.3\hat{T}_r$
Forward asynchronous	$T_l \leq 0.1\hat{T}_r$

$J = 1.85\,J_r$

220 V RMS	
Forward unperturbed	$0.7\hat{T}_r \leq T_l \leq 1.11\hat{T}_r$
230 V RMS	
Forward unperturbed	$0.8\hat{T}_r \leq T_l \leq 1.16\hat{T}_r$

$J = 1.65\,J_r$

220 V RMS	
Forward unperturbed	$0.4\hat{T}_r \leq T_l \leq 1.05\hat{T}_r$
230 V RMS	
Forward unperturbed	$0.6\hat{T}_r \leq T_l \leq 1.12\hat{T}_r$

Table 4.10 Quadratic load simulation results for starting.

motion is unstable. Long quasi-periodic motions are observed to occur, but do not remain stable. As a result, the motor does not operate at synchronous speed. However, the average speed is non zero and is in the forward direction. This is described as *forward asynchronous* motion. Near the load threshold at which asynchronous motion begins, the average speed is close to the synchronous speed. As the load is reduced further towards zero, the average speed decreases but still remains positive. The resistive losses are similar to the perturbed motion losses in the low load range.

Table 4.10 also shows the ranges for forward unperturbed motion corresponding to $J = 1.85\,J_r$ and $J = 1.65\,J_r$. In these examples, decreasing the moment of inertia decreases the maximum starting load. This occurs because decreasing the inertia in-

creases speed ripple which reduces the pullout torque. However, at the other extreme, if the inertia if too large there is insufficient acceleration for synchronisation to occur.

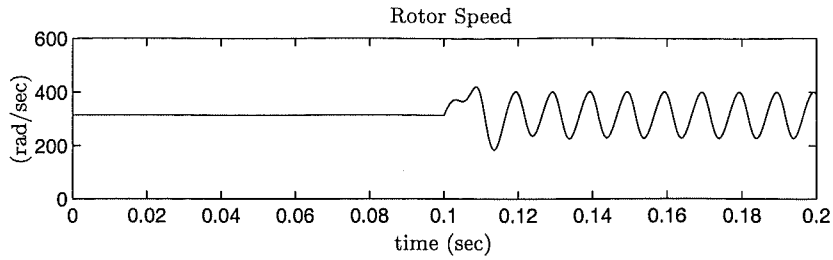

Figure 4.43 Motion due to a step change in the load. The quadratric load is reduced from $T_l = \hat{T}_r$ to $0.5\hat{T}_r$ at $t = 0.1$ seconds. $J = 2\,J_r$, 220 V RMS.

Once started in the forward direction, the motor will continue to run synchronously in the forward direction. This occurs even for very large variations in the load. Fig. 4.43 shows an example of the motion where a step change in the load from its rated value to 50% of its rated value occurs. The resulting motion is unperturbed. Table 4.10 shows that backward motion is also stable at this value of the load. The motor will also run in the backward direction if it starts in the backward direction. In either case, if the load is increased to its rated value, forward ripple free motion resumes again.

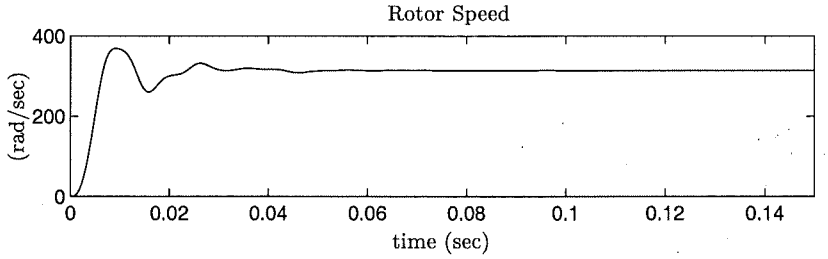

Figure 4.44 Simulation of starting for the rated linear load of $T_l = \hat{T}_r$. $J = 1.75\,J_r$, 220 V RMS, and $\epsilon = 0$.

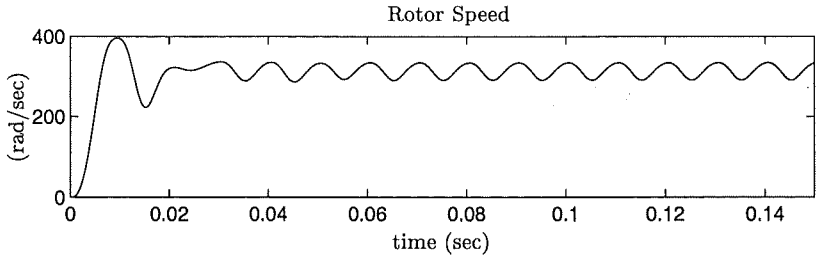

Figure 4.45 Simulation of starting for the rated linear load of $T_l = \hat{T}_r$. $J = 1.75\,J_r$, 230 V RMS, and $\epsilon = 0$. $a = 0.07$.

Fig.s 4.44 and 4.45 show starting characteristics for the rated linear load. Table 4.11 shows the linear load simulation results for starting. The results are for $J = 1.75\,J_r$. The inertia is reduced because backward stable results were found to occur near the rated load for $J = 2J_r$. This suggests that a higher backward instability ratio is required

$J = 1.75\, J_r$

220 V RMS	
Forward unperturbed	$0.6\,\hat{T}_r \leq T_l \leq 1.17\,\hat{T}_r$
Forward perturbed 50 Hz	$0.3\,\hat{T}_r \leq T_l \leq 0.5\,\hat{T}_r$
Forward asynchronous	$T_l \leq 0.2\,\hat{T}_r$

230 V RMS	
Forward unperturbed	$0.7\,\hat{T}_r \leq T_l \leq 1.23\,\hat{T}_r$
Forward perturbed 50 Hz	$0.3\,\hat{T}_r \leq T_l \leq 0.6\,\hat{T}_r$
Forward asynchronous	$T_l \leq 0.2\,\hat{T}_r$

Table 4.11 Linear load simulation results for starting.

for a linear load characteristic. For $J = 1.75\, J_r$, no backward stability is observed to occur for any value of the load. The forward unperturbed regions span useful load ranges.

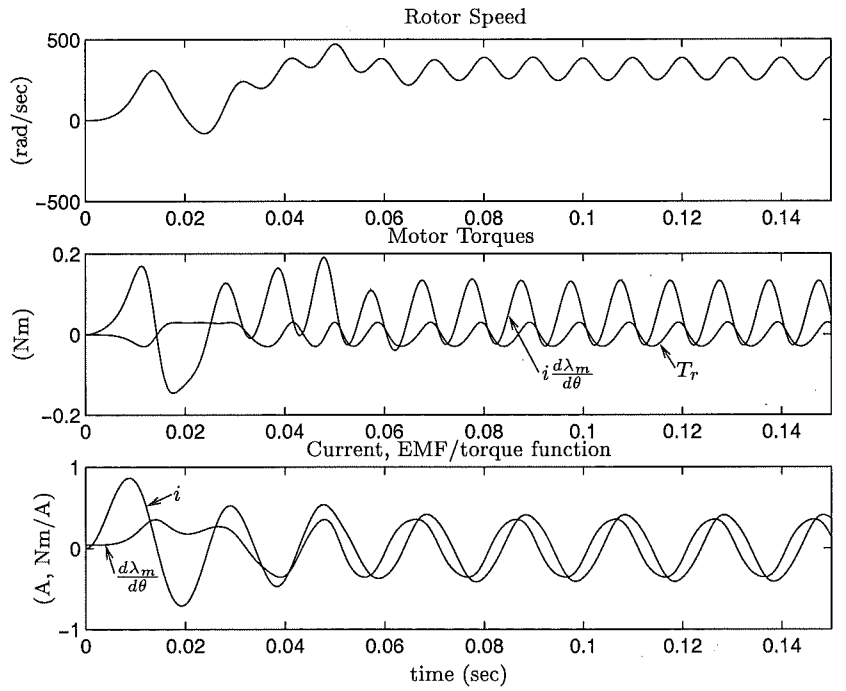

Figure 4.46 Simulation of starting for the conventional Siemens motor. Quadratic load at the rated value of 0.048 Nm, 220 V RMS, $J = 22 \times 10^{-7}$ Kg.m^2, and $\epsilon = 0$. $a = 0.22$.

Simulation results for the conventional Siemens water-pump motor are included for the purpose of comparison. The Siemens motor parameters of Table 4.1 are used. Fig. 4.46 shows a starting simulation corresponding to the rated water-pump load of $\overline{T} = 0.048$ Nm. The phase-magnet torque $i\frac{d\lambda_m}{d\theta}$ has negative dips, i and $\frac{d\lambda_m}{d\theta}$ are not in phase, and $a = 0.22$. Note also that the initial value of $\frac{d\lambda_m}{d\theta} = \hat{\lambda}_m \sin(\theta = \gamma_r = 7°)$ is relatively small. For simulations corresponding to the load angle where i and $\frac{d\lambda_m}{d\theta}$ are

in phase, the speed modulation reduces to $a = 0.19$.

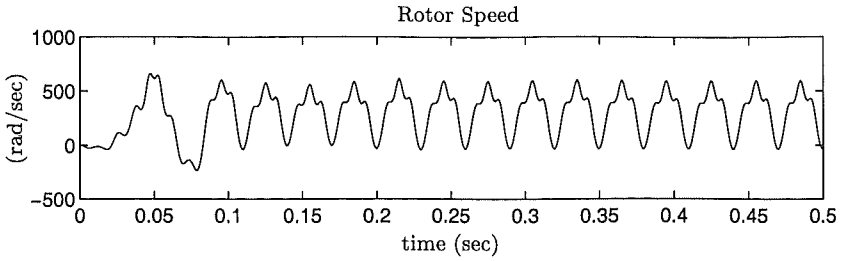

Figure 4.47 Simulation of starting for the conventional Siemens motor showing a $33\frac{1}{3}$ Hz perturbation. Quadratic load with magnitude $T_l = 0.05\,\overline{T}_p$, 220 V RMS, $J = 22 \times 10^{-7}$ Kg.m^2, and $\epsilon = 3\pi/2$.

Fig. 4.47 shows the speed characteristic where the load is reduced to 5% of the theoretical pullout load. A $33\frac{1}{3}$ Hz perturbation occurs and the resistive power loss over the interval is 15.1 W. This is 75% of the locked rotor resistive power loss. Table 4.12 shows the starting simulation results for the Siemens motor. The steady state direction of rotation may be either forwards or backwards, depending on ϵ, confirming the bidirectional nature of this type of motor.

Type of motion	Load magnitude
Bidirectional unperturbed	$T_l > 0.1\,\overline{T}_p$
Bidirectional perturbed $33\frac{1}{3}$ Hz	$T_l \leq 0.1\,\overline{T}_p$

Table 4.12 Simulation results for starting of the conventional Siemens motor using a quadratic load. $J = 22 \times 10^{-7}$ Kg.m^2, 220 V RMS. $\overline{T}_p = 0.095$ Nm.

The longer the period of the perturbation, the more complicated the resulting motion [Schemmann 1973]. This is illustrated by comparison of Fig.s 4.42 and 4.47. [Schemmann 1973] comments that a motor should be designed to exclude perturbed motion within the expected variations of supply voltage and load. The simulation results presented suggest that speed ripple and resistive loss are significantly higher if perturbed motion is encountered. If perturbed motion is encountered in a given application, then it must be determined whether the speed ripple and losses are acceptable. Simulation results show that it can be possible to eliminate perturbed motion by increasing the inertia, but care must be taken to ensure that synchronisation can still occur.

4.10 A 6-POLE UNIDIRECTIONAL MOTOR DESIGN USING FERRITE MAGNETS

In this section, the design of a 6-pole unidirectional motor which uses hard ferrite rotor magnets is described. The aim is to produce a 'ballpark' design of a unidirectional motor having multiple pole pairs. It is again demonstrated how the backward instability ratio may be used to obtain successful unidirectional running. In this case, increasing the

pole pair number allows lower performance PM material to be used with a rotor of a larger diameter. This is explained with reference to eqn. 4.103, where increasing p compensates for the reduction in the ratio $\hat{W}_r/J$ caused by using lower remanence magnets and a larger rotor diameter. The rotor diameter is 19 mm, and is the same as that of the conventional Siemens 2-pole ferrite motor.

The design is analogous, in most respects, to the unidirectional single pole pair design. Parallel magnetised rotor poles, closed stator slots, and most of the previously introduced design equations, are again applied. The final design is the result of a number of iterations and its success is evaluated by simulation.

4.10.1 Rotor and Airgap Design

The design of the rotor and airgap involves calculation of the PM reluctance torque, the backward instability ratio, and the EMF/torque function per turn.

4.10.1.1 PM Reluctance Torque

The airgap dimensions are listed in Table 4.13. The rotor overhangs the stator lamination stack by 2.5 mm at each end. The PM material characteristics are listed in Table 4.14. A linear recoil permeability is assumed and the remanence is the same as that of the conventional Siemens motor. The PM reluctance torque is calculated using the model developed in section 4.8. Fig. 4.48 plots the stored energy and the reluctance torque. The frequency spectrum of T_r shows that a small second harmonic is present, and that higher order harmonics are negligible. $\hat{W}_r$ and T_r are therefore approximated by their fundamental values.

4.10.1.2 The EMF/Torque function

Fig. 4.49 plots the EMF/torque function per turn. The frequency spectrum of $\frac{d\phi_m}{d\theta}$ shows that the third harmonic component is significant. The fundamental component $\frac{d\phi_{m1}}{d\theta}$ is phase shifted by angle β_1 due to the airgap modulation.

In an analogous manner to the single pole pair design, it is shown for a multiple pole pair design that with $p\,\gamma_r = \pi/4$ electrical radians, the corresponding phase shift of the fundamental component of the EMF/torque function $\frac{d\lambda_{m1}}{d\theta}$ exacerbates speed ripple. Simulation results show that speed ripple is minimised for the multiple pole pair motor if T_r and $\frac{d\lambda_{m1}}{d\theta}$ are aligned according to eqn. 4.104, such that $p\gamma_r - \beta_1 = \frac{\pi}{4}$. The β_1 versus γ_r characteristic for the multiple pole pair motor is nearly identical to that of the single pole pair characteristic shown in Fig. 4.33. Therefore, a nearly exact solution for the alignment of T_r and $\frac{d\lambda_{m1}}{d\theta}$ is given by eqn. 4.105, such that $p\gamma_r' = \frac{\pi}{4} + \beta_1(p\gamma_r = \frac{\pi}{4})$. In Fig. 4.49, $\frac{d\phi_m}{d\theta}$ is plotted for this value of γ_r.

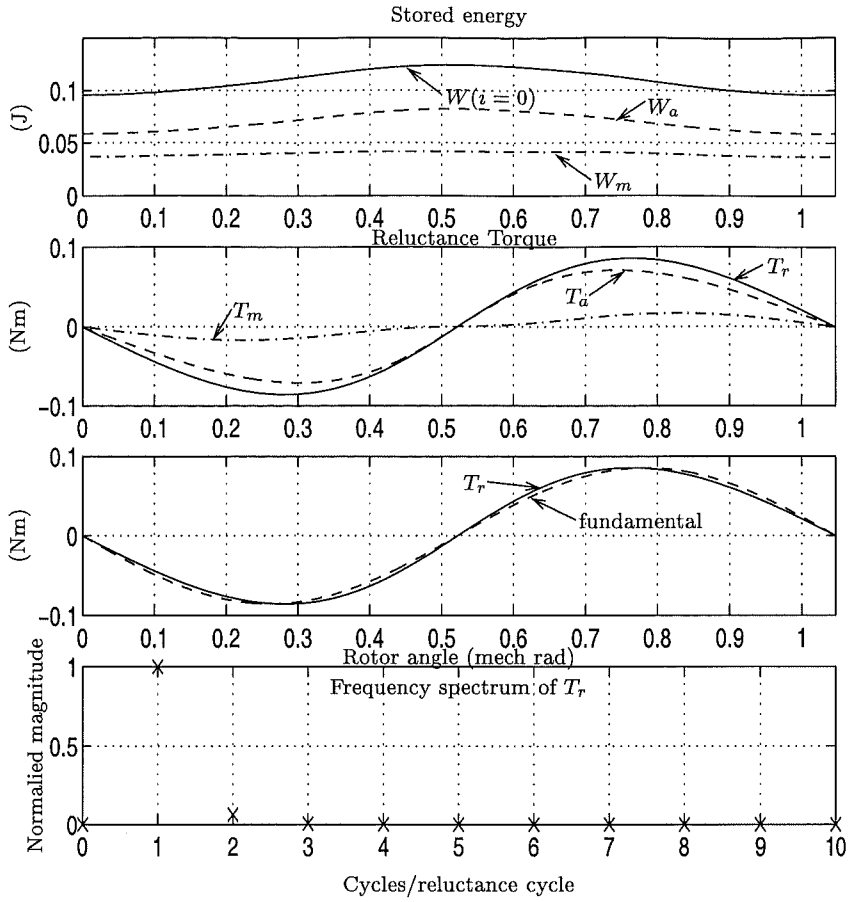

Figure 4.48 Stored energy and PM reluctance torque for the ferrite unidirectional motor. $p = 3$, and $\hat{W}_r = 0.0144$ J.

4.10.2 Stator Design

The 6-pole unidirectional motor is drawn in Fig. 4.50. The stator construction is analogous to that of the single pole pair design. The PM flux leakage is assumed to be higher than for the single pole pair design. This is because rotor poles of opposite magnetic polarity are in closer proximity to each other, and because the number of closed slots is higher. A more conservative value of the PM flux linkage factor of $\xi_m = 0.75$ is used.

The stator winding resistance is calculated as described in section 4.9.2.1. The stator winding inductance is calculated in an identical manner to that of section 4.9.2.2, except that the airgap and slot inductances are calculated in a slightly different manner which is more appropriate for the multiple pole pair geometry. The airgap inductance is calculated by assuming that the airgap follows a semicircular path spanning a pole shoe. The slot inductance is calculated assuming that the slot flux follows circular cross-slot paths around the arc of the slot. These paths link both coilsides in the slot.

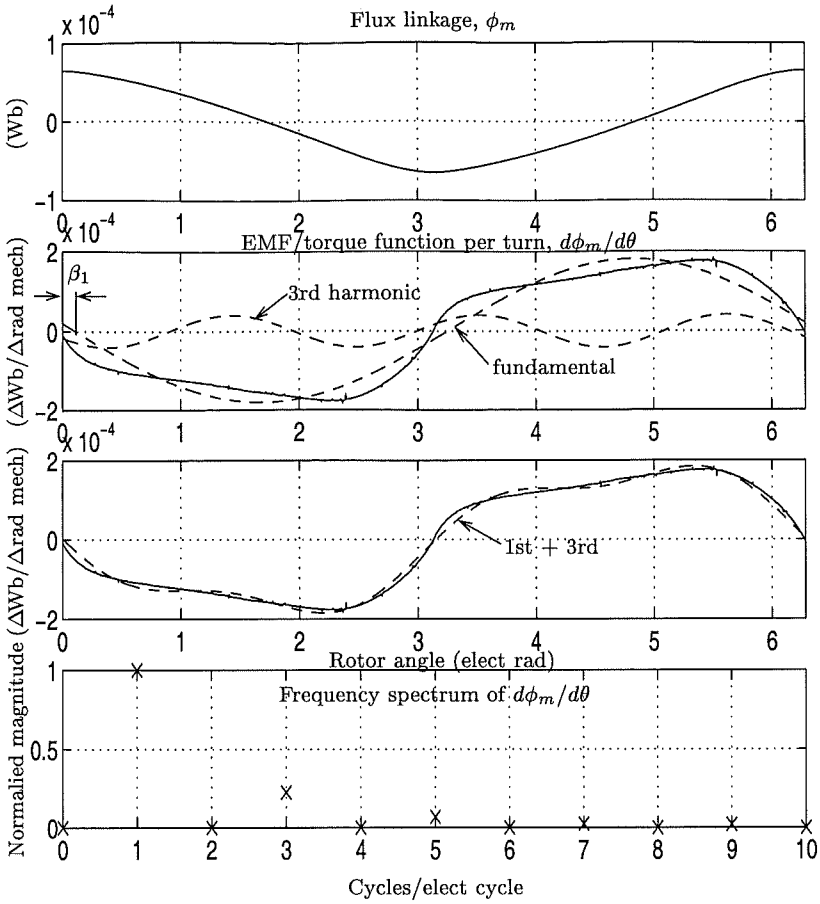

Figure 4.49 ϕ_m and $\frac{d\phi_m}{d\theta}$ for the ferrite unidirectional motor. $p = 3$, and $p\gamma_r = 51.1°$ electrical.

4.10.3 Design Synthesis

This section tabulates a selection of design, performance, and simulation parameters for the multiple pole pair design.

	value	units	comment
D_{yo}	58	mm	Motor diameter
L_{stk}	25	mm	Stack length
D_r	19	mm	Rotor diameter
L_r	30	mm	Rotor axial length
l_f	1	mm	
R_{so}	14.7	mm	
L_t	2.5	mm	
L_c	0.7	mm	
γ_r	17.0	mech deg	
θ_w	21	mech deg	
θ_e	17	mech deg	

Table 4.13 Physical dimensions

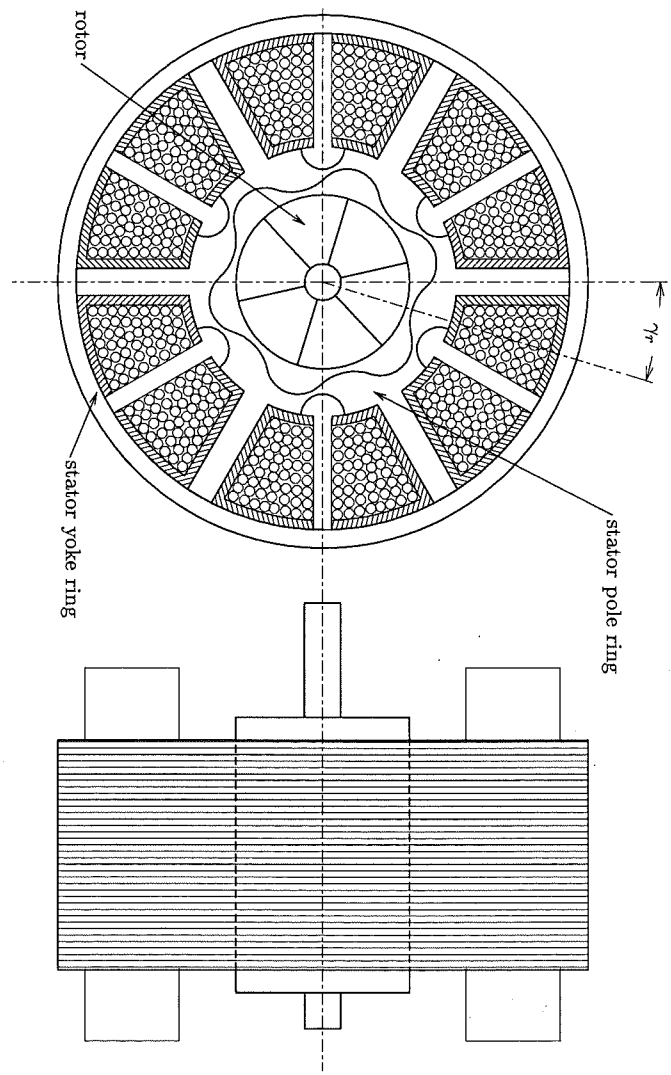

Figure 4.50 6-pole ferrite unidirectional motor.

	value	units	comment
ϱ	4900	Kg/m^3	Density of ferrite rotor
B_r	0.42	T	Remanence of ferrite rotor
μ_r	1.07		Relative recoil permeability of ferrite
ξ_m	0.75		PM flux linkage factor
ξ_L	1.33		Stator flux linkage factor
D_c/D_i	0.9		Ratio of uninsulated to insulated wire diameters
V	220	V RMS	Terminal voltage for turn calculation

Table 4.14 Miscellaneous input parameters

	value	units	comment
$\hat{T}_r$	0.0864	Nm	Amplitude of PM reluctance torque, eqn. 4.52
$\overline{T}$	0.0864	Nm	Rated torque, $\overline{T} = \hat{T}_r$
RPM	1000		Revolutions per minute
P_{out}	9.05	W	$P_{out} = \overline{T}\omega_e/p$
TRV	12.2	kNm/m^3	Torque per unit rotor volume, eqn. 4.139
m_r	0.0417	Kg	Rotor mass, $\varrho\,(\pi/4)\,D_r^2 L_r$
J_r	18.8×10^{-7}	$Kg.m^2$	Rotor inertia, eqn. 4.67
$\frac{4\hat{W}_r p^2}{J\omega_e^2}$	1.40		Backward instability ratio, with $J = 2J_r$
A_w	78.7×10^{-6}	m^2	Coilside area per pole, eqn. 4.110
K_m	2.71×10^{-4}	Wb	PM flux linkage constant, eqn. 4.107
K_R	21.9×10^{-5}	Ω	Winding resistance constant, eqn. 4.113
K_L	7.29×10^{-7}	H	Inductance constant, eqn. 4.136
J_{RMS}	3.00	A/mm^2	RMS current density, eqn. 4.140
P_R	4.97	W	Resistive power loss, eqn. 4.141
η	0.65		Efficiency, $\eta = P_{out}/(P_{out} + P_R)$
n	2216	turns	Turns per pole, eqn. 4.137
N	13296	turns	Total stator turns, eqn. 4.138
$\hat{i}$	0.096	A	Amplitude of rated current, $\hat{i} = 4\hat{W}_r/\hat{\lambda_m}$
D_c	0.170	mm	Minimum diameter of copper wire required, $D_c = \sqrt{4A_c/n\pi}$
Γ	0.825		Pullout ratio, $\Gamma = \overline{T}/\overline{T}_p$, eqn. 4.49

Table 4.15 Calculated output parameters, excluding simulation parameters.

In Table 4.15, the torque per unit rotor volume is good, but the output power is lowered because the higher number of pole pairs reduces the mechanical speed to one third of the electrical speed. The values of backward instability ratio, resistive power loss, and pullout ratio Γ are all similar to those of the single pole pair design. The current density is not high. However, the coilside area per pole and stator diameter cannot be reduced. This is because doing so increases Γ, as explained in section 4.9.3, and Γ is already at its upper limit in this design.

	value	units	comment
$\hat{v}$	$\sqrt{2}\,220/\sqrt{2}\,230$	V	
f	50	Hz	
p	3		
$\hat{\lambda}_{m1}$	0.601	V.sec	Eqn. 4.106
$\hat{\lambda}_{m3}$	0.045	V.sec	
R	1075	Ω	Eqn. 4.112
L	3.58	H	Eqn. 4.136
$\hat{W}_r$	0.0144	J	
γ_r	17.0	mech deg	
β_1	6.1	elect deg	
β_3	-25.4	elect deg	

Table 4.16 A selection of simulation parameters for the ferrite unidirectional motor design.

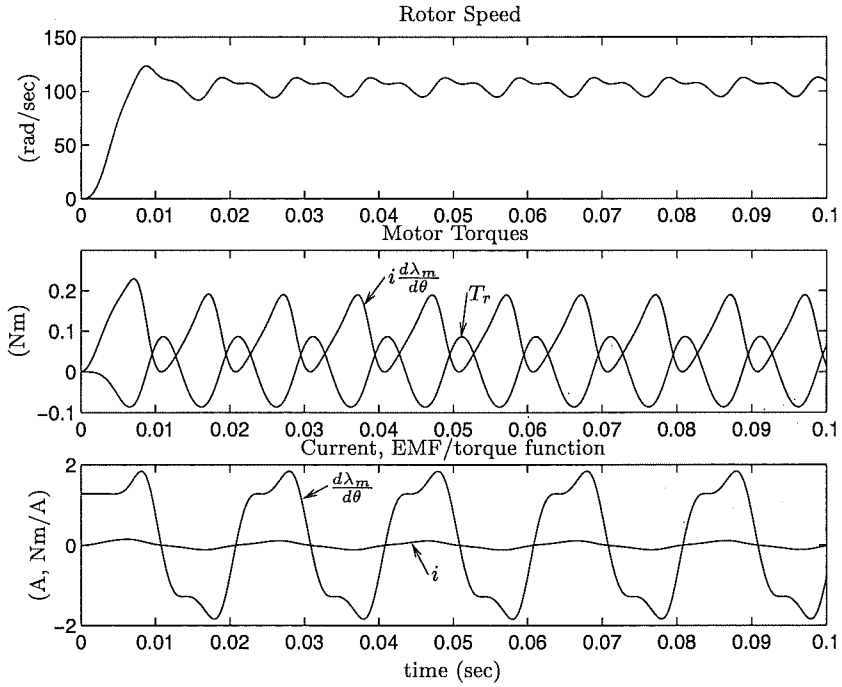

Figure 4.51 Simulation of starting for the rated quadratic load. $T_l = \hat{T}_r$, $J = 2J_r$, 220 V RMS, and $\epsilon = 0$. $a = p\hat{\theta}/\omega_e = 0.09$.

4.10.4 Simulation

The 6-pole unidirectional motor is simulated and assessed in the same manner as the 2-pole motor. Fig. 4.51 shows a starting characteristic for the rated quadratic load at 220 V RMS. There is an unperturbed (100 Hz) modulation in the steady state speed. This is caused by the third harmonic in the EMF/torque function which creates harmonics in the phase-magnet torque $i\frac{d\lambda_m}{d\theta}$. The current is also distorted. Whilst being non zero, the speed modulation still remains low.

Fig. 4.52 shows the speed characteristic where the magnitude of the quadratic

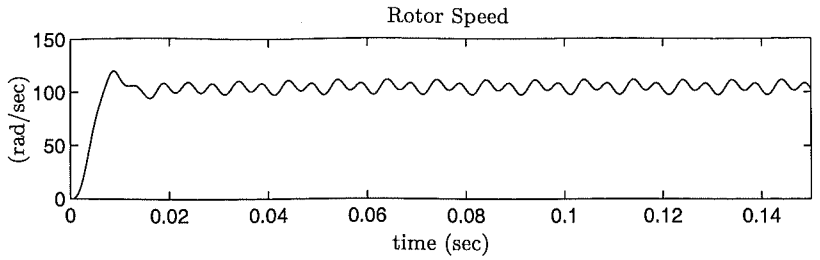

Figure 4.52 Simulation of starting for $T_l = 1.1\,\hat{T}_r$. The remaining parameters are the same as those of Fig. 4.51. $a = 0.07$.

load is increased to $T_l = 1.1\hat{T}_r$. The speed ripple is decreased slightly at this value of the load. Fig. 4.53 shows that the speed modulation is larger for a reduced load of $T_l = 0.9\,\hat{T}_r$.

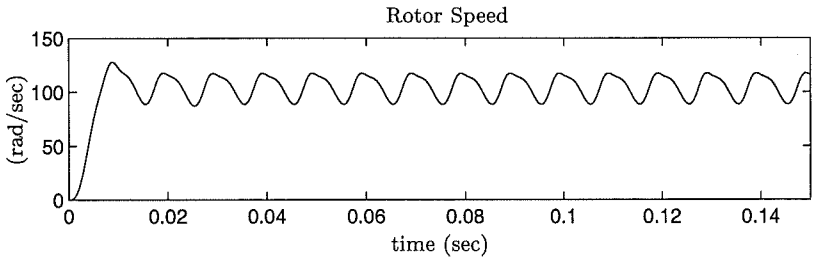

Figure 4.53 Simulation of starting for $T_l = 0.9\,\hat{T}_r$. The remaining parameters are the same as those of Fig. 4.51. $a = 0.14$.

$J = 2J_r$

220 V RMS		
Type of motion		Load range
Forward unperturbed		$0.75\,\hat{T}_r \le T_l \le 1.15\,\hat{T}_r$
Backward stable	unperturbed	$0.5\,\hat{T}_r \le T_l \le 0.7\,\hat{T}_r$
(Bidirectional)	perturbed 50 Hz	$T_l = 0.4\,\hat{T}_r$
Forward perturbed	50 Hz	$0.1\,\hat{T}_r \le T_l \le 0.3\,\hat{T}_r$
	25 Hz	$T_l = 0.05\,\hat{T}_r$

230 V RMS	
Forward unperturbed	$0.8\,\hat{T}_r \le T_l \le 1.24\,\hat{T}_r$
Backward stable unperturbed	$0.6\,\hat{T}_r \le T_l \le 0.75\,\hat{T}_r$
Forward unperturbed	$T_l = 0.5\,\hat{T}_r$
Backward stable perturbed 50 Hz	$T_l = 0.4\,\hat{T}_r$
Forward perturbed 50 Hz	$0.1\,\hat{T}_r \le T_l \le 0.3\,\hat{T}_r$
Forward asynchronous	$T_l \le 0.05\,\hat{T}_r$

Table 4.17 Quadratic load simulation results for starting.

Table 4.17 shows the quadratic load simulation results for starting. Forward unperturbed motion is obtained over a satisfactory range of the starting load. Perturbations

and backward stability can occur at lower load values. The results are similar to those of the 2-pole unidirectional motor.

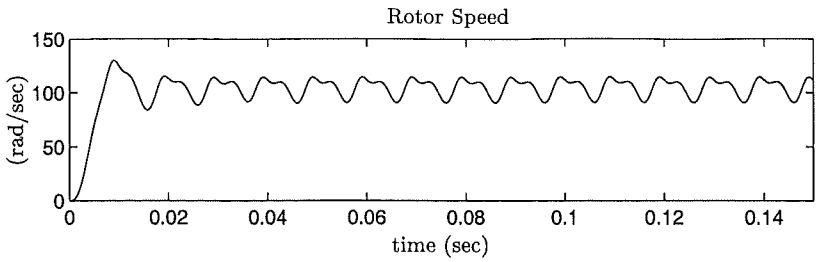

Figure 4.54 Simulation of starting for the rated linear load. $J = 1.75\,J_r$, 220 V RMS, and $\epsilon = 0$. $a = 0.11$.

Fig. 4.54 shows a starting characteristic for the rated linear load. Table 4.18 shows

$J = 1.75\,J_r$

220 V RMS	
Forward unperturbed	$0.7\,\hat{T}_r \leq T_l \leq 1.14\,\hat{T}_r$
Forward perturbed 50 Hz	$0.2\,\hat{T}_r \leq T_l \leq 0.6\,\hat{T}_r$
Forward asynchronous	$T_l \leq 0.1\,\hat{T}_r$

230 V RMS	
Forward unperturbed	$0.6\,\hat{T}_r \leq T_l \leq 1.21\,\hat{T}_r$
Forward perturbed 50 Hz	$0.2\,\hat{T}_r \leq T_l \leq 0.5\,\hat{T}_r$
Forward asynchronous	$T_l \leq 0.1\,\hat{T}_r$

Table 4.18 Linear load simulation results for starting.

the linear load simulation results for starting. The inertia is reduced to $J = 1.75\,J_r$ because backward stable results were found to occur near the rated load for $J = 2\,J_r$. This again suggests that a higher backward instability ratio is required for a linear load. The linear load results are very similar to those of the 2-pole motor.

In summary, the self-correcting ability and motion of this multiple pole pair motor are quite similar to that of the single pole pair motor. However, a small amount of speed ripple is unavoidable for a multiple pole pair motor at the rated load because of the presence of the third harmonic in the EMF/torque function .

4.11 CONCLUSIONS

The concept of the unidirectional single phase PM motor has been developed. It is shown that the theory of the conventional single phase synchronous PM motor provides a general framework for the unidirectional motor. Within this framework, the unidirectional motor is designed to operate at a specific load angle where the current

and the EMF/torque function are in phase. Steady state equations specific to this unidirectional load angle have been developed.

The backward instability ratio is proposed as an approximate measure of the ability of a unidirectional motor to self correct its direction of rotation. Two unidirectional motor designs which use this ratio as a design guide are completed. The first motor design uses a single pole pair ($p = 1$) and a higher grade of PM material, which is bonded Nd-Fe-B. The second design uses multiple pole pairs ($p = 3$) and ferrite grade magnets.

These designs use parallel magnetised rotor poles and closed stator slots. This allows the unidirectional motor concept to be implemented in a manufacturable construction. It is shown that the common single stator slot design cannot be used because a sufficiently large PM reluctance torque displacement angle γ_r cannot be obtained.

Theoretical models are developed for calculating the EMF/torque function and the PM reluctance torque of these designs. It is shown that a single pole pair parallel magnetised rotor yields a sinusoidal EMF/torque function. In the unidirectional design, phase shifting of the EMF/torque function occurs due to the sinusoidal airgap modulation. It is shown that as the number of pole pairs increases, a parallel magnetisation more closely approximates a radial magnetisation. This results in the third harmonic in the EMF/torque function becoming significant for pole pair numbers greater than one. The PM reluctance torque is obtained by calculating the stored field energy in the rotor and airgap. The model developed shows that parallel magnetised rotor poles and a sinusoidal airgap modulation yield a very good approximation of a sinusoidal reluctance torque.

Each motor is simulated using the equations of motion to evaluate design success. Mechanical loads which are either linear or quadratic functions of the rotor speed are used in the simulations. The 2-pole motor is shown to exhibit unidirectional behaviour over a satisfactory range of starting loads. Unidirectional motion without speed ripple is achieved at the rated load and rated terminal voltage. Simulation results show that this design is particularly well suited to quadratic loads such as water-pumps. The construction of the 2-pole motor is simple. However, production of this motor may be presently excluded because of the higher cost of bonded Nd-Fe-B magnet material in comparison to ferrite material. The use of bonded Nd-Fe-B yields a relatively high value of torque per unit rotor volume (TRV) in comparison to the conventional 2-pole ferrite motor designs.

The 6-pole ferrite motor is also shown to exhibit unidirectional behaviour over a satisfactory range of starting loads. However, it is shown that the third harmonic present in the EMF/torque function exacerbates speed ripple. The speed ripple at the rated load still remains relatively small compared to the conventional designs. This multiple pole pair motor is less attractive than the single pole pair motor in a number of

other respects. The cost of the ferrite material is acceptable but the cost and complexity of the construction is higher. A higher number of rotor poles are required. Each rotor pole is required to be individually magnetised prior to the assembly of the rotor. The stator construction is similarly more complex. The punching of stator laminations is more intricate. More windings and winding connections are required. A higher number of turns are required to be wound. Both the 2-pole and 6-pole designs deliver a similar amount of power even though the 6-pole motor is considerably larger. The 6-pole motor requires over three times as much copper as the 2-pole design. More stator iron is also required to accommodate the larger winding area. The output power is lowered because the higher number of poles reduces the mechanical speed to one third of the electrical speed. The reduction in the power density caused by the reduction in the rotor speed is identified as a major drawback of a multiple pole pair design in general. The 6-pole design uses the same rotor dimensions and ferrite material as the conventional 2-pole Siemens water-pump motor. The rated torque of the 6-pole motor is much higher than that of the Siemens motor. But to achieve the same power density (per unit rotor volume) as the Siemens motor, the rated torque of the 6-pole motor must be increased by 66%. This is not possible because the amplitude of the PM reluctance torque cannot be made larger without making the modulation of the rotor airgap excessively large. The stator would also become oversized.

Because the advantage of a high power density is lost, it would appear that a multiple pole pair motor is only of advantage if a slower synchronous shaft speed is required. The 6-pole motor is designed to run at a synchronous speed of 1000 RPM. This is a suitable speed for running a fan if the acoustic noise is required to be limited. The load of a fan is also a quadratic function of the rotor speed. The unidirectional nature of the motor ensures that air is not blown backwards after starting. However, being able to satisfactorily reduce the inertia of the fan blades to within the maximum allowable limit whilst still attaining the required airflow may prove to be challenging in such an application.

The unidirectional motor design, in general, offers solutions or improvements to several of the less desirable characteristics of the conventional 2-pole design. As mentioned in section 1.2.6, the twice electrical frequency speed oscillations of the conventional motor produce noise. This noise hampers the use of these motors in high quality household appliances [Altenbernd and Wahner 1996]. In contrast, the unidirectional motor is proposed to greatly reduce, or eliminate altogether, speed ripple about the rated value of the load.

The final direction of rotation is not predetermined for the conventional motor. This limits the application of the conventional motor to water-pumps and reciprocating loads if a mechanical device is not used to correct the direction of rotation. For the unidirectional motor, such a device may be omitted.

As mentioned in section 1.2.2, the magnitude of the PM reluctance torque available to move the rotor to a startable position is low because the PM reluctance torque displacement angle γ_r is limited. This places a restriction on the magnitude of any speed independent component of the load. For example, if the rotor is de-accelerating to rest after de-energisation, and the load torque is greater than the reluctance torque, then the rotor may come to rest at $\theta = 0$. In this case, the motor cannot restart. The PM reluctance torque of the unidirectional motor is equal to the rated torque at this rotor position. Therefore, in contrast, the unidirectional motor is capable of rotating the rotor to a startable position even if the speed independent load is nearly as large as the rated torque. This raises the possibility of using the unidirectional motor in load applications which the conventional motor cannot start.

The concept of the unidirectional motor has now been developed in detail. The theory and ideas presented now require experimental validation. This will identify any considerations which may have been overlooked, and will lead to further understanding and refinement of the ideas presented.

4.11.1 2-Pole Unidirectional Motor Designs using Ferrite Rotors

This section describes two proposed unidirectional motor designs which are considered to be more practical for production. In each design, the rotor is constructed using a 2-pole ferrite rotor. The rotor design is therefore cheap and simple. The 2-pole closed slot design of Fig. 4.34 is used.

The first design is described as follows. The proportionality relationship in eqn. 4.103 suggests that if the rotor diameter is made small enough, then a single pole pair rotor of ferrite construction will have a sufficiently high backward instability ratio. Analysis of the rotor and airgap design suggests that a rotor diameter of about 10 mm is at the upper limit for a 2-pole ferrite rotor design. The corresponding amplitude of the PM reluctance torque obtained corresponds to a rated output power of about 3.5 to 4 Watts. This rating is in the range of the motors originally described by [Thees 1965]. The conventional motors in this power range are limited to applications such as electric can openers, juicers, and aquarium pumps [Altenbernd and Wahner 1996]. The conventional single phase synchronous PM motor manufactured by Hozelock[3] is an example of a garden waterpump in this power range. A mechanical direction correcting device is employed to make the impeller rotation unidirectional. This device consists of a plastic arm which is pushed out by the waterflow into the impeller chamber to impede rotation only if the direction of rotation is incorrect. The proposed advantage of the unidirectional ferrite motor in such an application is that the correcting device is not required, and the pump is expected to run more quietly and smoothly.

[3]Nameplate details are: Hozelock Micro 450 model 3304-0000, 230 V, 50 Hz, 6 W (power input), 0.03 A. Maximum head height 1 metre, 450 litres/hr. Made in the UK.

The second design is described as follows. In order to obtain a sufficiently high backward instability ratio, the unidirectional motor may be described as having even tighter inertial constraints than the conventional motor. By removing the constraint of the backward instability ratio, the rotor diameter of the unidirectional motor may be made as large as the maximum permissible diameter of the conventional motor. This diameter is only limited by the starting acceleration. However, by removing the backward instability constraint, the unidirectional capability is lost. Fig. 4.4 shows that if the motor runs in the backward direction, then the torque pulsations are very high. The resulting speed ripple is significantly higher than the conventional motor, and there is no advantage in such a design. If, however, it is feasible to use a mechanical direction correcting device, the unidirectional motor will always run in the forward direction. At the rated load, speed ripple is then eliminated. The advantage of using a larger ferrite unidirectional motor with a direction correcting device is reduced noise under load, at a higher power rating.

Chapter 5

THE INDUCTIVE START SINGLE PHASE SYNCHRONOUS PM MOTOR

5.1 INTRODUCTION

Conventional single phase synchronous PM motor designs rely upon modifying the PM reluctance torque to achieve a non-zero displacement angle to allow starting. This is achieved by using either an asymmetric stator airgap or a saturating notch design, as described in section 1.2.2. Eqn. 2.64 shows that there are three torque producing mechanisms available in PM machines. The middle term of this equation identifies an *inductive reluctance* torque which is present when a winding is energised and the inductance of the winding is changing as a function of rotor position. This inductive reluctance torque is not exploited in the conventional designs. This chapter investigates the use of the inductive reluctance torque to enable a single phase PM motor to start.

5.2 THEORETICAL BASIS

Fig. 5.1(a) illustrates the PM reluctance torque concept developed in Chapters 1 and 4 where the PM displacement angle γ_r is set to 45 electrical degrees. This allows the PM reluctance torque available to move the rotor to a startable position to be maximised about the $\theta = 0$ position. Fig. 5.1(b) shows a waveform of the same phase and period,

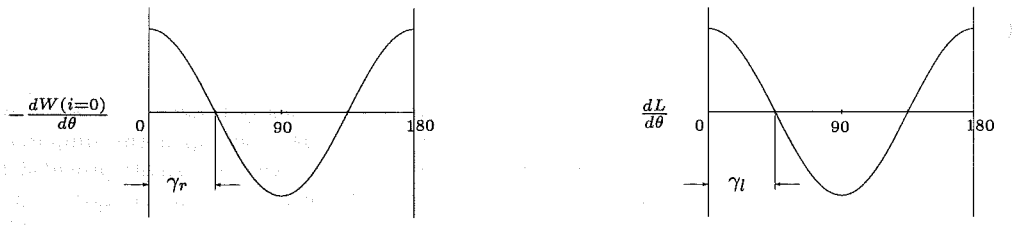

(a) Uni-directional.

(b) Inductive start.

Figure 5.1 Mechanisms for the provision of torque about rotor alignment angle $\theta = 0$ for single phase synchronous PM motor designs.

corresponding to the derivative of inductance with respect to rotor position. This is a hypothetical inductance characteristic. In eqn. 2.64, for the magnetically linear case, the inductive reluctance torque in the PM motor is given by[1]

$$T_{ind} = \frac{1}{2} i^2 \frac{dL}{d\theta} \tag{5.1}$$

Therefore, with the stator winding energised, the inductance characteristic of Fig. 5.1(b) also provides a torque to move the rotor to a startable position away from the $\theta = 0$ position. Furthermore, during switch-on, the current corresponds to the locked rotor current providing a significant boost to the inductive reluctance torque.

The aim of this chapter is not to design a motor with the characteristic of Fig. 5.1(b) implemented in order to attempt to achieve unidirectional motion, but to facilitate the starting of the motor only. As such, the motor will be referred to as the *inductive start* motor. The direction of final rotation still remains un-predetermined like the conventional motor.

5.2.1 Inductance

The inductance of the conventional motor varies as a function of both the rotor position and the stator winding current, such that $L = L(i, \theta)$. However, the modulation of the inductance is small compared to its DC value. By assuming the inductance to be constant, a model of the motor is simplified. The conventional motor is modelled sufficiently accurately by making this simplifying assumption.

For the inductive start motor, the assumption of constant inductance does not allow a reluctance torque model to be developed. For the inductive start motor, analysis of inductance modulation during start up must be included. The inductance can be calculated from

$$L = n^2 \mathcal{P} \tag{5.2}$$

where the permeance $\mathcal{P}$ is given by

$$\mathcal{P} = \mu_r \mu_o \frac{A}{l} \tag{5.3}$$

[1]The inductive reluctance torque is assumed to have this form. The total motor torque is given exactly by eqn. 2.62, but the reluctance components of torque are not clearly resolved. In eqn. 2.64, an attempt is made to resolve these components. However, eqn. 2.64 relies upon the simplifying assumption of separating the stored energy $W(i, \theta)$ into mutually exclusive components provided by the winding and magnet as given by eqn. 2.63. Eqn. 2.63, is however, an approximation. It is questionable whether $W(i, \theta)$ can be resolved exactly into two mutually exclusive components, which represent energies associated with the two reluctance torques. Thus it is questionable whether exact further resolution of eqn. 2.62 is possible. Thus, it is possible that neither the second nor third RHS terms of eqn. 2.64 are exact. However, eqn. 2.64 has been shown to model the motion of a single phase PM motor sufficiently accurately. In this current chapter, eqn. 5.1 is conveniently extracted from eqn. 2.64 for the purpose of developing a model.

In eqn. 5.3, the relative permeability μ_r can be defined by an effective value representing the entire magnetic circuit of the stator. Similarly, flux path cross-sectional area A, and flux path length l can be defined as effective quantities which represent the physical dimensions of the magnetic circuit. The ratio A/l is fixed if the physical dimensions of the magnetic circuit do not change. The modulation of the inductance of the conventional motor may therefore be described as being caused only by a modulation of μ_r, as motion of the rotor does not change the physical dimensions of the magnetic circuit. The modulation of μ_r is caused by modulation of the resultant MMF. The relationship between the resultant MMF and μ_r is nonlinear, and is dependent on the magnetisation characteristic of the stator iron used. If hysteresis is present, μ_r is a function of the magnetisation history as well as the resultant MMF.

The resultant MMF is the vector sum of MMF contributions from the energised stator winding, and the PM rotor. This is illustrated by Fig. 4.1, where the stator MMF is proportional to the stator current I, and the rotor MMF is proportional to fictitious current I_m. For the case where synchronous motion occurs at constant instantaneous speed with constant load, the amplitude of the stator current remains fixed. In this case the resultant MMF is fixed in amplitude, and varies sinusoidally as a function of both time and rotor angle.

The relative permeability not a function of the sign of the resultant MMF, but only of its absolute value. The relative permeability and permeance therefore complete two cycles of modulation per cycle of resultant MMF. The result is an inductance modulation which completes two cycles per electrical cycle. Fig. 4.1 shows that the phase and amplitude of the resultant MMF changes with load angle. The modulation of the inductance is therefore also affected by the load angle.

For the case where the rotor is stationary and locked at an arbitrary rotor position, the rotor MMF is represented by I_m remaining fixed with respect to time. With respect to the rotor, the stator current oscillates. The magnitude of the stator current over an electrical cycle may by represented by its RMS value. This RMS value is permanently aligned with the stator d-axis. This is illustrated by Fig. 5.2. Fig. 5.2 shows that the resultant locked rotor MMF does, however, vary sinusoidally as a function of the rotor position. This results in both the locked rotor permeance and inductance completing two cycles of modulation per mechanical cycle for a 2-pole motor.

The locked rotor inductance measurements of Fig. 5.22 show that the locked rotor inductance characteristic completes two cycles per electrical cycle. The inductance characteristics are quasi-sinusoidal. As a first approximation, the locked rotor inductance may then be described mathematically by

$$L = L_o + \hat{L}\cos 2(\theta - \gamma_l) \tag{5.4}$$

for a 2-pole motor where

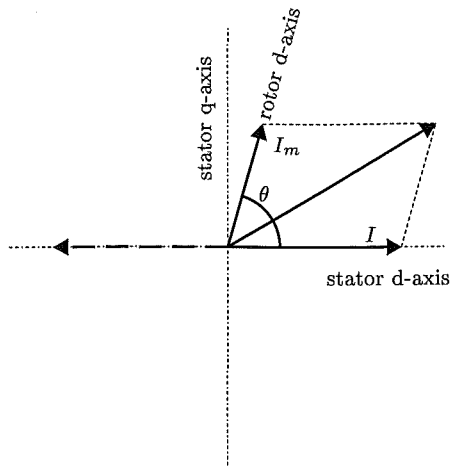

Figure 5.2 Locked rotor representation of the rotor and stator MMFs. The RMS value of the stator current I is fixed to the stator d-axis.

L_o = DC value of inductance
$\hat{L}$ = amplitude of the inductance modulation
γ_l = inductance displacement angle

Minimum inductance occurs when the rotor and stator poles are aligned about $\theta = 0$. Maximum inductance occurs when the rotor poles are aligned with the stator q-axis about $\theta = 90°$. The locked rotor inductance displacement angle for the conventional motor may therefore be set to $\gamma_l = 90°$. The derivative of the locked rotor inductance with respect to rotor position is given by

$$dL/d\theta = -2\hat{L}\sin 2(\theta - \gamma_l) \tag{5.5}$$

Assuming that eqn.s 5.1 and 5.5 are sufficiently accurate, the locked rotor inductive reluctance torque is given by

$$T_{ind} = -i^2\hat{L}\sin 2(\theta - \gamma_l) \tag{5.6}$$

In the worst case for starting an inductive start motor, the rotor may be held by a high static friction, or moves at a slow speed relative to the electrical angular speed. These situations approximate the locked rotor case. In these situations, eqn. 5.6 may be used to develop a model of the inductive start motor for starting. The mechanical equation of motion given by 4.53 is then extended by including the term for inductive reluctance torque to yield the angular acceleration during starting as

$$\frac{d\dot{\theta}}{dt} = \frac{1}{J}\left[i\hat{\lambda}_m \sin\theta - \hat{T}_r \sin[2(\theta - \gamma_r)] - i^2\hat{L}\sin[2(\theta - \gamma_l)] - T_l\right] \tag{5.7}$$

5.2.2 The Start Angle

As mentioned previously, for the conventional motor, the purpose of the non-zero PM displacement angle γ_r is to bring the rotor into a position where the phase-magnet torque $i\hat{\lambda}_m \sin\theta$ can proceed to bring the rotor into synchronism. The purpose of using an inductive reluctance torque is similar. Thus in an inductive start motor, the conventional method used to create a non-zero PM displacement angle γ_r can be eliminated. With an asymmetric stator airgap or saturating technique removed, γ_r becomes zero. However, the PM reluctance torque still remains. For example, if the techniques for creating a non-zero γ_r are removed from the designs of Fig. 1.2, cogging torques will act to align the rotor and stator direct axes[2]. Thus, for the inductive start motor, the rest angle when the stator is de-energised is $\theta = \gamma_r = 0$, and the rotor and stator poles are aligned.

The PM reluctance, as well as the phase-magnet and inductive reluctance torques may all be present near the rotor and stator alignment angle when the stator winding is energised. Because the purpose of the inductive reluctance torque is to bring the rotor to a startable position where the phase-magnet torque $i\hat{\lambda}_m \sin\theta$ can act significantly, the influence of the phase-magnet torque in this process will be ignored. With $\gamma_r = 0$, the PM reluctance torque opposes any rotation which disaligns the rotor and stator direct axes. The presence of the PM reluctance torque prevents the inductive reluctance torque from moving the rotor to the inductive torque rest position at $\theta = \gamma_l$. Instead, the rotor will come to rest at an equilibrium angle which will be called the *start angle* γ_{st}, if the influence of the phase-magnet torque is ignored. The start angle γ_{st} is defined for the purpose of quantitatively assessing the starting ability of an inductive start motor.

If the PM and inductive reluctance torques are assumed to be sinusoidal quantities then the start angle may be calculated using eqn. 5.7. The torques corresponding to the terms $i\hat{\lambda}_m \sin\theta$ and T_l are ignored. If the rotor is moving at a slow speed relative to the electrical angular speed, the inductive reluctance torque pulsates at twice the electrical frequency. Because the inductive torque is proportional to the square of the current, it can be represented by an average value corresponding to the RMS value of the locked rotor current I_{lkr}. Under this representation, the PM and inductive torques balance each other at static equilibrium when $\theta = \gamma_{st}$. The angular acceleration is zero. In this case, with $\gamma_r = 0$, eqn. 5.7 reduces to

$$-\hat{T}_r \sin 2\gamma_{st} - I_{lkr}^2 \hat{L} \sin 2(\gamma_{st} - \gamma_l) = 0 \tag{5.8}$$

The start angle may be obtained from eqn. 5.8.

[2]The q-axis notches in Fig 1.2(b) in this case remain, preventing PM flux from short-circuiting the windings. The d-axis notches are filled in.

Note that the start angle is not the angle at which acceleration to synchronisation finally occurs. Synchronisation is discussed in section 1.2.3.

5.2.2.1 Experimental Measurement of the Start Angle

The start angle may be measured experimentally by coupling a sufficiently large moment of inertia to the rotor shaft. This method is explained with reference to eqn. 5.7. With a sufficiently large J the phase-magnet torque $i\hat{\lambda}_m \sin\theta$ is able to generate only a very small angular acceleration over either a positive or negative half cycle of the locked rotor current. This acceleration is reversed over the subsequent half cycle. This results in the effective averaging of the phase-magnet torque to zero. It is impossible for synchronisation to occur. However, the PM and inductive reluctance torques do not average to zero. The angular acceleration provided by these two torques eventually rotates the rotor to the equilibrium position γ_{st}. The value of the additional moment of inertia is chosen such that electrical frequency oscillation of the shaft is visually imperceptible.

5.2.3 Modifying the Inductance

As described in section 5.2.1, the locked rotor inductance of the conventional motor varies as a function of rotor position. However, substitution of $\gamma_l = 90°$ into eqn. 5.6 shows that the inductive reluctance torque is zero at $\theta = 0$. To achieve a desirable inductance characteristic to allow starting, an appropriate additional inductance characteristic L_a must be superimposed upon the conventional characteristic L_c. Eqn. 5.4 may then be expressed as the sum of two components:

$$L = L_o + \hat{L}\cos 2(\theta - \gamma_l) = L_c + L_a \tag{5.9}$$

Given the first approximation of a sinusoidal characteristic, the conventional inductance may be described by

$$L_c = L_{oc} + \hat{L}_c \cos 2(\theta - \gamma_{lc}) \tag{5.10}$$

where $\gamma_{lc} = 90°$. By assuming a sinusoidal characteristic, the additional locked rotor inductance may be described by

$$L_a = L_{oa} + \hat{L}_a \cos 2(\theta - \gamma_{la}) \tag{5.11}$$

where L_{oa} is the DC value contributed by the additional inductance The additional inductance may be physically realised by attaching a specially designed iron lamination to the rotor. The theory and design of an iron rotor lamination is described in section 5.2.4. Eqn.s 5.10 and 5.11 may be substituted into eqn. 5.9. Differentiation with

respect to rotor position followed by substitution into eqn. 5.1 then yields eqn. 5.6 resolved into two components of inductive reluctance torque:

$$T_{ind} = -i^2 \hat{L} \sin 2(\theta - \gamma_l) = -i^2 \hat{L_c} \sin 2(\theta - \gamma_{lc}) - i^2 \hat{L_a} \sin 2(\theta - \gamma_{la}) \tag{5.12}$$

Substitution of eqn. 5.12 into eqn. 5.8 with $\theta = \gamma_{st}$ and $i = I_{lkr}$ yields the torque balance between the PM reluctance torque and the two inductive torque components:

$$-\hat{T_r} \sin 2\gamma_{st} - I_{lkr}^2 \hat{L_c} \sin 2(\gamma_{st} - \gamma_{lc}) - I_{lkr}^2 \hat{L_a} \sin 2(\gamma_{st} - \gamma_{la}) = 0 \tag{5.13}$$

To be feasible, an inductive start motor should have a start angle γ_{st} as least as large as the PM reluctance torque displacement angle γ_r of a comparable conventional motor. For an inductive start motor design where γ_{st} has been specified, the required amplitude of the additional inductance $\hat{L}_a$ will be obtained from eqn. 5.13. Assuming that the Siemens motor can be modified to become an inductive start motor, a calculation of the required value of $\hat{L}_a$ is of initial interest. Values of relevant parameters corresponding to the conventional Siemens motor are listed in Table 5.1.

	value	units	comments
γ_r	7	elect deg	Measured
$\hat{T_r}$	0.03	Nm	Approximate value
L_{oc}	1.528	H	Average measured locked rotor value over an inductance cycle at 220 V RMS
$\hat{L_c}$	0.108	H	Measured locked rotor value at 220 V RMS
I_{lkr}	0.445	A (RMS)	Average measured locked rotor value over an inductance cycle at 220 V RMS
γ_{lc}	90	elect deg	

Table 5.1 Conventional Siemens motor parameters. The method of inductance measurement is described in section 5.5.5.1 and the inductance measurements correspond to Fig. 5.22.

Setting $\gamma_{la} = 45°$ produces a $dL_a/d\theta$ characteristic equivalent to Fig. 5.1(b). This ideally provides for maximum inductive reluctance torque at $\theta = 0°$. For the conventional Siemens motor, $\gamma_r = 7°$. The value of $\hat{L}_a$ calculated for $\gamma_{st} = 7°$ is 0.0096 H. This amplitude represents 0.6% of the average inductance L_{oc}. This calculation suggests that only a small $\hat{L_a}$ is required. Fig. 5.3 plots the inductances used in this example.

The DC value of additional inductance L_{oa}, may however, be considerably larger than $\hat{L}_a$. For the purpose of illustration, a value of $L_{oa} = 8\hat{L}_a$ is used in Fig. 5.3. Fig. 5.4 plots the corresponding derivatives of inductances with respect to rotor position.

Fig. 5.5 plots the conventional inductive reluctance torque which is identified by $T_{ind\,c}$, the additional inductive reluctance torque which is identified by $T_{ind\,a}$, the PM reluctance torque T_r, and the resultant of all three of these torques. The resultant

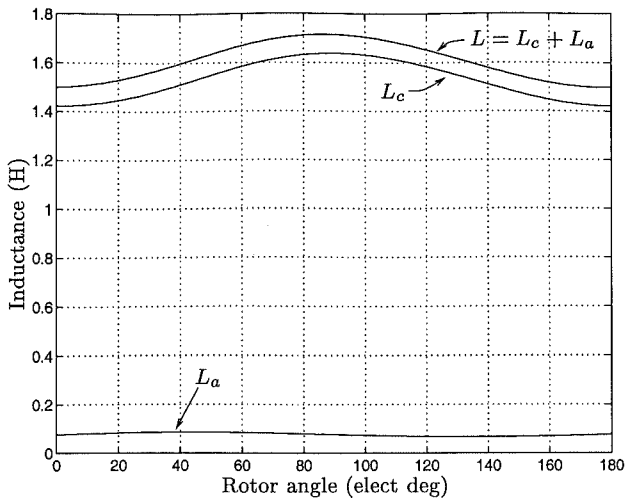

Figure 5.3 Inductive start motor ideal inductance waveforms: L_c as defined by eqn. 5.10 using L_{oc} and $\hat{L}_c$ measurements listed in Table 5.1; L_a as defined by eqn. 5.11 with $L_{oa} = 0.077$ H, $L_a = 0.0096$ H, and $\gamma_{la} = 45°$.

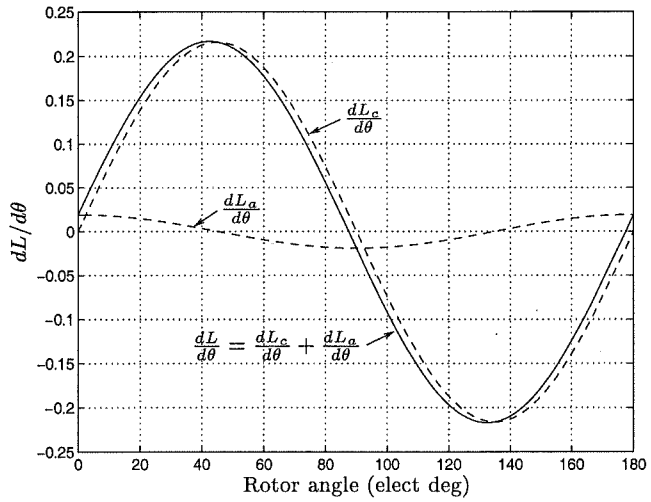

Figure 5.4 Derivatives of inductances with respect to rotor position corresponding to Fig. 5.3.

torque is non-zero at $\theta = 0$ with a phase angle $\gamma_{st} = 7°$. $T_{ind\,c}$ and T_r are in anti-phase. $T_{ind\,c}$ directs the rotor to the quadrature position while T_r directs the rotor in an opposite direction to the aligned position. The value of the PM reluctance torque amplitude $\hat{T}_r$ listed in Table 5.1 is approximate and is measured with the stator winding de-energised. In this example, it is assumed that $\hat{T}_r$ is unaffected by saturation caused by the locked rotor current.

For the example of sinusoidal torques, Fig. 5.5 allows a comparison of the torque available at $\theta = 0$ to be made between the conventional and the inductive start motors for equivalent displacements $\gamma_r = \gamma_{st} = 7°$. For the conventional motor, after the stator is de-energised the rotor comes to rest at $\theta = \gamma_r$. During this time no inductive reluctance torques are acting. Only the PM reluctance torque is present. At $\theta = 0$,

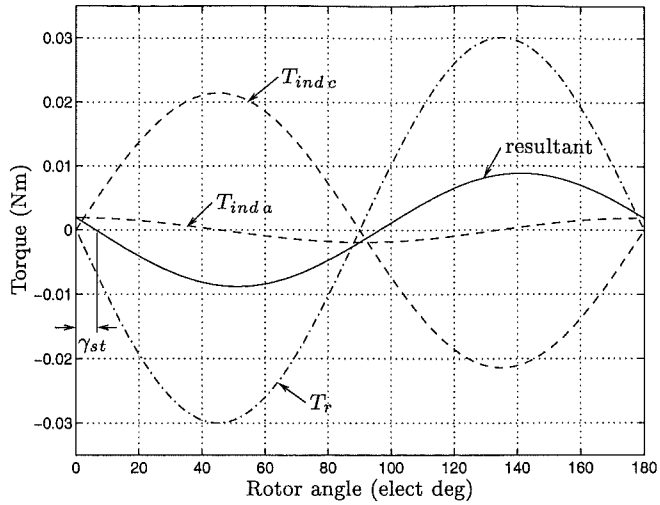

Figure 5.5 Inductive start motor ideal waveforms: PM and inductive reluctance torques corresponding to $\gamma_{st} = 7°$.

the magnitude of the PM reluctance torque available corresponds to the absolute value of T_r at $\theta = \gamma_{st}$ in Fig. 5.5. This value is seen to be several times larger than the resultant torque at $\theta = 0$ for the inductive start motor. The resultant torque at $\theta = 0$ for the inductive start motor is equal to $T_{ind\,a}$ at this position. Thus, in this theoretical example, if a high static friction torque is present, the conventional motor may have a better chance of moving the rotor to a startable position away from $\theta = 0$.

However, in Fig. 5.5, $T_{ind\,a}$ has been calculated using I_{lkr}, the RMS value of the locked rotor current. The peak value of $T_{ind\,a}$ is given by $(\sqrt{2}I_{lkr}/I_{lkr})^2 \times T_{ind\,a} = 2T_{ind\,a}$. The peak value of inductive torque at $\theta = 0$ is therefore twice the RMS value. The peak torque may be sufficient to dislodge a rotor held by high static friction.

5.2.4 Design of an Iron Rotor Lamination

This section investigates the theoretical feasibility of implementing the desired additional inductance characteristic L_a by attaching iron laminations to the rotor. Fig. 5.6(a) illustrates the design where one or more iron laminations may be attached to an end of the PM rotor. The lamination consists of a strip of iron. In this example, the long axis of the lamination is displaced $\gamma_{la} = -45°$ from the stator d-axis. The shape of the lamination is designed to increase the permeance $\mathcal{P}$ seen by the stator winding when the lamination is aligned at the position $\theta = \gamma_{la}$. At a quadrature position, as illustrated by Fig. 5.6(b), the permeance seen by the stator winding due to the rotor lamination is intended to be smaller than that at $\theta = \gamma_{la}$.

The rotor lamination is attached to the rotor at an angle γ_{la} with respect to the d-axis of the rotor. Thus, as the rotor lamination rotates toward alignment with the stator d-axis, the rotor rotates towards a startable position.

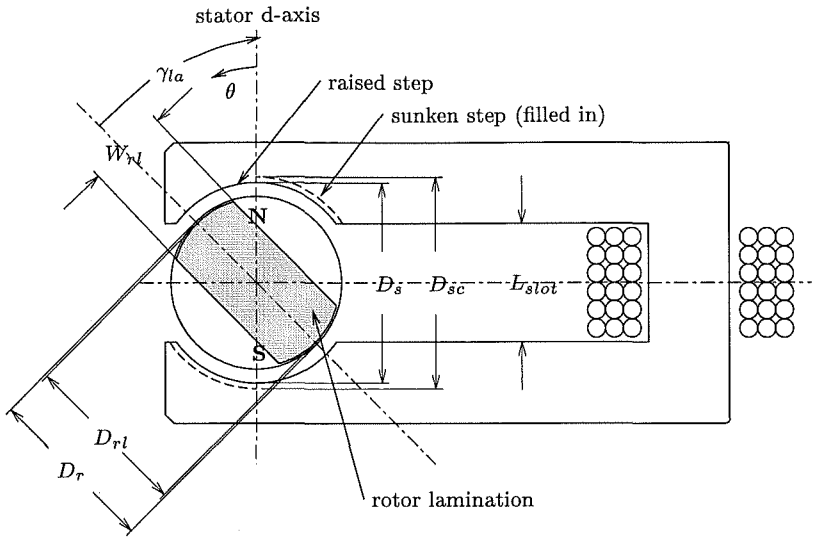

(a) $\theta = 0$. $\gamma_{la} = -45°$ in this drawing.

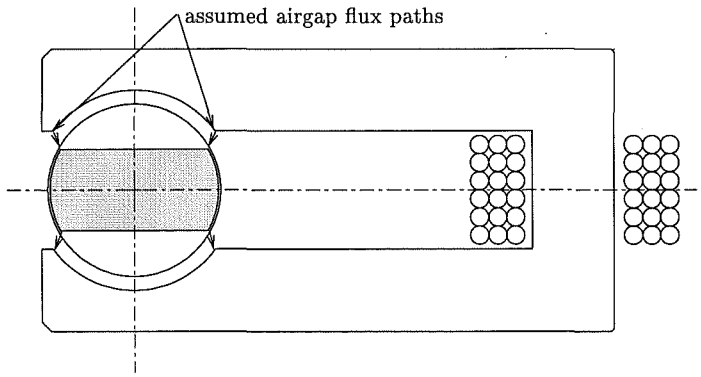

(b) $\theta = \gamma_{la} \pm 90°$.

Figure 5.6 Inductive start motor: design and placement of an iron lamination on the rotor. The single slot design of the Siemens motor is used in this example. The sunken step used in the conventional motor design is filled in.

	value	unit	comment
γ_{la}	45	elect deg	
W_{rl}	9	mm	
D_{rl}	18.5	mm	
l_t	0.5	mm	Rotor lamination thickness
D_s	22	mm	Siemens
D_r	19	mm	Siemens
L_{slot}	13	mm	Siemens
N	3100		Siemens serial winding turns

Table 5.2 Parameters for physical calculation of $\hat{L}_a$.

A very approximate calculation of the number of rotor laminations required to achieve $\hat{L}_a = 0.0096$ H may be made using the information in Fig. 5.6 and Table 5.2. The following calculation neglects saturation to stator and rotor laminations which may be caused by the PM rotor and the stator winding current. It is assumed that rotor laminations are axially aligned to stator laminations. In this example, the 'sunken steps' of the conventional Siemens motor are filled in. The stator airgap diameter D_s remains constant at the minimum allowable value.

Flux due to winding current crosses the airgaps linking stator and rotor laminations. Due to the fringing of this flux, the effective airgap area per rotor lamination is approximated by $A = \pi D_{rl}\, l_t/4$. At $\theta = \gamma_{la}$, the effective airgap length is approximated by $l = D_s - D_{rl} = 3.5$ mm. At $\theta = \gamma_{la}$, L_a is maximum and is approximated by $L_{r\,(max)} = N^2\mathcal{P}_{max} = N^2\mu_o A/l = 0.025$ H per rotor lamination.

Fig. 5.6(b) shows assumed flux paths corresponding to the quadrature position $\theta = \gamma_{la} \pm 90°$ for the calculation of the minimum value of L_a. The effective airgap area A is assumed to become halved, and the effective airgap length is approximated by $l = L_{slot} - W_{rl} = 4$ mm. This yields $L_{r\,(min)} = 0.011$ H. Then, for a single lamination, $\hat{L}_a = (L_{r\,(max)} - L_{r\,(min)})/2 = 0.007$ H. Approximately two laminations, each of 0.5 mm thicknesses are therefore required to achieve $\hat{L}_a = 0.0096$ H.

Approximating the moment of inertia per rotor lamination by $1/4\, \varrho_{iron} \pi l_t (D_{rl}/2)^4$ where $\varrho_{iron} = 7.8 \times 10^3$ Kg/m^3 yields 2.2×10^{-8} Kg.m^2. An appropriate value of J for the rotor, excluding laminations, is 14×10^{-7} Kg.m^2. In this example, each rotor lamination therefore increases the inertia of the rotor by about 1.6%. The very small increase in J caused by attaching this amount of iron lamination to the rotor is most unlikely to create starting difficulties.

The rotor of the Siemens motor is 5 mm longer than the stator lamination stack. If the rotor and stator lengths and their relative axial positions are left unmodified, the effective airgap lengths will be considerably larger than those used in the example above. An alternative approach which maintains the magnet overhang over the stator stack is to split the rotor into two sets of North-South pole halves. The rotor laminations

are placed in between the two halves. The rotor laminations are then located at the centre of the lamination stack after assembly. However, this approach increases the complexity of rotor construction and requires pole alignment of the two sets of magnet poles.

5.3 THEORETICAL COMPARISON

Sections 5.3.1 and 5.3.2 provide a theoretical comparison of the inductive start and conventional motors.

5.3.1 Starting

The PM reluctance torque provided by the conventional motor at $\theta = 0$ is obtained from eqn. 1.8 as

$$T_{r\,(\theta=0)} = \hat{T}_r \sin 2\gamma_r \tag{5.14}$$

The magnitude of this torque must be sufficient to overcome friction to bring the rotor to rest at a startable position. Substitution of $\gamma_{la} = 45°$, $\theta = 0$, and $i = \sqrt{2}I_{lkr}$ into the second RHS term of eqn. 5.12 yields the corresponding peak inductive reluctance torque provided by the inductive start motor upon energisation:

$$T_{ind\,(\theta=0)} = 2I_{lkr}^2 \hat{L}_a \tag{5.15}$$

For the conventional motor, γ_r is typically limited as discussed in section 1.2.2. The PM reluctance torque at $\theta = 0$ is therefore not easily increased. However, the inductive motor torque at $\theta = 0$ may be increased by adding more rotor laminations to increase $\hat{L}_a$.

Similarly, by adding more rotor laminations, the start angle may also be increased.

5.3.2 Synchronous Motion

The inductive start motor design enables the conventional stator asymmetric step, or the saturating notch technique, to be eliminated. Elimination of the asymmetric step enables the average airgap clearance between rotor and stator to be reduced. This increases the PM flux linkage per turn ϕ_m and the peak flux linkage $\hat{\lambda}_m$. With reference to the single slot design of Fig. 5.6(a), the increase in $\hat{\lambda}_m$ is a function of the sunken step's width. The increase in $\hat{\lambda}_m$ is also a function of the sunken step depth, $(D_{sc} - D_s)/2$, relative to the airgap clearance $(D_s - D_r)/2$.

Modelling constant inductance for steady state synchronous motion allows the conventional equations for motor performance to be applied to the inductive start

motor. This enables comparative calculations of torque and efficiency to be made using eqn.s 4.11 and 4.17, respectively. The pullout torque may be given by

$$\overline{T}_p = \frac{\hat{\lambda}_m(\hat{v} - \omega_e \hat{\lambda}_m \cos\alpha)}{2\sqrt{R^2 + (\omega_e L)^2}} \tag{5.16}$$

Increasing the PM flux ϕ_m by reducing the average airgap increases $\hat{\lambda}_m$, as $\hat{\lambda}_m = N\hat{\phi}_m$. If $\hat{\lambda}_m$ was previously set at a desirable magnitude, then increasing ϕ_m will require the number of turns N to be reduced to re-establish this magnitude. The impedance is reduced if the number of turns can be reduced. This does not change α, as the resistance and inductance are both proportional to the square of the turn number. But decreasing the impedance increases the pullout torque. However, adding laminations to the rotor increases the inductance by a value of L_{oa}, and may increase PM flux leakage at the rotor ends. This increases the impedance and decreases $\hat{\phi}_m$. But increasing the inductance also increases α, which increases the pullout torque. It is therefore difficult to determine if the pullout torque increases in an inductive start design by this theoretical comparison.

The theoretical model and design developed in the preceding sections suggest the following. First, only a small $\hat{L}_a$ is required to achieve a useful start angle. Secondly, a simple physical implementation is achievable. This suggests that the inductive start motor may be technically feasible. The theoretical analysis presented provides motivation to now proceed to an experimental investigation of the inductive start motor.

5.4 AN EXPERIMENTAL DESIGN

A conventional Siemens motor is modified to become an inductive start motor. This permits a useful comparison of both motor designs.

5.4.1 Rotor Lamination Design

Preliminary experiments were first carried out to determine an effective rotor lamination shape. The shapes of Fig. 5.7 were stamped out of silicon steel sheet. The rotor and its housing were removed from the Siemens stator lamination stack. Each of the rotor lamination shapes was centred, in turn, inside the stator airgap supported by a small shaft. The stator winding was energised at 220 V RMS and the torque exerted on each rotor lamination was felt via finger pressure. The shape in Fig. 5.7(b) produced the largest aligning torque. Various widths (corresponding to dimension W_{rl} in Fig. 5.6(a)) of this shape were then tested. Fig. 5.7(b) shows the dimensions of the finalised rotor lamination design. The dimension $W_{rl} = 9$ mm was considered by this experimental process to be approximately optimal for reluctance torque production

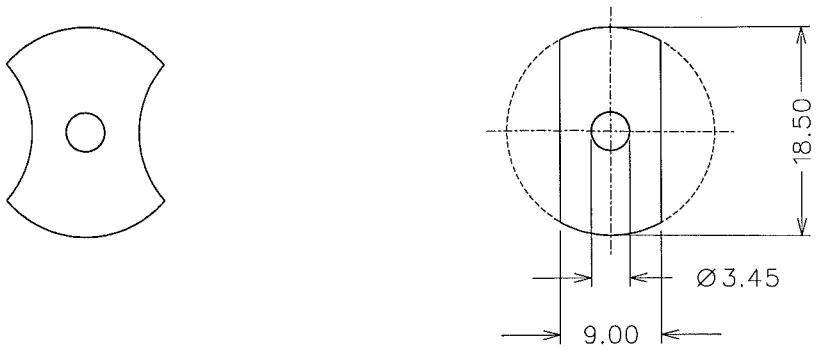

(a) (b) Final dimensions (in mm).

Figure 5.7 Rotor lamination shapes.

for the Siemens stator. The final rotor laminations were cut out of 0.5 mm non-grain orientated sheet using EDM.

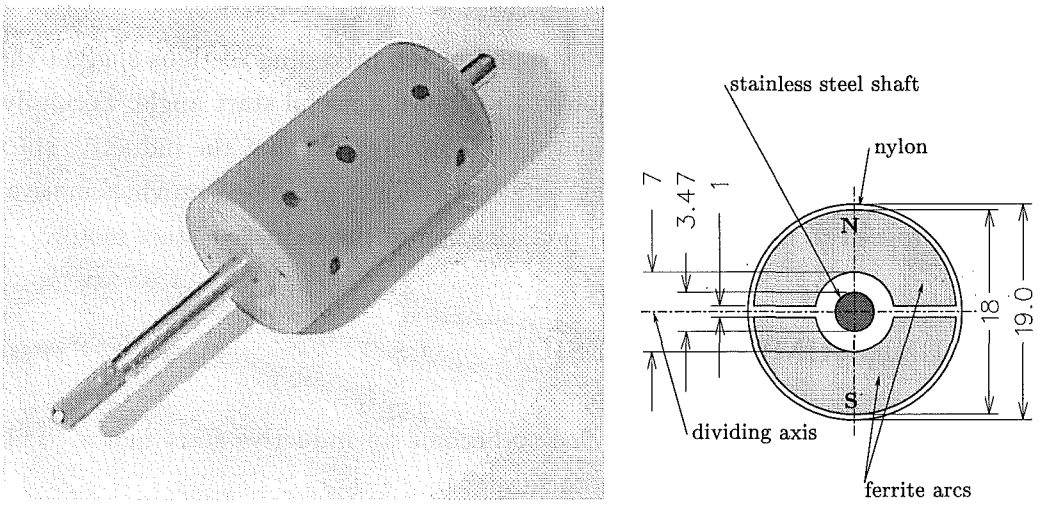

(a) (b) Section showing construction (approximate dimensions in mm).

Figure 5.8 Siemens rotor.

A value of γ_{la} should be selected which maximises the inductive reluctance torque at $\theta = 0$. The maximum reluctance torque was found to occur by this experimental process at approximately $\gamma_{la} = \pm 55°$. Fig. 5.8(a) shows a photograph of the Siemens rotor. Fig. 5.8(b) illustrates the construction of the rotor. The rotor consists of two ferrite magnet arcs and a stainless steel shaft embedded in a nylon matrix. The ferrite magnets are magnetised along the N-S axis at an angle perpendicular to the *dividing axis* drawn in Fig. 5.8(b). This angle of magnetisation is confirmed experimentally in section 5.5.1.1.

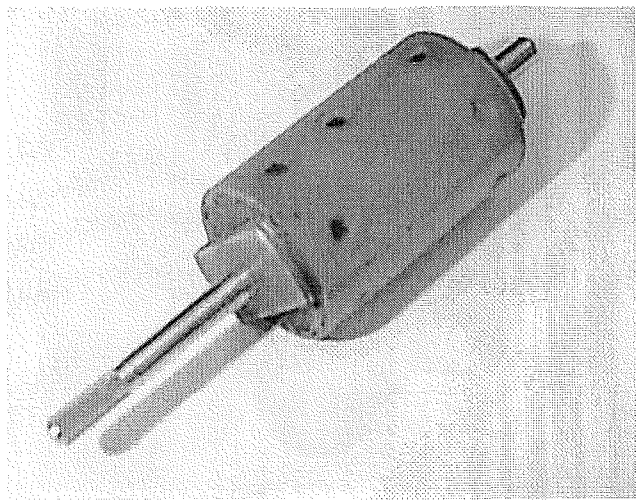

Figure 5.9 Inductive start rotor. Four laminations are located at the impeller (long) end of the shaft, and two laminations are placed at the thrust bearing (short) end of the shaft.

For the experimental design, rotor laminations are placed at the ends of the rotor magnets. The rotor laminations should be placed as close to the ferrite magnets as possible. This reduces the axial airgap distance between rotor and stator laminations after the motor is assembled. To achieve this, the nylon at each end of the rotor, visible at one end in Fig. 5.8(a), was machined off to expose the ferrite magnets. The nylon still remaining on the rotor was found to be sufficient to maintain the mechanical strength of the construction for the purpose of experimentation. Rotor laminations were then threaded onto the shaft using a 'finger pressure fit' and secured in place using an anaerobic adhesive. With reference to Fig. 5.6(a), the rotor laminations are secured in place at $\gamma_{la} = -55°$. This corresponds to rotating only the lamination drawn in Fig. 5.6(a) an angle of $+10°$ in the anti-clockwise direction. At rotor position $\theta = 0$, the inductive torque due to the rotor laminations when the stator is energised is then clockwise. In contrast, the PM reluctance torque in the conventional motor at rotor position $\theta = 0$ with $\gamma_r = +7°$ is anti-clockwise. Fig. 5.9 shows a photograph of the completed inductive start rotor.

5.4.2 Stator Airgap Design

Two options are available concerning the stator lamination design. The first option involves cutting out a completely new stator lamination stack using EDM. The dimensions of each lamination are identical to the conventional lamination, except that the asymmetric step is removed. The stator airgap then has the diameter D_s drawn in Fig. 5.6(a). Ideally, the grade and thickness of steel sheet used should be the same as the conventional sheet to gauge comparative performance. Fig. 5.10 shows a photograph of the rotor housing. The Siemens stator laminations are pushed onto the rotor housing forming an interference like fit. The effective filling in of the stator sunken step

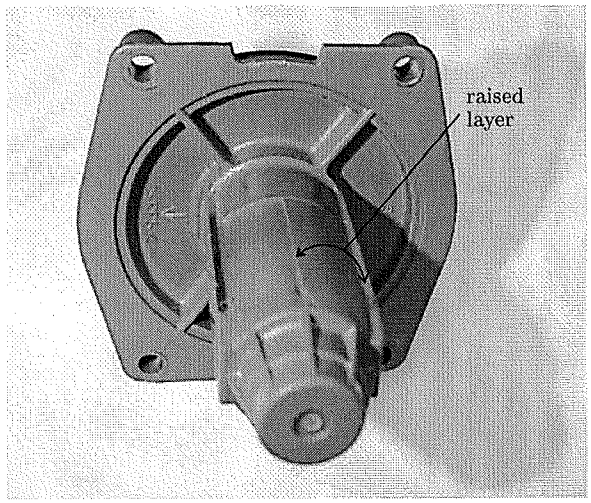

Figure 5.10 Siemens rotor housing.

therefore also requires removal of the raised layer of housing plastic identified in Fig. 5.10 to allow assembly. This is the ideal design option.

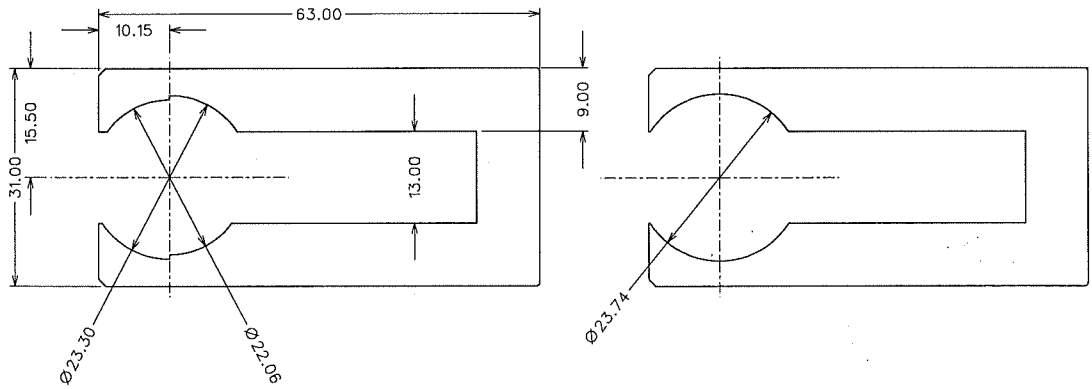

(a) Dimensions of the Siemens stator lamination (in mm).

(b) Dimensions of the inductive start stator lamination (in mm).

Figure 5.11

The second option involves using the existing Siemens laminations and removing the stator step using EDM to diameter D_{sc} defined in Fig. 5.6(a). The stator lamination stack still fits firmly onto the rotor housing. The average stator airgap is now slightly larger and $\hat{\lambda}_m$ is reduced. This option was chosen because it is an easier modification. Fig. 5.11(a) shows the dimensions of the conventional Siemens stator lamination. Fig. 5.11(b) shows the stator after EDM. Dimension D_{sc} has been increased from 23.30 mm in Fig. 5.11(a) to 23.74 mm in Fig. 5.11(b). The Siemens laminations are not annealed after stamping. Some magnetic hardening around the stator airgap is therefore expected. The stamped sunken step in Fig. 5.11(a) corresponding to diameter D_{sc} may then have some magnetic hardening. The EDM process produces

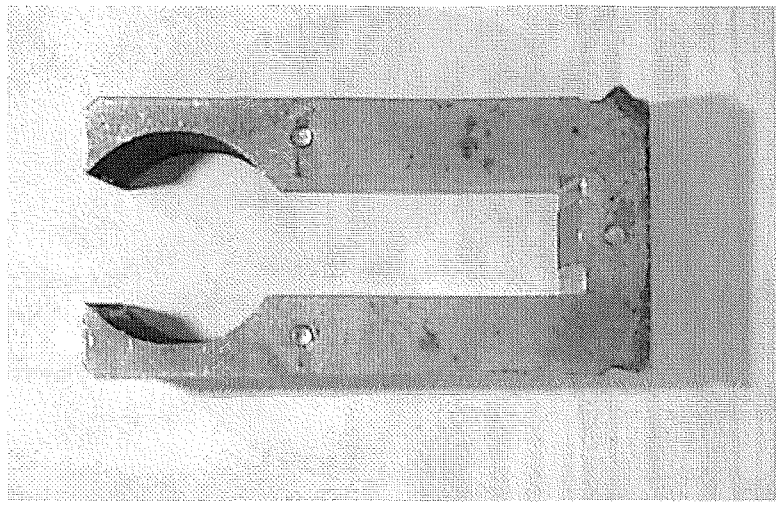

Figure 5.12 Inductive start motor stator lamination stack.

a cut without magnetic hardening. EDM cutting of the raised step back to diameter D_{sc} cuts away any material hardened from stamping. This creates a potential problem where the rotor may align itself towards the original displacement angle. This is due to non-homogenous magnetic properties around the stator airgap caused by the selective EDM cutting. Increasing D_{sc} by using EDM cuts out any magnetic hardening up to diameter D_{sc} along the sunken step as well as the raised step. Any magnetic hardening is reduced. This provides a remedy to this potential problem. Approximately 0.22 mm of steel is removed along the airgap in Fig. 5.11(b) corresponding to each sunken step. Fig. 5.12 shows a photograph of the lamination stack after EDM. The displacement angle γ_r of the inductive start motor is measured in section 5.5.1.1.

5.5 EXPERIMENTAL RESULTS

Experimental results for the inductive start motor are presented in this section. These results are compared to those of a conventional Siemens motor where appropriate.

5.5.1 Preliminary Measurements

5.5.1.1 Measurement of γ_r and the Angle of Rotor Magnetisation

For an inductive start motor, the PM displacement angle γ_r is zero. In section 5.4.2, the precaution of increasing airgap diameter D_{sc} is taken to help ensure that this also occurs in the modified motor. In section 5.4.1, the Siemens rotor is described as being magnetised at an angle perpendicular to the 'dividing axis' drawn in Fig. 5.8(b). In this section both γ_r and the angle of rotor magnetisation are measured.

These measurements are achieved as follows. Fig. 5.13 shows a photograph of the conventional rotor supported by an aluminium disc. A protractor is fixed to the

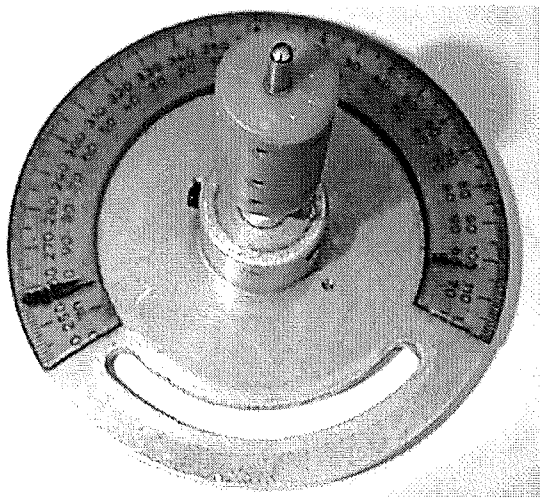

Figure 5.13 Conventional rotor attached to the aluminium disc.

disc. The angle between the protractor and rotor is adjustable, and is secured by a grub screw tightened against the stainless steel shaft of the rotor. By using a dividing head and a milling machine, the axis of the rotor perpendicular to the dividing axis is aligned as accurately as possible to a mark on the protractor.

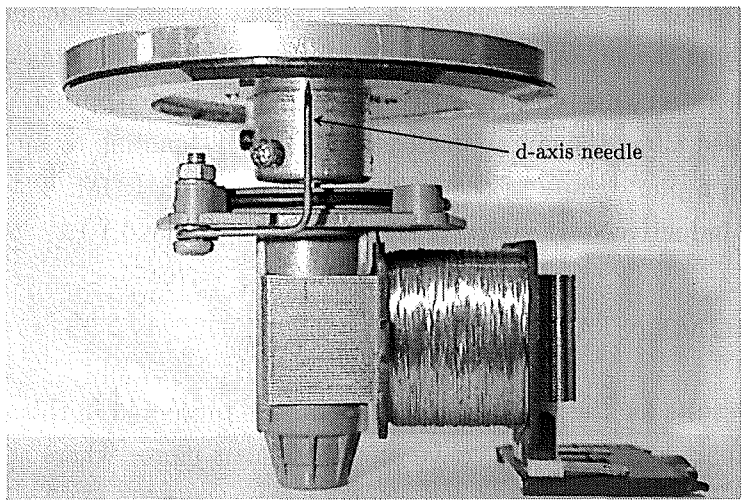

Figure 5.14 Start angle measurement arrangement.

The rotor housing is fitted into the inductive stator lamination stack. The rotor, which is attached to the aligned aluminium disc, is then inserted into the rotor housing. This assembly is shown in Fig. 5.14. The *d-axis needle* identified in Fig. 5.14 attached to the rotor housing allows the protractor to be referenced to the stator d-axis. A surface plate and a height gauge are used to align the needle to the stator d-axis.

The protractor position at which the line perpendicular to the dividing axis aligns up to the stator d-axis is then known. Upon assembly, the rotor comes to rest at the angle where the PM reluctance torque is zero. The difference between these two positions

was found to be 1.4°. Assuming that the rotor magnetisation is perpendicular to the dividing axis, then the measurement result gives $\gamma_r = -1.4°$ corresponding to clockwise rotor rotation to the rest angle. This direction of rotation is opposite to that expected to be caused by uneven magnetic hardening around the stator airgap. Assuming no magnetic hardening, $\gamma_r = 0$ and the rotor magnetisation is 1.4° anticlockwise of the axis perpendicular to the dividing line on the rotor. The greatest contribution to the difference of 1.4° is most likely to be measurement error. Given the relatively small magnitude of this difference, it is assumed that $\gamma_r = 0$ and the rotor magnetisation is perpendicular to the dividing line.

5.5.1.2 Measurement of γ_r for the Conventional Siemens Motor

The PM displacement angle γ_r of the conventional Siemens motor is measured. The method of measurement is identical to that described in section 5.5.1.1 except that the conventional lamination stack is used. The experimental result was $\gamma_r = +6.4°$. This value is very close to the manufacturer's specification of $\gamma_r = 7°$.

5.5.2 Start Angle Measurements

The following subsections select through experimentation the best distribution and number of rotor laminations for the inductive start motor. The aim of this selection process is to maximise the start angle whilst at the same time enabling the motor to operate as a water-pump using the existing rotor housing design.

5.5.2.1 The Rotor Housing Design of the Siemens Motor

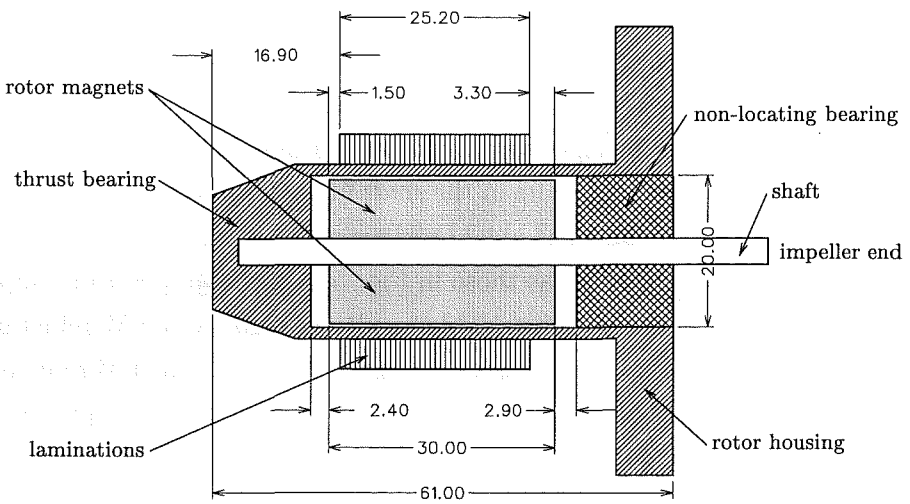

Figure 5.15 Section through the stator d-axis of the Siemens motor showing the rotor housing, rotor, and stator stack. Dimensions in mm.

The section[3] of Fig. 5.15 through the stator d-axis of the Siemens motor shows the rotor housing, rotor, stator lamination stack, and bearings. The bearings comprise of a thrust bearing and a non-locating bearing. The bearings are constructed out of nylon with spun glass. The clearance around the stainless steel shaft within the non-locating bearing allows water to flood the rotor housing cavity. The rotor has been drawn with the nylon at each end of the magnets machined off. About 2 mm of nylon is machined off from the thrust bearing end, and about 0.5 mm from the other end. The axial clearances specified between the rotor magnets and each bearing indicate the maximum spaces available to place laminations on either side of the rotor magnets.

The stator lamination stack is composed of 38 laminations. Each lamination has a thickness of approximately 0.65 mm. The stator stack begins approximately 16.9 mm from the thrust bearing end of the rotor housing as drawn. This axial dimension is used to define the conventional stator position.

The positions of the stator stack and rotor magnets are drawn for the conventional Siemens motor. The diagram shows that the stator stack and the rotor magnets are not axially aligned. The axial dimensions corresponding to the misalignment are shown. The misalignment causes a PM reluctance force to act axially, pulling the rotor into the housing. This force locates the shaft into the thrust bearing. This force counteracts the twice electrical frequency fluid pressure fluctuations described in section 1.2.6 which bounce off the thrust bearing end of the rotor housing cavity.

5.5.2.2 Design A

Four rotor laminations were first placed on the shaft next to the rotor magnets at the thrust bearing end. Upon energising under no-load, the rotor was observed to jostle forward into the non-locating bearing. This is caused by an inductive reluctance force between stator and rotor laminations exceeding the opposing PM reluctance force.

Fig. 5.16 shows a design which eliminates axial movement upon energising. This design is called *design A*. The rotor lamination design is that of Fig. 5.9. The stator lamination stack has been pushed approximately 1.9 mm towards the impeller end of the rotor housing. This design results in the shaft being located into the thrust bearing upon energising under no-load. The axial overlaps of the rotor magnets over the stator stack are approximately the same as those in Fig. 5.15 but swapped from impeller end to thrust bearing end and vice versa. This results in zero axial PM reluctance force occurring when the shaft is about 1 mm off the thrust bearing. The PM reluctance force which occurrs when the shaft is located against the thrust bearing opposes location, but is small. Under no-load running, the inductive reluctance force is dominant and locates the shaft. The higher number of rotor laminations on the impeller end of the

[3] A more detailed section drawing is found in [Altenbernd and Wahner 1996, Fig. 2].

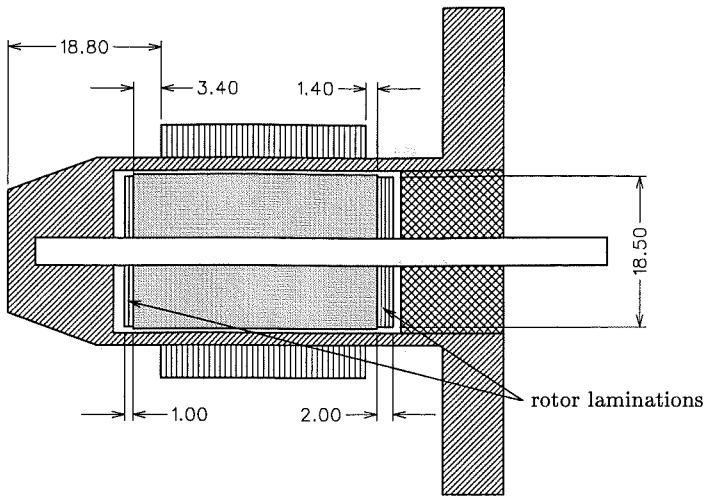

Figure 5.16 Section through the stator d-axis of design A. Dimensions in mm.

rotor and the closer proximity of the stator stack to these laminations ensures that the net inductive reluctance force is locating.

Voltage (V RMS)	Locked rotor current (A RMS)	Start angle γ_{st} (elect deg)
220	0.433	-10.5
230	0.461	-12.5

Table 5.3 Start angle measurements for design A.

Measurement of the start angle is made by the method described in section 5.2.2.1. The arrangement of Fig. 5.14 is used with the shaft orientated vertically with the aluminium disc above the rotor. The weight of the disc ensures that the shaft is located against the thrust bearing for all measurements. Start angle measurements for design A corresponding to the rated terminal voltages are shown in Table 5.3. The negative values of the start angles correspond to clockwise rotation. The results demonstrate that it is feasible to obtain significant start angles even with large axial and radial airgap distances between rotor and stator laminations.

5.5.2.3 Design B

This design is shown in Fig. 5.17. The rotor lamination design of Fig. 5.9 is used again. The stator stack is pushed further toward the impeller end of the rotor housing until the leading edges of the impeller end stator and rotor laminations align. The aim of this design is to further increase the start angle.

A PM reluctance torque pulls the rotor onto the non-locating bearing even when the motor is energised and running under no-load. This makes this design impractical. Table 5.4 presents the start angle measurements.

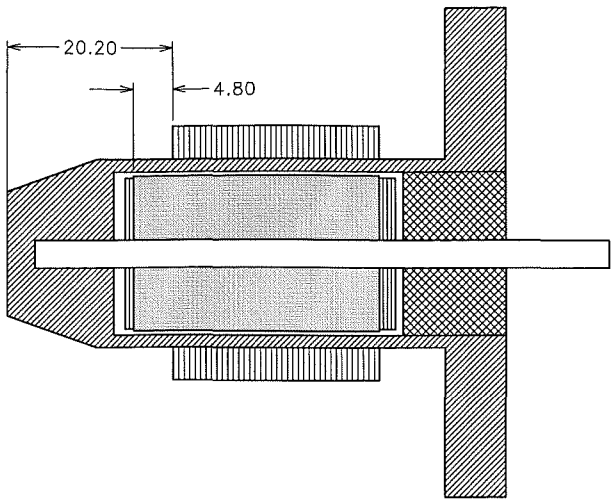

Figure 5.17 Section through the stator d-axis of design B. Dimensions in mm.

Voltage (V RMS)	Locked rotor current (A RMS)	Start angle γ_{st} (elect deg)
220	0.433	-12
230	0.460	-14.5

Table 5.4 Start angle measurements for design B.

Only the four rotor laminations at the impeller end are effectively contributing reluctance torque because the distance between the two rotor laminations and the stator on the thrust bearing end is large. For designs in which all the rotor laminations are in closer proximity to the stator laminations, it is expected that the start angle may be extended still further. Such examples are a design in which the rotor magnet overlap of the stator stack is reduced, or one in which rotor laminations may lie underneath stator laminations.

5.5.3 Flux Linkage Measurement

This section measures by how much the increased average stator airgap of the experimental inductive start motor decreases the peak flux linkage. More significantly, the effect on the peak flux linkage of adding laminations to the rotor is assessed.

The peak flux linkage is measured using the method of driving the motor as a generator and measuring the voltage induced at the open circuited terminals. The peak flux linkage is calculated by

$$\hat{\lambda}_m = \sqrt{2}E/\omega_m \tag{5.17}$$

where ω_m is the mechanical angular speed and E is the fundamental RMS value of the induced voltage. For all measurements the induced voltage was found to contain a

small component of third harmonic. The magnitude of the third harmonic lay between 3-5% of the fundamental. While strictly the fundamental value of the induced voltage should be used, instead the true RMS value was used to calculate the flux linkage. Measurements from three motors are made for the purpose of comparison. These motors are described as follows:

1. The conventional Siemens motor.

2. A motor using the inductive start stator and the conventional rotor. The stator lamination stack is located at the conventional axial position. The conventional rotor does not have rotor laminations. The purpose of this motor is to determine how the larger stator airgap diameter D_{sc} reduces the flux linkage in relation to the conventional motor.

3. The inductive start motor using design A. This measurement allows the influence of the rotor laminations to be assessed. The rotor laminations 'short circuit' PM flux at the ends of the magnets creating a reduction in the flux linkage.

The motors tested were driven by a small DC motor at a speed of over 4000 RPM. Measurements were taken with the shaft of each tested motor located against the thrust bearing. Experimental results are shown in Table 5.5. The measured value of $\hat{\lambda}_m$ for the

Motor	$\hat{\lambda}_m$ (Volt.sec.)
1- Conventional Siemens	0.355
2- Inductive start stator/conventional rotor	0.334
3- Inductive start (design A)	0.321

Table 5.5 Flux linkage measurements.

conventional motor agrees with the manufacturer's specification. For the second motor, $\hat{\lambda}_m$ is reduced by 6%. In contrast, an increase in $\hat{\lambda}_m$ of about the same magnitude is expected for the ideally built inductive start stator design described in section 5.4.2. This is because the ideal design reduces the average airgap length. By then adding rotor laminations, $\hat{\lambda}_m$ is reduced. The difference in flux linkage between the last two measurements is the amount of PM flux short-circuited by the rotor laminations in motor 3. The rotor laminations reduce the flux linkage by 4%. Therefore, for an ideally constructed inductive start motor a small net increase in $\hat{\lambda}_m$ is possible.

5.5.4 Water Pumping Tests

In this section the inductive start motor (design A) is tested to determine whether it can start reliably. The water pumping performance of the conventional Siemens motor and the inductive start motor are compared.

5.5.4.1 Experimental Set-up

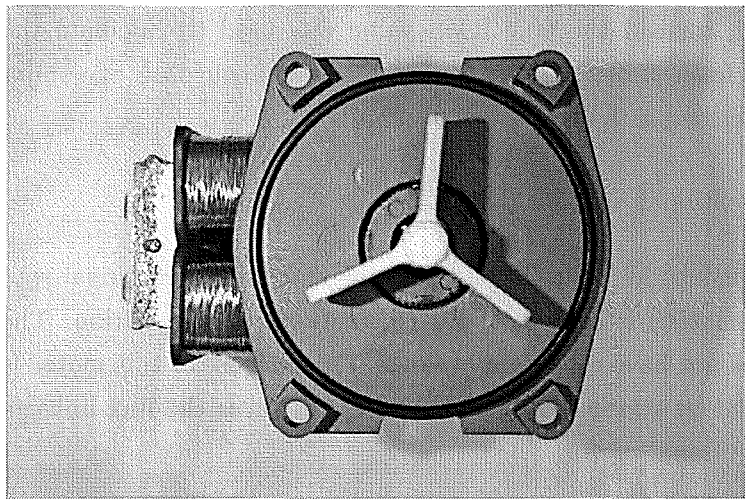

Figure 5.18 Assembled rotor housing (viewed from impeller end).

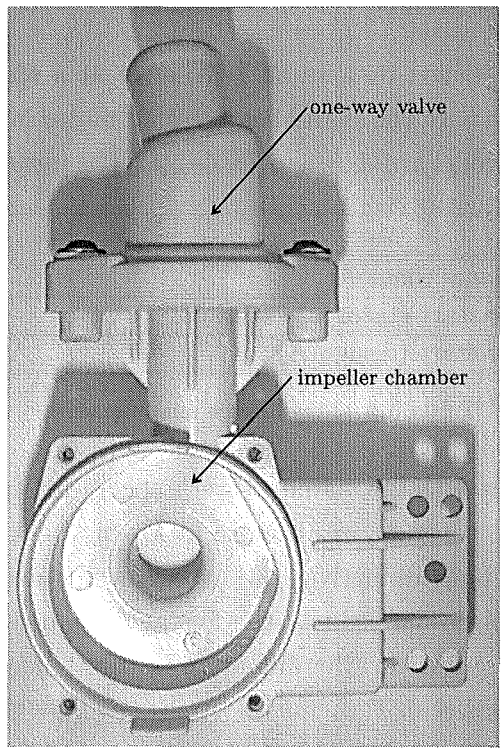

Figure 5.19 Impeller housing.

Fig. 5.18 shows a photograph of the fully assembled rotor housing. The impeller is visible and is attached to the end of the shaft. Fig. 5.19 shows a photograph of the impeller housing. The rotor and impeller housings clamp together. Water is drawn in through the hole in the impeller chamber and accelerated around the chamber walls and up through the one-way valve. The one-way valve prevents water from flowing

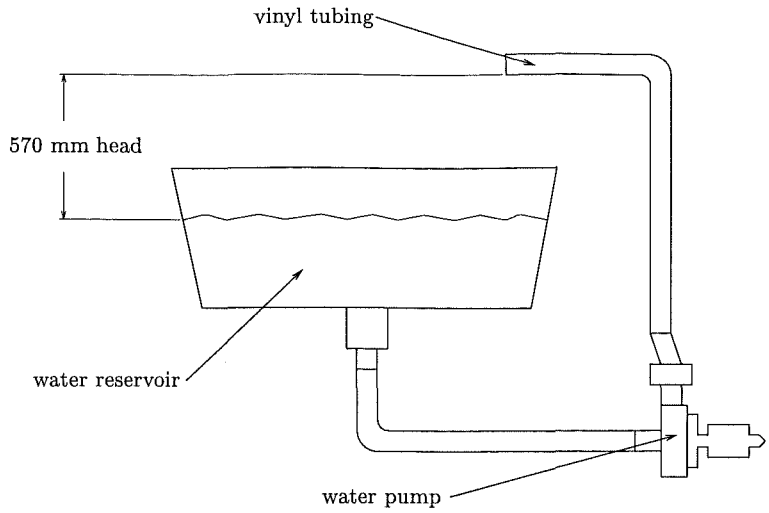

Figure 5.20 Experimental water-pumping set-up.

back through the pump into the washing machine once the motor is de-energised. Fig. 5.20 shows a diagram of the experimental water-pumping set-up. The one-way valve is used. A water head height of 570 mm is used in the experiment. The water-pump sits beneath the water reservoir. Three metres of 20 mm diameter clear vinyl tubing is used.

A clearance of about 5 mm between each impeller blade tip and the impeller chamber walls reduces the chance of blockage. The impeller efficiency is low. The energy transferred by the impeller is apportioned into gravitational potential energy corresponding to the head height, kinetic energy of the water, and losses. The losses include wall friction and turbulence losses in both the impeller housing and the tubing. Only the gravitational potential energy is simple to calculate. As a result, the output power of the motor is not determined in this experiment. However, given a constant head height and length of tubing, it is assumed that a measurement of the flow rate gives a relative indication of the output power between motors. The input power to each motor is measured using a power meter. Tests show that raising the head height or constricting the tubing decreases the flow rate. The motor is not loaded to pull-out at the maximum head height where the flow rate is zero and water is simply pumped around the impeller chamber. Adjustment of the head height results in only small changes of input power. The load is therefore not easily controlled and the pullout load cannot be measured in the water-pumping set-up. The low sensitivity to head height makes the selection of a 570 mm head non-critical. The instantaneous rotor speed is not measured in the experimental set-up. The enclosed nature of the rotor within the pump housings makes this difficult.

A method of applying an adjustable and measurable load is described in [Schemmann 1971, pp. 85-93]. The load is a constant function of speed and is frictional. This differs from the quadratic load function of the water-pumping set-up described here.

Emphasis is placed here on testing the inductive start motor for the water-pumping application.

5.5.4.2 Starting

The following test is used to determine the ability of the inductive start motor to start in the water-pumping application. The motor is placed in the experimental set-up and energised one hundred times at each of the rated voltages of 220 and 230 V RMS. The motor started pumping water successfully for all the tests. Oscilloscope measurements showed a uniform spread of the supply voltage angles at switch-on.

5.5.4.3 Steady State Comparison

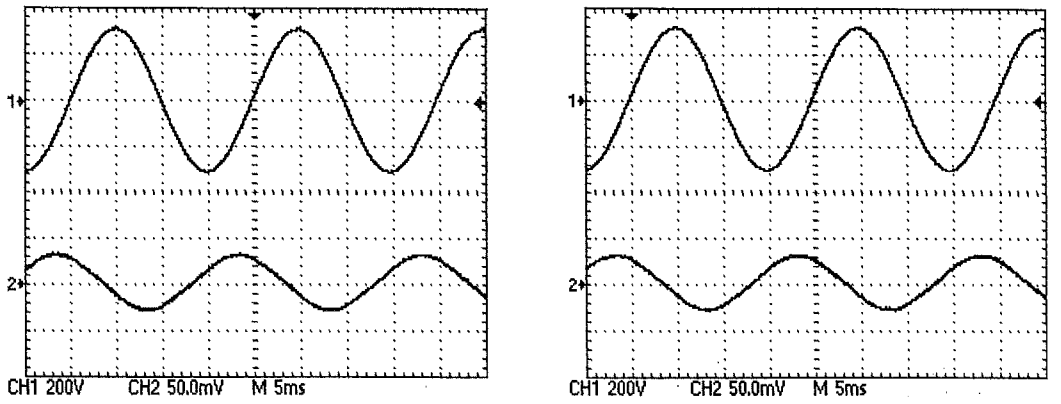

(a) Siemens motor.

(b) Inductive start motor.

Figure 5.21 Waveforms corresponding to terminal voltage of 220 V RMS. Channel 1: terminal voltage. Channel 2: current, 500 mA/div.

The steady state water-pumping performance of the conventional and inductive start motors are compared in this section. Fig. 5.21 shows the terminal voltage and current waveforms for each motor corresponding to the rated voltage of 220 V RMS. A small third harmonic current is present which ranges in magnitude between 2-4% of the fundamental for both motors in all tests. The magnitude of the third harmonic increases towards the higher end of this range for both motors at the rated voltage of 230 V RMS.

Table 5.6 shows water-pumping test results for both motors. The values given for currents are approximate as these are affected by motor running time. To within the accuracy of the power meter, the input powers[4] and power factors are the same for

[4]The nameplate input power rating of the conventional Siemens motor tested here is 28 W. The model number of this motor is 1737222180, which is different to the model number 710.600 00/1 of the motor simulated in section 4.4.3. The nameplate input power rating of the 710.600 00/1 motor

		Units	Siemens motor	Inductive start motor
220 V RMS				
Current		A RMS	approx. 0.285	approx. 0.285
Power Factor			0.45	0.45
Input Power		W	29	29
Flow Rate	higher	Litres/sec.	0.385 ± 0.003	0.385 ± 0.003
	lower	Litres/sec.	0.350 ± 0.003	0.349 ± 0.003
230 V RMS				
Current		A RMS	approx. 0.305	approx. 0.303
Power Factor			0.44	0.44
Input Power		W	31	31
Flow Rate	higher	Litres/sec.	0.390 ± 0.003	0.388 ± 0.003
	lower	Litres/sec.	0.354 ± 0.003	0.354 ± 0.003

Table 5.6 Water-pumping test results.

both motors. Two distinctive higher and lower flow rates occurring at both voltages were recorded for both motors. Either flow rate is established at start-up. The flow rates are nearly identical for both motors. It is suggested that these two distinctive flow rates are caused by differing hydrodynamic actions inside the impeller chamber. This may be caused by the asymmetric shape of the impeller chamber visible in Fig. 5.19. This may favour a higher flow rate in one direction of impeller rotation than the other.

Given that the flow rates of both motors are nearly identical, it is assumed that the output power of both motors are about the same. Motor efficiency is therefore expected to be about the same for both motors.

5.5.5 Inductance

Stator winding inductance is measured in this section to determine how it is affected by the addition of iron rotor laminations.

5.5.5.1 Method of Inductance Measurement

The stator winding resistance of the Siemens motor is much higher than that of the experimental triangular motor. This created practical difficulty in applying the DC inductance method to the measurement of the Siemens motor inductance using the existing set-up. The following method of AC inductance measurement was used instead. The rotor is locked in position and the stator is energised using AC. The impedance is

is 25 W. Model 1737222180 is a later model. Motor photographs and test results correspond to the later model. Both motors are identical except that the pump construction of the later model has been changed.

calculated from measurement of the RMS voltage and current. After recording of the RMS voltage and current the stator winding is immediately de-energised and the DC winding resistance is measured. The inductance is calculated by

$$L = \sqrt{(Z^2 - R^2)/\omega_e^2} \tag{5.18}$$

5.5.5.2 Experimental Results

Inductance measurements are shown in Fig.s 5.22-5.25. Experimental results are measured over one inductance cycle corresponding to 180° electrical. The positive angle of rotation is defined with reference to Fig. 5.6(a). The axis of rotation is viewed from the thrust bearing end of the rotor and positive rotation is anti-clockwise. The inductance characteristic about $\theta = 0$ is of particular interest for the analysis of starting torque. The $-145°$ to 35° rotor angle range plotted allows the inductance characteristic through $\theta = 0$ to be clearly observed. Two sets of inductance measurements are taken for each motor. The first set is taken at locked rotor current corresponding to 220 V RMS. This measurement is of importance because the inductive reluctance torque at starting corresponds to locked rotor current. The second set corresponds to the steady state running current measured in the water-pumping tests described in section 5.5.4. This measurement is of importance in determining the effects of adding rotor laminations to steady state performance. For all plots, the values of voltage averaged over an inductance cycle, corresponding to locked rotor current, range between 220.5-220.9 V RMS. The corresponding average locked rotor currents range between 0.414-0.445 A RMS. For the running current measurements, the average voltages range between 156.5-158 V RMS and the average currents range between 0.277-0.296 A RMS. Polynomial curves are fitted to the measured points using least squares.

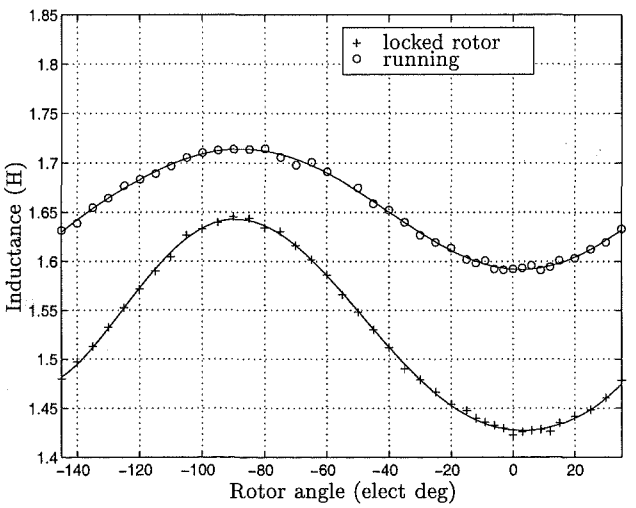

Figure 5.22 Conventional Siemens motor inductance waveforms. Locked rotor: $L_o = 1.528$ H, $\hat{L} = 0.108$ H. Running: $L_o = 1.655$ H, $\hat{L} = 0.061$ H.

Fig. 5.22 shows inductance measurements for the conventional Siemens motor. The inductance characteristics are predominantly DC with a small quasi-sinusoidal component. In both curves the saturating effects of the PM rotor flux on inductance, explained in section 5.2.1, are visible. The saturating effect of the stator current is also clearly visible. Increasing the current increases saturation which lowers the DC inductance L_o. However, increasing the current increases the modulation amplitude $\hat{L}$. Note that the locked rotor characteristic reaches its minium value at about $\theta = 4°$ rather than $\theta = 0$. This was initially suggested to be caused by the raised steps in the stator airgap establishing maximum PM flux linkage, and thus maximum saturation, at the rotor position corresponding to the observed minimum.

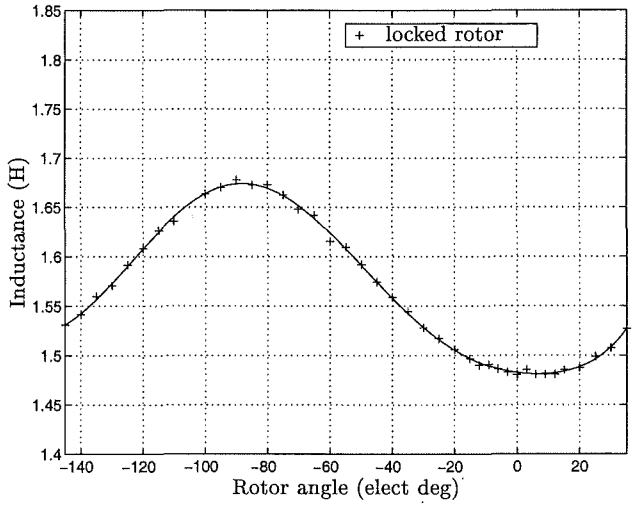

Figure 5.23 Inductive start stator (design A) with the conventional rotor. The inductance waveform corresponds to locked rotor current. $L_o = 1.571$ H, $\hat{L} = 0.096$ H.

Fig. 5.23 shows the locked rotor current inductance characteristic for the motor composed of the inductive start stator (design A) and the conventional rotor. With PM displacement angle $\gamma_r = 0$, and the asymmetric airgap eliminated, the inductance characteristic was expected to be symmetric about $\theta = 0$. However, the characteristic reaches its minimum value at a non-zero position. The characteristic is very similar to the corresponding curve in Fig. 5.22. The slightly larger average stator airgap reduces saturation resulting in a slightly higher value of L_o.

Fig. 5.24 shows inductance measurements for the inductive start motor of design A. The values of L_o are higher than in the previous figures due to the presence of the rotor laminations. The locked rotor characteristic is similar to that of Fig. 5.23. The DC value of the additional inductance due to the rotor laminations is obtained as the difference between the corresponding values of L_o in Fig.s 5.23 and 5.24. This yields $L_{oa} = 0.069$ H at locked rotor current for design A. A phase shifting of the running current characteristic is visible. Both the maximum and minimum points are phase shifted approximately $+12°$. This phase shift is caused by the position of the rotor

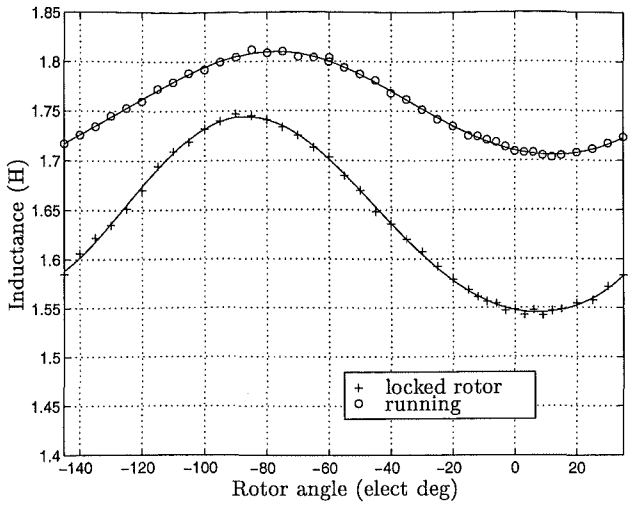

Figure 5.24 Inductive start (design A) motor inductance waveforms. Locked rotor: $L_o = 1.640$ H, $\hat{L} = 0.100$ H. Running: $L_o = 1.757$ H, $\hat{L} = 0.052$ H.

lamination axis relative to the stator d-axis as rotation occurs. Comparison of both characteristics in Fig. 5.24 with respect to phase shifting shows that the influence of the rotor laminations is more predominant at the lower current. This implies that $\hat{L}_a$ is greater at lower current for the inductive start motor. This also implies that the rotor laminations become more saturated as the current is increased.

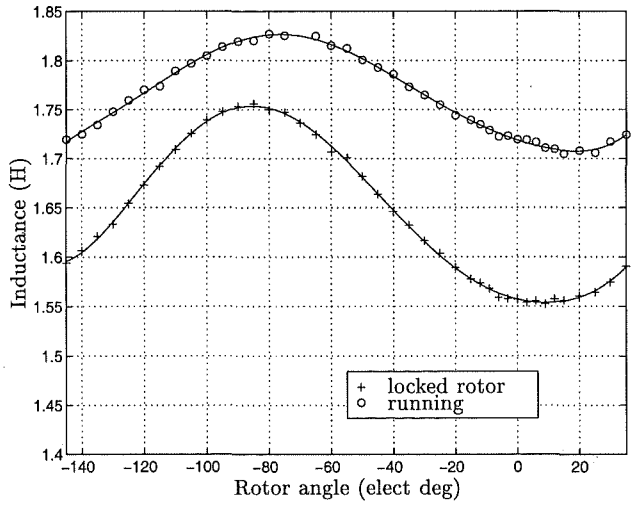

Figure 5.25 Inductive start (design B) motor inductance waveforms. Locked rotor: $L_o = 1.648$ H, $\hat{L} = 0.100$ H. Running: $L_o = 1.767$ H, $\hat{L} = 0.060$ H.

Fig. 5.25 shows inductance measurements for the inductive start motor of design B. This design yields the largest start angles shown in Table 5.4. The phase shifting influence of the rotor laminations is most clearly seen in these characteristics, particularly in the running current characteristic. From Fig.s 5.23 and 5.25, $L_{oa} = 0.077$ H at locked rotor current.

In Fig.s 5.22-5.25, all four locked rotor inductance characteristics appear to have

similar and small non-zero slopes at $\theta = 0$. Section 5.5.6 examines the torques at this position for these motors.

5.5.6 Starting Torque about Rotor and Stator Alignment

The following experiments are undertaken to determine more information about the PM and inductive reluctance torques about $\theta = 0$.

The method of start angle measurement described in section 5.2.2.1 is first applied to the motor composed of the inductive start stator (design A) and the conventional rotor. Before the stator winding is energised, the rotor is at rest at $\theta = \gamma_r = 0$ and the PM reluctance torque is zero. Upon energising at 220 V RMS no rotation occurs. The zero rotation implies that the inductive reluctance torque is also zero at $\theta = 0$. In section 5.5.2, it is shown that the inductive start motors of designs A and B have non-zero start angles. Inductive reluctance torques at $\theta = 0$ must therefore be present in both these motors to achieve the non-zero start angles. The design A and B start angle tests, and the test described above, show that the locked rotor inductance characteristics of Fig.s 5.22-5.25 do not give reliable indications of the presence of inductance reluctance torque at $\theta = 0$.

	stable	unstable	stable
PM reluctance torque, T_r	0	90	180
PM and inductive reluctance torques at locked rotor current, $T_r + T_{ind\,c}$	0	88.5	179

Table 5.7 Rest angle measurements for the motor composed of the inductive start stator (design A) and the conventional rotor. Angles in elect. degrees.

In the example of Fig. 5.5 corresponding to an ideal inductive start motor, torque waveforms $T_{ind\,c}$ and T_r are shown in anti-phase. For the motor composed of the inductive start stator and the conventional rotor, these torques are also present but $T_{ind\,a}$ is eliminated. This allows an opportunity to determine experimentally whether T_r dominants $T_{ind\,c}$ under locked rotor current. To do this, the PM reluctance rest angles over a PM reluctance cycle are first measured. These angles are shown in Table 5.7 and agree with theory. The large artificial moment of inertia of the start angle measurement method is then attached to the shaft. The rest angles corresponding to locked rotor current are then measured. The rest angles correspond to the superposition of $T_{ind\,c}$ and T_r. These rest angles are also shown in Table 5.7. These results show that the direction of torque and the rest angles remain essentially unchanged. This demonstrates that T_r dominants $T_{ind\,c}$ under locked rotor current over all rotor positions for an inductive start motor. For example, at about $\theta = 90°$, the inductance is maximised and is therefore assumed to provide a stable rest position for $T_{ind\,c}$. However, Table 5.7 shows that this position remains unstable corresponding to the dominance of the PM reluctance

torque.

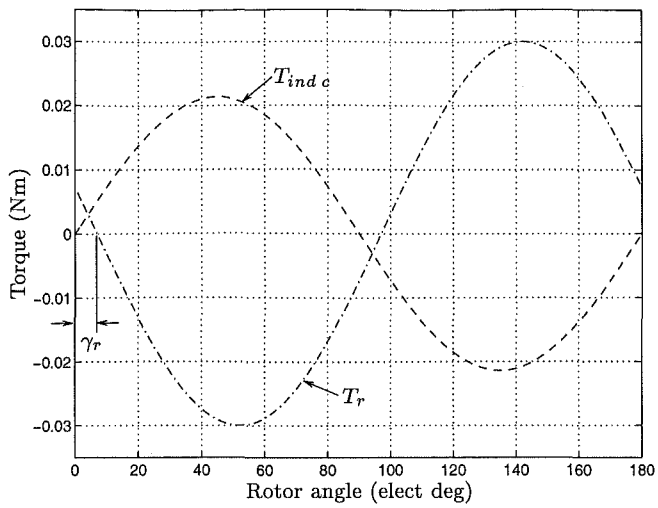

Figure 5.26 Conventional Siemens motor: ideal torque waveforms corresponding to the start angle measurement test.

For the conventional motor, a different result is obtained upon applying the method of start angle measurement. Before the stator winding is energised, the rotor is at rest at $\theta = \gamma_r = +7°$ and the PM reluctance torque is zero. Upon energising, the rotor rotates to $\theta = +10°$. This rotation is explained as being the result of a non-zero $dL/d\theta$ at $\theta = +7°$ providing an inductive reluctance torque, $T_{ind\,c}$. The rotor angle is sufficiently displaced from $\theta = 0$ for $T_{ind\,c}$ to be significant and T_r is zero. The inductive reluctance torque rotates the rotor towards the inductance maximum at $\theta = 90°$. This torque is not equally counteracted by T_r until $\theta = +10°$ because $T_{ind\,c}$ and T_r are not in anti-phase. Fig. 5.26 provides a qualitative illustration of both torque waveforms assuming sinusoidal characteristics. The phase difference between $T_{ind\,c}$ and T_r in Fig. 5.26 is $\gamma_r = 7°$. The waveforms are calculated using the Siemens motor parameters of Table 5.1. The equilibrium angle in Fig. 5.26 is greater than $\theta = 20°$, and is much larger than the measured equilibrium of $\theta = 10°$. While obtaining the experimental results of Table 5.7, it was noticed that the magnitude of the resultant torque comprising of anti-phase components $T_{ind\,c}$ and T_r was larger than that of T_r alone with the stator de-energised. The difference was felt by hand. This implies that T_r increases in magnitude under locked rotor current. This observation provides an explanation for the greater equilibrium angle in Fig. 5.26; drawing a larger T_r waveform corresponding to locked rotor current reduces the equilibrium angle to a value closer to the measured one.

The direct way of comparing the torques at $\theta = 0$ between the conventional and the inductive start motors is to measure them. For the Siemens motor the value of PM reluctance torque at this position is in the order of 7 mNm. For the purpose of comparison, measurement accuracy close to 1-2 mNm is required. Attempts were made to measure torque at $\theta = 0$. This involves measuring the torque T_r at $\theta = 0$ for the

conventional motor with the stator winding de-energised. It also involves using the start angle measurement set-up to measure $T_{ind\,a}$ at $\theta = 0$ at locked rotor current for the inductive start motor. However, for each experiment it was found to be too difficult to obtain consistent measurements. This is due to the small magnitude of the torque required to be measured. However, 'finger pressure' measurement of the torques of both motors suggests similar magnitudes at $\theta = 0$. The finger pressure torque felt from the inductive start motor is an averaged value, and not the peak value.

5.6 CONCLUSIONS

A single phase synchronous PM motor which uses inductive reluctance torque to facilitate starting has been proposed. A theoretical model has been developed. A practical design for this inductive start motor has been developed and tested. It has been demonstrated through the measurement of the start angle that the inductive start motor offers an alternative starting mechanism to that of the conventional designs. For a water-pumping application, the inductive start motor developed has been shown to achieve the same water-pumping performance as the conventional motor.

A comparison of the inductance characteristics for the conventional and unidirectional motors shows that the modulation of the inductances is similar. This suggests that the inductance of the unidirectional motor may also be assumed to be constant for the purpose of simulating the unidirectional motor at synchronous speed. This assumption also allows the conventional synchronous performance equations to be applied to the unidirectional motor.

A description of advantages and disadvantages of the inductive start motor with respect to the conventional motor is made as follows. The advantages are described first. The inductive start motor has the flexibility to increase the starting torque at the stator and rotor alignment position, and also the start angle, by adding more laminations to the rotor. The start angles of the inductive start motor designs have been demonstrated to be significantly larger than the PM displacement angle of the conventional Siemens motor. The inductive start motor simplifies the stator lamination design by eliminating the conventional asymmetric airgap steps, or alternative saturating notches. For the specific example of the Siemens motor, the manufacture of both the stator laminations and the rotor housing are simplified by the elimination of the airgap steps. The rotor housing is simplified through the removal of the raised layer of plastic identified in Fig. 5.10. Filling in of the conventional asymmetric airgap steps, or alternative saturating notches, increases the PM flux linkage. However, for the experimental inductive start motor, the peak flux linkage was decreased by cutting out the raised steps. As was observed in section 5.5.3, this resulted in a 6% reduction in peak flux linkage. As discussed in section 5.4.2, the ideal inductive start stator design fills in the sunken steps rather than cutting out the raised steps. The airgap diameter of the inductive start

stator is then minimised. In this case a gain of about 6% will be assumed. However, this increase is reduced by the short circuiting effect of adding rotor laminations. This reduction was 4%. Thus for an ideally modified Siemens motor, it is expected that a small net increase in peak flux linkage is likely to occur.

Disadvantages are described as follows. The rotor moment of inertia is increased by the addition of rotor laminations. However, the number of rotor laminations required contributed to only a very small increase in rotor inertia. The construction of the rotor is more complex. From a manufacturing perspective, a reliable method of aligning and securing the rotor laminations at the correct angle with respect to the rotor magnetisation is required. This might be achieved more easily by attaching the rotor laminations before magnetisation. Before a water pumping application can be considered, a reliable method of water proofing the rotor laminations is required to prevent rusting. A nylon enclosure which seals and secures the rotor laminations might offer a possible solution.

In section 5.5.5.2, the DC value of inductance is shown to increase by the addition of rotor laminations. It is difficult to predict the impact of adding rotor laminations without first considering saturation levels and building the ideal inductive start motor. Both the PM flux, and the inductance increase. The pullout torque may be expected to remain approximately the same for comparative conventional and inductive start designs.

Chapter 6

CONCLUSIONS AND SUGGESTIONS FOR FURTHER RESEARCH

This chapter summarises the conclusions presented in Chapters 2-5. Suggestions for further research are also included.

In Chapter 2, it has been shown how to determine torques or forces in machines containing permanent magnets using energy methods. This is achieved by first determining the energy stored in the electromechanical coupling field. In doing this, the energy stored in a PM system has been defined. The energy-coenergy relationship for a PM system has been determined. It is proven that $W'(i=0) = -W(i=0)$ for a PM system having arbitrary magnetisation characteristics and zero currents. A specific example of a PM system comprising of a PM material having a linear demagnetisation characteristic, and an airgap or linear region, for zero currents, is presented. It is shown that the stored energy or coenergy of the magnet should not be neglected in the calculation of reluctance torque. It has been shown how residual magnetism can be incorporated into classical electromechanical coupling theory. It is therefore shown how general equations for torques and forces, which include non-zero currents, can be derived for PM systems from classical electromechanical coupling theory. In doing this, it is proven that the relationship $W + W' = \lambda i$ holds for a PM system. The approximation made in deriving a simplified equation for torque in a linear system is described. The validity of the first quadrant representation of the rate of change of coenergy within a PM material, relevant to CAD systems, is also demonstrated. This work establishes a solid theoretical base for a selection of torque or force equations used by both machine and CAD system designers, as well as some less obvious equations.

In Chapter 3, an analytical method of calculating PM reluctance torque has been developed. The method uses an elementary expression for the magnetic field to obtain the stored energy. This enables an analytical expression for the reluctance torque waveform to be obtained. Because the stored energy is an analytical expression, the error in taking the derivative with respect to rotational displacement to obtain the torque is zero. It is shown that the method does not require the magnetic field to be accurately resolved into its normal and tangential components, unlike the Maxwell

stress method. This is possible because of the *global* nature of stored energy. The method is demonstrated to provide a powerful and fast design tool. The method can be generally applied to reluctance torque problems where the airgap is reasonably smooth. However, application of the method is likely to exclude cogging torque problems due to stator slotting because the field is unlikely to be described with sufficient accuracy.

The remaining conclusions concern the three novel single phase PM motors described in Chapters 3-5.

Chapter 3 has also examined the *triangular motor* which implements the *constant instantaneous torque concept* described in Chapter 1. This concept uses a specially designed PM reluctance torque to flatten out the twice electrical frequency torque pulsation characteristic of single phase machines. Alternatively explained in terms of counter rotating field theory, the PM reluctance torque cancels out the effect of the backward rotating stator field. The triangular motor requires a triangular PM reluctance torque, and a trapezoidal back EMF. It is shown that it is possible to design a triangular reluctance torque. The required reluctance torque and EMF are implemented adequately by the experimental axial flux double airgap motor. This demonstrates that it is possible to produce a high quality torque in a PM motor using only a single phase winding. A single phase DC to AC inverter and rotor position sensors are required to drive the triangular motor. In section 1.2.7, the characteristics which limit the application of the conventional single phase synchronous PM motor have been listed. A triangular motor, in combination with an electronic driver, eliminates all of these limiting characteristics. But it has been noted in section 3.9 that the triangular motor is unlikely to be able to compete in general with brushless PM motor drives.

In Chapter 4, the concept of the *unidirectional motor* has been developed. The unidirectional motor achieves a constant instantaneous torque with the aid of a PM reluctance torque of sinusoidal shape. The unidirectional motor is directly connected to an AC supply, and is described as being a special case of the conventional single phase synchronous PM motor. The backward instability ratio is proposed as an approximate measure of the ability of a unidirectional motor to self correct its direction of rotation. Two theoretical unidirectional motor designs which use this ratio as a design guide have been completed. The first motor design uses a single pole pair and a higher grade of PM material, which is bonded Nd-Fe-B. The second design uses multiple pole pairs and ferrite grade magnets. These designs employ a manufacturable construction consisting of parallel magnetised rotor poles and closed stator slots, in a radial airgap. A theoretical model is developed for calculating the EMF/torque function, which shows that as the number of pole pairs increases, a parallel magnetisation more closely approximates a radial magnetisation. This results in the third harmonic in the EMF/torque function becoming more significant for pole pair numbers greater than one. The unidirectional motor concept is shown to be simply implemented in the 2-pole design described above. In this 2-pole design, PM reluctance torque and EMF/torque function waveforms of

high sinusoidal quality are shown to be achievable. Simulation results show that the 2-pole motor achieves unidirectional motion without speed ripple at the rated load and voltage. Unidirectional motion is also shown to occur over a satisfactory range of starting loads. The unidirectional motor eliminates several of the limiting characteristics listed in section 1.2.7: the unidirectional motor self corrects its direction of rotation, the availability of rated torque at all rotor angles ensures initial starting capability, and speed ripple, which can cause noise problems, is either eliminated or reduced. However, it is shown that an even tighter inertial constraint than the conventional motor is required to create sufficient backward instability for unidirectional motion.

There is considerable scope for further unidirectional motor research and development. The theory and ideas presented require experimental validation. Section 4.11.1 describes two unidirectional motor designs which are considered to be more practical for production. These designs use 2-pole ferrite rotors. The first design uses a small enough rotor diameter to ensure sufficient backward instability. The second design uses a larger rotor diameter, and has the same inertial constraint on rotor diameter as the conventional 2-pole motor. In this design, a mechanical direction correcting device is required, and speed ripple is eliminated at the rated load, reducing noise. A third possibility is to remove the inertial constraint altogether by using the simple triac circuit described in section 1.3.1. The unidirectional motor may be more attractive to use in such a triac circuit because it offers a higher quality torque than the conventional motor.

In Chapter 5, a single phase synchronous PM motor which uses inductive reluctance torque to facilitate starting has been proposed. A theoretical model has been developed. A practical design for this *inductive start* motor, which uses iron rotor laminations, has been developed and tested. It has been demonstrated through the measurement of the start angle that the inductive start motor offers an alternative starting mechanism to that of the conventional designs. For a water-pumping application, the inductive start motor was shown to achieve the same steady state water-pumping performance as the conventional motor. The start angle was shown to be up to twice as large as the displacement angle of the conventional motor.

For further research, the development of a set of equations of motion which reliably model the starting transient of the inductive start motor would be of use. Unlike the conventional model, the inductance cannot be assumed to be constant. Detailed experimental measurements of starting transients are first required before the development of such a model can be attempted. Experimental validation that the motor can be modelled using the conventional equations under steady state running is also required.

Appendix A

PUBLISHED PAPERS

STRAHAN, R.J., 'Energy conversion by nonlinear permanent magnet machines', *IEE Proc.-Electr. Power Appl.*, Vol. 145, No. 3, May 1998, pp. 193–198.

STRAHAN, R.J. AND WATSON, D.B., 'Effects of airgap and magnet shapes on permanent magnet reluctance torque', *IEEE Trans. Magn.*, Vol. 35, No. 1, January 1999, pp. 536–542.

Energy conversion by nonlinear permanent magnet machines

R.J.Strahan

Indexing terms: Energy conversion, Permanent magnet machines, Coupling theory, Reluctance torque, Electromagnetics

Abstract: Stored energy and coenergy are defined for a permanent magnet system. It is shown that either stored energy or coenergy may be used to determine permanent magnet reluctance torque where the magnetisation characteristics of regions within the system are arbitrary. It is shown how residual magnetism may be incorporated into classical electromechanical coupling theory. It is, therefore, shown how general equations for torque can be derived for nonlinear permanent magnet systems from classical electromechanical coupling theory. The approximation made in deriving a simplified equation for torque in a linear system is described. Finally, the validity of the first quadrant representation of the rate of change of coenergy within a permanent magnet material, relevant to CAD systems on electromagnetics, is demonstrated.

1 Introduction

Energy methods are widely used and well understood for determining the torque or force in magnetically nonlinear machines that do not contain permanent magnets. Energy methods are employed to calculate torques or forces of magnetic origin after determination of the energy stored in the electromechanical coupling field. The origins of this theory date back at least as far as [1] where the equation for the force resulting from the 'mechanical action between two circuits' in the absence of magnetic material is expressed in terms of currents and inductance coefficients. The scope of this analysis was extended in [2] to provide general equations for an arbitrary number of circuits which may contain iron, either saturated or not, but are assumed to have no hysteresis. This has been followed by comprehensive treatments of electromechanical coupling theory [3–5]. The increasing use and improving technology of permanent magnet materials has generated a need to incorporate materials exhibiting residual magnetism into this theory. The purpose of this paper is to show how the classical theory can accommodate residual magnetism. By addressing the magnetisation process it shows how stored energy may be defined in a permanent magnet system. By then examining energy methods, a solid theoretical base for a selection of torque equations used by both machine and CAD system designers, as well as some less obvious equations, is provided. (In this paper, equations for force may be obtained from torque equations by replacing the rotational displacements with linear displacements.)

IEE Proceedings online no. 19981863

Paper first received 23rd September 1997 and in revised form 5th January 1998

The author is with the Department of Electrical and Electronic Engineering, University of Canterbury, Private Bag 4800, Christchurch, New Zealand

2 Energy stored in a permanent magnet system

In classical electromechanical coupling theory stored energy is a physical quantity which can be measured experimentally. The stored energy is the energy which can be transferred to or from a conservative electromechanical coupling field via mechanical or electrical terminals. In this Section the definition of stored energy extended to a system exhibiting significant residual magnetism or permanent magnetism remains essentially the same. The specification of a conservative electromechanical coupling field thus excludes hysteresis from the calculation of torque.

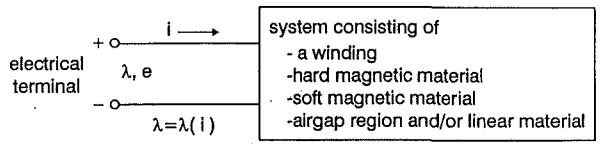

Fig. 1 *Electrical terminal pair representation of a permanent magnet system*

Fig. 1 shows a representation of a permanent magnet system consisting of a winding and a hard magnetic material. The winding has a flux linkage λ and current i and its terminals are depicted in Fig. 1. An airgap or linear region and a soft magnetic material may also be included in the system. The soft magnetic material is modelled as being anhysteretic with the **B**–**H** characteristic passing through the origin. Energy may be transferred to the system electrically or mechanically. To simplify the calculation of energy transferred to the system, the energy transferred to the system is accounted for electrically. This is achieved by treating the hard magnetic material as being initially unmagnetised such that initially $\lambda = 0$ when $i = 0$ and any forces or torques of magnetic origin are zero. All frictional and resistive losses excluding hysteresis loss are modelled externally to the system. The system may therefore be nonconservative during the magnetisation process. The system is first mechanically assembled with λ held at zero and the mechanical energy transferred to the system is zero. The flux linkage is then raised from zero

and a voltage $e = d\lambda/dt$ is induced across the electrical terminals by the magnetic field. The energy transferred is obtained, in this case, by the classical equation for stored energy in a singly excited system:

$$\vartheta = \int_0^{\lambda} id\lambda \tag{1}$$

The energy transferred is absorbed as energy which is recoverable and also as energy which is not recoverable. However, eqn. 1 and the $\lambda - i$ characteristic do not, in general, provide sufficient information to allow the components of recoverable and nonrecoverable energy to be determined. Eqn. 1 is equivalently expressed in terms of the energy density of the magnetic field corresponding to vectors **B** and **H** integrated over the volume of the system by

$$\vartheta = \int_V \int_0^{\mathbf{B}} \mathbf{H} \cdot d\mathbf{B} dv \tag{2}$$

This mathematical transformation is described in [6], pp. 122–124. The field may be due to both currents and residually magnetised material. Eqn. 2 allows the energy transferred to the system to be separated using **B–H** characteristics into components within elements of the system volume as follows. Fig. 2*a* shows a **B–H** characteristic for a hard magnetic material. From **B** = 0 the characteristic follows the initial magnetisation curve until the saturation flux density $\mathbf{B}_{sat}$ is reached.

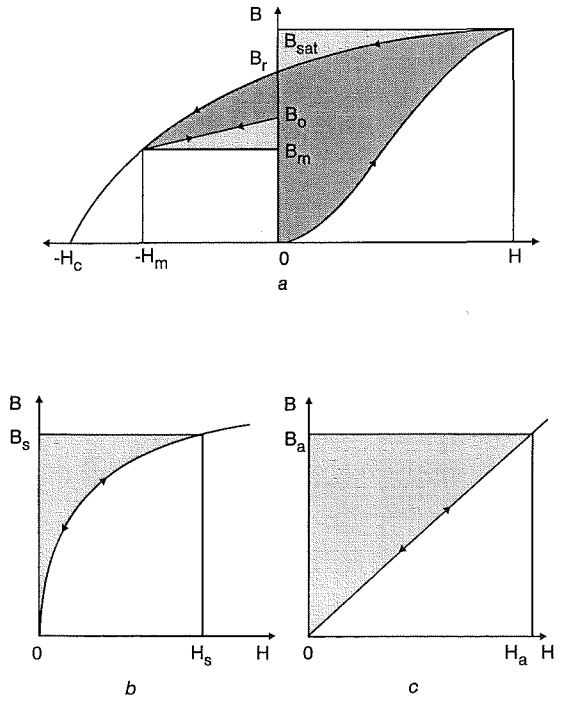

Fig. 2 *B–H characteristics and energy densities*
a Hard magnetic material
b Soft magnetic material
c Air or linear material

The energy density corresponding to energy absorbed by this magnet region is depicted by both shaded areas in the first quadrant. The field intensity **H** is then reduced to zero and the flux density follows the major hysteresis curve from $\mathbf{B}_{sat}$ to $\mathbf{B}_r$ in which $\mathbf{H} \cdot d\mathbf{B}$ is negative and recoverable energy is returned to the electrical terminals or absorbed by some other region or both. The recoverable energy corresponds to the lighter shaded area in the first quadrant. The darker shaded area corresponds to nonrecoverable energy. This energy is nonrecoverable because the magnetisation characteristic cannot be retraced back to **B** = 0 at **H** = 0 from within the first quadrant. The recoverable energy will be defined as the 'stored energy'. At **H** = 0 with **B** = $\mathbf{B}_r$ no more energy is recoverable and the stored energy is zero. (Note: After completion of a full cycle of a hysteresis loop, the magnetisation is returned its original condition, and nonrecoverable energy has been dissipated as heat called the hysteresis loss [7]. Similarly, if the *B–H* characteristic in Fig. 2*a* is extended into the 2nd and 3rd quadrants such that a hysteresis loop is compeleted returning to **B** = **H** = 0, the nonrecoverable energy of the first quadrant has been dissipated as hysteresis loss.)

The flux density is now reduced to $\mathbf{B}_m$ by a demagnetising field $\mathbf{H}_m$ during which $\mathbf{H} \cdot d\mathbf{B}$ is positive and energy corresponding to the areas of both shaded regions in the second quadrant is absorbed. The demagnetising field is now reduced to zero and it is assumed that a minor hysteresis loop is followed to $\mathbf{B}_o$. The hysteresis loss in cycling between **H** = 0 and $\mathbf{H}_m$ is assumed to be small such that the minor loop can be approximated by a recoil line. Therefore upon initially reaching $\mathbf{B}_o$, the darker shaded area in the second quadrant corresponds to nonrecoverable energy, and the lighter shaded area to stored energy returned to the electrical terminals or absorbed by some other region or both. For subsequent movement of the operating point along the recoil line, or as long as the characteristic remains single-valued within the limits of integration $\mathbf{B}_o$ to $\mathbf{B}_m$, hysteresis is excluded and the permanent magnet stored energy is given by

$$W_m = \int_{V_m} \int_{\mathbf{B}_o}^{\mathbf{B}_m} \mathbf{H}_m \cdot d\mathbf{B}_m dv_m \tag{3}$$

Fig. 2*b* and *c* show **B–H** characteristics for a single-valued soft magnetic material, and air or linear material, respectively. The areas of the shaded regions correspond to stored energies. Given that the hard magnetic material has reached a single-valued state within the limits described above, the electromechanical coupling field is conservative, and the stored energy of the permanent magnet system is given by

$$\begin{aligned} W = & \int_{V_m} \int_{\mathbf{B}_o}^{\mathbf{B}_m} \mathbf{H}_m \cdot d\mathbf{B}_m dv_m \\ & + \int_{V_s} \int_0^{\mathbf{B}_s} \mathbf{H}_s \cdot d\mathbf{B}_s dv_s \\ & + \frac{1}{2} \int_{V_a} \mathbf{B}_a \cdot \mathbf{H}_a dv_a \end{aligned} \tag{4}$$

The inner integrals of the three RHS terms of eqn. 4 are the energy density functions of the permanent magnet, soft material, and linear material, respectively. Some examples of these energy density functions are given in [8, 9].

An equation is given in [10] where the stored energy of the permanent magnet system is calculated by integrating over only the volume of the magnet using

$$W = \frac{1}{2} \int_{V_m} \int [\mathbf{H}_m \cdot d\mathbf{B}_m - \mathbf{B}_m \cdot d\mathbf{H}_m] dv_m \tag{5}$$

Eqn. 5 is exactly equivalent to

$$W = \int_{V_m} \int_{\mathbf{B}_o}^{\mathbf{B}_m} \mathbf{H}_m \cdot d\mathbf{B}_m dv_m - \frac{1}{2} \int_{V_m} \mathbf{B}_m \cdot \mathbf{H}_m dv_m \tag{6}$$

From eqn. 39 in the Appendix (Section 9.1) it can be shown that

$$-\frac{1}{2}\int_{V_m}\mathbf{B}_m\cdot\mathbf{H}_m dv_m=\frac{1}{2}\int_{V_a}\mathbf{B}_a\cdot\mathbf{H}_a dv_a \quad (7)$$

if all currents are zero. Eqns. 5 and 6 are, therefore, only valid if the region outside the permanent magnet is linear and all currents are zero.

Expressions for **B** and **H** may be derived as functions of electrical and mechanical terminal quantities. Eqns. 4–6 may therefore be expressed as functions of rotational displacements for the calculation of reluctance torque. For a rotational displacement θ with the winding de-energised, or removed, the resulting reluctance torque is defined as the negative rate of conversion of stored energy into mechanical energy:

$$T_{rel}=-\frac{dW(i=0)}{d\theta} \quad (8)$$

The definition of stored energy given here yields expressions for stored energy which, when used in eqn. 8, are shown to give accurate values of permanent magnet reluctance torque [8, 9].

The definition of stored energy provided here permits determination of the relationship of the mathematical quantity 'coenergy' to stored energy where all currents are zero, in Section 3. Energy methods are examined more generally in Sections 4.1 and 4.2 to include nonzero currents.

3 Coenergy of a permanent magnet system

For the system described in Section 2, the transferred coenergy may be determined from

$$\vartheta'=\int_0^i\lambda di \quad (9)$$

Eqn. 9 is equivalently expressed by

$$\vartheta'=\int_V\int_0^{\mathbf{H}}\mathbf{B}\cdot d\mathbf{H}dv \quad (10)$$

After completing the magnetising sequence described in Section 2, the coenergy density corresponding to $\mathbf{H}=\mathbf{H}_m$ is shown by the shaded area in Fig. 3*a*. As long

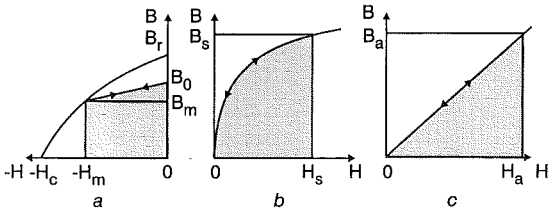

Fig. 3 *Coenergy densities*
a Hard magnetic material
b Soft magnetic material
c Air or linear material

as the demagnetising field remains within limits in which the characteristic remains single-valued, the permanent magnet coenergy is given by

$$W'_m=\int_{V_m}\int_0^{\mathbf{H}_m}\mathbf{B}_m\cdot d\mathbf{H}_m dv_m \quad (11)$$

Fig. 3*b* and *c* show the areas corresponding to coenergy for a single-valued soft magnetic material and air or linear material, respectively. The coenergy of the permanent magnet system is given by

$$W'=\int_{V_m}\int_0^{\mathbf{H}_m}\mathbf{B}_m\cdot d\mathbf{H}_m dv_m+\int_{V_s}\int_0^{\mathbf{H}_s}\mathbf{B}_s\cdot d\mathbf{H}_s dv_s+\frac{1}{2}\int_{V_a}\mathbf{B}_a\cdot\mathbf{H}_a dv_a \quad (12)$$

For a permanent magnet system, with the winding de-energised, eqn. 41 in the Appendix (Section 9.1) shows that

$$W'(i=0)=-W(i=0) \quad (13)$$

Substitution of eqn. 13 into eqn. 8 shows that the reluctance torque is obtained in terms of coenergy by

$$T_{rel}=\frac{dW'(i=0)}{d\theta} \quad (14)$$

4 Electromechanical coupling

4.1 Permanent magnets and single energised winding

Fig. 1 is now extended to include a mechanical terminal such that simultaneous electrical and mechanical energy conversion may occur. If current and flux linkage are now defined to be state functions then hysteresis is excluded, the functional relationship between these variables is single-valued, and the system is conservative [3]. The conservation of power may then be described by

$$\frac{dW}{dt}=i\frac{d\lambda}{dt}-T\frac{d\theta}{dt} \quad (15)$$

such that the differential energy is given by

$$dW(\lambda,\theta)=id\lambda-Td\theta \quad (16)$$

whereby the torque is obtained in terms of stored energy by the classical result:

$$T=-\frac{\partial W(\lambda,\theta)}{\partial\theta} \quad (17)$$

where the partial derivative is taken with λ held constant. The differential energy $dW(\lambda, \theta)$ must have the properties of a state function for eqn. 16, and thus eqn. 17, to hold. However, this does not imply that $dW(\lambda, \theta)$ or $W(\lambda, \theta)$ are required to have the properties of state functions for all values of independent variables λ and θ. This imposes the constraint that if any of the independent variables are outside of a range where $W(\lambda, \theta)$ has the properties of a state function, then the torque cannot be obtained using eqn. 17 for those values of the independent variables.

The stored energy is obtained by integration of eqn. 16:

$$W(\lambda,\theta)=\int_{0,0}^{\lambda,\theta}id\lambda-Td\theta \quad (18)$$

The line integral of eqn. 18 is simplified by assembling the system by the method described in Section 2 such that the energy transferred to the system in raising the flux linkage to a final value is given by eqns. 1 and 2. To determine the stored component of transferred energy, eqn. 2 must be used. In raising the flux density of the magnet from zero to $\mathbf{B}_o$, the system is not conservative. However, because the magnetisation history is known, the stored energy can be calculated within these limits, and is found to be zero. Therefore, the stored energy is obtained by raising the flux density of the magnet from $\mathbf{B}_o$ to $\mathbf{B}_m$, through which the stored energy is regarded to have the properties of a state

function and is given by eqn. 4. The stored energy is regarded to have the properties of a state function if the demagnetising field $\mathbf{H}_m$ remains within limits such that the demagnetising characteristic remains single-valued. The state function requirement of eqn. 16 is therefore satisfied allowing the torque of the permanent magnet system to be given by eqn. 17.

In a conservative system the relationship between energy and coenergy is given by a Legendre transformation:

$$W' = \lambda i - W \tag{19}$$

which is necessarily shown in the Appendix (Section 9.2) (by setting $J = 1$) to hold for a permanent magnet system. This relationship allows the torque to be equivalently expressed by the remaining classical results:

$$T = \frac{\partial W'(\lambda, \theta)}{\partial \theta} - \lambda \frac{\partial i(\lambda, \theta)}{\partial \theta} \tag{20}$$

$$T = \frac{\partial W'(i, \theta)}{\partial \theta} \tag{21}$$

$$T = i \frac{\partial \lambda(i, \theta)}{\partial \theta} - \frac{\partial W(i, \theta)}{\partial \theta} \tag{22}$$

where the partial derivatives of eqns. 21 and 22 are taken with i held constant. The coenergy W' for a permanent magnet system is obtained by eqn. 12. Eqns. 17, 20–22 each allow the torque to be obtained for a nonlinear permanent magnet system. For these equations, it is essential to hold the independent variable λ or i constant while taking the partial derivative analytically or numerically. Note that eqns. 17 and 21 are more general forms of eqns. 8 and 14.

4.2 Permanent magnets and multiple energised windings

Fig. 1 is now extended to include J electrical and K mechanical terminal pairs. The energy differential is then given by

$$dW = \sum_{j=1}^{J} i_j d\lambda_j - \sum_{k=1}^{K} T_k d\theta_k \tag{23}$$

whereby the torque obtained at the kth mechanical terminal is obtained in terms of stored energy by

$$T_k = -\frac{\partial W(\lambda, \theta)}{\partial \theta_k} \tag{24}$$

where (λ, θ) is now an abbreviation for $(\lambda_1, ..., \lambda_J; \theta_1, ..., \theta_K)$. If the system is assembled in an analogous manner to that described in Section 2, the energy transferred to the system in raising the flux linkages to their final values is given by eqn. 2 and also by

$$\vartheta = \int_{0,...,0}^{\lambda_1,...,\lambda_J} \sum_{j=1}^{J} i_j d\lambda_j \tag{25}$$

where $i_j = i_j(\lambda_1, ..., \lambda_J; \theta_1, ..., \theta_K)$. If there is no hard magnetic material in the system and the functional relationships between variables is single-valued, eqn. 25 obtains the stored energy as a state function given that independence of path is demonstrated by satisfying the following equalities:

$$\frac{\partial i_1}{\partial \lambda_2} = \frac{\partial i_2}{\partial \lambda_1}, \quad \frac{\partial i_1}{\partial \lambda_3} = \frac{\partial i_3}{\partial \lambda_1}, \quad \frac{\partial i_2}{\partial \lambda_3} = \frac{\partial i_3}{\partial \lambda_2}, \ldots \tag{26}$$

If a permanent magnet is present, the stored energy is determined by eqn. 4. The Appendix (Section 9.2) shows that the relationship

$$W + W' = \sum_{j=1}^{J} \lambda_j i_j \tag{27}$$

holds for a permanent magnet system with multiple energised windings. Application of eqn. 27 allows the torque to be equivalently expressed by

$$T_k = \frac{\partial W'(\lambda, \theta)}{\partial \theta_k} - \sum_{j=1}^{J} \lambda_j \frac{\partial i_j(\lambda, \theta)}{\partial \theta_k} \tag{28}$$

$$T_k = \frac{\partial W'(i, \theta)}{\partial \theta_k} \tag{29}$$

$$T_k = \sum_{j=1}^{J} i_j \frac{\partial \lambda_j(i, \theta)}{\partial \theta_k} - \frac{\partial W(i, \theta)}{\partial \theta_k} \tag{30}$$

where (i, θ) is an abbreviation for $(i_1, ..., i_J; \theta_1, ..., \theta_K)$. With CAD packages on electromagnetics, it is known that values of torque can be accurately determined from the rate of change of the total coenergy computed by integrating the coenergy density over the volume of the system, as demonstrated by [11]. This confirms the validity of eqn. 29. The validity of torque eqns. 24, 28 and 30 are demonstrated by mathematical equivalence to eqn. 29, resulting from the proof of eqn. 27 given in the Appendix (Section 9.2). (Note: The 'work function' formulation in [9] is equivalent to eqn. 30, and is supported numerically by comparison to Maxwell stress results.)

In many CAD packages, a representation of permanent magnets described in Section 6 is useful for numerical computation. This representation is shown in Section 6 to give an identical rate of change of permanent magnet coenergy to that of the second quadrant representation of coenergy given in Section 3 by eqn. 11. Thus coenergy, as defined by eqn. 12, is also shown by equivalence to yield accurate values of torque.

5 Torque equations for a linear permanent magnet system

In the absence of iron saturation, where a single winding is energised, the flux linkage of the winding may be given by

$$\lambda = \lambda_m(\theta) + L(\theta) i \tag{31}$$

where λ_m is the flux linkage due to the magnet, and L is the inductance of the winding. Substituting eqn. 31 into eqn. 22 yields

$$T = i \frac{d\lambda_m}{d\theta} + i^2 \frac{dL}{d\theta} - \frac{\partial W(i, \theta)}{\partial \theta} \tag{32}$$

The stored energy $W(i, \theta)$ is determined by eqn. 4. Fig. 2*a* shows that if $\mathbf{B}_m$ increases towards $\mathbf{B}_o$ due to, for example, a winding current increase, the stored energy of the magnet decreases. A corresponding increase in $\mathbf{B}$ in a region surrounding the magnet yields an increase in the stored energy in that region. Eqn. 32 can be simplified by approximating the energy stored to correspond to mutually exclusive components provided by the winding and the magnet, whereby

$$W = W(i = 0, \theta) + 1/2\, L(\theta) i^2 \tag{33}$$

and the torque is approximated by

$$T = i \frac{d\lambda_m}{d\theta} + \frac{1}{2} i^2 \frac{dL}{d\theta} - \frac{dW(i = 0, \theta)}{d\theta} \tag{34}$$

which is given in [12] and is shown to model the motion of a single phase permanent magnet motor sufficiently accurately in [13]. The first term in eqn. 34 is used to calculate the torque due to the coupling between a magnet and an energised winding in brushless permanent magnet machines. The remaining two terms describe the torques obtained due to reluctance variation with rotational displacement. Eqn. 34 is particularly useful for experimental purposes because all of the quantities can be measured from electrical and mechanical terminals.

6 Current sheet model of a permanent magnet

In a permanent magnet material the relation of **B** to **H** may be expressed in the form of [6], pp. 13, 129:

$$\mathbf{B} = \mu_o[\mathbf{H} + \mathbf{M}(\mathbf{H}, \mathbf{M}_o) + \mathbf{M}_o] \quad (35)$$

M is the induced polarisation defined by $\mathbf{M} = \chi_m \mathbf{H}$ where magnetic susceptibility χ_m is defined by $\chi_m = \partial\mathbf{M}/\partial\mathbf{H}$. $\mathbf{M}_o$ is the residual magnetisation which is nonzero in permanent magnet regions such that **B** is nonzero when $\mathbf{H} = 0$. $\mathbf{M}_o$ is interpreted as a source of the field. $\mathbf{M}_o$ may be replaced by a stationary volume distribution of current throughout the volume of the magnet of density

$$\mathbf{J} = \text{curl}\,\mathbf{M}_o \quad (36)$$

and with a current distribution on the surface bounding the magnet volume of density

$$\mathbf{K} = \mathbf{M}_o \times \mathbf{n} \quad (37)$$

where **n** is the unit outward normal to the surface ([6], p. 129). With $\mathbf{M}_o$ replaced by an equivalent current sheet, eqn. 35 reduces to $\mathbf{B} = \mu_o[\mathbf{H} + \mathbf{M}]$ which describes a **B–H** characteristic of the first quadrant passing through the origin. The shifted curve representation is shown in Fig. 4*b*.

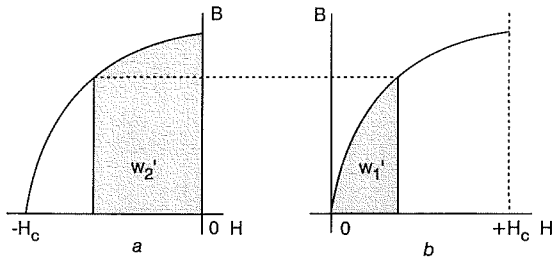

Fig. 4 *Representations of permanent magnet coenergy density*
a Second quadrant demagnetisation curve
b Curve shifted to first quadrant

CAD packages on electromagnetics use the technique of shifting the second quadrant demagnetisation curve to the origin and introduce a suitable current carrying coil for modelling a permanent magnet [14]. The torque may be obtained from the current sheet model using Maxwell stress [14] or some other method.

With CAD packages, it is known that values of torque can be accurately determined from the rate of change of the total coenergy using the first quadrant representation of permanent magnet coenergy, as demonstrated by [11]. Coenergy density for the first quadrant representation of a permanent magnet is shown by the shaded region in Fig. 4*b*. The relationship between first and second quadrant coenergy representations is given by

$$w_1' = w_2' + w_{1H_c}' \quad (38)$$

where w_2' is a negative coenergy density. The term w_{1H_c}' is the area under the shifted curve from 0 to H_c and is a constant. The rate of change of coenergy is therefore the same for both representations, thus yielding identical values of torque. This relationship provides first: a supporting theoretical basis for the first quadrant representation; and secondly supporting evidence for the experimental validity of the second quadrant representation.

However, caution must be observed if stored energy rather than coenergy is used, as the respective first and second quadrant rates of change of stored energy are different. In this case, only a second quadrant representation has a theoretical basis.

7 Conclusions

Stored energy and coenergy have been defined for a permanent magnet system. It has been shown that either stored energy or coenergy may be used to determine permanent magnet reluctance torque where the magnetisation characteristics of regions within the system are arbitrary. It has also been shown how residual magnetism may be incorporated into classical electromechanical coupling theory. It has therefore been shown how general equations for torque can be derived for nonlinear permanent magnet systems from classical electromechanical coupling theory. In doing this it has been shown that the relationship $W + W' = \lambda i$ holds for a permanent magnet system. The approximation made in deriving a simplified equation for torque in a linear system has been described. Finally, the validity of the first quadrant representation of the rate of change of coenergy within a permanent magnet material, relevant to CAD systems, has been demonstrated.

8 References

1 MAXWELL, J.C.: 'A treatise on electricity and magnetism', vol. 2 (republished Dover, New York, 1954, 3rd edn.), Art. 583
2 DOHERTY, R.E., and PARK, R.H.: 'Mechanical force between electric circuits', *Trans. AIEE*, 1926, **45**, pp. 240–252
3 WHITE, D.C., and WOODSON, H.H.: 'Electromechanical energy conversion' (J. Wiley & Sons, New York, 1959)
4 FITZGERALD, A.E., KINGSLEY, C., and UMANS, S.D.: 'Electric machinery' (McGraw–Hill, New York, 1992, 5th edn.)
5 WOODSON, H.H., and MELCHER, J.R.: 'Electromechanical dynamics. Part I: Discrete systems' (J. Wiley & Sons, New York, 1968)
6 STRATTON, J.A.: 'Electromagnetic theory' (McGraw–Hill, New York, 1941)
7 CHIKAZUMI, S.: 'Physics of magnetism' (J. Wiley & Sons, New York, 1964), p. 17
8 HOWE, D., and ZHU, Z.Q.: 'Influence of finite element discretisation on the prediction of cogging torque in permanent magnet excited motors', *IEEE Trans. Magn.*, 1992, **28**, (2), pp. 1080–1083
9 MARINESCU, M., and MARINESCU, N.: 'Numerical computation of torque in permanent magnet motors by Maxwell stresses and energy method', *IEEE Trans. Magn.*, 1988, **24**, (1), pp. 463–466
10 ZIJLSTRA, H.: 'Permanent magents; theory' *in* WOHLFARTH, E.P. (Ed.): 'Ferromagnetic materials', vol. 3 (North–Holland, 1982), chapter 2
11 BRAUER, J.R., LARKIN, L.A., and OVERBYE, V.D.: 'Finite element modelling of permanent magnet devices', *J. Appl. Phys.*, 1984, **55**, (6), pp. 2183–2185
12 KAMERBEEK, E.M.H.: 'Electric motors', *Philips Techn. Rev.*, 1973, **33**, (8/9), pp. 215–234
13 SCHEMMANN, H.: 'Theoretische und experimentelle untersuchungen uber das Dynamische verhalten eines Einphasen–synchron–motors mit dauermagnetischem laufer'. PhD thesis, Technische Hogeschool, Eindhoven, Oct. 1971
14 GUPTA, R., YOSHINO, T., and SAITO, Y.: 'Finite element solution of permanent magnetic field', *IEEE Trans. Magn.*, 1990, **26**, (2), pp. 383–386
15 BROWN, Jr. W.F.: 'Magnetostatic principles in ferromagnetism' (North–Holland, 1962), pp. 44–45

9 Appendix

9.1

A quasistatic permanent magnet system with all windings de-energised satisfies curl $\mathbf{H} = 0$ and div $\mathbf{B} = 0$, from which it can be shown that [10, 15]

$$\int_V \mathbf{H} \cdot \mathbf{B} dv = 0 \tag{39}$$

where V is volume of the permanent magnet system. By applying the rule of differentiation, whereby $d(\mathbf{H} \cdot \mathbf{B}) = \mathbf{H} \cdot d\mathbf{B} + \mathbf{B} \cdot d\mathbf{H}$, eqn. 39 is expressed as

$$\int_V \left[\int \mathbf{H} \cdot d\mathbf{B} + \int \mathbf{B} \cdot d\mathbf{H} \right] dv = 0 \tag{40}$$

which according to eqns. 4 and 12 may be written as

$$W(i = 0) + W'(i = 0) = 0 \tag{41}$$

where the magnetisation characteristics of regions within the system are arbitrary.

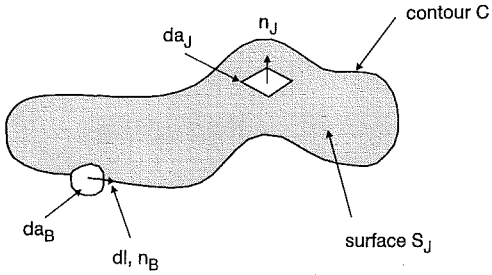

Fig.5 *Contour of flux*

9.2

The permanent magnet system of Section 9.1 is now extended to the case where curl $\mathbf{H} = \mathbf{J}_f$ and div $\mathbf{B} = 0$, where $\mathbf{J}_f$ is the free current density which will be attributed to winding currents. The integral forms of the field equations described above are respectively given by

$$\oint_C \mathbf{H} \cdot d\mathbf{l} = \int_{S_J} \mathbf{J}_f \cdot \mathbf{n}_J da_J \tag{42}$$

and

$$\oint_S \mathbf{B} \cdot \mathbf{n} da = 0 \tag{43}$$

These integral forms enable the circuit quantities λ and i to be deduced. Contour C is chosen so as to follow any single contour of flux, where $\mathbf{H}$ is related to $\mathbf{B}$ by eqn. 35. Eqn. 43 will be written in the modified form of

$$\mathbf{B} \cdot \mathbf{n}_B da_B = \phi \tag{44}$$

where da_B may be any surface element of near infinitesimal area which is orthogonal to an element of length $d\mathbf{l}$ and bisects C once and only once, as shown in Fig. 5. Unit normal vector $\mathbf{n}_B$, $\mathbf{B}$, and $d\mathbf{l}$ are parallel. ϕ is the integrated flux which will be required to remain constant wherever eqn. 44 is evaluated over contour C. The path chosen for C ensures that $\mathbf{B} \cdot \mathbf{n} \neq 0$ such that $\phi \neq 0$. Multiplying eqn. 42 by eqn. 44 gives

$$\mathbf{B} \cdot \mathbf{n}_B da_B \oint_C \mathbf{H} \cdot d\mathbf{l} = \phi \int_{S_J} \mathbf{J}_f \cdot \mathbf{n}_J da_J \tag{45}$$

The LHS of eqn. 45 is transformed as follows. Let $\oint_C \mathbf{H} \cdot d\mathbf{l} = \Sigma_{i=1}^{\infty} \mathbf{H}_i \cdot d\mathbf{l}_i = \Sigma_{i=1}^{\infty} \mathbf{H}_i \cdot \mathbf{n}_{B_i} \Delta l_i$, giving

$$\mathbf{B} \cdot \mathbf{n}_B da_B \oint_C \mathbf{H} \cdot d\mathbf{l} = \sum_{i=1}^{\infty} (\mathbf{H}_i \cdot \mathbf{n}_{B_i} \Delta l_i)(\mathbf{B}_i \cdot \mathbf{n}_{B_i} \Delta a_{B_i}) \tag{46}$$

which is equal to

$$\sum_{i=1}^{\infty} (|\mathbf{H}_i||\mathbf{n}_{B_i}| \cos \gamma_{H_i})(|\mathbf{B}_i||\mathbf{n}_{B_i}| \cos \gamma_{B_i}) \Delta v_i \tag{47}$$

where $\Delta v_i = \Delta l_i \Delta a_{B_i}$ is an element of volume. Eqn. 47 is simplified by letting $|\mathbf{n}_{B_i}| = 1$ and $\cos \gamma_{B_i} = 1$ to yield

$$\sum_{i=1}^{\infty} |\mathbf{H}_i||\mathbf{B}_i| \cos \gamma_{H_i} \Delta v_i \tag{48}$$

γ_{H_i} is also the angle between $\mathbf{H}_i$ and $\mathbf{B}_i$, therefore

$$\sum_{i=1}^{\infty} |\mathbf{H}_i|\mathbf{B}_i| \cos \gamma_{H_i} \Delta v_i = \sum_{i=1}^{\infty} \mathbf{H}_i \cdot \mathbf{B}_i \Delta v_i = \int_{V_C} \mathbf{H} \cdot \mathbf{B} dv_C \tag{49}$$

V_C is the filament volume corresponding to contour C. The RHS of eqn. 45 is transformed as follows. The integral $\int_{S_J} \mathbf{J}_f \cdot \mathbf{n}_J da_J$ may be expressed as a sum of contributions from winding currents crossing surface S_J by $\Sigma_{j=1}^{J} \nu_j i_j$ where i_j is the current of the jth winding and ν_j is a coefficient corresponding to the jth winding which may for some values of j be a fractional number or zero. The RHS of eqn. 45 may then be expressed by

$$\phi \sum_{j=1}^{J} \nu_j i_j = \sum_{j=1}^{J} \lambda_{C_j} i_j \tag{50}$$

where $\lambda_{C_j} = \phi \nu_j$. The flux ϕ is a function of the currents and $\mathbf{M}_o$ such that $\phi = \phi(i_1, \ldots, i_J, \mathbf{M}_o)$ and $\lambda_{C_j} = \lambda_{C_j}(i_1, \ldots, i_J, \mathbf{M}_o)$. Eqn. 45 is then expressed as

$$\int_{V_C} \mathbf{H} \cdot \mathbf{B} dv_C = \sum_{j=1}^{J} \lambda_{C_j} i_j \tag{51}$$

By then summing the contributions from all the filaments into which the field has been resolved yields

$$W + W' = \sum_{j=1}^{J} \lambda_j i_j$$

Effects of Airgap and Magnet Shapes on Permanent Magnet Reluctance Torque

R. J. STRAHAN, and D. B. WATSON

Abstract

This paper examines the permanent magnet reluctance torques produced by three different configurations of permanent magnet, airgap, and iron. These configurations are briefly described here as rectangular magnet/triangular airgap, rectangular magnet/sinusoidal airgap, and sinusoidal magnet/sinusoidal airgap. The analysis of the torques is achieved by developing analytical solutions. Equations for magnet reluctance torque are obtained by finding the derivative of the stored field energy with respect to position. The triangular airgap configuration is shown to produce a torque waveform which approximates a triangular waveform, and both the sinusoidal airgap configurations are shown to produce torque waveforms which approximate sinusoids.

I. Introduction

This paper examines the torques produced by three different configurations of permanent magnet, airgap, and iron. These configurations are briefly described here as rectangular magnet/triangular airgap, rectangular magnet/sinusoidal airgap, and sinusoidal magnet/sinusoidal airgap. The analysis of the torque is achieved by development of analytical solutions. The advantages of the analytical approach over numerical approaches, such as finite elements, are that the former affords greater insight into the influence of design parameters, and imposes less of a computational burden. Equations for magnet reluctance torque are obtained analytically from the derivative of the stored field energy with respect to position. The stored field energy is obtained with the use of an elementary expression for the magnetic field. The approach taken to obtain the torque contrasts with that of integration of the tangential Maxwell stress along an arc in the airgap, in that the latter requires accurately determined values for the tangential and normal flux density components.

II. Basis of Analysis

A. Reluctance Torque and Stored Field Energy

For a quasi-static electromagnetic device, energy may be stored by the magnetic field. The magnetic field energy is supplied by mechanical and electrical sources [1]. If there are no electrical sources, energy is transferred only between the magnetic field and the mechanical source. In this case, for a rotational displacement θ_r, the resulting reluctance torque is defined as the negative rate of conversion of stored energy into mechanical energy:

$$T = -\frac{\partial W}{\partial \theta_r} \tag{1}$$

In the configurations listed above, the magnetic field permeates air, iron, and permanent magnet regions. The stored field energy is obtained by summing the energies of the three regions:

$$W = W_{air} + W_{iron} + W_{pm} \tag{2}$$

The authors wish to express their gratitude to Dr J. D. Edwards of the University of Sussex for performing the finite element analysis in this paper.

R. J. Strahan and D. B. Watson are with the Department of Electrical & Electronic Engineering, University of Canterbury, Christchurch, New Zealand.

In general, the stored energy per unit volume is given by [2]

$$w = \int H dB \tag{3}$$

and the total stored energy is obtained by integrating over the whole volume

$$W = \int w dV \tag{4}$$

For air, the linear relationship between B and H is given by $B = \mu_o H$. In terms of flux density, the energy density of the air is

$$w_{air} = \frac{B^2}{2\mu_o} \tag{5}$$

Howe and Zhu [2] provide equations for the magnetisation and stored energy of iron. Unless the iron is heavily saturated, thus yielding a low relative permeability, the iron energy density is unlikely to be large. For the sake of simplicity, the stored energy contribution due to the iron will be made zero. The stored field energy will therefore be approximated by the contributions from the air and permanent magnet regions only.

The demagnetisation characteristic for the permanent magnet material will be assumed to be linear over the second quadrant with recoil permeability $\mu_o \mu_r$, given by

$$B_{pm} = B_r + \mu_o \mu_r H_{pm} \tag{6}$$

where B_r is the remanence. To calculate the energy stored in the permanent magnet region, the magnet flux density will be assumed to be parallel to the direction of magnetisation. The permanent magnet stored energy density is then given by [2]

$$w_{pm} = \frac{(B_r - B_{pm})^2}{2\mu_o \mu_r} \tag{7}$$

B. Approximation of the Direction and the Magnitude of the Magnetic Flux Density

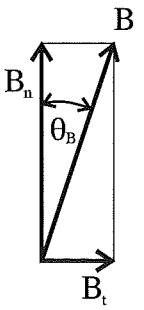

(a) Components of flux density.

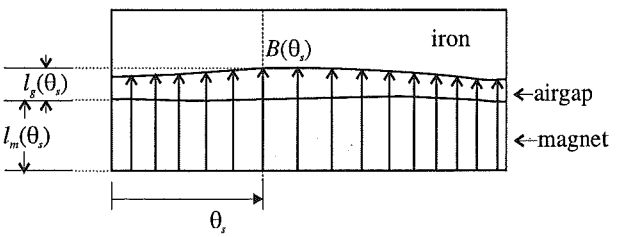

(b) Normal lines of flux.

Fig. 1.

The flux density in any element of area consists of normal and tangential components, as shown by Fig. 1(a). Fig. 1(b) shows a general magnet/airgap configuration where a rotary permanent magnet and iron structure is laid out linearly. Flux lines link a permanent magnet, an airgap, and an iron return path of infinite permeability. Flux lines have been drawn only in regions where the stored energy is calculated. The flux density

is approximated to lie in the normal direction only, given the presence of the following requirements:

1. The magnet is uniformly magnetised in the normal direction. The relative permeability of the magnet, μ_r, is also low.
2. The ratio of airgap area to airgap length is large.
3. The modulation of the airgap length is small.

The magnitude of the flux density at spatial angle θ_s is then obtained by taking the ratio of airgap length l_g, and the magnet length l_m:

$$B(\theta_s) = \frac{B_r}{1 + \frac{l_g(\theta_s)}{l_m(\theta_s)}\mu_r} \tag{8}$$

where magnet and airgap areas are equal. Therefore, under these conditions, where the angle θ_B in Fig. 1(a) is small, the amount of stored energy is approximated by only considering the normal component of the flux density.

III. Rectangular Magnet and Triangular Airgap

(a) Stable detent position, $\theta_r = 0$.

(b) Unstable detent position, $\theta_r = \pi$.

Fig. 2. Rectangular magnet and triangular airgap.

Fig. 2(a) shows a rectangular magnet/triangular airgap configuration where a rotary permanent magnet and iron structure is laid out linearly. The triangular iron shape modulates the airgap volume in a triangular manner, repeating a cycle every 2π radians. The magnet is rectangular, uniformly magnetised in the normal direction, and extends over π radians. In Fig. 2(a), the magnet is aligned at the stable detent position, and in Fig. 2(b) the magnet is aligned at the unstable detent position one half reluctance cycle later.

A. Analytical Derivation of Torque

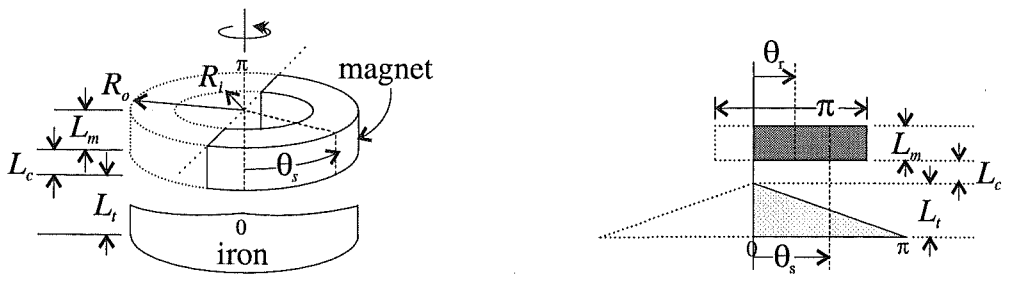

(a) Axial orientation.

(b) Rolled out view of Fig. 3(a).

Fig. 3. Rectangular magnet and triangular airgap.

In this configuration, and in following configurations, the direction of magnet magnetisation is taken as being parallel to the axis of rotation. The flux is in the axial direction, and the airgap is perpendicular to the shaft. This axial orientation is shown for the rectangular magnet and triangular airgap configuration in Fig. 3(a). Fig. 3(b) shows a rolled out view of Fig. 3(a) from which an analytical equation for the reluctance torque is obtained. From eqn.s 4, 5, and 7, the stored energy is obtained by

$$W' = \int \frac{(B_r - B)^2}{2\mu_o\mu_r} dV_{pm} + \int \frac{B^2}{2\mu_o} dV_{air} \tag{9}$$

where B is given by eqn. 8. With reference to Fig. 3(b) and eqn. 8, $l_m(\theta_s) = L_m$ along the angular width of the magnet, and $l_g(\theta_s) = (\theta_s/\pi)L_t + L_c$ where $0 \leq \theta_s \leq \pi$. With reference to Fig. 3(a), the volume of the magnet from zero up to angle θ_s is given by $V_{pm}(\theta_s) = \frac{1}{2}(R_o^2 - R_i^2)\theta_s L_m$ where the magnet is an arc of π radians, with an outer radius R_o, and an inner radius R_i. Then, for eqn. 9

$$dV_{pm} = \frac{1}{2}(R_o^2 - R_i^2)L_m d\theta_s \tag{10}$$

Up to angle θ_s the volume of the airgap is given by $V_{air}(\theta_s) = (R_o^2 - R_i^2)\theta_s^2 L_t/4\pi + (R_o^2 - R_i^2)\theta_s L_c/2$, and

$$dV_{air} = \frac{(R_o^2 - R_i^2)}{2}\left(\frac{L_t\theta_s}{\pi} + L_c\right)d\theta_s \tag{11}$$

Substitution of eqn.s 8, 10, and 11 into eqn. 9 yields

$$W' = \int \frac{B_r^2 k_a(L_t\theta_s + L_c\pi)L_m}{4\mu_o(\pi L_m + \theta_s L_t\mu_r + \pi\mu_r L_c)} d\theta_s \tag{12}$$

where

$$k_a = R_o^2 - R_i^2 \tag{13}$$

For the case described by Fig. 3(b) where the magnet extends π radians, the airgap symmetry about $\theta_s = 0$ allows the total stored energy to be given over an angle of rotation of $-\pi/2 \leq \theta_r \leq \pi/2$ by

$$W = W'\Big|_0^{\pi/2+\theta_r} + W'\Big|_0^{\pi/2-\theta_r} \tag{14}$$

Because the airgap modulation is discontinuous, mathematically the angle of rotation is restricted to $\theta_r = -\pi/2 \ldots \pi/2$, and W is a piecewise function. Integrating eqn. 12 yields

$$W' = \frac{k_a L_m B_r^2}{4\mu_o\mu_r}\left[\theta_s - \frac{L_m\pi \ln(\pi L_m + \theta_s L_t\mu_r + \mu_r\pi L_c)}{\mu_r L_t}\right] \tag{15}$$

From eqn.s 1 and 14, the magnet reluctance torque is then obtained as

$$T = \frac{-\pi k_a B_r^2 L_m^2}{2\mu_o\mu_r} \frac{\theta_r}{\left(\frac{\pi L_m}{L_t\mu_r} + \frac{\pi L_c}{L_t} + \frac{\pi}{2} + \theta_r\right)\left(\frac{\pi L_m}{L_t\mu_r} + \frac{\pi L_c}{L_t} + \frac{\pi}{2} - \theta_r\right)} \tag{16}$$

where $-\pi/2 \leq \theta_r \leq \pi/2$. If $|\theta_r| \ll \frac{\pi L_m}{\mu_r L_t} + \frac{\pi L_c}{L_t} + \frac{\pi}{2}$, eqn. 16 is approximated by

$$T \approx \frac{-\pi k_a B_r^2 L_m^2}{2\mu_o\mu_r} \frac{\theta_r}{\left(\frac{\pi L_m}{\mu_r L_t} + \frac{\pi L_c}{L_t} + \frac{\pi}{2}\right)^2} \tag{17}$$

and $T(\theta_r)$ approximates a straight line. A second piece-wise function, similar to that of eqn. 16, can be obtained for the second half of the cycle to demonstrate a triangular reluctance torque. Eqn. 16 suggests that if $L_m > L_t\mu_r$, a high quality triangular reluctance torque waveform can be obtained with triangular airgap modulation.

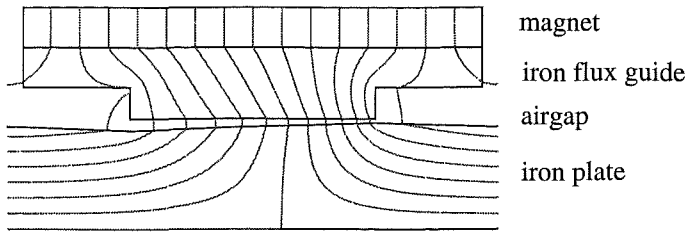

Fig. 4. Finite element flux plot, 3rd order solution. Magnet thickness $L_m = 5$ mm, maximum triangular airgap modulation length $L_t = 1$ mm, un-modulated airgap clearance $L_c = 0.5$ mm, $B_r = 0.68$ T, magnet relative recoil permeability $\mu_r = 1.25$.

B. Finite Element and Experimental Results

The following results are obtained for another configuration where the airgap is also modulated triangularly. However, these results are not directly applicable to the configuration described by Fig. 3. Fig. 4 shows a finite element flux plot for a linear configuration, from top to bottom, consisting of a permanent magnet, iron flux guide, airgap, and triangularly modulated iron plate. The iron flux guide and the magnet are attached together. The triangular modulation on the iron plate completes a reluctance cycle. The magnet is rectangular and extends for nearly a full reluctance cycle. The lower portion of the iron flux guide extends for half a reluctance cycle. The magnet is magnetised in the normal direction (up the page), and is modelled as a linear material specified by its remanence and recoil permeability. The iron regions are represented by the magnetisation curve of a silicon sheet steel. Half periodic boundary conditions are specified at the left and right sides of the model.

The magnet and iron flux guide are shown at a position corresponding to $\theta_r = 3\pi/2$ where the reluctance torque is at its peak magnitude. A tangential force on the magnet and flux guide pulls the two components to the right. A derivation of an analytical force solution for this more complex configuration has not been attempted. The linear two dimensional model of Fig. 4 was designed to represent an experimental axial device. For the experimental device, a radius at which the tangential force acted was assumed to lie where the magnet surface areas inside and outside the radius were equal. This enabled an equivalent linear model magnet length to be calculated. An equivalent magnet width was then selected such that the magnet surface areas of the linear model and those of the experimental device were the same. The heights of linear model and of experimental device components remained identical. The value of the radius at which the tangential force acted could then be used to convert linear model forces into torques.

Table I presents torques, obtained from finite element analysis forces, at four selected positions over the reluctance torque cycle. The correct values of the reluctance torque at angles $\theta_r = 0$ and $\theta_r = \pi$ are zero, and the non-zero values at these positions give an indication of the magnitude of the finite element error. The number of positions plotted still do not present a detailed picture of the waveform shape. Figure 5 presents an experimental plot of the reluctance torque corresponding to $\theta_r = 0 \ldots \pi$. The solid line drawn over the measured points shows that a triangular waveform shape is clearly discernible, with a rounded curve at $\theta_r = \pi/2$. Unfortunately, the magnitudes of the experimental reluctance torque points cannot be compared to those in Table I. This is because the grade of stainless steel used to support the magnet and iron flux guide was discovered to have a small but significant relative permeability of approximately three. This caused more flux to be shunted away from the triangular airgap which reduced the amplitude of the reluctance torque. This effect was not modelled in the finite element analysis to allow comparison.

Reluctance angle θ_r, (rad.)	Torque (Nm)
0	0.019
$\pi/2$	-0.596
π	0.009
$3\pi/2$	0.604

TABLE I

RELUCTANCE TORQUES CORRESPONDING TO THE CONFIGURATION OF FIG. 4.

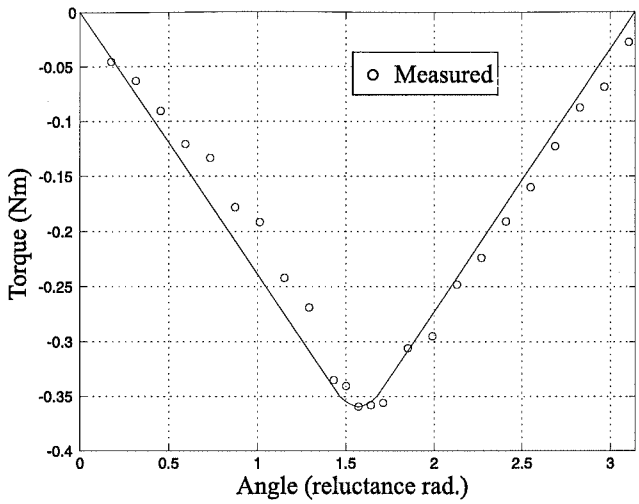

Fig. 5. Experimental measurement of the magnet reluctance torque corresponding to the configuration of Fig. 4.

IV. RECTANGULAR MAGNET AND SINUSOIDAL AIRGAP

A. Axial Magnetisation

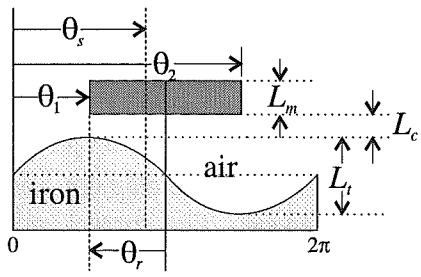

Fig. 6. Rectangular magnet and sinusoidal airgap.

Fig. 6 shows a rolled out view of an axially magnetised permanent magnet and iron structure. The magnet is rectangular and the airgap is sinusoidal. The three dimensional depiction of this axial configuration is similar to that of Fig. 3(a), except that the airgap is modulated sinusoidally for this example. The magnet is uniformly magnetised in the normal (axial) direction, and extends between angles θ_1 and θ_2. The use of variables θ_1 and θ_2 allows the magnet width to be arbitrarily adjusted, under the constraint that $0 \leq \theta_2 - \theta_1 \leq 2\pi$. Again, only the normal flux paths through the magnet, and in the airgap underneath the magnet, are considered. The stored energy is obtained by integration of

the energy across the angular width of the magnet:

$$W = \int_{\theta_1}^{\theta_2} w(\theta_s) d\theta_s \tag{18}$$

where W is obtained using eqn. 9, and B is obtained using eqn. 8. The magnet and airgap lengths in eqn. 8, with reference to Fig. 6, are respectively given by

$$l_m(\theta_s) = L_m \tag{19}$$

$$l_g(\theta_s) = (L_t/2)\Big[1 + \cos(\theta_s - \theta_r)\Big] + L_c \tag{20}$$

The magnet and airgap volumes are represented in a similar manner to the rectangular magnet and triangular airgap configuration shown in Fig. 3(a). For a magnet with an angular width extending from θ_1 to θ_2, the magnet volume up to spatial angle θ_s is given by $V_{pm}(\theta_s) = \frac{1}{2} k_a L_m (\theta_s - \theta_1)$, where k_a is defined by eqn. 13, therefore

$$dV_{pm} = \frac{k_a}{2} L_m d\theta_s \tag{21}$$

The volume of air underneath the magnet up to angle θ_s is given by $V_{air}(\theta_s) = \frac{k_a}{2}(\theta_s - \theta_1) l_{g_{av}}(\theta_s)$ where

$$l_{g_{av}}(\theta_s) = \frac{1}{\theta_s - \theta_1} \int_{\theta_1}^{\theta_s} \left(\frac{L_t}{2}\Big[1 + \cos(\theta_s - \theta_r)\Big] + L_c \right) d\theta_s \tag{22}$$

The derivative of the air volume with respect to θ_s is then obtained as

$$dV_{air} = \frac{k_a L_t}{4}\Big[1 + \cos(\theta_s - \theta_r) + L_c\Big] d\theta_s \tag{23}$$

Eqn. 18 then becomes

$$\begin{aligned} W &= \int_{\theta_1}^{\theta_2} \frac{B_r^2 L_m k_a \left(L_t\Big[1 + \cos(\theta_s - \theta_r)\Big] + 2L_c \right)}{4\mu_\circ \left(2L_m + L_t \mu_r \Big[1 + \cos(\theta_s - \theta_r)\Big] + 2L_c \mu_r \right)} d\theta_s \\ &= \frac{B_r^2 L_m k_a}{2\mu_\circ \mu_r} \left\{ \frac{L_m}{\sqrt{L_m + \mu_r(L_t + L_c)}\sqrt{L_m + \mu_r L_c}} \left[\arctan\left(\frac{\sqrt{L_m + \mu_r L_c}}{\sqrt{L_m + \mu_r(L_t + L_c)}} \tan a \right) \right.\right. \\ &\quad \left.\left. + \varphi_a - \arctan\left(\frac{\sqrt{L_m + \mu_r L_c}}{\sqrt{L_m + \mu_r(L_t + L_c)}} \tan b \right) + \varphi_b \right] - a + b \right\} \end{aligned} \tag{24}$$

where

$$a = \frac{1}{2}(\theta_r - \theta_2) \tag{25}$$

$$b = \frac{1}{2}(\theta_r - \theta_1) \tag{26}$$

and

$$\varphi_a = \left\lfloor \frac{a - \pi/2}{\pi} \right\rfloor \pi + \pi$$

$$\varphi_b = \left\lfloor \frac{b - \pi/2}{\pi} \right\rfloor \pi + \pi$$

where the floor function $\lfloor x \rfloor$ rounds x to the nearest integer towards $-\infty$. φ_a and φ_b are staircase functions, and are included in eqn. 24 in order to aid in the correct numerical evaluation of $\arctan(K \tan\theta)$, when $\theta = a$ or $\theta = b$ are outside the range of $0 \ldots \pi/2$ radians.

From eqn.s 1 and 24, the magnet reluctance torque is then obtained as

$$T(\theta_r) = \frac{k_a B_r^2 L_t}{4\mu_o} \times \left[\frac{\cos^2 a - \cos^2 b}{\cos^2 a \cos^2 b \left(\frac{L_t \mu_r}{L_m}\right)^2 + \frac{L_t \mu_r}{L_m}\left(\cos^2 a + \cos^2 b\right)\left(1 + \frac{L_c \mu_r}{L_m}\right) + \left(\frac{L_c \mu_r}{L_m}\right)^2 + 2\frac{L_c \mu_r}{L_m} + 1} \right] \tag{27}$$

If the ratio's $L_t \mu_r / L_m$ and $L_c \mu_r / L_m$ are small, then the reluctance torque can be approximated as

$$T(\theta_r) \approx \frac{k_a B_r^2 L_t}{4\mu_o}\left(\cos^2 a - \cos^2 b\right) \tag{28}$$

If the angular width of the magnet is bisected at $\theta_s = \pi$, then $\theta_2 = 2\pi - \theta_1$. Substituting $\theta_2 = 2\pi - \theta_1$ into eqn. 25 then gives a as

$$a = \frac{1}{2}(\theta_r - 2\pi + \theta_1) \tag{29}$$

Substituting eqn.s 29 and 26 into eqn. 28 yields

$$T \approx -\frac{k_a B_r^2 L_t}{4\mu_o} \sin\theta_r \sin\theta_1 \tag{30}$$

Eqn. 30 shows that the rectangular magnet and sinusoidal airgap configuration produces a reluctance torque which approximates a sinusoid. In addition, eqn. 30 shows that the amplitude of the torque varies approximately sinusoidally as a function of the angular width of the magnet. Maximum torque amplitude occurs where the magnet angular width is π radians.

B. Radial Magnetisation

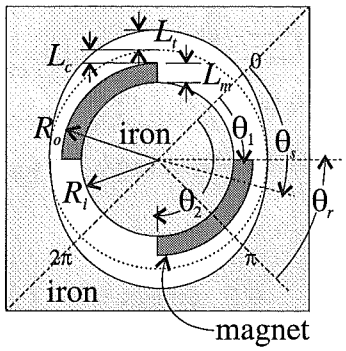

Fig. 7. Rectangular magnet and sinusoidal airgap with radial magnetisation. Two magnets, and two airgap reluctance cycles are drawn, where the angles are in units of reluctance radians.

Fig. 7 shows a rectangular magnet and sinusoidal airgap configuration where the magnets are radially magnetised. Fig. 7 is analogous to Fig. 6 except that two magnets, and two airgap reluctance cycles have been drawn. Again, only the flux paths through the magnets, and in the airgaps radially outside the magnets are considered. The flux density is radial, and its magnitude is again a function of the ratio of magnet to airgap length, in

this case along a radial path. The equations used to construct the stored energy integral are identical to the axial magnetisation example of section IV-A, except that the airgap and magnet volumes are obtained by integrating over cylindrical coordinates. The magnet and airgap volumes can be obtained respectively from

$$V_{pm}(\theta_s) = H_a \int_{\theta_1}^{\theta_s} \int_{R_i}^{R_o} r dr d\theta_s \tag{31}$$

$$V_{air}(\theta_s) = H_a \int_{\theta_1}^{\theta_s} \int_{R_o}^{R_o+(L_t/2)\left[1+\cos(\theta_s-\theta_r)\right]+L_c} r dr d\theta_s \tag{32}$$

where H_a is the axial height of the magnet and airgap, all angles are in units of reluctance radians, and the integrations are performed over only a single airgap reluctance cycle. If the angular width of the magnet is bisected at $\theta_s = \pi$, then $\theta_2 = 2\pi - \theta_1$, and the torque is given by

$$T = \frac{qH_aB_r^2(A+B)}{4\mu_o(C+D)} \tag{33}$$

where

$$\begin{aligned}
A &= 2L_tR_o(v^2-u^2) + L_t^2(v^4-u^4) + 2\tfrac{L_t^3}{L_m^2}R_o\mu_r^2(v^2u^4-v^4u^2) + 2\tfrac{L_t^3}{L_m}(v^4u^2-v^2u^4) \\
&\quad +2\Big(\tfrac{L_t}{L_m}\Big)^3\mu_r^2(R_o^2-R_i^2)(v^4u^2-v^2u^4) + \Big(\tfrac{L_t}{L_m}\Big)^2\mu_r(R_o^2-R_i^2)(v^4-u^4) \\
B &= -2\tfrac{L_t}{L_m^2}\mu_rL_c^2R_o(v^2-u^2) + 2\tfrac{L_t}{L_m^3}\mu_r^2L_c^2(R_o^2-R_i^2)(v^2-u^2) + \\
&\quad 2\tfrac{L_t^2}{L_m^3}\mu_r^2L_c(R_o^2-R_i^2)(v^4-u^4) + 2\tfrac{L_t}{L_m^2}\mu_rL_c(R_o^2-R_i^2)(v^2-u^2) + \\
&\quad 2\tfrac{L_t}{L_m}\mu_rL_c^2(v^2-u^2) + 2\tfrac{L_t^2}{L_m}\mu_rL_c(v^4-u^4) + 2L_tL_c(v^2-u^2) \\
&\quad -2\tfrac{L_t^2}{L_m^2}\mu_r^2L_cR_o(v^4-u^4) \\
C &= \Big(\tfrac{L_t\mu_r}{L_m}\Big)^4u^4v^4 + 2\Big(\tfrac{L_t\mu_r}{L_m}\Big)^3(v^2u^4+v^4u^2) + \Big(\tfrac{L_t\mu_r}{L_m}\Big)^2(4v^2u^2+u^4+v^4) + \\
&\quad 2\tfrac{L_t\mu_r}{L_m}(v^2+u^2) + 1 \\
D &= 6\mu_r^2\tfrac{L_t}{L_m^2}L_c(u^2+v^2) + 2\mu_r^4\tfrac{L_t^3}{L_m^4}L_c(u^2v^4+u^4v^2) + \mu_r^4\tfrac{L_t^2}{L_m^4}L_c^2(u^4+v^4+4u^2v^2) + \\
&\quad 2\mu_r^4\tfrac{L_t}{L_m^4}L_c^3(u^2+v^2) + 6\mu_r^3\tfrac{L_t}{L_m^3}L_c^2(u^2+v^2) + \mu_r^3\tfrac{L_t^2}{L_m^3}L_c(8u^2v^2+2v^4+2u^4) + \\
&\quad \Big(\tfrac{\mu_rL_c}{L_m}\Big)^4 + 4\Big(\tfrac{\mu_rL_c}{L_m}\Big)^3 + 6\Big(\tfrac{\mu_rL_c}{L_m}\Big)^2 + 4\Big(\tfrac{\mu_rL_c}{L_m}\Big) \\
u &= \cos\tfrac{1}{2}(\theta_r-\theta_1) \\
v &= \cos\tfrac{1}{2}(\theta_r+\theta_1)
\end{aligned}$$

and q is the number of airgap reluctance cycles per mechanical cycle. If $L_c = 0$, then $B = D = 0$. If the ratio $L_t\mu_r/L_m$ is assumed to be negligible, then $C = 1$. If the ratio's L_t/L_m, L_t^3/L_m, and L_t^3/L_m^2 are assumed to be negligible, term A is also simplified. If these assumptions are applied, and if $\theta_1 = \pi/2$ such that each magnet is an arc of π reluctance radians, then eqn. 33 reduces to

$$T \approx -\frac{qH_aB_r^2}{4\mu_o}(2R_oL_t + L_t^2)\sin\theta_r \tag{34}$$

and the magnet reluctance torque waveform approximates a sinusoid.

V. Sinusoidal Magnet and Sinusoidal Airgap

Fig. 8 shows a rolled out view of an axially magnetised permanent magnet and iron structure where both the magnet and the airgap have sinusoidal shapes. The magnet is uniformly magnetised in the normal (axial) direction, and extends over a fixed angular

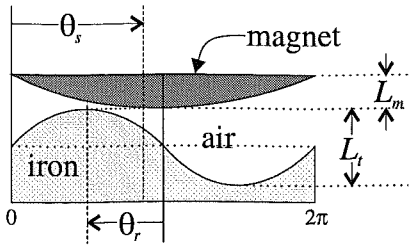

Fig. 8. Sinusoidal magnet and sinusoidal airgap.

width of 2π reluctance radians. An airgap clearance L_c has been neglected in this example. The stored energy is obtained by integrating the energy across the magnet:

$$W = \int_0^{2\pi} w(\theta_s) d\theta_s \tag{35}$$

where W is again obtained using eqn. 9. The magnet and airgap lengths, with reference to Fig. 8, are respectively given by

$$l_m(\theta_s) = L_m \sin \frac{1}{2}\theta_s \tag{36}$$

$$l_g(\theta_s) = (L_t/2)\Big[1 + \cos(\theta_s - \theta_r)\Big] + L_m\Big[1 - \sin \frac{1}{2}\theta_s\Big] \tag{37}$$

The volume of the magnet up to angle θ_s is given by $V_{pm}(\theta_s) = k_a L_m(1 - \cos \frac{1}{2}\theta_s)$, therefore

$$dV_{pm} = \frac{1}{2} k_a L_m \sin \frac{1}{2}\theta_s \, d\theta_s \tag{38}$$

The volume of air underneath the magnet up to angle θ_s is given by $V_{air}(\theta_s) = \frac{1}{2} k_a \theta_s l_{g_{av}}(\theta_s)$, where $l_{g_{av}}(\theta_s)$ is the average airgap length up to angle θ_s, and

$$dV_{air} = k_a \left[\frac{L_m}{2}\Big(1 - \sin \frac{1}{2}\theta_s\Big) + \frac{L_t}{4}\Big(1 + \cos(\theta_s - \theta_r)\Big)\right] d\theta_s \tag{39}$$

Eqn. 35 then becomes

$$W = \int_0^{2\pi} -\frac{B_r^2 k_a L_m \Big\{\Big[2L_m + L_t + \cos(\theta_s - \theta_r) L_t\Big] \sin \frac{1}{2}\theta_s + 2L_m\Big(\cos^2 \frac{1}{2}\theta_s - 1\Big)\Big\}}{4\mu_o\Big[(\mu_r - 1)2L_m \sin \frac{1}{2}\theta_s - 2\mu_r L_m - \mu_r L_t\Big(1 + \cos(\theta_s - \theta_r)\Big)\Big]} d\theta_s \tag{40}$$

With the simplification $\mu_r = 1$, eqn. 40 can, at least, be determined analytically in closed form. However, the solution is very complicated. Fig. 9 plots eqn. 40 integrated numerically for three different values of L_t. The corresponding reluctance torques are also plotted. All three torque waveforms in eqn. 40 are very close approximations of sinusoids. Numerical analysis of eqn. 40 suggests that if the magnet relative permeability μ_r is equal to unity, then there is no appreciable deviation of the torque waveform from a sinusoid. This occurs regardless of the size of the L_t/L_m ratio. However, as μ_r grows larger than one, the torque waveform develops harmonics. This distortion is further increased with the combination of both the ratio L_t/L_m and μ_r increasing. However, for the near unity values of the relative permeabilities of many magnet materials, this distortion is very small.

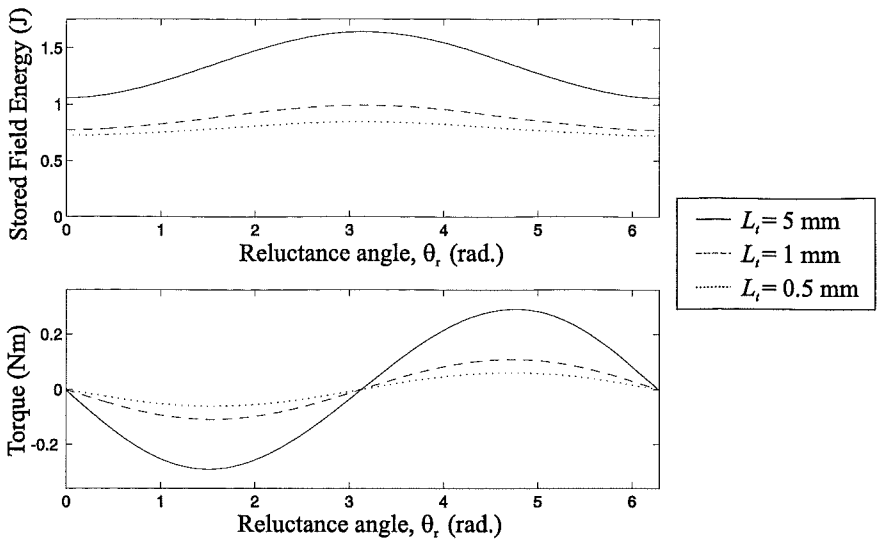

Fig. 9. Sinusoidal magnet and sinusoidal airgap configuration stored energies and torques corresponding to three values of airgap length L_t. For each airgap length, $\mu_r = 1.25$, $L_m = 5$ mm, $B_r = 0.68$ T, and $k_a = 1875\,\text{mm}^2$.

VI. Conclusions

For the axial rectangular magnet/triangular airgap configuration, the magnet reluctance torque is shown analytically to approximate a triangular waveform when $L_m > L_t\mu_r$, where L_m = magnet thickness, L_t = maximum modulated airgap length, and μ_r = relative permeability of the magnet. The approximation improves as the ratio $L_m/L_t\mu_r$ increases. A more complex magnet/iron flux guide/triangular airgap configuration is shown experimentally to produce a triangular reluctance torque.

For the axial rectangular magnet/sinusoidal airgap configuration, the magnet reluctance torque is shown analytically to approximate a sinusoidal waveform where $L_m > L_t\mu_r$. The approximation also improves as the ratio $L_m/L_t\mu_r$ increases. The amplitude of the torque is shown to vary approximately as a sinusoidal function of the angular width of the magnet. Maximum torque amplitude occurs where the magnet angular width is π radians. For the radial rectangular magnet/sinusoidal airgap configuration, an analytical equation for the reluctance torque is derived, and the torque is shown to approximate a sinusoidal waveform.

For the axial sinusoidal magnet/sinusoidal airgap configuration, an integral for the magnetic stored field energy is derived. Numerical analysis of this integral shows that the reluctance torque approximates a sinusoidal waveform. The numerical analysis suggests that there is no appreciable deviation from a sinusoidal torque with respect to the ratio L_m/L_t if μ_r is approximately equal to one.

The analysis in this paper is not generally applicable to magnet reluctance torque problems, such as cogging torque, unless the magnet field density can be described accurately by analytical method. However, if a triangular or sinusoidal magnet reluctance torque waveform is required, this paper describes how such a waveform can be obtained.

References

[1] D. C. White and H. H. Woodson, *Electromechanical Energy Conversion*, John Wiley & Sons, p. 21, 1959.

[2] D. Howe and Z. Q. Zhu, "Influence of finite element discretisation on the prediction of cogging torque in permanent magnet excited motors," *IEEE Trans. Magn.*, vol. 28, no. 2, pp. 1080–1083, 1992.

REFERENCES

ALTENBERND, G. (1991), 'Actual aspects of the development of fractional horse-power single phase synchronous motors with permanent magnetic rotor', *Internat. Conf. on the Evolution and Modern Aspects of Synchronous Machines*, Vol. 3, pp. 1083–9.

ALTENBERND, G. AND MAYER, J. (1990), 'Starting of fractional horse-power single-phase synchronous motors with permanent magnet rotor', *Electrical Drives Symposium*, Capri, Italy, Sept., pp. 131–137.

ALTENBERND, G. AND WAHNER, L. (1996), 'Power range of fractional horse-power synchronous motors with permanent magnetic rotor and one pole pair', *SPEEDAM*, Capri, Italy, 5-7 June, pp. 17–21.

BERTRAM, L. AND SCHEMMANN, H. (1976), 'Single-phase synchronous motors for pump drives', *IEE Conf. on Small Electrical Machines*, London, March, pp. 39–41.

BEVAN, T. (1962), *The Theory of Machines*, Longmans, London, 3rd ed.

BINNS, K.J. AND LAWRENSON, P.J. (1963), *Analysis and Computation of Electric and Magnetic Field Problems*, Pergamon Press, Oxford.

BRAUER, J.R. (Ed.) (1988), *What Every Engineer Should Know About Finite Element Analysis*, Marcel Dekker, Inc, New York.

BRAUER, J.R., LARKIN, L.A. AND OVERBYE, V.D. (1984), 'Finite element modeling of permanent magnet devices', *J. Appl. Phys.*, Vol. 55, No. 6, pp. 2183–2185.

BROWN JR., W.F. (1962), *Magnetostatic Principles in Ferromagnetism*, North-Holland.

CHIKAZUMI, S. (1964), *Physics of Magnetism*, John Wiley & Sons, New York.

CULLITY, B.D. (1972), *Introduction to Magnetic Materials*, Addison-Wesley.

DIEFENBACH, G. AND SCHEMMANN, H. (1989), 'Hybrid simulation of appliances driven by single phase synchronous motors', *3rd European Simulation Congress*, Edinburgh, Sept., pp. 426–432.

DOHERTY, R.E. AND PARK, R.H. (1926), 'Mechanical force between electric circuits', *Trans. AIEE*, Vol. 45, pp. 240–252.

EDWARDS, J.D. (1986), *Electrical Machines: An Introduction to Principles and Characteristics*, MacMillan, London, 2nd ed.

ELMQVIST, H., ASTROM, K.J., SCHONTHAL, T. AND WITTENMARK, B. (1990), *SIMNON User's Guide for MS-DOS Computers Version 3.0*, SSPA Systems, Goteborg, Sweden, Jan.

ERVENS, W. AND WILMESMEIER, H. (1985-1994), 'Magnetic materials', In GERHARTZ, W. (Ed.), *Ullman's Encyclopedia of Industrial Chemistry*, VCH Publishers, Deerfield Beach, FL, USA.

FEUCHT, D.L. (1993), 'Sensorless start-up positioning of brushless motors', *Power Conversion and Intelligent Motion*, March.

FITZGERALD, A.E., KINGSLEY, C. AND UMANS, S.D. (1983), *Electric Machinery*, McGraw-Hill, New York, 4th ed.

FORSYTHE, G.E., MALCOLM, M.A. AND MOLER, C.B. (1977), *Computer Methods for Mathematical Computations*, Prentice-Hall.

GIERAS, J.F. AND WING, M. (1997), *Permanent Magnet Motor Technology - Design and Applications*, Marcel Dekker, Inc., New York.

GUPTA, R., YOSHINO, T. AND SAITO, Y. (1990), 'Finite element solution of permanent magnetic field', *IEEE Trans. on Magn.*, Vol. 26, No. 2, March, pp. 383–386.

HAMDI, E.S. (1994), *Design of Small Electrical Machines*, John Wiley & Sons, New York.

HENDERSHOT, J.R. AND MILLER, T.J.E. (1994), *Design of Brushless Permanent Magnet Motors*, Magna Physics & Clarendon Press, Oxford.

HOWE, D. AND ZHU, Z.Q. (1992), 'Influence of finite element discretisation on the prediction of cogging torque in permanent magnet excited motors', *IEEE Trans. Magn.*, Vol. 28, No. 2, pp. 1080–1083.

HUGHES, E. (1960), *Electrical Technology*, Longmans, London.

JABBAR, M.A., TAN, T.S. AND BINNS, K.J. (1992), 'Recent developments in disk drive spindle motors', *International Conference on Electrical Machines*, Manchester, UK, Sept., pp. 381–85.

JAHNS, T.M. AND SOONG, W.L. (1996), 'Pulsating torque minimization techniques for permanent magnet ac motor drives - a review', *IEEE Trans. Ind. Electron.*, Vol. 43, No. 2, April, pp. 321–330.

JONES, C.V. (1967), *The Unified Theory of Electrical Machines*, Butterworths, London.

KAMERBEEK, E.M.H. (1973), 'Electric motors', *Philips Techn. Rev.*, Vol. 33, No. 8/9, pp. 215–234.

KREYSZIG, E. (1988), *Advanced Engineering Mathematics*, John Wiley & Sons, New York, 6th ed.

LEE, P.W. AND POLLOCK, C. (1992), 'Rotor position detection techniques for brushless permanent-magnet and reluctance motor drives', In *Proceedings of the IEEE Industry Applications Society Annual Meeting*, Houston, TX, USA, pp. 448–55.

LI, T. AND SLEMON, G. (1988), 'Reduction of cogging torque in permanent magnet motors', *IEEE Trans. Magn.*, Vol. 24, No. 6, pp. 2901–2903.

LOWTHER, D.A. AND SILVESTER, P.P. (1986), *Computer-Aided Design in Magnetics*, Springer-Verlag, Berlin.

MAGNET 5.2 (1996), *MagNet 5.2 finite-element package for electromagnetic analysis*, Infolytica Corporation, Montreal.

MARINESCU, M. AND MARINESCU, N. (1988), 'Numerical computation of torque in permanent magnet motors by maxwell stresses and energy method', *IEEE Trans. Magn.*, Vol. 24, No. 1, pp. 463–466.

MATLAB (1994), The MathWorks, Inc, Mass., USA. version 4.2c.

MATSUI, N. AND TAKESHITA, T. (1994), 'A novel starting method of sensorless salient-pole brushless motor', *Conf. Record of the 1994 Industry Applications Twenty-Ninth IAS Annual Meeting*, Denver, Co, USA, pp. 386–92.

MAXWELL, J.C. (1891), *A Treatise on Electricity and Magnetism*, Vol. II, Art. 583, (republished Dover, New York, 1954, 3rd ed.).

MAYER, J.S. AND WASYNEZUK, O. (1989), 'Analysis and modelling of a single-phase brushless dc motor drive system', *IEEE Trans. on Energy Conversion*, Vol. 4, No. 3, pp. 473–479.

MCPHERSON, G. (1981), *An Introduction to Electrical Machines and Transformers*, John Wiley & Sons, New York.

MILLER, T.J.E. (1989), *Brushless Permanent-Magnet and Reluctance Motor Drives*, Oxford University Press.

MOHAN, N., UNDELAND, T.M. AND ROBBINS, W.P. (1989), *Power Electronics: Converters, Applications, and Design*, John Wiley & Sons, New York.

NASAR, S.A. AND UNNEWEHR, L.E. (1983), *Electromechanics and Electric Machines*, John Wiley & Sons, New York.

PECKNER, D. AND BERNSTEIN, I.M. (1977), *Handbook of Stainless Steels*, McGraw-Hill, New York.

RAMO, S., WHINNERY, J.R. AND DUZER, T.V. (1994), *Fields and Waves in Communication Electronics*, John Wiley & Sons, New York, 3rd ed.

SAY, M.G. AND NASAR, S.A. (1987), In NASAR, S.A. (Ed.), *Handbook of Electric Machines*, McGraw-Hill, New York, Chap. 1.

SCHEMMANN, H. (1971), *Theoretische Und Experimentelle Untersuchungen Uber Das Dynamische Verhalten Eines Einphasen-Synchron-Motors Mit Dauermagnetischem Laufer*, PhD thesis, Technische Hogeschool, Eindhoven, Oct.

SCHEMMANN, H. (1973), 'Stability of small single phase synchronous motors', *Philips Techn. Rev.*, Vol. 33, No. 8/9, pp. 235–243.

SILVESTER, P. (1968), *Modern Electromagnetic Fields*, Prentice-Hall, Englewood Cliffs, NJ, USA.

STEINMETZ, C.P. (1911), 'Mechanical forces in magnetic fields', *Trans. AIEE*, Vol. 30, pp. 357–413.

STRATTON, J.A. (1941), *Electromagnetic Theory*, McGraw-Hill, New York.

THEES, R. (1965), 'Small electric motors', *Philips Techn. Rev.*, Vol. 26, No. 4/5/6, pp. 143–147.

VEINOTT, C.G. (1987), 'Small electric motors', In NASAR, S.A. (Ed.), *Handbook of Electric Machines*, McGraw-Hill, New York, Chap. 6.

VEINOTT, C.G. AND MARTIN, J.E. (1986), *Fractional and Subfractional Horsepower Electric Motors*, McGraw-Hill, New York, 4th ed.

WHITE, D.C. AND WOODSON, H.H. (1959), *Electromechanical Energy Conversion*, John Wiley & Sons, New York.

WOODSON, H.H. AND MELCHER, J.R. (1968), *Electromechanical Dynamics Part I: Discrete Systems*, John Wiley & Sons, New York.

ZIJLSTRA, H. (1982), 'Permanent magnets; theory', In WOHLFARTH, E.P. (Ed.), *Ferromagnetic Materials*, North-Holland, Chap. 2.